Prediction of Propeller-Induced Hull-Pressure Fluctuations

Proefschrift

ter verkrijging van de graad van doctor
aan de Technische Universiteit Delft,
op gezag van de Rector Magnificus Prof.ir. K.C.A.M. Luyben,
voorzitter van het College voor Promoties,
in het openbaar te verdedigen op vrijdag 25 november 2011 om 12:30 uur

door

Hendrik Cornelis Jacobus VAN WIJNGAARDEN

Werktuigbouwkundig Ingenieur
geboren te Utrecht

On the cover: *video snapshot of a cavitating propeller* (container vessel #2 in this thesis)

CONTENTS

1 INTRODUCTION

…in which the cavitating propeller is identified as a major source of noise and vibration on board ships. The importance of accurately predicting propeller-induced vibratory hull forces is explained along with the need for improved prediction techniques based on scale model experiments and computer simulations. Several topics are selected for further investigation.

1.1 Noise and Vibration on Board Ships

Noise and vibration on board ships may cause discomfort to passengers and crew. It may also impair the efficient execution of the crew's duties, be the cause of damage to sensitive equipment, structural parts of the ship and cargo, and even compromise the safety of the vessel [Asmussen2001]. Nowadays, people on board are less willing to accept discomfort due to noise and vibration, leading to increasingly strict requirements. As these are usually not easily met, noise and vibration have become important factors in ship design [DnV2003].

Noise and vibration levels are determined by the characteristics of source, transmission and receptor. Low frequency noise and vibration (say, up to a few hundred Hz) are notoriously hard to damp and addition of mass and stiffness in the 'remedial' design stage is costly and cumbersome, if at all possible. Therefore, noise and vibration problems must be avoided through identification and treatment of the major sources during early design stages of the vessel.

The cavitating propeller often forms the primary source of noise and vibrations [ISSC2006]. The ship propeller acts as a source in various ways. One way is that time-varying shaft forces and moments directly excite the ship through the driving train (viz., the bearings and thrust block). Another way, and the focus of this thesis, is that the cavitating propeller causes pressure fluctuations in the surrounding water, which are transmitted as hydroacoustic waves to the hull plating above the propeller, which they excite.

Propeller blades passing underneath the afterbody cause pressure fluctuations by their displacement effect as well as by the load they carry. When the local pressure in the water is low enough for it to evaporate, a phenomenon called *cavitation*, vapor pockets are generated. These vapor pockets are known as *cavities*. Due to variations in ambient pressure and blade loading during a revolution, the cavities may rapidly change in volume and location over time, thus causing pressure fluctuations in the surrounding water. Figure 1.1 presents an overview of the types of cavitation that may occur on or in the immediate vicinity of propeller blades. The great majority of ship propellers suffers from sheet and tip vortex cavitation, which are the

prime cause of propeller-induced excitation forces. Although propeller-hull vortex cavitation can cause much higher pressure pulses on the hull surface, it is far less often encountered.
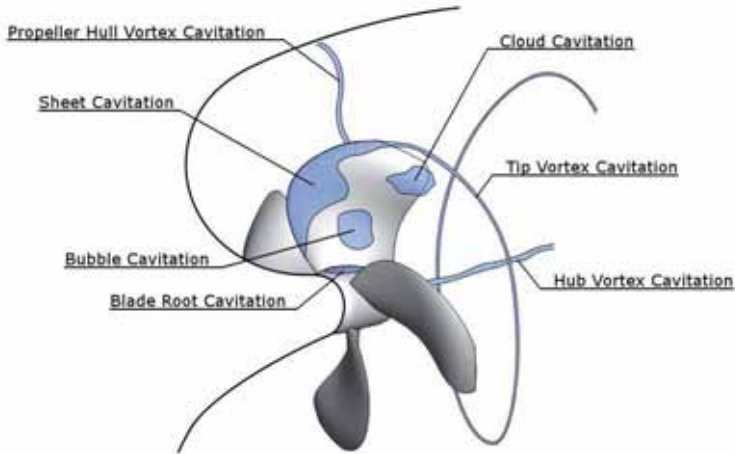
Figure 1.1: Types of cavitation that may appear on propellers.

In order to meet comfort requirements, propeller cavitation must be reduced by making adjustments to the ship and propeller design. This is often accompanied by a reduction of propulsive efficiency. Ligtelijn [Ligtelijn2010] roughly estimates such efficiency losses to be in the range of 5 to 10%. The design relies heavily on how comfort and propulsive efficiency are balanced. Therefore, the accurate prediction of efficiency and propeller-induced hull-excitation forces is essential in the assessment of the ship design.

It is the task of ship model basins to assist the ship designer, yard and ship owner in testing the ship design with regard to specific contract requirements. For this purpose model basins have developed prediction capabilities, which involve tests on scale models of ships as well as computational simulations of the hydrodynamics involved. Although model basins have often been quite successful in employing their predictive capabilities, this is not generally the case [Ligtelijn2004/2006]. Several fundamental problems are still hampering a more accurate prediction of propeller-induced excitation forces. This may lead to comfort levels inferior to those listed in contract specifications, or to efficiency losses greater than expected or necessary.

Therefore, an investigation of a number of important limiting factors in the prediction of propeller-induced excitation forces is well justified, also in light of the development of fuel prices. The main objective of the present thesis can thus be stated as,

> *the development of improved prediction capabilities for propeller-induced hull-excitation forces based on experimental and computational procedures.*

After all, as Richard P. Feynman put it, '*the test of science is its ability to predict*'.

An outline of the thesis, which also serves as a plan of approach for the investigations, is presented in the next section.

1.2 Outline of Thesis

At present, predictions of propeller-induced hull-pressure forces do not give consistently accurate results. In search of the major sources of uncertainty, Chapter 2 uses the proceedings of the *International Towing Tank Conference* (ITTC) to provide some background on the state-of-the-art concerning propeller hydrodynamics, cavitation, acoustic radiation and scattering, as well as their computational and experimental simulation in scale model tests performed in towing tanks and cavitation tunnels. From knowledge thus obtained, a set of research topics can be selected of which a number is treated in this thesis:

- model to full scale correlation procedures involving the determination of the propeller's source strength;
- the scale effect on the effective wake and its influence on sheet cavity dynamics;
- the influence of hull vibrations on measurements of hull pressures; and,
- the development of practical numerical methods for the simulation of propeller-induced hull-pressures.

Further research topics, e.g.,

- cavitating vortex dynamics; the use of two-phase flow numerical methods;
- advanced data reduction techniques for the analysis of broadband excitation; and,
- the effect of nuclei and gas content on cavitation inception and dynamics.

are investigated by Bosschers and Van Rijsbergen, all within the scope of a background research programme at the *Maritime Research Institute Netherlands* (MARIN). In the present thesis, cavitation inception issues are not studied in detail. It is tacitly assumed that whenever the propeller causes serious noise and vibration problems, cavitation is well-developed, also on model scale.

Chapter 3 presents a theoretical framework for the description of propeller-induced hull-pressures for use in computational simulation methods. From a variety of mathematical models, a choice is made on the basis of the model's ease of use, low computational cost and expected predictive capability. The selected mathematical models are converted into two computational methods, both based on the potential flow assumption. The methods employ the *Boundary Element Method* (BEM, also known as the *surface panel method*) for the discretization. One method is used for the numerical simulation of propeller flows. It is called PROCAL (*PROpeller CALculator*) and has been developed by Vaz and Bosschers. The other method is for the acoustic scattering effect of the hull and free surface. It is called EXCALIBUR (*EXcitation CALculation with Improved BURton and Miller method*) and was developed by the author.

Chapter 4 reviews prediction procedures practiced in scale model experiments with an assessment of sources of measuring and modeling error causing uncertainty in predictions. One such source is treated in Chapter 5, in which it is shown how the scale model vibratory response to propeller excitation forces causes a possibly significant parasitic contribution to the measured hull-pressure field. An approach based on the EXCALIBUR computational

method is taken to eliminate the vibration-induced pressure field using measurements of hull-surface vibrations.

Chapter 6 describes experiments performed in the *Depressurized Towing Tank* (DTT) of MARIN for the validation of the numerical methods described in Chapter 3. Cases involving non-cavitating propellers are used.

Chapter 7 takes up the issue of the scale effect on the ship's wake, which is hypothesized to be the most important cause of inaccuracy in the prediction of hull-excitation forces. It is studied how the scale effect on the wake field, caused by failing to adhere to the full scale flow Reynolds number similarity in model scale experiments, mainly affects propeller loading, hence cavitation dynamics and eventually hull-pressure fluctuations. Sheet cavitation is considered. The chapter treats a first attempt to use a RANS (*Reynolds Averaged Navier-Stokes*) method to inversely design a scale model hull that generates a wake field more closely resembling the ship scale target wake field than do the geometrically similar hull models that are conventionally used. As a demonstration, a scale model hull of a container vessel has been designed, manufactured and tested in the DTT. The results obtained from the latter test case are used to further validate the numerical methods used in Chapter 6 for a propeller operating in cavitating conditions.

Having developed ways of improving the prediction of propeller-induced hull-pressure fluctuations, a correlation study is needed to judge their effect in practice. As a preamble to such a study, Chapter 8 gives a critical account of the way in which measured hull-pressure amplitudes are compared with maximum allowable values specified in contracts. For comparative purposes as well as to judge the accuracy of predictive hull-pressure data, it is advocated that they must be converted into meaningful figures of merit regarding excitation forces and acoustic source characteristics. The use of propeller source strengths and hull forces are proposed for this purpose. Ways of modeling the propeller action are studied, including cavitation, by means of acoustic point sources, the strengths of which are proposed as a basis for comparing hull vibratory excitation predictions and reality. To this end, the acoustic Boundary Element Method developed is used in an inverse way with measured hull-pressure data as input and source strengths as output. This enables the distinction of the main contributing source types to the pressure field. The concept of the inversely determined propeller source strength is also used to derive the complete pressure distribution on the hull based on a scarce set of measuring data. Thus, the forcing terms for input into Finite Element Analyses (FEA) are produced.

Chapter 9 finalizes the thesis by drawing conclusions regarding the quality of prediction methods in use at present, and improved procedures for predicting fluctuating hull pressures from model tests and computations. Recommendations are made for further research.

2 PREDICTION OF HULL-PRESSURE FORCES

…in which the past and present state-of-the-art in the prediction of propeller-induced hull-pressure forces is reviewed. Topics are identified that need further improvement.

2.1 Introduction

Although an account of propeller design is beyond the scope of this thesis, it is important to understand that comfort requirements have to be treated in conjunction with propulsive and safety requirements. Figure 2.1 schematically shows where the propeller-induced fluctuating hull-pressure field (encircled in red) appears in the evaluation of a propeller design. Propulsive requirements aim at achieving the ship's design speed at a target propeller RPM ('*Revolutions Per Minute*') and at the lowest possible power. Safe operation requires the propeller to stay intact while maintaining its function. This practically means that parts should not fail structurally or erode and blade spindle torques should not preclude making necessary pitch changes. Comfort requirements, finally, limit noise and vibration levels. Limiting hull vibration levels are given by the ISO 6954 guideline [ISO1984/2000]. Also blade singing, caused by resonances induced by vortex shedding at the blade's trailing edge, must be safeguarded against. Contractual specifications may include limitations on vibratory excitation forces of shafts and bearings, but also on fluctuating hull-excitation forces or pressures.

In Figure 2.2, a breakdown is made of the hull-pressure field's constituents with an indication of significance. Causes of fluctuating hull-pressures not induced by the propeller, such as free surface wave impacts and turbulent boundary layer flow are not considered (see item '*Flow-induced*' in Figure 2.2). The two main causes of propeller-induced hull-pressure fluctuations are indicated as '*Blade passages*', with a lower importance, and '*Cavity dynamics*', which is later shown to be of a higher importance. Propeller blade passages exert fluctuating pressures on the hull due to the blades' displacement and loading. The main contribution to hull pressures is in the form of cavity dynamics, which can be divided into contributions from sheet cavitation dynamics and tip or leading edge vortex pulsations[1].

For a proper prediction of hull vibratory forces, a chain of cause and effect relations must be considered. The chain runs from the effective ship wake field at the location of the propeller disc, via the propeller design, its operating conditions and the resulting cavitation dynamics to the radiation of pressure fluctuations and the formation of the hull-pressure field

---

[1] The strong interaction between sheet and vortex cavity dynamics in modern propellers often precludes the suggested break-down, a fact that makes the experimental study of either one of them in isolation difficult in practical cases.
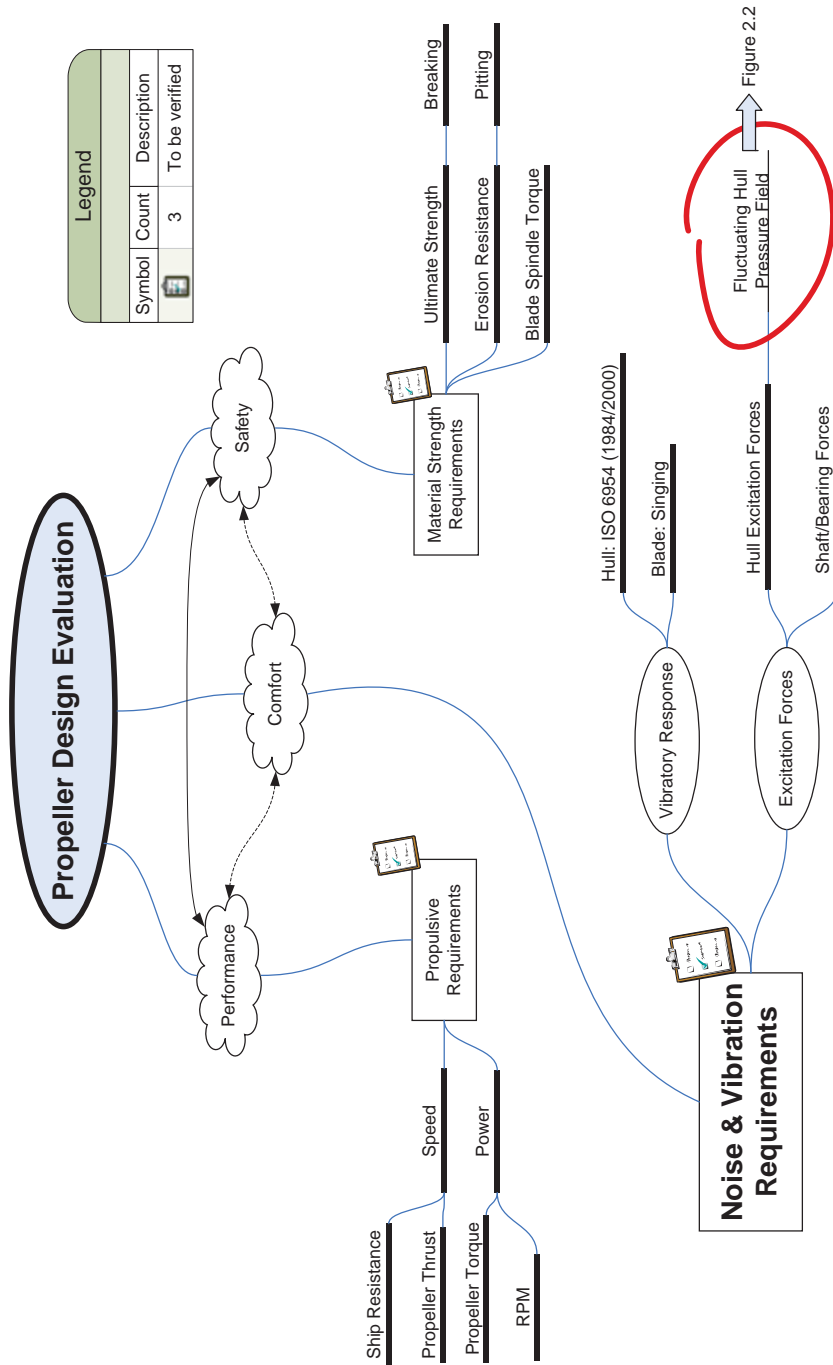
Figure 2.1: Hull pressures in propeller design evaluation (continued in Figure 2.2).
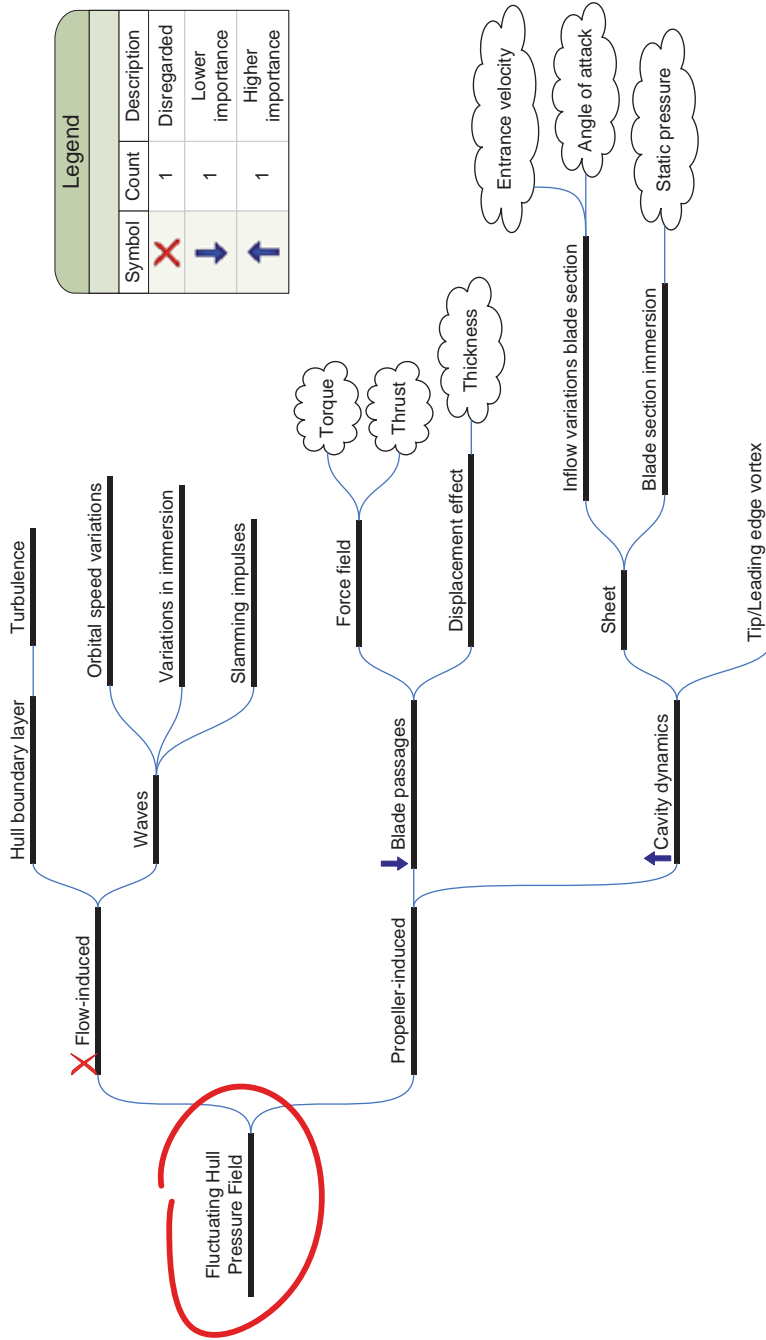
Figure 2.2: Break-down of the fluctuating hull-pressure field (continuation from Figure 2.1).
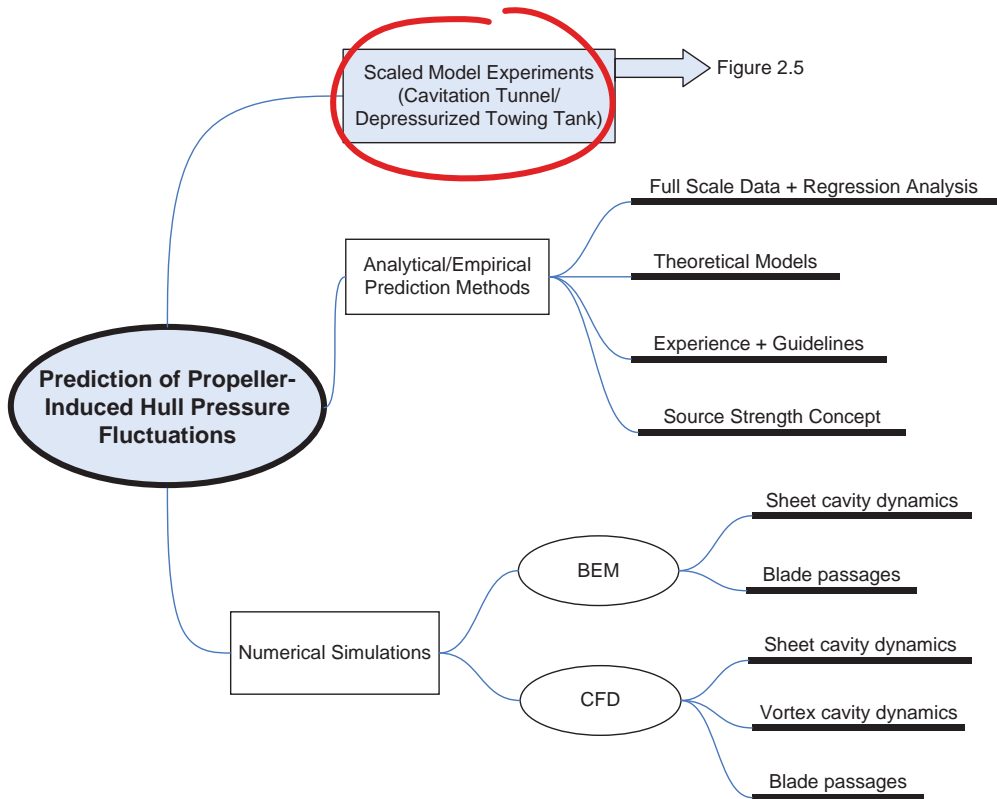
Figure 2.3: Prediction of propeller-induced ship hull forces (continued in Figure 2.5).

itself [Wijngaarden2005]. After spatial integration over the afterbody the vibratory hull force results.

The prediction of hull-excitation forces can be performed by empirical, numerical and experimental means (see Figure 2.3). The empirical approach involves analytical models in which full scale data is often used to determine regression coefficients. Empirical methods may be used to predict the pressures or forces on the hull directly, or to deliver values for propeller acoustic source strengths. The numerical approach involves elaborate computer codes based on, e.g., the Boundary Element Method or viscous flow methods from the field of *Computational Fluid Dynamics* (CFD). The experimental approach centers around scale model testing in cavitation tunnels or depressurized towing tanks (encircled in red). As an example of the latter type of testing facility, Figure 2.4 shows the DTT at MARIN. The top picture shows a drawing of the towing tank with the harbor (bottom left picture) from which the ship models are launched. The grey measuring frame connects to the ship model and enters the air lock after which evacuation takes place. Then, the measuring frame enters the evacuated towing tank and connects to the towing carriage (i.e., the blue frame in the bottom right picture).
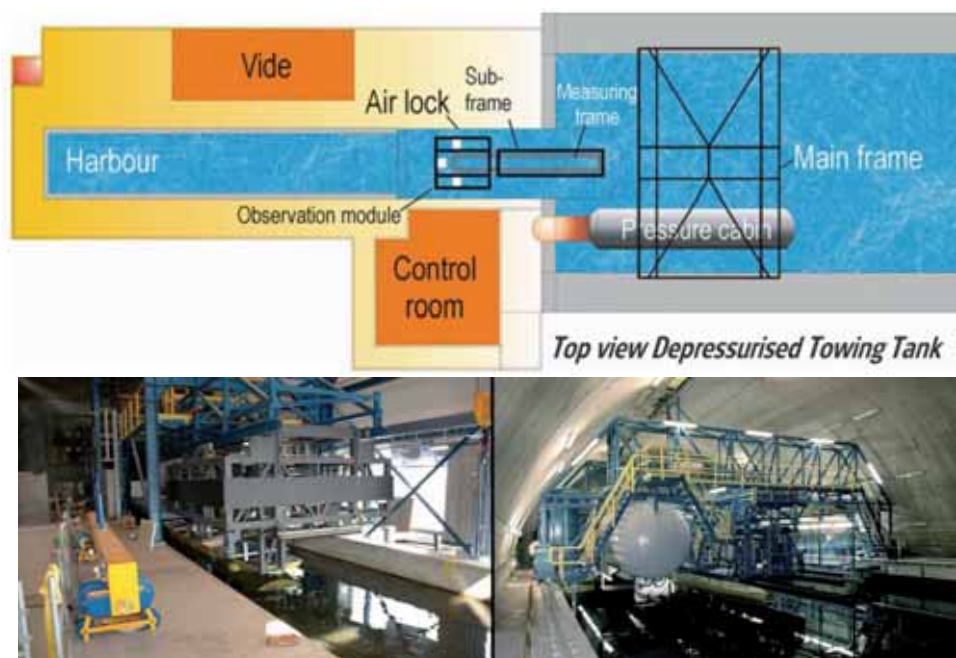
Figure 2.4: Depressurized Towing Tank of MARIN (bottom left: harbor; bottom right: carriage).

The prediction of hull pressures by experimental means is further elaborated in Figure 2.5, where several factors are indicated that affect the quality of the predictions made in an experimental cavitation facility. For the correct model scale representation of the source, both cavity dynamics and blade passage effects should be modeled. This means meeting certain geometric, kinematic and dynamic similarity conditions[2]. Blade passage effects are determined by blade thickness and loading, both of which are modeled in most facilities by accurate geometric similarity of the propeller, ship and appendages, and applying the correct propeller thrust loading. In a towing tank, propeller revolutions are set according to the Froude number, thus preserving the ratio of gravity and inertia forces on model scale. Similarity of the ratio of inertia and viscous forces as expressed in the Reynolds number is not feasible and is a cause of error.

Cavitation effects are much harder to reproduce. Achieving dynamic similarity is the most challenging, demanding that also the pressure in excess of the vapor pressure, i.e., the *pressure reserve*, be scaled according to the cavitation number. Simultaneously maintaining Froude number similarity and cavitation number identity is not a conflicting requirement in a depressurized towing tank. Reynolds number identity is, however, impossible to achieve and inevitably leads to scaling issues. In this respect, think of scale effects on the propeller inflow leading to deviations from similarity of entrance velocity and angle of attack. Also the proper inception of cavitation may be delayed because of Reynolds number disparity. Especially, the inception of vortex cavities is affected by this.

---

[2] The reader is referred to Chapter 4 for details on scaling parameters involved in model testing.
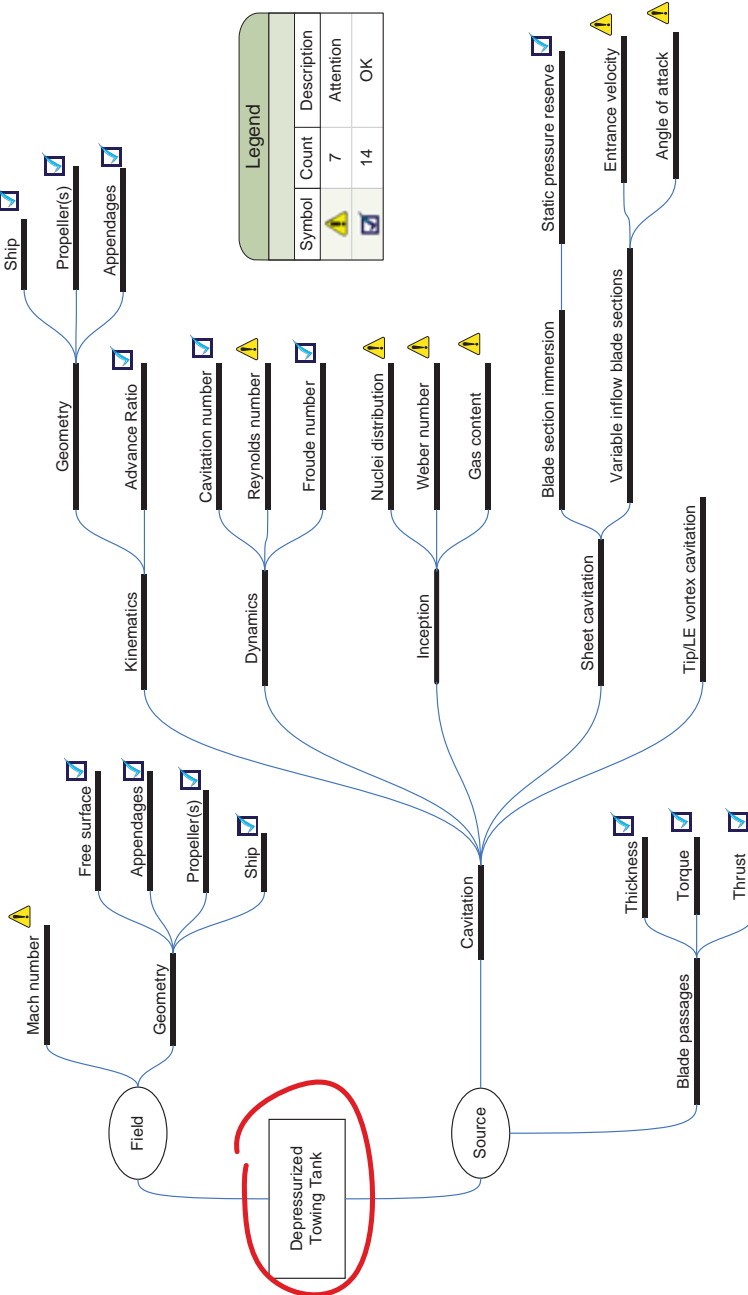
Figure 2.5: Scale model testing (continuation from Figure 2.3). Check marks are placed behind items that are generally not considered to cause significant prediction errors, whilst warning signs are placed when scaling errors may indeed occur.

Other inception issues are related to non-similar gas content and nuclei size distributions. A lack of similarity in Weber number may cause delayed cavitation inception.

For the correct model scale representation of the radiated pressure field, geometric similarity of diffracting bodies is required (ship, free surface, but also unwanted tank or tunnel wall reverberation effects). Also interference effects should be modeled by adhering to Mach number identity. The latter requirement conflicts with that imposed by Froude number equivalence and may therefore be another source of error.

Instead of further elaborating on all of these issues at this stage, the ones that impose the most stringent limitations on the accuracy of predictions must be identified and studied. For that purpose, the next section uses the research literature reviews that are available through the ITTC proceedings.

2.2 Research Efforts in Historical Perspective

In the past, when considering ways in which the propeller action could excite the aft body structure, the fluctuating pressure field induced by the blades passing the hull surface would have come to mind first. This pressure field is built up of components related to the blade thickness and thrust loading, showing a rotating displacement and force field effect. As a consequence of the source motion, the fluctuating pressure field on the hull surface in the immediate vicinity of the blades shows large phase differences across the area. Hence, the net vibratory force production remains limited. Locally, however, the excitation pressures may be substantial.

Until the end of the 1960s, scale model testing focused on the measurement of the non-cavitating propeller-induced hull-pressure field above the propeller (see Figure 2.6). The effect of cavitation on the performance of propellers (i.e., thrust breakdown) was well-understood when the 3rd ITTC [ITTC1935] stated that propeller back cavitation '*may exist to an appreciable extent before it is visible in the performance characteristics. That is there may be a condition giving very satisfactory trial results but yet producing considerable blade erosion.*' Apparently, one was well aware of some of the detrimental effects of cavitation, but not of its influence on noise and vibration hindrance. Since then, many cavitation tunnels were built with a view to the study of cavitation thrust breakdown and erosion. At the 9th ITTC [ITTC1960], Burrill started his contribution on model to ship correlation for (erosively) cavitating propellers stating that '*two of the primary functions of a propeller cavitation tunnel are to supply information about thrust and torque coefficients when there is cavitation breakdown, and to offer guidance on the reduction of cavitation erosion.*'

The first time the ITTC proceedings gave an account of propeller-induced vibratory surface forces was at the 11th ITTC [ITTC1966] where Schwanecke wrote: '*The exciting pressure fluctuations at the hull plating close to the propeller, the bossings, rudders, etc. will be found out either by model tests and full scale experiments respectively by means of inductive or strain gauge mounted pressure pickups or they will be found out by calculating the propeller pressure near field by means of the potential theory. Within the last year computer programs have been developed by which the pressure fluctuations for nearly all types of ships' hulls can be calculated, but presently without considering the wake. The results of these calculations show, that the prevailing portion of the pressure fluctuations has*

Figure 2.6: Time line showing important research events.

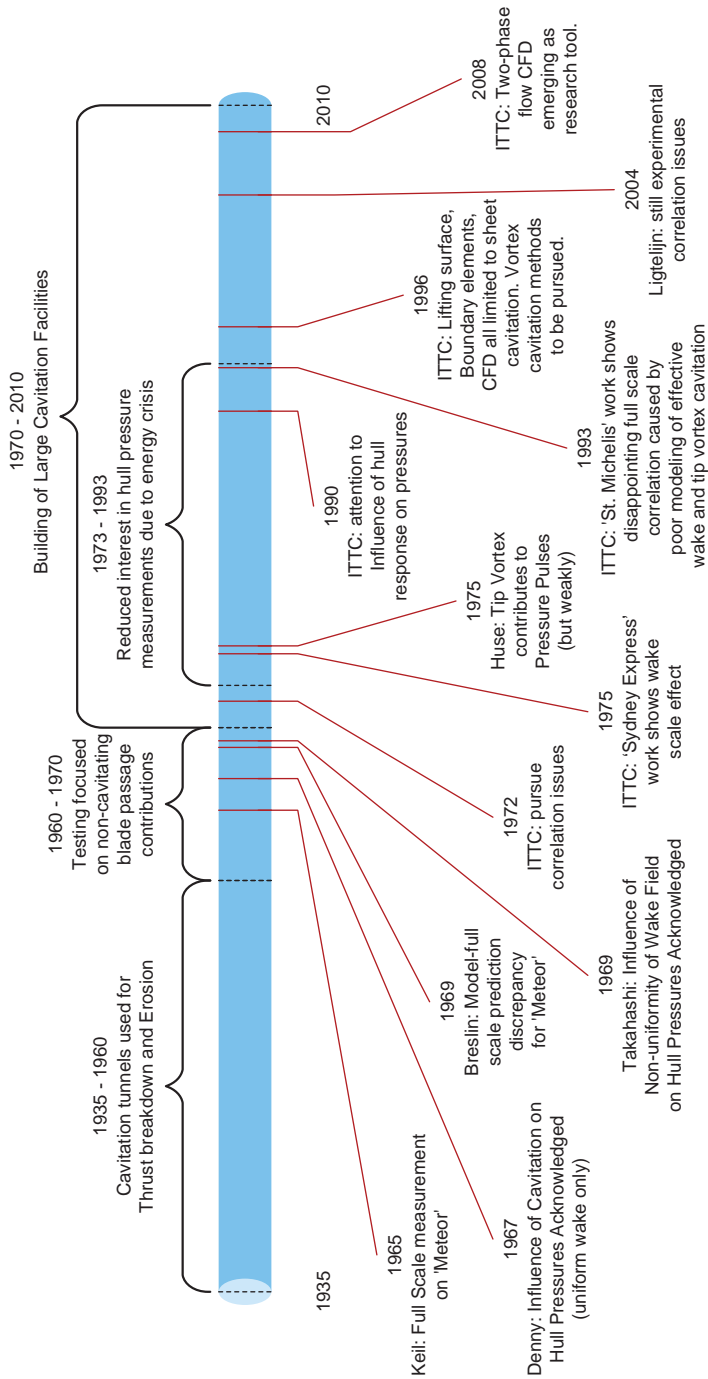*a frequency corresponding to the product of number of blades and number of revolutions. The pressure fluctuations with frequencies corresponding to multiples of the aforementioned product have been found out to be of less importance. Model experiments have shown the great importance of the lower harmonics of the wake distribution on the pressure amplitudes. That means, a scale effect is taken into consideration when the exciting pressure fluctuations will be found out by model tests. The main parameters for the exciting pressure fluctuations are propeller loading, radial load distribution, diameter, number of blades, blade thickness, number of revolutions, tip clearance, and axial clearance before and behind the propeller. Owing to the blade thickness the pressure maximum is shifted slightly abaft the propeller plane. Measurements performed with highly loaded propellers have shown but small differences of the exciting amplitudes at the hull plating for propellers differing only with respect to the number of blades.*' Despite the remark that computations disregarded the non-uniformity of the wake, many research groups had then already started the development of lifting surface methods for propellers operating in non-uniform wakes.

Meanwhile, full scale data on pressure fluctuations had been measured by Keil on '*Meteor*' [Keil1965]. The measured amplitudes were five to eight times those measured on a flat plate. Comparable model measurements were only reasonable below a certain RPM as Breslin reported in the 12th ITTC proceedings [ITTC1969]. In the written contribution of these proceedings Takahasi and Ueda reported on a study of the influence of cavitation on fluctuating surface pressures. They measured pressures on a flat plate above a propeller in a cavitation tunnel and compared pressure amplitudes for cavitating and non-cavitating conditions in uniform and non-uniform flow. It was concluded that '*the fluctuating pressures around the propeller are considerably influenced by the cavity on the propeller blade.*' In the case of the uniform wake the added thickness effect of the sheet cavity was considered to be the cause of the pressure difference, whereas in the non-uniform case the cavity pulsations in reaction to the varying inflow were assumed to generate pressure pulses. Denny [Denny1967] had already published the results of a similar investigation, although no results were presented for cavitating propellers in non-uniform flow.

After these publications, the study of the prediction of propeller-induced hull-pressure forces became widespread. The 13th ITTC [ITTC1972] recommended continuing to correlate propeller-induced pressures on hulls, and to investigate the effects of propeller cavitation on fluctuating forces and moments and the instantaneous pressures on nearby hull surfaces. Having become well aware of the importance of a correct representation of the propeller effective wake field model basins started building large cavitation research facilities in which complete geometrically scaled ship models (so-called '*geosims*') could be tested.

By the time of the 14th ITTC [ITTC1975] it had become clear '*that propeller cavitation has only a minor effect on the bearing forces. It may, however, be of major importance in determining the hull surface forces.*' A great many publications on the subject had appeared by then. Huse wrote an overview in the proceedings. He concluded that cavitation contributes to hull pressures in three ways, namely through (i) the motion of the cavities; (ii) the volume variations of the cavities; and (iii) the cavitating tip vortex. Pulsating or collapsing cavities on or in the vicinity of propeller blades are considered to be the most important cause of hull excitation. Stationary cavities rotating with a propeller blade show a displacement effect much like blade thickness, i.e., a dipole type source. However, the net cavity volume variations that are also present form a source of monopole character. Such sources produce pressure fluctuations that are largely in phase over the aft body surface, thereby being very effective in

generating hull excitation forces. Huse regarded the cavitating tip vortex as a weaker source of noise.

For the '*Sydney Express*', a full scale case pursued by the ITTC, the Japanese Ship Research Institute applied two target wake distributions. One nominal wake from the towing tank experiments, the other with an estimate of the full scale wake made with flow liners. An overprediction of hull pressures was found in the nominal wake case, whereas in the estimated full scale wake results showed a reasonable agreement with the full scale measurements. It may be concluded that also in this case the ability to represent the full scale wake in model scale experiments proved essential.

The 19th ITTC cavitation committee [ITTC1990] recommended that '*work on measuring techniques for the model and full scale hull pressure fluctuations due to propeller cavitation should be monitored. Special attention should be given to the influence of the hull response to the pressure measurements*'.

The 20th ITTC cavitation committee [ITTC1993] stated that the energy crisis caused a reduced interest in the measurement of hull-pressure fluctuations during the seventies and eighties. The increase in the economical speed following this period would lead to a stronger interest in the prediction of vibratory hull excitation. The committee infers that '*the experimental and theoretical techniques to predict the risk of vibrations are still crude and further development is required.*' Meanwhile, the assessment of practiced testing techniques was continued on the tanker '*St. Michelis*'. From comparative measurements by six Japanese model basins it was concluded that the full scale correlation was still disappointing, although there appeared to be reasonable agreement on pressure fluctuations amongst the facilities. Hence, '*from this it can be concluded that the cause of the discrepancy[3] is not the model measurement technique of the pressure fluctuations, but is a result of a poor estimate of the full scale wake and simulation of the TVC[4].*'

By this time, on the numerical side, linearized lifting surface theories were being further developed and non-linear BEM computer programs appeared on the scene. The committee regarded the modeling of the detachment and closure of the sheet cavity as a serious problem that still needed to be overcome. Furthermore, in light of the modeling of tip and leading edge vortex cavitation, it was suggested that a new propeller theory should include a leading edge separation vortex and a tip vortex separating from the blade, and '*CFD is one of the most promising tools to predict them*'.

As did the 19th, the 20th cavitation committee acknowledged the fact that flush mounted hull pressure transducers are affected by vibrations of the hull, both on model and full scale, and stated that '*to correct the measured hull pressures for the hull response, a separation into propeller-induced and hull vibration-induced components of the measured pressures is necessary*'. The committee recommended '*when hull pressure amplitudes measured at model scale are compared with full scale data, the hull response, both at model and full scale, should be taken into account.*'

The committee finally concluded that the '*development of a validated and acceptably accurate approach for the correct interpretation of propeller-induced unsteady hull pressures remains unsettled.*' It was advised to investigate the possibility '*to incorporate some concepts or techniques of the "reciprocal method" to take advantage of the separation of the problem into the determination of the source strength of propeller cavitation and the transfer process of*

---

[3] Here one refers to the discrepancy between model and full scale.
[4] TVC stands for Tip Vortex Cavitation.

hydrodynamic pressure variations into the hull and appendages.' Also the measurement of the total wake on full scale and its computation by means of RANS methods was becoming possible and recommended.

The 21st cavitation committee [ITTC1996] stated that '*the major tankery cavitation issues are analytical predictions, model-scale experimental determination and full-scale scaling of developed cavitation patterns and the resulting unsteady hull pressure fluctuations. A review of the analytical prediction of cavitation patterns on propellers performed using a lifting surface theory, a surface panel method and/or a computational fluid dynamics method is summarized. Most of these methods are limited to sheet type cavitation and future efforts should be directed to the development of a more reliable model to cover bubble, cloud, and vortex types of cavitation.*' A specialist committee on cavitation-induced pressure pulses was formed.

At the 22nd and 23rd ITTC conferences [ITTC1999/2002], the specialist committee on cavitation-induced pressure pulses reported on some of the fundamentals of the problem, together with a state-of-art on computational methods, full scale measurement and model scale experiments. The committee recommended that measurements of hull pressures have to be accompanied by vibration measurements, although it is acknowledged that in some references the vibration-induced component to the measured hull pressure at the blade rate frequency is negligible at full scale. It is concluded that the intermittency effects of sheet cavitation together with tip vortex dynamics strongly influence hull pressure fluctuations. Furthermore, the method of wake simulation, facility size and low Reynolds number are mentioned as factors that seriously affect the outcome of model scale measurements. The committee put forward recommended procedures for model and full scale hull pressure measurements and suggested to investigate how tip vortex cavitation dynamics influence unsteady hull pressure excitation. Furthermore, it was recommended to study the causes of cavitation intermittence and review the consequences of wake scaling and turbulence on propeller-induced unsteady pressures. The specialist committee finalized the work by making recommendations for procedures on predicting pressure fluctuations caused by cavitating propellers, both numerically and experimentally. The need for sophisticated full scale investigations for validation purposes was stressed.

The 25th propulsion committee [ITTC2008] referred to a study of Ligtelijn *et al.* [Ligtelijn2004] (see also [Wijngaarden2003]) on the model to full scale correlation of five ships with regard to propulsion and cavitation behavior. For a podded cruise vessel, a very good correlation was obtained for propulsion and first blade rate pressure pulses. For two large container vessels the blade rate pressure pulses were overpredicted. These results are in line with some of the results already mentioned in this overview. A possible explanation for this is the fact that the wake field for cruise vessels is amongst the easier to represent on model scale, whilst the wake fields of the new generation of very large container vessels is more difficult.

The 25th specialist committee on cavitation surveyed the practical state-of-the-art in numerically predicting pressure pulses. Around 2007, the great majority of the survey respondents was using computational tools for pressure pulse analysis, although modeling techniques were still not believed to be fully matured. Remarkable is the large scatter in the judgment of the accuracy of CFD tools for cavitation. The most widespread believe is that the use of advanced CFD codes for, e.g., higher-order blade rate pressure pulses will take several years. In every day practice, potential flow methods for sheet cavitation are used most often. Some excerpts are quoted: '*The development of algorithms to solve the RANS*

equations and perform viscous CFD simulations – as well as the necessary computer power – has only recently impacted cavitation modeling. Previously, hydrodynamicists have used the assumptions of inviscid and irrotational flow to develop potential-flow methods to solve for the flows in the vicinity of ship hulls, propellers, rudders, and other geometries of interest. For cavitation modeling, these hydrodynamicists have developed lifting-surface, panel, vortex-lattice, or boundary-element methods that model the cavities, as well as the geometry. One can also solve the inviscid Euler equations, without the assumption of irrotational flow. Because of their efficiency, these potential-flow methods are still used for propeller design and for predictions over a range of flow and cavitation conditions. These methods can address non-uniform inflows and predict fluctuating forces and pressures produced by sheet cavitation. Several researchers […] *have developed corrections for viscous-flow effects by using RANS predictions for the incoming wake and vorticity fields or by incorporating boundary-layer integral solvers or viscous empirical corrections into the potential-flow methods.*'

The 25th specialist committee on cavitation presented an overview of the status in multi-phase flow cavitation modeling, by which the cavitating flows on propellers are computed by CFD codes involving void-fraction modeling or at least two phase flow models. The developments in this field are very interesting although much has still to be investigated. Kawamura *et al.* [Kawamura2008] were amongst the first to produce results for hull-pressure fluctuations.

2.3 Selection of Research Topics

From this historical research perspective it is concluded that room for improvement in the prediction of propeller-induced hull-pressure forces should be sought in:

- the experimental simulation of the ship's effective wake field. The disparity in Reynolds numbers between model and ship scale warrants the warning sign in Figure 2.5. Differences in the effective wake affect sheet cavitation dynamics through incorrect entrance velocities and angles of attack (Figure 2.2). Chapter 7 is devoted to this important scale effect.

- the modeling of mechanisms underlying the action of the cavitating tip and leading edge vortex is very much unknown territory. In order to limit the scope of the study to a manageable size it was decided not to consider cavitating tip and leading edge vortices, nor the pertaining experimental, numerical and theoretical modeling. At MARIN, Bosschers has taken up the study of this topic.

- the reduction of the influence of parasitic vibration-induced pressures on the hull. This issue has been mentioned several times in ITTC proceedings. Chapter 5 presents a numerical method to alleviate the influence of hull vibrations on pressure measurements.

- the use of reciprocal techniques in prediction procedures. Chapter 8 introduces an inverse BEM technique for the derivation of the propeller source strength.

- the development of computational prediction techniques. In Chapter 3, the computational prediction is treated through a study in which a propeller BEM is coupled to a BEM for acoustic radiation and scattering. This numerical approach is validated for cavitating (Chapter 7) and non-cavitating cases (Chapter 6). The same acoustic BEM is used for inverse source strength determination and computation of vibration-induced pressures. The application of more advanced two-phase flow modeling is investigated by Bosschers.

Comparing Figure 2.5 with the above ITTC list of topics, the issues regarding inception of cavitation seem to have been neglected. In fact, cavitation inception has not been ignored by the ITTC, but has simply not been treated within the scope of propeller-induced hull-pressure pulses. In line with this, in this thesis, it is assumed that developed sheet cavitation exists on the propeller and inception issues are of minor influence. As this condition is not always met, the topic is still marked with a warning sign in Figure 2.5. At MARIN, Van Rijsbergen is investigating issues related to water quality and inception.

3   MATHEMATICAL METHODS

…in which a theoretical framework is presented for the numerical simulation of propeller-induced hull-pressure fluctuations. From a variety of mathematical methods a hybrid approach is selected, in which a hydrodynamic (incompressible flow) method for the propeller noise sources is used in combination with two alternative methods for the scattering effect of the ship hull. One is an acoustic (compressible flow) method, the other a hydrodynamic method for the lower propeller blade passage frequencies.

3.1   Introduction

This chapter gives an overview of mathematical methods and their numerical implementation for the computation of the fluctuating pressure field exerted by the propeller on the wetted ship hull. The sources of pressure fluctuations and their radiation into the surrounding water, including hull scattering effects, are modeled separately, thereby neglecting their interaction. This means that the pressure field on the propeller blades as well as the formation of cavities are considered not to be affected by the scattering effect of nearby bodies, such as appendages, hull and free surface.

Although the assumption of separating the description of the source region from that of the field is a standard approach in acoustics, it may not be immediately clear from a hydrodynamicist's point of view. After all, the effect of nearby bodies on the propeller inflow and the ambient pressure field at the propeller disc cannot be neglected. However, these effects are usually considered to be part of the hydrodynamic description of the source region. An important example of this is the propeller-hull interaction effect on the propeller inflow. The propeller inflow, i.e., the effective wake field, is usually computed separately by a viscous flow method for the flow around the hull. Subsequently, this field is utilized as input to the actual computation of the cavitating flow around the propeller. A simplified schematic of the mathematical modeling of the hull pressures is given in Figure 3.1.

Separation of source and field regions allows for a separate treatment of effects due to dynamic propeller cavitation, propeller thickness and loading on the one hand, and the diffracted pressure field on the hull on the other hand. This suggests the use of a hybrid method in which advantage can be taken of simplifications admissible in each separate model.

Most demanding is the modeling of the cavitating propeller. In principle, one could define a source region in the fluid around the propeller, for which a complete, viscous, multi-phase flow would be computed, with the liquid phase possibly regarded as incompressible. Such an approach leads to the computing-time intensive methods used in the field of multi-phase flow

CFD [ITTC2008, Salvatore2009]. Extension of the rotating computational domain of the propeller to include the non-rotating ship hull is possible, but only at the expense of a further increase in computational cost and complexity. The latter because of the necessity to communicate data from the rotating to the non-rotating grid through, e.g., a sliding interface.

The boundary of the computational domain is usually not located in the acoustic far field in order to limit the number of grid points. Also, at some distance from the source region, acoustic interference effects become noticeable and the incompressibility assumption no longer holds. Therefore, outside the source or near field region acoustic assumptions are made, such as the neglect of the effect of viscosity and the introduction of compressibility, sometimes also including mean flow effects.

The combination of a 'hydrodynamic' source region and an 'acoustic' field belongs to the specialty of CAA ('*Computational AeroAcoustics*', see e.g., [Wang2006, Lyrintzis2003, Bailly2006, Roeck2007, Wells1997, Költzsch2000/2001/2004]). Multi-phase flow CFD is still in a maturing stage and computational demands are so heavy that application on a day-to-day basis, which is considered a prerequisite here, is not yet feasible. Therefore, such methods will not be considered here.
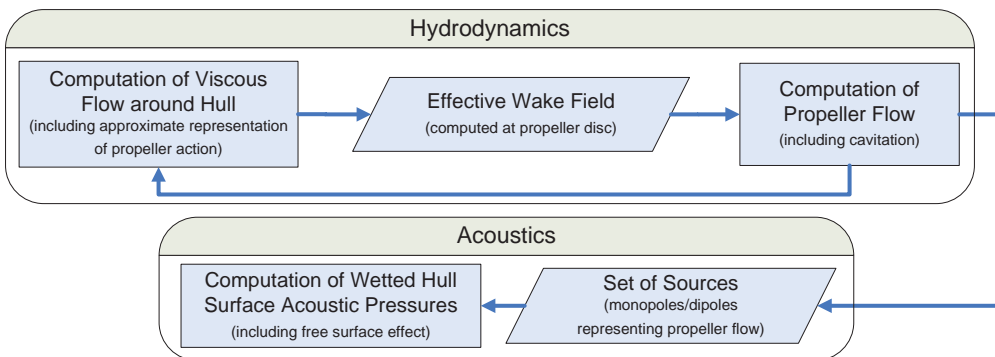
Figure 3.1: Separating hydrodynamic and acoustic models.

To determine whether further simplifications are admissible, the main causes of the hull-pressure field must be determined. For decades, for low Mach numbers, the effects of propeller blade thickness and loading have been represented using inviscid, incompressible flow models. Also, the dynamic activity of cavities, the main cause of vibratory hull forces, has been reasonably modeled without resorting to viscous flow models (see [Vaz2005] for an overview). However, the latter is only (partly) true for sheet cavity dynamics. The dynamic action of cavitating tip vortices need to be accounted for by multi-phase flow CFD methods such as RANS or LES ('*Large Eddy Simulation*'). This topic is worth an in-depth study and has been taken up by Bosschers [Bosschers2007/2008/2009a/b/c]. It will not be further considered here. Until better insights regarding the mechanisms of dynamic tip vortex cavitation are obtained, it is chosen to revert to the approximation of inviscid, incompressible flow around the propeller with sheet cavitation.

For inviscid flows, formulations based on both surface integral methods (e.g., Boundary Element Methods) and field methods (e.g., based on the Euler equations) are available. Euler methods are preferable when the interest is not limited to irrotational flow. Boundary Element Methods show advantages in computational speed and in the fact that only the surfaces need to be discretized on which the solution is subsequently evaluated. Another advantage of integral formulations is that in the far field the elementary solutions distributed on the surface possess the desired behavior, not affected by numerical dissipation and dispersion.

Because our interest is primarily in the pressure on the hull surface itself and rotational flow effects are assumed negligible, a surface integral equation formulation has been chosen. In particular, the BEM worked out by Vaz in his PhD thesis [Vaz2005] has been selected, since it is a state-of-the-art method which has been available for the present study. The method is based on incompressible potential flow. The neglect of compressibility is admissible, because the region where the cavity dynamics takes place is compact (at least in the frequency range of interest) and can be considered as a hydrodynamic near field. The effect of vorticity in the wake cannot be neglected and is incorporated in the form of vortex sheets attached to the blades trailing edges. These vortex sheets are part of the surface in the surface integral equation formulation.

Outside the near field of the propeller, an acoustic model is needed for the scattering of the propeller-induced pressures on the hull and the radiation into the far field. Because of the high value of the speed of sound in water as well as the relatively low rotation rates of ship propellers, the distance from the top of the propeller disc to locations on the aft ship hull is usually small in terms of acoustic wave lengths. Therefore, at the lower blade rate frequencies compressibility may be neglected. However, Bloor [Bloor2001], as well as Kinns and Rath-Spivack ([Kinns2003/2004, RathSpivack2004]) argue that the effect of compressibility can still be significant when the pressure distribution on the complete hull is considered.

Considering the low Mach number flows for ships, in a first approximation the effect of convective flow velocities may be (linearized or) neglected and a (convected) wave equation for the perturbation velocity potential may suffice. Because of the repetitive nature of the excitation (i.e., for stationary effective ship wakes) and the frequency dependent response of the ship hull, the excitation pressures on the hull are preferably given in the frequency domain. A boundary element description based on the (convected) Helmholtz equation for a harmonic perturbation velocity potential would therefore appear to be a suitable starting point for the analysis. In integral form this leads to the Kirchhoff-Helmholtz integral equation for the complex amplitude of the acoustic field perturbation potential at any given frequency.

In aeronautics, alternative models are in use that do not require the potential flow assumption. Instead, they are based on the more general theory of the acoustic analogy pioneered by Lighthill, and lead to the FW-H equation ('*Ffowcs Williams and Hawkings equation*') [FfowcsWilliams1969]. As opposed to Kirchhoff formulations, in FW-H formulations there is no need for the integration surface to be in the linear flow regime. Recast in a form suitable for scattering analysis in the frequency domain, FW-H formulations could also serve as an acoustic method.

To provide guidance on the choice of formulation, a study of available surface integral equation methods (i.e., variations on the Kirchhoff and FW-H themes) is performed. In Appendix A various potential flow models are presented that lend themselves to a boundary element type of approach. Appendix B treats a set of alternative formulations based on the FW-H equation. Section 3.3 discusses the suitability of the formulations presented in the appendices and a choice is made from the alternatives. The acoustic model finally adopted is

a Kirchhoff-Helmholtz integral equation formulation for the perturbation velocity potential, with a pressure-based integral equation formulation for incompressible flow as a low-frequency alternative. The acoustic model is described in Section 3.4 together with its coupling to the already existing propeller flow method. Appendix F.1 gives a full account of the implementation of the selected boundary integral equation method.

The next section summarizes the hydrodynamic method for the propeller action that should provide the sources of propeller noise to the acoustic scattering method.

3.2 Hydrodynamic Method for Propeller Noise Sources

The present hydrodynamic propeller method is defined as consisting of a Boundary Element Method for inviscid, incompressible and irrotational perturbations of the flow around a propeller. As such, the method is expected to be well-suited to the simulation of the effects on pressure pulses of blade thickness and loading as well as the pulsating action of sheet cavities. However, the method will not be capable of reproducing effects related to vortical types of cavitation and cloud cavitation.

The formulation is in the time domain and based on the Morino integral formulation as used by Vaz [Vaz2005] (see also references [Fine1992/1993, Kinnas1992a/b, Hoshino1991/1993]. In this formulation, the propeller-induced velocity disturbances are considered irrotational, and therefore a scalar variable, ϕ', is defined as the *disturbance velocity potential*. Then,

$$\mathbf{v}(\mathbf{x},t) = \mathbf{v}_0(\mathbf{x},t) + \nabla \phi'(\mathbf{x},t) \tag{3.1}$$

in which t is time and Cartesian position vectors, $\mathbf{x} = x_i = (x_1, x_2, x_3)^T = (x, y, z)^T$, are used relative to a frame of reference translating and rotating with the propeller (see Figure 3.2, drawn in red). Note that vector quantities are written in boldface and disturbances are primed. The velocity, $\mathbf{v}(\mathbf{x},t)$, is the total velocity relative to the operating propeller. The axis of rotation is the x-axis, which points in the upstream direction. The y-axis points to port at the instant the z-axis points in the upward direction. The yz-plane coincides with the propeller plane[5]. The origin is at the propeller centre, which is defined as the intersection of the axis of rotation and the propeller plane. The constant propeller translation velocity equals the ship speed, v_s, in the positive x-direction.

The velocity, $\mathbf{v}_0$, undisturbed by the propeller, can be written as the sum of the ship's effective wake field velocity, $\mathbf{v}_w$, in the propeller plane,

$$\mathbf{v}_w(\mathbf{x},t) = \left(-\frac{v_{w,x}}{v_s}, \frac{v_{w,y}}{v_s}, \frac{v_{w,z}}{v_s} \right)^T v_s \tag{3.2}$$

---

[5] The propeller plane may be defined as the plane containing the quarter chord point at 70% of the propeller radius and which is orthogonal to the propeller shaft line. Other definitions are in use as well.

and the effect of the constant propeller angular velocity, $\mathbf{\Omega}$, i.e.,

$$\mathbf{v}_0(\mathbf{x},t) = \mathbf{v}_w(\mathbf{x},t) - \mathbf{\Omega} \times \mathbf{x} \tag{3.3}$$
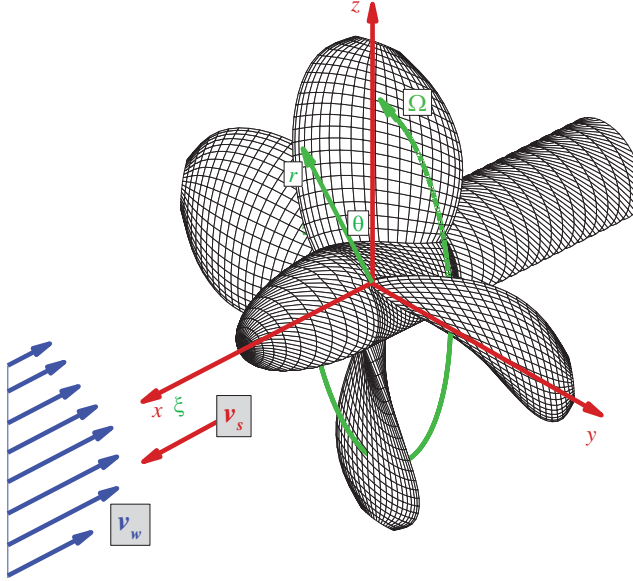
Figure 3.2: Reference system for the hydrodynamic propeller model (adapted from [Vaz2005]). The figure displays the propeller at time zero with the cap on the upstream side. The propeller is right-handed, i.e., rotating in clockwise direction when viewed from behind.

The azimuthal velocity is taken positive in clockwise direction, when the propeller is viewed from behind (i.e., in upstream direction). The ship effective wake field is usually given as a steady velocity field in a system of reference translating, but not rotating, with the propeller. As a consequence, the wake field becomes time-dependent in the propeller's rotating system of reference. The connection between the two wake field representations is conveniently expressed using a cylindrical coordinate system, $\mathbf{\xi} = (\xi, r, \theta)^T$ (see Figure 3.2, drawn in green), which shares its origin with the Cartesian system, and in which ξ denotes the axial coordinate coincident with x . The radial coordinate r is in the yz-plane, and θ is the azimuthal coordinate in the same plane measured from the z-axis in clockwise direction. Thus, $\xi = x$, $r = \sqrt{y^2 + z^2}$, $\theta = \arctan(-y/z)$, and Eq. (3.3) becomes,

$$\mathbf{v}_0(\mathbf{\xi},t) = \mathbf{v}_w(\xi, r, \theta, t) - \omega r \mathbf{e}_\theta = \mathbf{v}_w(\xi, r, \vartheta - \omega t) - \omega r \mathbf{e}_\theta \tag{3.4}$$

Here, it is assumed that, at $t = 0$, the z-axis is in the upward position, and that ϑ is the angle corresponding to θ at $t = 0$. Furthermore, the propeller angular velocity is determined by its axial component, $\mathbf{\Omega} = (\omega, 0, 0)^T$. Finally, $\mathbf{e}_\theta$ denotes the unit vector in the θ-direction.

The flow is assumed incompressible with constant density, ρ_0. Therefore, Laplace's equation applies to the disturbance velocity potential,

$$\nabla^2 \phi'(\mathbf{x}, t) = 0 \tag{3.5}$$

The pressure, p, follows from Bernoulli's equation for unsteady incompressible potential flow,

$$\rho_0 \frac{\partial \phi'}{\partial t} + p + \tfrac{1}{2} \rho_0 |\mathbf{v}|^2 - \rho_0 gh = p_{ref} + \tfrac{1}{2} \rho_0 |\mathbf{v}_0|^2 \tag{3.6}$$

The reference pressure is given by, $p_{ref} = p_{atm} - \rho_0 gh_{shaft}$, with p_{atm} as the atmospheric pressure at the free surface, and submergence, h, at the shaft as, h_{shaft}.

In order to solve Eq. (3.5), boundary conditions have to be imposed on the rotating surface, $S(t)$, consisting of $S_B(t)$, the wetted body part (i.e., the non-cavitating propeller surface), $S_C(t)$, the cavity surface, and $S_W(t)$, the wake sheets behind the trailing edge of the propeller blades. Figure 3.3 shows a supercavitating case with S_{Bc} and S_{Wc} respectively denoting those parts of S_B and S_W that are covered by the sheet cavity.
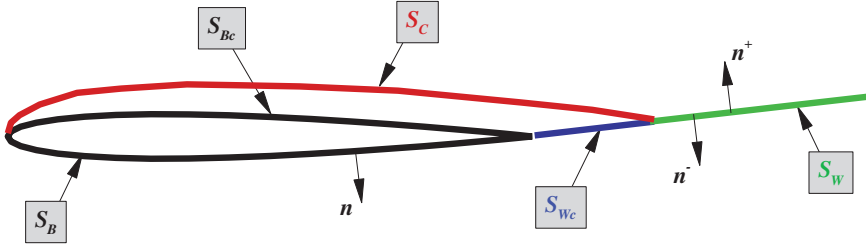
Figure 3.3: Definition of surfaces: propeller blade section (black), cavity surface (red), and wake surface (green) (adapted from [Vaz2005]).

On $S_B(t)$, an impermeability condition of the Neumann type is imposed, $\nabla \phi' \cdot \mathbf{n} = -\mathbf{v}_0 \cdot \mathbf{n}$, with the unit vector normal to the boundary, $\mathbf{n}$, pointing *into* the fluid. The position of the cavity surface itself, $S_C(t)$, is unknown. Hence, two boundary conditions are needed there, viz., a kinematic condition stating that the surface is a material surface of the flow, and a dynamic condition requiring that the pressure equals the vapor pressure. The wake surface, $S_W(t)$, is a vortex sheet, being generated at the blade's trailing edge, where the flows over the upper and lower surfaces meet. On this sheet a kinematic boundary condition is imposed stating that the sheet should be a material surface of the flow. A dynamic (Rankine-Hugoniot) boundary condition is added by requiring a zero pressure difference between both sides of the sheet. At the trailing edge this is the so-called Kutta condition. The cavities are considered thin enough to allow for the application of the boundary conditions at S_{Bc} and S_{Wc} (see

Figure 3.3), i.e., the projection of S_C on the blade and the wake sheets, respectively, instead of at S_C itself. Fine and Kinnas [Fine1993] refer to this model as the *partially non-linear model.* Finally, at infinity, the velocity perturbations are assumed to vanish.

Applying Green's third identity (see Appendix G.3) to the disturbance velocity potential, $\phi'(\mathbf{x},t)$, for points, $\mathbf{x} \in \{S_B \cup S_C\}$, ϕ' can be written as Eq. (3.7), with $G_L(\mathbf{x},\mathbf{y}) = -1/4\pi|\mathbf{x}-\mathbf{y}|$ as the Green's function for the Laplace equation (see Appendix A.2). The normal at $\mathbf{y}$, i.e., $\mathbf{n_y}$, points away from the body *into* the flow volume, V. Furthermore, $\Delta\phi' = \phi'^+ - \phi'^-$ denotes the difference between the potential on the upper and lower side of the wake sheet. A similar definition applies to the normal component of the gradient of $\Delta\phi'$. Here, the plus sign refers to the wake vortex sheet trailing from the suction side of the blade; the minus sign to the pressure side (see Figure 3.3). The normal on S_W points into the volume from the side bearing the plus sign. Thus, one obtains,

$$
\begin{aligned}
\frac{1}{2}\phi'(\mathbf{x},t) =& \int\limits_{S_{B\cup Bc}(t)} \left(\frac{\partial\phi'(\mathbf{y},t)}{\partial n_\mathbf{y}} G_L(\mathbf{x},\mathbf{y}) - \phi'(\mathbf{y},t)\frac{\partial G_L(\mathbf{x},\mathbf{y})}{\partial n_\mathbf{y}} \right) dS_\mathbf{y} \\
&+ \int\limits_{S_W(t)} -\Delta\phi'(\mathbf{y},t)\frac{\partial G_L(\mathbf{x},\mathbf{y})}{\partial n_\mathbf{y}} \, dS_\mathbf{y} \\
&+ \int\limits_{S_{Wc}(t)} \left(\Delta\left(\frac{\partial\phi'(\mathbf{y},t)}{\partial n_\mathbf{y}}\right) G_L(\mathbf{x},\mathbf{y}) - \Delta\phi'(\mathbf{y},t)\frac{\partial G_L(\mathbf{x},\mathbf{y})}{\partial n_\mathbf{y}} \right) dS_\mathbf{y}
\end{aligned}
\tag{3.7}
$$

The solution is in terms of monopole ($\nabla\phi'\cdot\mathbf{n}$, $\Delta(\nabla\phi'\cdot\mathbf{n})$) and dipole ($\phi'$, $\Delta\phi'$) source distributions on (S_B, S_W). More specifically, on S_B, the monopole distribution follows directly from the surface impermeability constraint, and the dipole distribution is determined using Eq. (3.7). On S_{Bc}, the monopole distribution is determined from Eq. (3.7) with zero left-hand-side, and the dipole distribution follows from the dynamic boundary condition that the pressure equals the vapor pressure. On S_W, the monopole distribution is zero and the dipole distribution follows from the dynamic boundary condition that there is no pressure difference across the wake vortex sheets. Finally, on S_{Wc}, the monopole distribution is determined by Eq. (3.7) in the form given by Fine [Fine1992],

$$
\begin{aligned}
\phi'^+(\mathbf{x},t) =& \int\limits_{S_{B\cup Bc}(t)} \left(\frac{\partial\phi'(\mathbf{y},t)}{\partial n_\mathbf{y}} G_L(\mathbf{x},\mathbf{y}) - \phi'(\mathbf{y},t)\frac{\partial G_L(\mathbf{x},\mathbf{y})}{\partial n_\mathbf{y}} \right) dS_\mathbf{y} \\
&+ \int\limits_{S_W(t)} -\Delta\phi'(\mathbf{y},t)\frac{\partial G_L(\mathbf{x},\mathbf{y})}{\partial n_\mathbf{y}} \, dS_\mathbf{y} + \frac{1}{2}\Delta\phi' \\
&+ \int\limits_{S_{Wc}(t)} \left(\Delta\left(\frac{\partial\phi'(\mathbf{y},t)}{\partial n_\mathbf{y}}\right) G_L(\mathbf{x},\mathbf{y}) - \Delta\phi'(\mathbf{y},t)\frac{\partial G_L(\mathbf{x},\mathbf{y})}{\partial n_\mathbf{y}} \right) dS_\mathbf{y}
\end{aligned}
\tag{3.8}
$$

and the dipole distribution follows from the dynamic boundary condition as on S_W. The potential, ϕ'^+, is determined by demanding the pressure to be equal to the vapor pressure (on both sides of the wake vortex sheet).

The solution is obtained upon discretization of Eqs. (3.7) and (3.8). This is carried out by approximating the surface, S, by a set of quadrilateral panels (i.e., boundary elements) on which the monopole and dipole distributions are assumed piecewise constant. The boundary elements for monopoles are flat, the ones for dipoles are hyperboloidal in shape. In case of Eq. (3.7), S_B and S_w are approximated by N_b and N_w panels, respectively, as, $\tilde{S}_i$, $i = 1.. N_b + N_w$. On each panel, a collocation point, $\mathbf{x}_i$, $i = 1.. N_b + N_w$, is chosen, at which Eq. (3.7) is enforced. Thus, a system of $N_b + N_w$ equations, linear in the unknown strength of the monopoles and dipoles, is obtained from which $N_b + N_w$ values follow for the monopole and dipole parameters on the panels at the k-th time step, with $k = 1.. N_t$, during a revolution. Finally, the solution may be obtained in terms of the pressure through the application of Bernoulli's equation, Eq. (3.6),

$$p(\mathbf{x},t) = p_{atm} + \rho_0 g\left(h(\mathbf{x},t) - h_{shaft}\right) - \rho_0 \frac{\partial \phi'(\mathbf{x},t)}{\partial t} - \tfrac{1}{2}\rho_0\left(\left|\mathbf{v}(\mathbf{x},t)\right|^2 - \left|\mathbf{v}_0(\mathbf{x},t)\right|^2\right) \qquad (3.9)$$

At MARIN, this Boundary Element Method has been implemented under the name PROCAL, which is used in this thesis whenever reference is made to the method.

At a distance of several panel diagonals from the propeller and wake surfaces, the sources distributed on the surfaces may be represented as point sources (see Appendix C for a mathematical description of moving point sources). The integrands may then be taken outside the integral, e.g.,

$$\int_{\tilde{S}_j} G_L(\mathbf{x}_i,\mathbf{y}_j)\, dS_{\mathbf{y}_j} \cong G_L(\mathbf{x}_i,\mathbf{y}_j)\Box\,\tilde{S}_j \qquad (3.10)$$

and

$$\frac{1}{2}\delta_{ij} + \int_{\tilde{S}_j} \frac{\partial G_L(\mathbf{x}_i,\mathbf{y}_j)}{\partial n_{\mathbf{y}_j}}\, dS_{\mathbf{y}_j} \cong \frac{1}{2}\delta_{ij} + \frac{\partial G_L(\mathbf{x}_i,\mathbf{y}_j)}{\partial n_{\mathbf{y}_j}}\Box\,\tilde{S}_j \qquad (3.11)$$

for unit strength monopoles (Eq. (3.10)) and dipoles (Eq. (3.11)), respectively. The panel surface area is denoted by $\Box\,\tilde{S}_j$. Thus, at some distance, the rotating panels may be effectively replaced by rotating point monopoles and dipoles of strength,

$$\nabla\phi'\cdot\mathbf{n} \quad \text{(on blade surfaces)}; \quad \Delta\left(\nabla\phi'\cdot\mathbf{n}\right) \quad \text{(on wake vortex sheets)} \qquad (3.12)$$

and,

$$\phi' \quad \text{(on blade surfaces)}; \quad \Delta\phi' \quad \text{(on wake vortex sheets)} \qquad (3.13)$$

respectively. The field induced by these point sources is diffracted by the hull and free surface. In the next section, a method for the determination of diffraction effects is selected.

3.3 Acoustic Methods for Hull Scattering

Having represented the cavitating propeller by a set of rotating, hydrodynamic point sources of monopole and dipole type, an acoustic method for the scattering effect on the ship hull and free surface has to be derived. In Appendices A and B an overview is given of acoustic methods that can be written as boundary integral equations and solved using the Boundary Element Method. They are based on the Kirchhoff (Appendix A) and Ffowcs Williams and Hawkings (Appendix B) formulations. These formulations provide the basis for candidate methods to be used in conjunction with the hydrodynamic potential flow method for the propeller described in the preceding section. Now, from the available acoustic formulations a suitable choice must be made. Before doing so, a brief overview of the methods is given with their pros and cons. For derivations of the various methods the reader is referred to Appendices A and B.

In the following, for determining the ship-diffracted hull-pressure fluctuations, use is made of position vectors, $\mathbf{x} = x_i = (x_1, x_2, x_3)^T = (x, y, z)^T$, relative to a frame of reference translating with the ship. The velocity, $\mathbf{v}(x, t)$, must therefore be interpreted as the total velocity relative to the ship. The x-axis points in the longitudinal direction from stern to bow. The y-axis points to port and the z-axis is in the upward direction. The origin is amidships on the projection of the centre line and on the still free surface. As before, the constant translation velocity equals the ship speed, v_s, in the positive x-direction.

3.3.1 Kirchhoff methods

Laplace approximation

The most straightforward approach to compute the hull-surface pressures induced by the propeller is to use the propeller hydrodynamic potential flow method itself. Then, the Laplace equation for the ship hull scattered disturbance velocity potential in the integral form of Eq. (A.62),

$$\frac{1}{2}\varphi'(\mathbf{x}, t) = -\int_{S_H} \varphi'(\mathbf{y}, t)\frac{\partial G_L}{\partial n_{\mathbf{y}}}\, dS_{\mathbf{y}} + q_\phi \tag{3.14}$$

must be solved for locations on the wetted hull surface, S_H, at each time step, entirely neglecting compressibility. In Eq. (3.14), the diffracted disturbance velocity potential is denoted by, φ', to avoid confusion with the propeller-induced free-field disturbance velocity potential, ϕ'. The sources inside the flow volume, V, are denoted by q_ϕ and consist of the rotating monopole and dipole propeller point sources determined through Eqs. (3.10)-(3.13). In Eq. (3.14) the wetted hull surface is assumed to be rigid. From the computed hull velocity potential, hull pressures are determined using Bernoulli's equation for points stationary on the hull,

$$p'(\mathbf{x}, t) = -\rho_0 \frac{\partial \varphi'(\mathbf{x}, t)}{\partial t} - \tfrac{1}{2}\rho_0 \left(\left|\mathbf{v}(\mathbf{x}, t)\right|^2 - \left|\mathbf{v}_0(\mathbf{x}, t)\right|^2 \right) \tag{3.15}$$

The result is a hull-pressure disturbance[6] time series that can be Fourier transformed to give the hull pressure harmonic amplitudes and phases. The advantage of this approach lies in its simplicity and the fact that the pressure can be accurately determined from the values of the potential, i.e., without the need to linearize or neglect the quadratic velocity term in Bernoulli's equation.

However, the application of Eq. (3.15) requires knowledge of the main stream velocities at the hull surface. As this information is not readily available, a pressure-based alternative to Eq. (3.14) may be more convenient to use,

$$\frac{1}{2} p'(\mathbf{x}, t) = - \int_{S_H} p'(\mathbf{y}, t) \frac{\partial G_L}{\partial n_{\mathbf{y}}} \, dS_{\mathbf{y}} + q_p \tag{3.16}$$

The rotating propeller sources are now denoted by q_p, and consist of monopole and dipole point sources of which the strengths are derived in Appendix C.

If the accurate computation of the normal pressure derivative on the propeller blades and their wake sheets is feasible, the presented pressure formulation does yield the pressure without neglecting the dynamic pressure component term from the Bernoulli equation. When, furthermore, the terms related to the wake sheets in Eq. (C.11) turn out to be negligible, the pressure-based formulation would become the preferred option. This is because, although the contribution from the vortex sheets enables the accurate computation of the propeller surface potential (and pressure), the vortex sheet model is not well-suited for the computation of field potentials (and pressures) abaft the propeller. In reality, the vortex sheets roll up and further aft of the propeller vorticity is concentrated in the form of line vortices that have no close resemblance to the helicoidal vortex sheets used here.

Although the pressure-based formulation enhances the accuracy by incorporating the dynamic pressure term from the Bernoulli equation, compressibility effects are lost. At frequencies low enough for the wave lengths to be large in comparison with hull dimensions the combination of the hydrodynamic method with the pressure-based formulation yields a viable alternative.

Kirchhoff approximation

In the introduction, it was stated that some references (e.g., [Bloor2001]) suggest that, although the Mach number of the convected ship flow is much smaller than unity, compressibility may not be neglected *a priori*. This is because the wetted ship hull is large enough for interference effects to become noticeable even at low blade passage frequencies and higher harmonics thereof. Also in view of the occasional determination of scattered far field pressures, compressibility effects would have to be included. Thus, one arrives at the Kirchhoff integral equation, Eq. (A.71), (see also Figure A.4),

---

[6] Note that the hydrodynamic formulation uses the absolute pressure, because of cavitation phenomena, whereas the acoustic formulation only needs to use the disturbance pressure.

$$\frac{1}{2}\varphi'(\mathbf{x},t) = \frac{1}{4\pi}\int_{S_H}\left[\left(\frac{\varphi'}{r^2}+\frac{\dot{\varphi}'}{cr}\right)\frac{\partial r}{\partial n_{\mathbf{y}}}\right]_{t-\frac{r}{c}}dS_{\mathbf{y}} + \frac{1}{4\pi}\int_{V}\left[\frac{q}{r}\right]_{t-\frac{r}{c}}dV_{\mathbf{y}} \qquad (3.17)$$

in which c denotes the speed of sound and the integrands over the rigid hull surface and the propeller sources are to be evaluated at the retarded time, $\tau = t - r/c$, as indicated by the brackets (see Appendix G.2). Strictly speaking, the ship flow is neglected, the domain of integration is kept fixed to the ship and the pressure needs to be computed on the basis of the transient term in Bernoulli's equation only, viz. Eq. (A.17), $p' = -\rho_0\dot{\psi}'$. It is then possible to restate the Kirchhoff integral equation in terms of pressure, see Eq. (A.72),

$$\frac{1}{2}p'(\mathbf{x},t) = \frac{1}{4\pi}\int_{S_H}\left[\left(\frac{p'}{r^2}+\frac{\dot{p}'}{cr}\right)\frac{\partial r}{\partial n_{\mathbf{y}}}\right]_{t-\frac{r}{c}}dS_{\mathbf{y}} + \frac{1}{4\pi}\int_{V}\left[\frac{q}{r}\right]_{t-\frac{r}{c}}dV_{\mathbf{y}} \qquad (3.18)$$

Note that it is not consistent to use Eq. (3.18) in conjunction with the pressure-based hydrodynamic source formulation, because the source system q_p (i.e., the second integral on the right-hand-side of the equation) would contain both the dynamic and transient terms from Bernoulli's equation, whereas, Eq. (3.18) is based on the transient term only.

Morino/Farassat-Myers approximation

When both compressibility and convective effects are significant, within the linear domain of application of a Kirchhoff type of method, the Green's function (Eq. (A.55)) associated with the convected wave equation (Eq. (A.13)) should be used. For this situation [Morino2003] gives the integral equation, Eq. (A.73), for the potential followed by Eq. (A.11) for the pressure.

Alternatively, for a system of reference not moving with the ship the wave equation may still be used, but then the integration surfaces are not stationary anymore. For this case Farassat and Myers developed an integral equation [Farassat1988], viz., Eq. (A.74), often referred to as the *moving Kirchhoff* method.

Considering the low advance speeds of vessels it is not expected that these more elaborate formulations are necessary here. They are treated in Appendix A for reference.

Frequency domain alternatives

The methods described so far form natural extensions to the time domain propeller source method. However, computational demands are heavier for the time-domain method than for their frequency domain alternatives, because for the latter method often only a few harmonics of the blade passing frequency are needed. The simple incompressible model is an exception as its Green's function is independent of frequency. With periodic source motion, frequency domain models become an attractive option. In order to realize such models the rotating propeller sources must be replaced by stationary ones distributed along the circular paths of rotation.

In the frequency domain, Eq. (3.16) for the incompressible case is still valid for harmonics of the pressure (indicated by a caret symbol),

$$\frac{1}{2}\hat{p}'(\mathbf{x}) = -\int_{S_H} \hat{p}'(\mathbf{y})\frac{\partial G_L}{\partial n_{\mathbf{y}}}\,dS_{\mathbf{y}} + \hat{q}_p \tag{3.19}$$

In the compressible case without mean flow, instead of the wave equation, the Helmholtz equation (Eq. (A.25)) is used and the Kirchhoff-Helmholtz integral equation (Eq. (A.64)) has to be solved for each frequency component,

$$\frac{1}{2}\hat{\varphi}'(\mathbf{x}) = \int_{S_H} \hat{\varphi}'(\mathbf{y})\frac{\partial G_H}{\partial n_{\mathbf{y}}}\,dS_{\mathbf{y}} + \hat{q}_\phi \tag{3.20}$$

The Green's function for the Helmholtz equation is defined as, $G_H(\mathbf{x},\mathbf{y};k) = -\exp(ikr)/4\pi r$, see Eq. (A.34). As before, the pressure needs to be computed on the basis of the transient term in Bernoulli's equation only, viz., Eq. (A.24), $\hat{p}' = ik\rho_0 c\hat{\varphi}'$, and one can restate the Kirchhoff-Helmholtz integral equation in terms of pressure, although this is of no further advantage. The rotating propeller sources, q_ϕ, have been replaced by stationary ones along the circular paths of rotating. Harmonic components of the stationary source system are denoted as, $\hat{q}_\phi$. Appendix E gives a full account of this procedure. Table 3.1 presents an overview of the formulations treated in this section.

Table 3.1: Kirchhoff-Helmholtz formulations for determining hull scattering effects.

Compressible Flow	Convected Flow	Variable	Dynamic pressure	Time domain	Frequency domain
No	Yes	Potential	Not practical	(3.14)	(3.14) for $\hat{\varphi}'$
No	Yes	Pressure	Yes	(3.16)	(3.19)
Yes	No	Potential	No	(3.17)	(3.20)
Yes	No	Pressure	No	(3.18)	(3.20) for $\hat{p}'$
Yes	Yes	Potential	Yes (linear)	(A.73)/(A.74)	(A.65)

3.3.2   FW-H methods

More recently, 'competing' models have been derived for scattering based on the FW-H equation, Eq. (B.23). This form of the equation is in terms of the pressure disturbance and a linear relationship with the density disturbance is assumed. The FW-H equation includes convection effects, compressibility and allows for the decoupling of the source from the scatterer. When cast in integral form, the integration surfaces do not need to be outside the non-linear domain (although the observer does). The standard integral form of the FW-H

equation, known as Farassat's formulation 1A assumes non-penetrable surfaces of integration. For the application to cavitating propellers, Salvatore *et al.* [Salvatore2002/2006] derive a version of the equation for porous surfaces, keeping the surface of integration coincident with the rotating blades, like in the hydrodynamic propeller method used in this thesis.

Usually, the FW-H equation is applied to radiation rather than scattering problems. However, recently, Gennaretti presented a formulation (Eq. (B.44)) for scattering purposes [Gennaretti2006]. It does not rely on the potential flow assumption. It can be elegantly recast in a frequency domain version (Eq. (B.45)), but involves an additional surface integral over the incident (i.e., propeller-induced) pressure.

Brentner [Brentner1997/1998] has shown that when the pressure disturbances are proportional to the density variations, the moving Kirchhoff and FW-H formulation are equivalent, except for a source term involving Reynolds stresses in the FW-H formulation. An overview with derivations of FW-H formulations is found in Appendix B.

3.3.3   Selection of method

The above discussion of methods to be used in conjunction with the hydrodynamic propeller source method seems to favor the newly developed formulation of Gennaretti [Gennaretti2006] in its frequency domain form. Also, Testa [Testa2008a] and Testa *et al.* in [Testa2008b] recommend this formulation. Notwithstanding this, given the low Mach numbers, using a 'convected' formulation seems unnecessary for the low-frequency pressure fluctuations considered in this thesis. The Kirchhoff-Helmholtz integral equation, based on the Helmholtz differential equation, therefore seems to be an appropriate potential flow method. The fact that the author had already developed a code based on exactly this method makes the method also the most cost-effective solution.

It is concluded that although the FW-H scattering formulation may be the most appealing method to choose, its advantages in the use for cavitating propellers do not warrant the development for the sake of this thesis. Instead, for the 'higher' harmonics of the blade passage frequency the Kirchhoff-Helmholtz integral equation is selected in combination with an incompressible Laplace method for the 'lower' harmonics, whenever the dynamic pressure components (in Bernoulli's equation) are not entirely negligible.

The next section describes in some detail an acoustic method based on Eq. (3.20). Only small modifications are needed to encapsulate the option of Eq. (3.19) into this method.

3.4 Description of Acoustic Scattering Method

The acoustic model for the scattering effect of the hull and free surface is defined as consisting of a Boundary Element Method for the acoustic potential in the frequency domain satisfying the Kirchhoff-Helmholtz integral equation. The main inflow to the propeller (i.e., the stationary effective wake field) is disregarded and the only potential flow field present is due to the propeller-induced sources and the scattering of the hull and the free surface.

Assume an inviscid, irrotational, compressible flow within a domain V with bounding surface S, now consisting of S_H, the submerged part of the hull, and S_F, the free surface.

Combining Eq. (A.71) with the moving point source formulations of Appendix D, the disturbance velocity potential, $\varphi'(\mathbf{x}, t)$, can be written as,

$$\frac{1}{2}\varphi'(\mathbf{x},t) = -\frac{1}{4\pi} \int_{S_H \cup S_F} \left[\frac{1}{r} \frac{\partial \varphi'(\tau)}{\partial n_y} + \frac{\partial r}{\partial n_y} \left(\frac{\varphi'(\tau)}{r^2} + \frac{1}{cr} \frac{\partial \varphi'(\tau)}{\partial t} \right) \right]_{ret} dS_y +$$

$$+ \frac{1}{4\pi} \sum_{i=1}^{N_b + N_w} \left[\frac{\sigma_i(\tau)}{r_s(\tau)(1 - M_r(\tau))} + \frac{\partial}{\partial n_i} \left(\frac{\mu_i(\tau)}{r_s(\tau)(1 - M_r(\tau))} \right) \right]_{ret} \tag{3.21}$$

Here, Cartesian position vectors, $\mathbf{x} = x_i = (x_1, x_2, x_3)^T = (x, y, z)^T$, are used relative to a frame of reference translating with the ship. The x-axis points in the upstream direction. The y-axis points to port and the z-axis is in the upward direction. The origin is above the centre line amidships at the undisturbed free surface. The normal on the body surface is pointing *into* V. All quantities in Eq. (3.21) are to be taken at the retarded time, as indicated by the subscript $_{ret}$. The Mach number, M_r, is defined as the ratio of the speed at which the source is approaching the point of observation and the speed of sound. The summation is over $N_b + N_w$ monopole and dipole propeller sources with normal directions n_i, and strengths σ_i and μ_i for the ith propeller surface panel, $\tilde{S}_i$, that makes up the source system. The instantaneous distance from the observer to a point source is denoted by $r_s = |\mathbf{x} - \mathbf{x}_s(t)|$, with $\mathbf{x}_s$ as the source coordinates. The source strengths are determined by evaluating the panel integrals,

$$\sigma_i(\mathbf{y}_i,t) = \begin{cases} \dfrac{\partial \phi'(\mathbf{y}_i,t)}{\partial n_y} \square \tilde{S}_i & \text{for} \quad \tilde{S}_i \subset \left(S_B \cup S_{B_C} \right) \\[2ex] \Delta\left(\dfrac{\partial \phi'(\mathbf{y}_i,t)}{\partial n_y} \right) \square \tilde{S}_i & \text{for} \quad \tilde{S}_i \subset \left(S_{W_C} \right) \end{cases} \tag{3.22}$$

and

$$\mu_i(\mathbf{y}_i,t) = \begin{cases} -\phi'(\mathbf{y}_i,t) \square \tilde{S}_i & \text{for} \quad \tilde{S}_i \subset \left(S_B \cup S_{B_C} \right) \\[1ex] -\Delta\phi'(\mathbf{y}_i,t) \square \tilde{S}_i & \text{for} \quad \tilde{S}_i \subset \left(S_W \cup S_{W_C} \right) \end{cases} \tag{3.23}$$

in which, $\square \tilde{S}_i$, denotes the surface area of a quadrilateral panel. Eq. (3.21) may be further simplified as follows. The condition that the potential must equal zero at the free surface can be enforced at the undisturbed water surface by mirroring the submerged part of the hull surface into the free surface, and assuming the mirrored potentials to be the negative of their submerged counterparts. Therefore, in the remainder, S_H and S_F are replaced by the so-called 'double hull', S_{DH}, and the source summation is over twice the number of sources. Furthermore, the ship hull is considered a rigid scattering object, hence the normal component of the gradient of the surface potential vanishes. Then, Eq. (3.21) becomes,

$$\frac{1}{2}\varphi'(\mathbf{x},t) = -\frac{1}{4\pi}\int_{S_{DH}}\left[\frac{1}{r}\frac{\partial r}{\partial n_y}\left(\frac{\varphi'}{r}+\frac{1}{c}\frac{\partial\varphi'}{\partial t}\right)\right]_{ret}dS_y\ +$$

$$+\frac{1}{4\pi}\sum_{i=1}^{2(N_b+N_w)}\left[\frac{\sigma_i}{r_s\left(1-M_r\right)}+\frac{\partial}{\partial n_i}\left(\frac{\mu_i}{r_s\left(1-M_r\right)}\right)\right]_{ret}$$

(3.24)

for points, $\mathbf{x}\in S_{DH}$. Eq. (3.24) constitutes an integral equation in the time domain for the velocity disturbance potential on the rigid, wetted hull surface scattering the incident waves generated by a set of rotating point sources of monopole and dipole type. The disturbance pressure, p', may be obtained from the potential through Eq. (A.17).

As the aim is to obtain a frequency domain description, Eq. (3.24) has to be Fourier transformed. For that purpose, the rotating sources have to be 'replaced' by stationary ones by expanding the former along their paths of rotation. The result is a set of $2(N_b+N_w)N_t$ stationary monopoles and dipoles placed at N_t positions, i.e., the locations each of the panels (and their mirror images) assume during a time-discretized revolution (see Appendix E for a derivation). The strengths of the sources are periodic in time at the fundamental frequency, ω_1, given by $\omega_1=Z\Omega$, with Z the number of propeller blades and Ω the propeller revolution rate. Using, $\mathrm{sinc}(x)=\sin(x)/x$, the complex amplitude of the nth harmonic, $\hat{\sigma}_n(\mathbf{x}_{ij})$, can be expressed as,

$$\frac{\hat{\sigma}_n(\mathbf{x}_{ij})}{\sigma_{ij}}\frac{N_t}{Z} = \mathrm{sinc}\left(\omega_n\frac{\Delta t}{2}\right)e^{+i\omega_n t_j} = \mathrm{sinc}\left(nZ\frac{\Delta\theta}{2}\right)e^{+inZ(\theta_{i0}+j\Delta\theta)} = \mathrm{sinc}\left(\pi n\frac{Z}{N_t}\right)e^{+inZ\left(\theta_{i0}+j\frac{2\pi}{N_t}\right)}$$ (3.25)

for monopoles and a similar expression for dipoles. As before, in Eq. (3.25) the caret symbol is used to denote frequency domain variables. Furthermore, the points in time are spaced Δt apart and ω_n denotes the nth BPF ('*Blade Passage Frequency*'). The angular spacing of the sources in the propeller disk is expressed as $\Delta\theta$. Finally, θ_{i0} denotes the angular starting position of the ith panel. Now using Eq. (A.64) with zero normal velocity at the boundary, the frequency domain expression, equivalent to Eq. (3.24), becomes,

$$\frac{1}{2}\hat{\varphi}'_n(\mathbf{x}) = -\int_{S_{DH}}\hat{\varphi}'_n(\mathbf{y})\frac{\partial}{\partial n_y}\left(\frac{\exp(ik_nr)}{4\pi r}\right)dS_y\ +$$

$$+\sum_{i=1}^{2(N_b+N_w)}\sum_{j=1}^{N_t}\left[\hat{\sigma}_n(\mathbf{x}_{ij})\frac{\exp(ik_nr_{ij})}{4\pi r_{ij}}+\hat{\mu}_n(\mathbf{x}_{ij})\frac{\partial}{\partial n_i}\frac{\exp(ik_nr_{ij})}{4\pi r_{ij}}\right]$$

(3.26)

In Eq. (3.26), r_{ij} is the distance from the point of observation, $\mathbf{x}$, here assumed to be located on the boundary, to the ith source, located at the collocation point of the ith panel at the jth

time instant, $\mathbf{x}_i^{col}(t_j) = \mathbf{x}_{ij}$, for each harmonic component, n. Furthermore, the wave number obeys, $k_n = \omega_n/c$.

It must be noted that Eq. (3.26) becomes singular at the so-called *characteristic* or *irregular* frequencies. At those frequencies the Kirchhoff-Helmholtz integral equation for the exterior Neumann problem fails to possess a unique solution. In principle, the derivative of Eq. (3.26) in a direction normal to the boundary also solves the exterior scattering problem. Burton and Miller [Burton1971] use this fact in deriving a formulation that can be used to obtain a unique solution at *all* frequencies. For the numerical solution of Eq. (3.26) a discretization procedure using Burton and Miller's method and based on the BEM is presented in Appendix F. This discretization procedure was implemented in a computer programme called EXCALIBUR (*EXcitation CALculation with Improved BURton and Miller method*). The reader is referred to [Visser2004] for an overview of alternative methods to counteract non-uniqueness problems in the Kirchhoff-Helmholtz integral equation.

4 MODEL SCALE EXPERIMENTS

…which describes the experimental simulation of propeller cavitation and its effect in terms of hull pressures, as practised in model basins on scale models of ships and propellers. Scaling laws are reviewed and applied to the model testing procedures of the Depressurized Towing Tank at MARIN.

4.1 Introduction

When performing ship scale model experiments in a cavitation tunnel or depressurized towing tank with the aim of predicting hull-pressure fluctuations and the resulting vibratory hull-excitation forces, one must ascertain that geometric, kinematic and dynamic similarity in model and prototype are preserved. This means similarity in relevant aspects of lengths, displacements, velocities, accelerations and forces [Bertram2000]. Then, ship scale quantities may be predicted from their model scale counterparts by a proportionality factor.

The next section reviews the fundamentals of scaling for model testing. Then, following van der Kooij [Kooij1979], experimental procedures are described that have become standard practice in the DTT of MARIN (see Figure 2.4). The latter facility is implied throughout this thesis when referring to scale model experiments.

4.2 Similarity Requirements

For the correct prediction of forces on the basis of scale model experiments proper geometric scaling is usually regarded as a necessary condition. Geometric features that are proportionally scaled comprise propeller shape, hull form, appendages and waves. When a length scale L is chosen (e.g., the length of the ship), then all other lengths (such as the propeller diameter, D) should scale accordingly. With index m denoting 'model' scale and index s denoting 'ship' scale,

$$\frac{D_m}{L_m} = \frac{D_s}{L_s} \quad \Rightarrow \quad D_m = \frac{D_s}{\lambda} \tag{4.1}$$

in which $\lambda = L_s / L_m$ is the length scale factor. If small scale detail is needed, such as for propeller leading edge geometries, manufacturing accuracy may limit geometric similitude. Sometimes, only partial geometric similitude is necessary, because only those parts of the

geometry need to be represented that influence the forces that are of interest. In Chapter 7 use is made of this by abandoning the '*geosim*' (i.e., the geometrically scaled) ship model.

For kinematic similarity, the ratios between displacements, velocities, and accelerations on model scale have to be equal in magnitude and direction to the corresponding ratios at ship scale. This implies that the flow will undergo geometrically similar motions in both cases. E.g., for kinematic similarity of ship models with propellers it is required to conduct model tests at equal advance coefficient, J ,

$$J = \frac{V_a}{nD} \tag{4.2}$$

in which V_a is the propeller's advance velocity, and n and D its rotation rate and diameter, respectively. The advance velocity differs from the ship speed, V_s , by a factor of $(1-w)$,

$$V_a = V_s(1-w) \tag{4.3}$$

in which w denotes the *effective* ship wake fraction[7]. The latter is the ratio of the slipstream velocity in axial direction and the ship speed, averaged over the stream tube flowing into the propeller disc. The concept of slipstream velocity includes the suction effect of the propeller on the flow around the ship. Without the latter propeller-hull *interaction* component the effective wake fraction would become the *nominal* wake fraction. The effective ship wake plus *propeller induction* velocities forms the so-called *total* wake field (see Figure 4.1). Equal advance coefficients on model and prototype scale ensure that the propeller advances by the same number of diameters during the same number of revolutions,

$$J_m = J_s \quad \Rightarrow \quad \frac{V_{a,m}}{n_m D_m} = \frac{V_{a,s}}{n_s D_s} \quad \Rightarrow \quad \frac{V_{a,m}}{n_m} = \lambda \frac{V_{a,s}}{n_s} \tag{4.4}$$
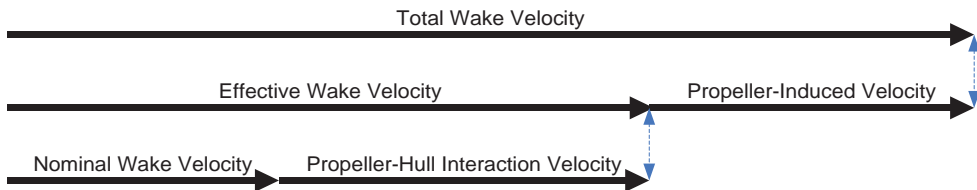
Figure 4.1: Overview of wake velocity components [Carlton1994].

Sufficient dynamic similarity is reached when all important forces act on the model to the same proportion as on the prototype. Hence, the condition for dynamic similarity is to keep the non-dimensional ratios of forces equal. Similarity laws can be derived by non-dimensionalizing the equations that govern the flow. These equations comprise the

---

[7] If the advance coefficient is based on ship speed rather than advance speed, it is termed J_V .

conservation laws of mass, momentum and energy, supplemented by equations of state ('material laws') and appropriate boundary conditions. In the following, these equations and the similarity laws that follow from them are treated. Conservation of energy, however, is not expected to play a significant role in the context of hull-pressure fluctuations and is therefore discarded. From the conservation of mass no scaling laws follow that are not already present in the momentum equation.

4.3 Non-dimensional Conservation Laws

4.3.1   Conservation of momentum

The version of the Navier-Stokes equations that expresses conservation of momentum for *compressible* Newtonian fluids [White2006] reads,

$$\rho\left(\frac{\partial \mathbf{v}}{\partial t} + (\mathbf{v}\cdot\nabla)\mathbf{v}\right) = -\nabla p + \frac{\partial}{\partial x_j}\left[\mu\left(\frac{\partial v_i}{\partial x_j} + \frac{\partial v_j}{\partial x_i}\right) + \delta_{ij}\mu_b\left(\nabla\cdot\mathbf{v}\right)\right] + \mathbf{f} \tag{4.5}$$

In Eq. (4.5), ρ denotes the fluid's mass density, p the pressure, and μ and μ_b its dynamic and bulk (or second) viscosity, respectively. Furthermore, t is time, $\mathbf{v}$ the velocity, v_i a velocity component in one of three orthogonal directions, x_i, and $\mathbf{f}$ a general body force. For example, the gravity force may be expressed as $\mathbf{f} = \rho\mathbf{g}$, with $\mathbf{g}$ as the acceleration due to gravity. Finally, δ_{ij} denotes Kronecker's delta function. For incompressible flows, for which $\nabla\cdot\mathbf{v} = 0$, of constant viscosity and mass density, ρ_0, Eq. (4.5) simplifies to,

$$\rho_0\left(\frac{\partial \mathbf{v}}{\partial t} + (\mathbf{v}\cdot\nabla)\mathbf{v}\right) = -\nabla p + \mu\nabla^2\mathbf{v} + \mathbf{f} \tag{4.6}$$

Scaling parameters are now chosen as in Table 4.1. Then, using the asterisk symbol, non-dimensional variables are defined as in Table 4.2. Substituting these variables into Eq. (4.6) yields,

$$\rho_0 Vf\frac{\partial \mathbf{v}^*}{\partial t^*} + \frac{\rho_0 V^2}{L}(\mathbf{v}^*\cdot\nabla^*)\mathbf{v}^* = -\frac{\rho_0 V^2}{L}\nabla^* p^* + \frac{\mu V}{L^2}\nabla^{*2}\mathbf{v}^* + \rho_0 g\mathbf{g}^* \tag{4.7}$$

in which f and V denote a characteristic flow frequency and velocity, respectively, and g is the magnitude of $\mathbf{g}$. Dividing by $\rho_0 V^2/L$ gives,

$$\frac{fL}{V}\frac{\partial \mathbf{v}^*}{\partial t^*} + (\mathbf{v}^*\cdot\nabla^*)\mathbf{v}^* = -\nabla^* p^* + \frac{\mu}{\rho_0 VL}\nabla^{*2}\mathbf{v}^* + \frac{gL}{V^2}\mathbf{g}^* \tag{4.8}$$

Using the non-dimensional numbers identified in Table 4.3 the *incompressible* form of the Navier-Stokes equations can be written as,

$$\text{St}\frac{\partial \mathbf{v}^*}{\partial t^*} + (\mathbf{v}^* \cdot \nabla^*)\mathbf{v}^* = -\nabla^* p^* + \frac{1}{\text{Re}}\nabla^{*2}\mathbf{v}^* + \frac{1}{\text{Fr}^2}\mathbf{g}^* \tag{4.9}$$

in which the Strouhal (St), Reynolds (Re) and Froude (Fr) numbers appear.

Table 4.1: Scaling parameters

Parameter	Description	Dimensions
L, D	Characteristic lengths	[length]
V	Characteristic speed	[length/time]
V_a	Advance velocity	[length/time]
f	Characteristic frequency	[1/time]
n	Propeller rotation rate	[1/time]
ρ_0	Characteristic density	[mass/length^3]
p_0	Characteristic pressure	[mass/length/time^2]
p_v	Vapor pressure	[mass/length/time^2]
g	Gravitational acceleration	[length/time^2]
S	Surface tension	[mass/time^2]
μ	Dynamic viscosity	[mass/length/time]
c	Speed of sound	[length/time]
T_p	Propeller thrust	[mass*length/time^2]
Q_p	Propeller torque	[mass*length^2/time^2]

Table 4.2: Non-dimensional parameters

Non-dimensional variables	Description
$t^* = ft$	Time
$\mathbf{x}^* = \mathbf{x}/L$	Position
$\mathbf{v}^* = \mathbf{v}/V$	Velocity
$p^* = p/\rho_0 V^2$	Pressure
$\mathbf{g}^* = \mathbf{g}/g$	Gravitational acceleration
$\nabla^* = L\nabla$	Gradient operator
$\rho^* = \rho/\rho_0$	Density

Table 4.3: Non-dimensional numbers

Non-dimensional numbers	Description
$J = V_a / nD$	Advance coefficient
$K_t = T_p / \rho_0 n^2 D^4$	Thrust coefficient
$K_q = Q_p / \rho_0 n^2 D^5$	Torque coefficient
$St = fL / V$	Strouhal number
$Fr = V / \sqrt{gL}$	Froude number
$Re = \rho_0 VL / \mu$	Reynolds number
$\sigma = (p_0 - p_v) / \frac{1}{2} \rho_0 V^2$	Cavitation number
$We = \rho_0 V^2 L / S$	Weber number
$Ma = V / c$	Mach number

When the non-dimensional parameters have been defined properly, they are of equal order of magnitude. Then, the non-dimensional numbers can be used to judge the relative importance of each of the terms in Eq. (4.9). However, locally in the flow, the non-dimensional flow variables (indicated by an asterisk) may become of a different order, thus causing the non-dimensional numbers to lose their comparative meaning. As an example, assume the Reynolds number to be based upon mainstream quantities. The Reynolds number may then become very large, from which it follows that the viscous term in Eq. (4.9) may be neglected. However, locally, in the boundary layer, the term $\nabla^{*2} \mathbf{v}^*$ is no longer of order one. Although part of the viscous stress term will turn out to be negligible, not the whole term is. In such a case it must be concluded that the choice of the scaling parameters was not appropriate for the boundary layer flow.

For dynamic similarity between model and prototype scale, the non-dimensional numbers derived above must match. In the following, the relationship between the actual hydrodynamic forces and the non-dimensional numbers is clarified so as to provide physical insight with regard to their use.

The inertia effects, that are used to relate other forces to, are a measure of the *convective* acceleration of the fluid. In oscillatory flows, also the *local* fluid acceleration may be an important force that scales as $\rho V L^3 f$, with frequency scale f, e.g., a vortex shedding frequency. Then, the Strouhal number becomes,

$$St = \frac{\rho_0 V L^3 f}{\rho_0 V^2 L^2} = \frac{fL}{V} \tag{4.10}$$

Note that the advance coefficient, defined in Eq. (4.2), is in fact another variant of this number. Scaling according to Froude number identity implies for Strouhal number scaling that,

$$\frac{f_m L_m}{V_m} = \frac{f_s L_s}{V_s} \quad \Rightarrow \quad f_m = f_s \sqrt{\lambda} \tag{4.11}$$

Gravity governs many aspects of fluid flow, such as buoyancy, the behavior of free surface waves, and the hydrostatic pressure. For example, wave making effects are governed by the ratio of inertia and gravity forces. Inertia forces scale as $\rho_0 V^2 L^2$, and gravity forces scale as $\rho_0 g L^3$. The ratio between them is the square of the Froude number, Fr,

$$\text{Fr} = \sqrt{\frac{\rho_0 V^2 L^2}{\rho_0 g L^3}} = \frac{V}{\sqrt{gL}} \tag{4.12}$$

Similitude of these forces is achieved when the Froude number at model scale matches that at ship scale. Thus,

$$V_m = \sqrt{\frac{g_m}{g_s} \frac{L_m}{L_s}} V_s = \frac{V_s}{\sqrt{\lambda}} \tag{4.13}$$

As the constant of gravitational acceleration is identical for model and ship scale, Froude similitude implies that the velocity scales as the root of the scale factor. This also determines the model scale propeller rotation rate in the advance ratio (Eq. (4.4)) as being larger than the ship scale rotation rate by a factor of $\sqrt{\lambda}$.

Viscous forces scale as $\mu V L$. The ratio of inertia to viscous forces leads to the Reynolds number, Re,

$$\text{Re} = \frac{\rho_0 V^2 L^2}{\mu V L} = \frac{VL}{\nu} \tag{4.14}$$

with ν as the kinematic viscosity. Reynolds identity for model scale testing implies that

$$V_m = \frac{\nu_m}{\nu_s} \frac{L_s}{L_m} V_s = \lambda V_s \tag{4.15}$$

for equal viscosity of water on model and ship scale. The model speed should be the ship speed multiplied by the scale factor, which is prohibitively impractical in a towing tank or a cavitation tunnel. If Froude identity is maintained, thereby reducing the model speed by a factor of $\sqrt{\lambda}$, a scale effect on Reynolds number of $\lambda^{3/2}$ becomes inevitable. In practice, one may accept a discrepancy in Froude number in favor of a higher Reynolds number (though never achieving full Reynolds identity).

As a measure of the propeller load the advance coefficient of the full-scale propeller is used as well as the thrust and torque coefficients, K_t and K_q,

$$K_t = \frac{T_p}{\rho_0 n^2 D^4} \tag{4.16}$$

$$K_q = \frac{Q_p}{\rho_0 n^2 D^5} \tag{4.17}$$

with, T_p, as the propeller thrust and, Q_p, as its torque. The form of the torque coefficient is similar to the form of the thrust coefficient. The thrust coefficient itself is not directly obtained from the conservation of momentum. When the incompressible Navier-Stokes equations are given by Eq. (4.6) the gravity force is usually the only body force appearing. More generally, one could state that $\mathbf{f}$ denotes all possible body forces, one of which may be the force, $\mathbf{f}_p$, which the propeller exerts on the flow. Assume for the sake of simplicity that this force acts as a point force applied at $\mathbf{x} = \mathbf{x}_p$. Then, the body force, $\mathbf{f}_p$, can be expressed as a distribution in the following way,

$$\mathbf{f}_p = -T_p \delta(\mathbf{x} - \mathbf{x}_p) \sim T_p L^{-3} \tag{4.18}$$

in which Dirac's delta function is $\delta(\mathbf{y}) \equiv \delta(y_1)\delta(y_2)\delta(y_3)$, with the indices indicating the coordinate directions. With the propeller's diameter as length scale and nD as velocity scale, the ratio of inertia forces to propeller thrust forces becomes,

$$\frac{\rho_0 V^2 L^2}{T_p L^{-3} L^3} \propto \frac{\rho_0 n^2 D^4}{T_p} \tag{4.19}$$

i.e., the inverse of the thrust coefficient. Scaling according to the Froude number implies for the scaling of propeller loading that,

$$\frac{\rho_m n_m^2 D_m^4}{T_{p,m}} = \frac{\rho_s n_s^2 D_s^4}{T_{p,s}} \quad \Rightarrow \quad T_{p,s} = T_{p,m} \frac{\rho_s}{\rho_m} \lambda^3 \tag{4.20}$$

and similarly for the torque,

$$Q_{p,s} = Q_{p,m} \frac{\rho_s}{\rho_m} \lambda^4 \tag{4.21}$$

The thrust and torque at model scale thus become smaller than at full scale by factors of $\lambda^3 \rho_s / \rho_m$ and $\lambda^4 \rho_s / \rho_m$, respectively.

4.3.2   State equations

Apart from conservation laws of mass, momentum and energy, two further relations are needed to close the set of equations for the seven unknowns, pressure, mass density, temperature, internal energy, and three velocity components. Utilizing the thermodynamic state principle, two state equations can be introduced expressing the thermodynamic behavior of the fluid, e.g., a relation between the pressure, density, temperature and internal energy, e, such as $p = p(\rho, T)$ and $e = e(\rho, T)$. In a liquid, there is an almost linear relation between the density and pressure changes,

$$\delta p \approx c^2 \delta \rho \tag{4.22}$$

with c as the speed of sound. Following [White2006] it can be stated that the fluid is practically incompressible when,

$$\left|\frac{\delta \rho}{\rho_0}\right| << \left|\frac{\delta V}{V}\right| \tag{4.23}$$

If also, $\delta p \approx -\rho_0 V \delta V$, then,

$$\frac{V^2}{c^2} = Ma^2 << 1 \tag{4.24}$$

Here, the Mach number, Ma, is introduced, which governs compressibility effects in flows. The speed of sound follows from the bulk modulus of elasticity, E_v,

$$E_v = \rho_0 \frac{dp}{d\rho} = \rho_0 c^2 \tag{4.25}$$

and may be interpreted as Hooke's law for fluids.

The ratio of inertia forces ($\rho_0 V^2 L^2$) to elastic forces ($E_v L^2$) leads to the square of the Mach number, Ma,

$$Ma = \sqrt{\frac{\rho_0 V^2 L^2}{E_v L^2}} = \frac{V}{\sqrt{E_v/\rho_0}} = \frac{V}{\sqrt{dp/d\rho}} = \frac{V}{c} \tag{4.26}$$

In water, the speed of sound is hardly dependent on pressure (a reduction of only 5% is found at a depth of one kilometer), the velocity should be kept equal to the prototype velocity. However, if Froude scaling is required, the Mach number will be too small and the length of the sound waves will be too large by a factor of $\sqrt{\lambda}$. Thus, similarity in interference patterns at some distance from the source is lost.

4.3.3   Boundary conditions

At liquid-gas interfaces, velocity and pressure may be prescribed. In case an interface surface is present the boundary condition for the pressure difference on it is given by [White2006][8],

$$p_{liquid} = p_{gas} - S\left(r_1^{-1} + r_2^{-1}\right) \tag{4.27}$$

with the principal radii of interface curvature, r_1 and r_2. Surface tension is denoted by S. In non-dimensional form, using $r^* = r/L$, it follows,

$$\frac{p_{liquid} - p_{gas}}{\frac{1}{2}\rho_0 V^2} = -\frac{S}{\frac{1}{2}\rho_0 V^2 L}\left(r_1^{*-1} + r_2^{*-1}\right) \tag{4.28}$$

---

[8] It must be remarked that Eq. (4.27) is valid when there is no flow.

In [Rood1991], cavitation *inception* is defined as the initial rapid growth of vapor- and gas-filled bubbles, called nuclei, as a consequence of hydrodynamic forces. When there is no shortage of such nuclei in the flow and their growth is not hampered by surface tension effects, cavitation occurs once the local pressure reaches the vapor pressure, p_v, of the liquid. This limit is typically expressed as the cavitation number, σ,

$$\sigma = \frac{p_0 - p_v}{\frac{1}{2}\rho_0 V^2} = \frac{p_{atm} - p_v + \rho_0 gh}{\frac{1}{2}\rho_0 V^2} \tag{4.29}$$

with p_0 as some characteristic pressure in the liquid (p_{liquid}), rewritten as the sum of the atmospheric pressure at the free surface, p_{atm}, and the hydrostatic pressure. Here, h denotes the submergence and p_v is taken for the pressure in the gas, p_{gas}. Eq. (4.28) becomes,

$$\sigma = -\frac{2}{\text{We}}\left(r_1^{*-1} + r_2^{*-1}\right) \tag{4.30}$$

with the ratio of inertial to surface tension forces forming the Weber number,

$$\text{We} = \frac{\rho_0 V^2 L^2}{SL} = \frac{\rho_0 V^2 L}{S} \tag{4.31}$$

Although in principle the inception of cavitation takes place at the vapor pressure, in practice this may be far from the truth due to the nuclei being of such small diameter that their growth in low pressure regions is counteracted by surface tension effects. Using a bubble approach to model cavitation inception (see [Rijsbergen2010]), the critical pressure p_c below which a gas nucleus will grow exponentially is given by,

$$p_c = p_v - \tau = p_v - \frac{4S}{3R_c} \tag{4.32}$$

where τ is the tensile strength of water and R_c the critical bubble radius. In non-dimensional terms, the cavitation inception criterion can then be written as,

$$\sigma = -C_{p,\text{min}} - \frac{\tau}{\frac{1}{2}\rho_0 V^2} = -C_{p,\text{min}} - \frac{8}{3\text{We}} \tag{4.33}$$

with $C_{p,\text{min}}$ denoting the minimum pressure coefficient for minimum pressure, p_{min}, as,

$$C_{p,\text{min}} = \frac{p_{\text{min}} - p_0}{\frac{1}{2}\rho_0 V^2} \tag{4.34}$$

and the Weber number is based on the critical bubble radius.

For cavitation inception to take place at the vapor pressure, the Weber number should be large. Applying Froude scaling and assuming the density and surface tension to be approximately the same at model and ship scale, it can be written,

$$We_m = We_s \frac{1}{\lambda} \frac{R_{c,m}}{R_{c,s}}$$
(4.35)

Similar bubble Weber numbers on model and full scale would require λ times larger bubbles on model scale than on full scale. Without measurement and control of the nuclei spectrum, there remains a scale effect on cavitation inception, $\Delta\sigma_W$,

$$\Delta\sigma_W = \frac{8}{3We_s} \left(\lambda \frac{R_{c,s}}{R_{c,m}} - 1 \right)$$
(4.36)

Note that for developed cavitation, surface tension effects are usually negligible and Weber number scaling is not important.

4.4 DTT Testing Procedure

As in many of the larger cavitation tunnels in use around the world, the DTT is designed to work on the type of scale models of the ship and propeller that are used in standard speed-power calm water towing tank tests. This approach automatically satisfies the condition of geometric similarity and leads to the largest model sizes that are still practical. Van der Kooij [Kooij1979] states that for an accurate representation of propeller cavitation, the cavitation number, e.g., in a form based on $V = nD$ in Eq. (4.29),

$$\sigma_n = \frac{p_{atm} - p_v + \rho_0 gh}{\frac{1}{2}\rho_0 n^2 D^2}$$
(4.37)

should be equal for model and ship. Also, matching of propeller loading, K_t (Eq. (4.16)) is required. Finally, equal susceptibility of the water to cavitation inception must be ensured. From the required correspondence in cavitation number at all depths follows the propeller rotation rate on model scale,

$$n_m = n_s \sqrt{\lambda}$$
(4.38)

as well as the towing tank pressure,

$$p_{atm,m} = \frac{\rho_m}{\rho_s} \frac{1}{\lambda} \left(p_{atm,s} - p_{v,s} \right) + p_{v,m}$$
(4.39)

The scaling requirement on the cavitation number is compatible with Froude number identity everywhere in the flow. Hence, free surface interface pressures, water wave patterns and gravity forces are then also proportionally scaled.

The requirement of K_t identity is converted into one of advance coefficient identity,

$$\frac{V_m\left(1-w_m\right)}{n_m D_m} = \frac{V_s\left(1-w_s\right)}{n_s D_s} \quad \Rightarrow \quad V_m = \frac{\left(1-w_s\right)}{\left(1-w_m\right)}\sqrt{\lambda}V_s \tag{4.40}$$

The term involving model and ship scale wake fractions, w_m and w_s, respectively, on the right hand side of Eq. (4.40) represents the scale effect on the wake. A value different from (and usually greater than) one is caused by the fact that viscous forces are disproportionally large on model scale, or in other words, the model scale Reynolds number is much too small. Therefore, equal advance coefficients on model and ship scale can only be obtained by applying model ship advance velocities that are somewhat (say, a few percent) greater than would be prescribed by Froude identity. The propeller rotation rate still adheres to Eq. (4.38). Alternatively, the thrust coefficient could be used directly. As a matter of fact, since the scale effect on K_t is negligible and the determination of the wake scale effect in speed-power experiments is based on this very fact, thrust coefficient and advance ratio identity become interchangeable.

Cavitation inception susceptibility is governed by the presence of free gas nuclei, their number density and size distribution. Surface tension effects depending on the Weber number can prevent nuclei from growing at pressures below the vapor pressure. Artificial roughness is applied on the leading edges of propeller blades to stimulate the growth of nuclei in the low pressure wakes of the microscopic roughness elements. To increase the number of free gas nuclei, they are generated upstream of the propeller plane by means of electrolysis of the water. Van Rijsbergen et al. [Rijsbergen2010] give an update of the state-of-art with regard to such water quality issues.

The generation of nuclei and the application of artificial roughness are a necessary, but not always sufficient condition for cavitation inception to occur. The nuclei must reach the roughness elements and the pressure distribution on the propeller blades must resemble the one on ship scale. The requirements have a bearing on the viscous flow similarity between model and ship scale. The Reynolds number discrepancy may therefore also cause a scale effect here. As far as the inception of vortex cavitation is concerned the Reynolds number scale effect causes pressures in the vortex cores on model scale to be much higher than on ship scale, thereby considerably delaying cavitation inception.

The prediction of hull pressures may also be affected by scale effects on the acoustic hull diffraction. The use of a geometrically scaled ship model and correctly modeled ship wave pattern reduces this effect to a minimum. Still, the scattering of hull-pressure pulses may suffer somewhat from the non-matching Mach number. At low frequencies and close proximity to the cavities this error is usually considered negligible. Bottom and wall reflections were studied by Vehof [Vehof2001]. He concluded that the afterbody surface lies well within the critical distance and reverberation effects may be neglected.

Summarizing, experiments in the DTT are performed with geometrically similar ship and propeller models, at correct trim and sinkage, propeller thrust loading, cavitation and Froude numbers. Froude number identity is achieved by the choice of propeller rotation rate, whilst the speed at which the model is towed may be a few percent above the speed required for matching the Froude number in order to compensate the propeller loading for the wake scale effect.

The resulting dynamic propeller cavitation causes pressure fluctuations on the hull that are measured by a set of flush-mounted pressure transducers as seen in Figure 4.2. The pressures are sampled during a run through the tank at shaft synchronized instances (e.g., once per degree of propeller rotation) and subsequently analyzed harmonically. This is done by taking an integer number of propeller revolutions starting with the sample taken when a marked blade reaches its *top dead centre* (TDC, i.e., vertically upright) position. From the amplitudes and phase angles, thus gathered, an afterbody force can be determined for each harmonic component of interest (usually at orders of BPF).

Inevitably, hull-pressure fluctuations will cause vibrations of the model ship and it may be argued that for this reason the response of the model ship must also be properly scaled. However, this is not the case as one is interested in obtaining the ship scale hull-pressure field without the vibration-induced component. It is the latter pressure field that constitutes the vibratory excitation force. Therefore, it is concluded that for model experiments hull-pressure fluctuations must be measured on a rigid hull. As stated in Section 2.3, this effect, together with the Reynolds number scale effect on the ship wake and propeller flow, are considered dominating causes of error in the prediction of hull-pressure fluctuations. The vibration-induced pressure component is dealt with in the next chapter, and the wake scale effect in Chapter 7. Further possible scale effects on propeller (vortical) flows are investigated by Bosschers. For now, this thesis starts from the assumption that fully developed cavitating vortices are controlled by inertia. Then, no significant scale effects on hull-pressure fluctuations should be expected.

An overview of topics involved in the DTT testing procedure is given in Figure 2.5.
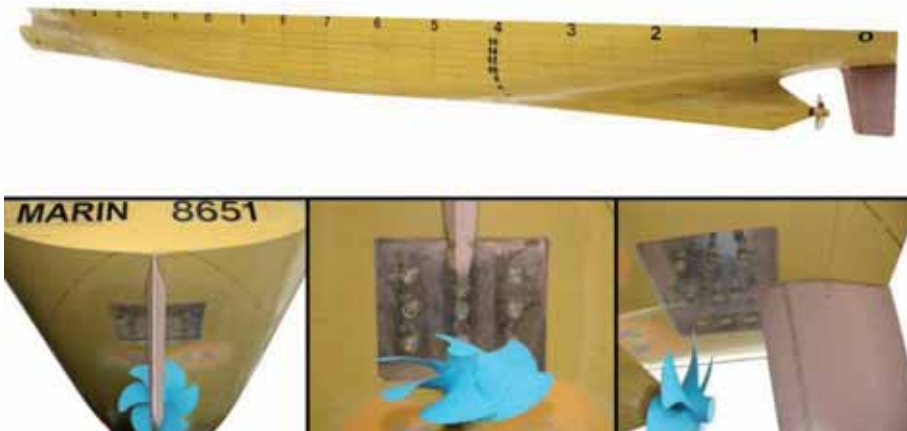

**Figure 4.2: Set of flush-mounted pressure transducers for measuring
the hull-pressure distribution on model scale.**

5 VIBRATION-INDUCED HULL PRESSURES

…in which ship model vibrations are found to sometimes cause significant errors in measuring propeller-induced hull-pressure fluctuations. It is shown how structural modifications to the model in combination with acoustic BEM tools limit the influence of model vibrations.

5.1 Introduction

When measuring propeller-induced hull-surface pressures it is tacitly assumed that the surface is perfectly vibration free, at least in the frequency range of interest (say, 30-200 Hz). This would ensure that true excitation forces are measured that may be directly used in a Finite Element Analysis (FEA) of the ship hull vibration. However, in reality, scale models of ships are usually made of non-rigid materials like wood, polyurethane or similar, with the inevitable result being vibrations of the measuring surface when excited by the propeller. If the hull surface is loaded by a relatively heavy fluid, vibration-induced pressures may become substantial and lead to inadmissible measuring errors. These errors are not only caused by water borne excitation, but may also be caused by the model's driving train. Examples are the motor exciting the bottom, small misalignments in shafting as well as gearing imperfections, both exciting the afterbody through the brackets or gondola.

Errors caused by vibration-induced pressures may become substantial as noted by the ITTC (see Section 2.2) and as witnessed by the author on many occasions, e.g., [Wijngaarden1988, Gent1989]. An example is presented in Section 5.4, in which the measurement of the maximum hull-pressure amplitude at BPF turned out to be affected by vibrations to an amount of 34% and 17% for two different propeller rotation rates.

In this chapter, the application of structural modifications in combination with a BEM is proposed to limit the influence of model vibrations.

5.2 Counteracting Ship Model Vibrations

Several measures have been proposed to counteract effects caused by the driving train [Nieuwenkamp2002]. Shaft and bearing tube alignment must be precise so as not to cause excessive friction. Also gearing using prime number gear tooth ratios is preferred. The motor must deliver its torque as uniformly as possible and should be placed on a heavy foundation, whilst being flexibly coupled to a stiff shaft. During testing, the model should ideally be rigidly connected to the outside world in order to suppress afterbody vibration. Often, the model can

only be fixed at the sides (e.g., in cavitation tunnels), or not at all (in free surface facilities like the DTT). In the latter case even a rigid, but freely floating model would still vibrate, be it only in its rigid modes. The amount of mass that can be added in the aft ship in order to reduce its acceleration response is then limited because of draught and trimming requirements.

An alternative approach is to increase the stiffness so as to shift the model's natural frequencies to frequencies above the range of interest. This may be effective when the model's afterbody weight is kept as low as possible, e.g., by filling up the afterbody with extra layers of light wood. Thus, also hogging and sagging effects in the afterbody would be automatically minimized and the shaft alignment would be maintained while the model is afloat. Suppose, the maximum allowable vibration-induced pressure level is set at 10% of the propeller-induced pressure level, or roughly one Pascal back-pressure for each Newton of vibratory excitation force. Then, Kampman [Kampman2005] states that it will not be practically possible to achieve this without carrying out extreme structural modifications.

However, when wooden models are three to four five-centimeter layers thick, the vibrations still present are of a modal density low enough to be accurately measured by a limited number of accelerometers. A BEM may then be used to computationally correct for the remaining vibrations. This procedure is presented in Figure 5.1, in which hull surface pressures are assumed to be measured in conjunction with hull surface vibrations. If considered necessary, the vibrations are input to a BEM for the computation of vibration-induced surface pressures, which are then subtracted from the hull pressures measured.

In the next section, an acoustic BEM is used for this purpose. This BEM, i.e., the one introduced in Section 3.4 for the determination of the scattering effect of the ship hull, is adapted for use in the computation of acoustic radiation from a vibration surface. Details of the method are found in Appendix F.2.
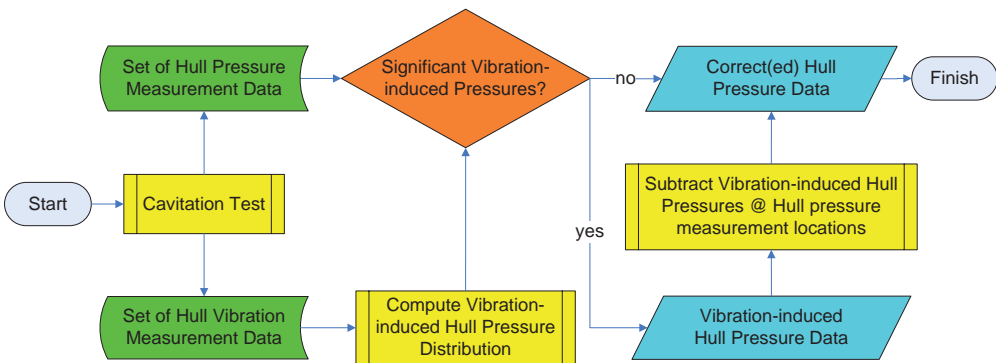

Figure 5.1: Procedure for correcting scale model vibrations in experiments.

5.3 Example Case: Twin Screw Ferry

The method of correcting for model vibration errors in measuring hull surface pressures, as introduced in the preceding section, is now applied to a practical case. However, there is one issue that must be resolved first. Although pressure pick-ups can be flush mounted in the

hull, this is rather awkward to achieve for accelerometers. Fortunately, with the flat sterns of so many modern vessels the acceleration levels might as well be measured on the (horizontal, flat) inside of the model. As a check on whether accelerometers on the bottom of the afterbody would show the same acceleration levels as their counterparts on the outside hull, a set of accelerometers was made watertight and fitted both on the inside and outside of a typical twin screw vessel model. In the frequency range of interest, but also at much higher frequencies, there was no noticeable difference between wetted accelerometer readings and their inboard counterparts. However, for more V-shaped hulls this approach will fail unless it is fair to assume that the vibratory displacements are predominantly in the vertical direction. Then, the outward normal component of the measured vertical acceleration can be used in the analysis. In the remainder of this chapter, this statement is assumed to be valid.

The minimum vibration-induced pressure level at low frequencies is to be expected in the range of 1.5% of the propeller-induced pressure level for a relatively heavy single screw ship, to 5.5% for a relatively light twin screw ship [Kampman2005]. This minimum level is caused by the three rigid body modes and cannot be changed for a given ship. For an average ship model, an estimated 18 global beam modes will have their natural frequency within the frequency range of interest, viz., 6 transverse modes and 12 torsional modes. Some of these modes can be shifted outside the frequency range of interest by stiffening the ship model by increasing the bottom thickness. However, not all of these modes can be eliminated.

With increasing mode number, the distance between the vibration nodes becomes smaller and more acceleration sensors are needed. These 'higher' modes may be eliminated by increasing the global stiffness of the ship. When the bottom thickness is 5 centimeters, as is the case for most ship models currently manufactured at MARIN, approximately 15-30 local plate modes have their natural frequency in the frequency range of interest. For some of these mode shapes, at least 64 acceleration sensors would be needed to accurately compute the vibration-induced pressures. When the plate thickness is increased to 25 centimeter, only four local plate modes still have their natural frequency in the range of interest. Then, only 16 acceleration sensors are needed to accurately calculate the pressures induced by these mode shapes.

As an example, consider the twin screw ship model displayed in Figure 5.2. The thickness of this model was increased up to 20 centimeters. Seventeen accelerometers were distributed over the full width of the afterbody (cf. Figure 6.3 for an example). An exciter, like the one depicted in Figure 6.3, placed on top of the afterbody right above the propeller, excited the ship in a frequency range encompassing the range of interest. Using the boundary element grid depicted in Figure 5.2, values for the amplitudes and phases at each boundary element's collocation point were interpolated from the measured values. Outside the measuring area, the accelerations were extrapolated to zero. The BEM described in the preceding section was used to compute the pressures at the locations of the 20 transducers, also indicated in Figure 5.2.

Figure 5.4 shows computed instantaneous vibration-induced pressure distributions on the afterbody at various frequencies (i.c., 60, 97 and 126 Hz). The deformed afterbody shape is determined by interpolation of the measured values at the accelerometer positions (grey cubes). The colored spheres indicate the measured vibration-induced pressure values, which are to be compared with the computed surface pressure distributions. Figure 5.3 shows the vibration-induced pressure (red line) as a function of frequency for one of the pressure transducers right above the propeller. The green line results when the computational

correction is performed with only 6 accelerometers. The accelerometers used are encircled in red in Figure 5.2. The blue line shows the vibration-induced pressure that remains after correction by the BEM using the data of all 17 accelerometers as input. In other words, the blue line constitutes the error in the computation of the vibration-induced pressure. Up to 200 Hz, this error stays within the limit of 1 Pa/N. It may be concluded that our aim can be reached with a considerable increase of bottom thickness and a reasonable number of accelerometers.
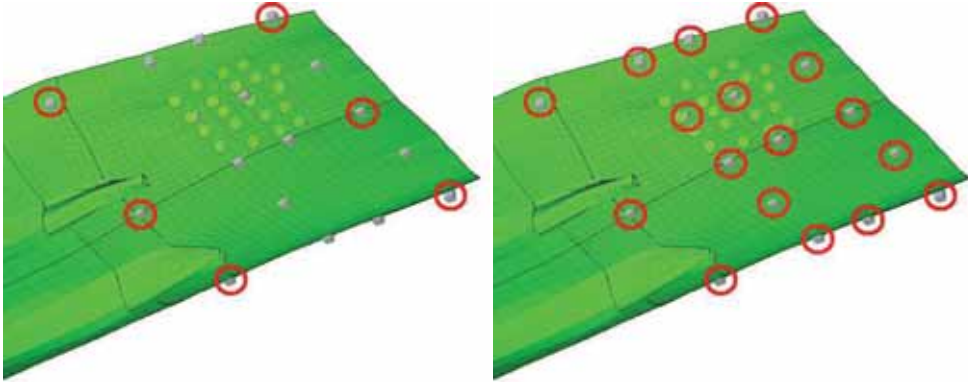

Figure 5.2: Accelerometers (grey cubes), Pressure transducers (green spheres).
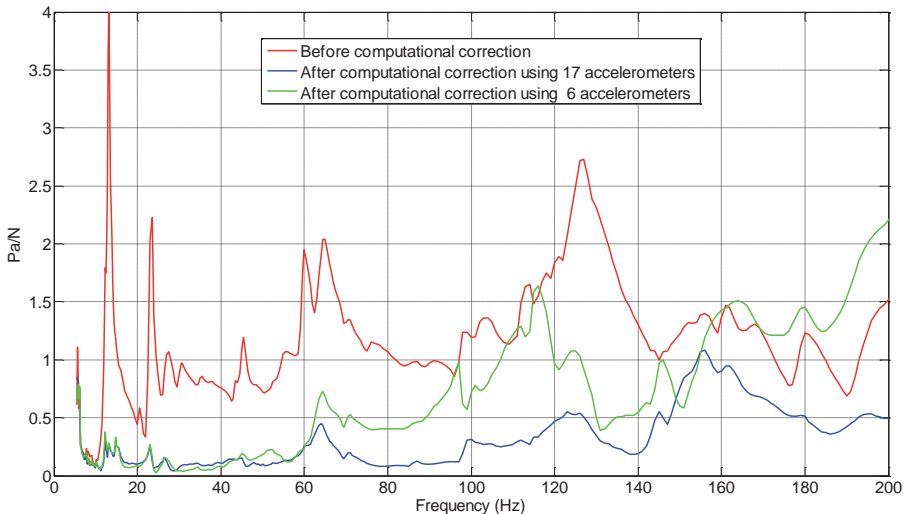

Figure 5.3: Vibration-induced pressure per unit force of excitation before (red line) and after (blue/green line) the application of the computational correction method to the measurements.
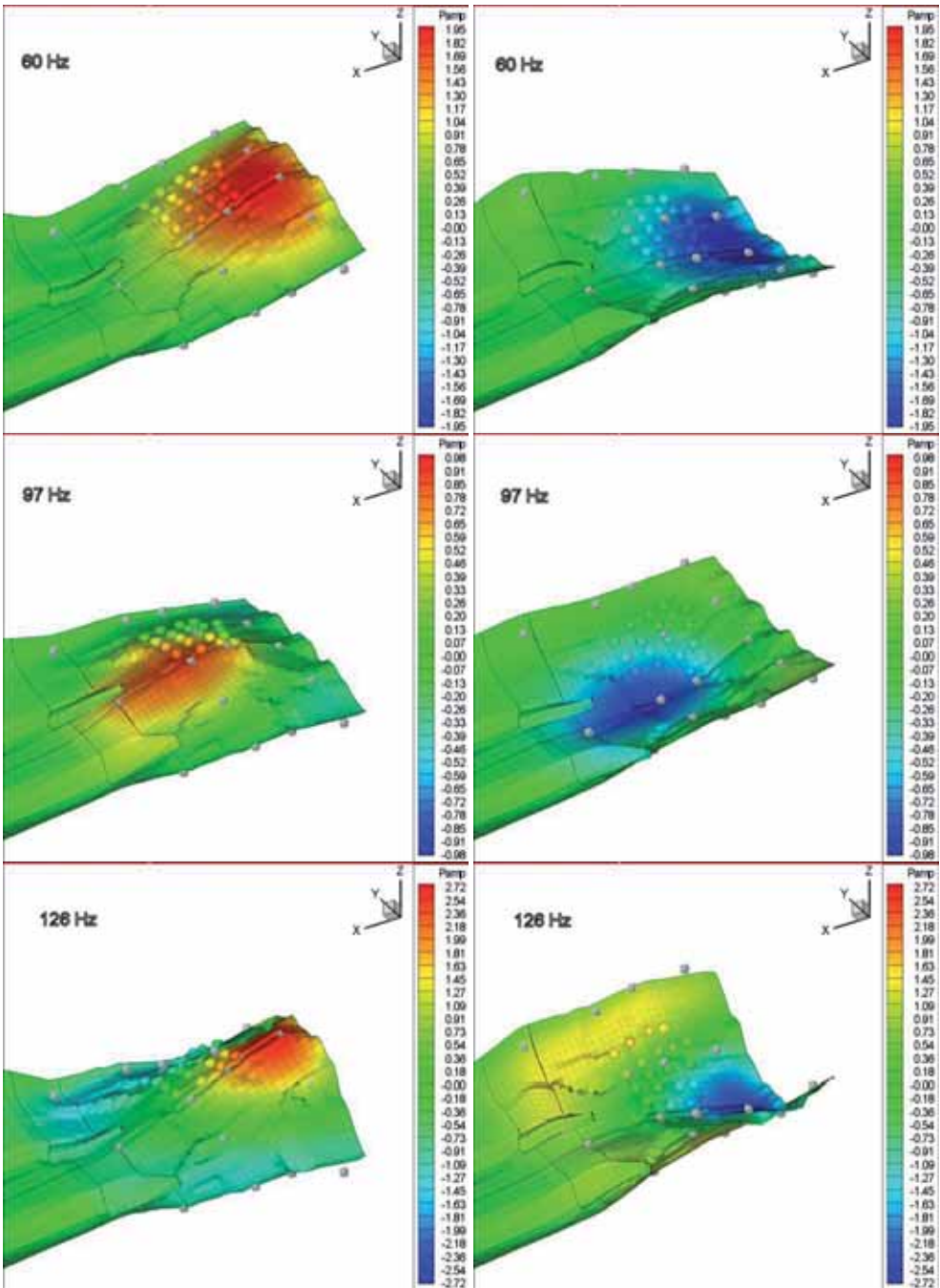
Figure 5.4: Mode shapes and pressure distributions. Top: 60 Hz; Center: 97 Hz; Bottom: 126 Hz. Grey cubes indicate accelerometer positions, spheres denote pressure transducer locations.

Kampman [Kampman2005] concludes that correcting for vibration-induced pressures leaving a remaining error of less than 10% of the propeller-induced pressures in the entire frequency range of interest[9], is possible provided the local bottom thickness in the aftship is at least 25 centimeter. Through the proposed correction method, all rigid body modes and most global beam modes can be eliminated. The local behavior in the aftship is then practically rigid and will not cause problems. In most cases, the measuring system at MARIN allows for 20-25 accelerometers to be used, which would meet the requirement.

5.4 Example Case: Container Vessel #1

The stiffening of ship models and the correction procedure for model afterbody vibrations, as treated above, have been applied in many cases. Although it is the author's experience that the procedure works reasonably well, practical test cases involving operating propellers cannot deliver proof of this for the simple reason that the vibration free results are unknown. Therefore, the following alternative procedure was adopted: perform a test using standard set points for speed and RPM based on thrust, Froude and cavitation number identity, followed by a repeat test at a different RPM and speed, while maintaining thrust identity. The assumption is that the small change in Froude and Reynolds numbers involved in the two measurements will not affect the cavitation behavior and the pressure fluctuation levels on the hull, but will affect the vibration behavior of the ship, due to the change in excitation frequencies.

The test case used is the large container vessel depicted in Figure 5.5. The model was stiffened in the afterbody and the pressure transducers were flush mounted above the propeller in a thick perspex window. The two RPM values at which the measurements were performed differed by 100 RPM, the largest RPM determined by Froude scaling. Initially, the measured results seemed to be quite different with normalized first BPF harmonics of 0.66 and 0.85, for the higher and lower RPM, respectively. This indicates scale effects on the wake due to the different model speeds, which were substantially above the Froude-scaled speed. However, after elimination of the model vibration-induced pressures, making use of only 6 accelerometers, the first harmonics became 1.00[10] and 1.02, respectively, showing that the difference had been caused almost entirely by model vibrations.

This example shows that at the low frequencies of first blade harmonics, the proposed method using a small number of accelerometers in the area of the pressure transducers already works, when the local model stiffness is high enough. Perhaps more importantly, the results show the significance of the vibration-induced pressure component, being 34% and 17%, respectively, in amplitude of the 'true' value after correction. The corrected values are significantly higher, indicating that ship model vibrations are largely in phase with the excitation, thus causing a pressure relief.

Also, in many other cases, the author found that although errors vary a lot, the net result of the vibration correction procedure is almost always a pressure increase at the BPF. It may therefore be concluded that whenever overpredictions of pressure fluctuations at BPF occur, they are not, in general, explained by parasitic vibration-induced pressures.

---

[9] Note that the error at the most significant blade rate frequencies will generally be much smaller.
[10] This value has been used in normalizing the pressure amplitudes measured on container vessel #1.

This conclusion is only valid provided the ship scale measurements have not been affected by vibration-induced pressures to a greater amount than their model scale counterparts. When no resonance vibration issues are occurring on the ship, the vibration levels are usually such that the vibration-induced pressures are not significant at the blade passage frequency.

A final remark about the robustness of the proposed vibration correction must be made. Whenever the source of vibration is outside the stiffened measuring area, the method may fail to produce accurate results. A notable example of such a case is a vibrating pod housing that directly radiates noise to the pressure transducer locations, or excites the afterbody through its Z-drive.
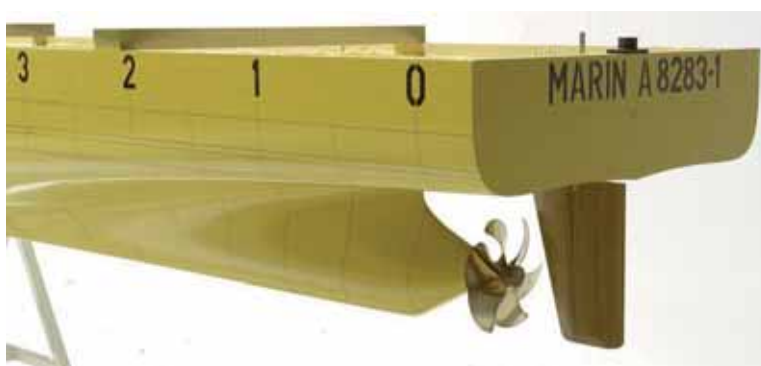

Figure 5.5: Test case: large container vessel.

Table 5.1: Effect of vibration-induced normalized pressure at BPF (normalized values).

RPM	Froude scaled	Froude scaled minus 100
Measured pressure	0.66	0.85
Corrected pressure	1.00	1.02
Amplitude difference	34%	17%

6 VALIDATION OF COMPUTATIONAL METHOD

*…in which model scale experimental procedures for measuring hull-pressure
fluctuations are applied to several configurations with non-cavitating propellers
with the aim to validate the mathematical method presented in Chapter 3.*

6.1 Introduction

In Chapter 3, a mathematical method is presented for the numerical determination of propeller-induced hull-pressure fluctuations based on two Boundary Element Methods. The first method computes the representation of the propeller sources of noise in terms of the strengths of sets of 'ring sources' of monopole and dipole type. The second method takes these sources as input and computes the scattered hull pressures that the sources generate.

The propeller method was implemented by Vaz and Bosschers [Vaz2006] under the acronym PROCAL (*PROpeller CALculator*). The hull scattering method was implemented by the author [Wijngaarden2006a] under the acronym EXCALIBUR (*EXcitation CALculation with Improved BURton and Miller method*). In this chapter, the combination of the two methods is validated by comparison of the obtained results with results from towing tank tests for non-cavitating model scale propellers.

In the computations, PROCAL's output consists of potential flow monopole and dipole source strengths at a number of time instances during a revolution. EXCALIBUR transforms these rotating time-domain sources into stationary frequency-domain sources and performs a scattering computation at a set of blade passage frequencies. For details on the methods, see Chapter 3 and Appendix F.1. The source transformation procedure is presented in Appendix E. An example result is shown in Figure 6.1. Alternatively, free-field pressures at the hull, computed by PROCAL, may be multiplied by diffraction factors. These are often called *Solid Boundary Factors* (SBF) and are also computed by EXCALIBUR.

6.2 Validation Experiment: Container Vessel #2

In order to validate the coupling procedure of PROCAL and EXCALIBUR, a series of hull-pressure measurements was performed in the DTT on a model of a single screw container vessel equipped with non-cavitating propellers; the latter not by virtue of the propeller design, but simply by keeping the pressure in the DTT at atmospheric level [Lafeber2007/2009]. The ship model (see Figure 6.3) is 8.5 meters long and 1.27 meters

wide. The draught has been varied between 0.388 and 0.531 meters. On the aftship, 21 pressure transducers were mounted flush with the hull (Figure 6.2).
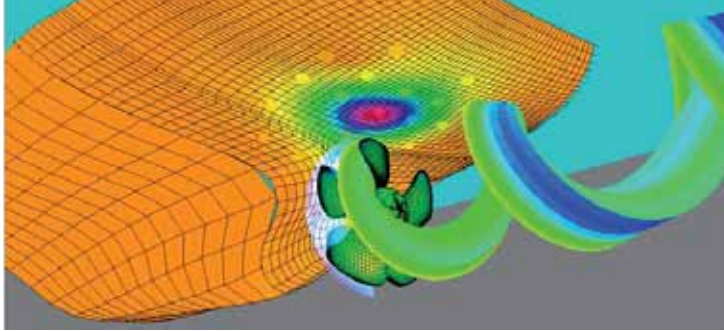

Figure 6.1: Hull-pressure amplitudes at BPF (propeller no. 6553). Measurement locations on the hull are indicated by colored dots. The propeller pressure distribution and shed vorticity are also shown. The transparent semi-circular disc at the propeller plane indicates where wake field data is supplied to the propeller analysis.
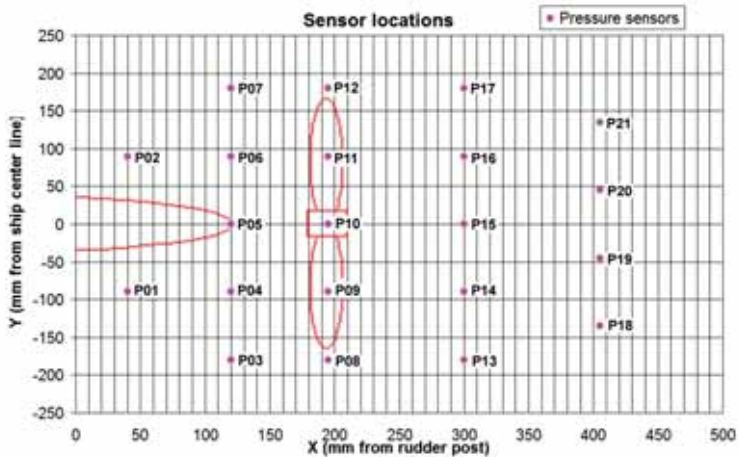
Figure 6.2: Locations of pressure transducers on the aftship, relative to the propeller plane and the rudder (top view, propeller rotates downwards over the top).

Table 6.1: Propeller models used in validation experiments.

Prop. No.	Blade number	Diameter [mm]	Tip Clearance (% diameter)	Remarks
6666	2	340.00	14%	Zero pitch to produce zero thrust
6553	5	295.79	24%	Thick blades at the tip
6724	6	259.64	34%	Original design for vessel
6458	4	261.54	34%	Small blade area and low pitch

Figure 6.3: Container vessel no. 2 in the harbor of the DTT (top left); Pressure transducers and propeller no. 6666 fitted (top right); Mounted accelerometers and exciter (bottom right and left).

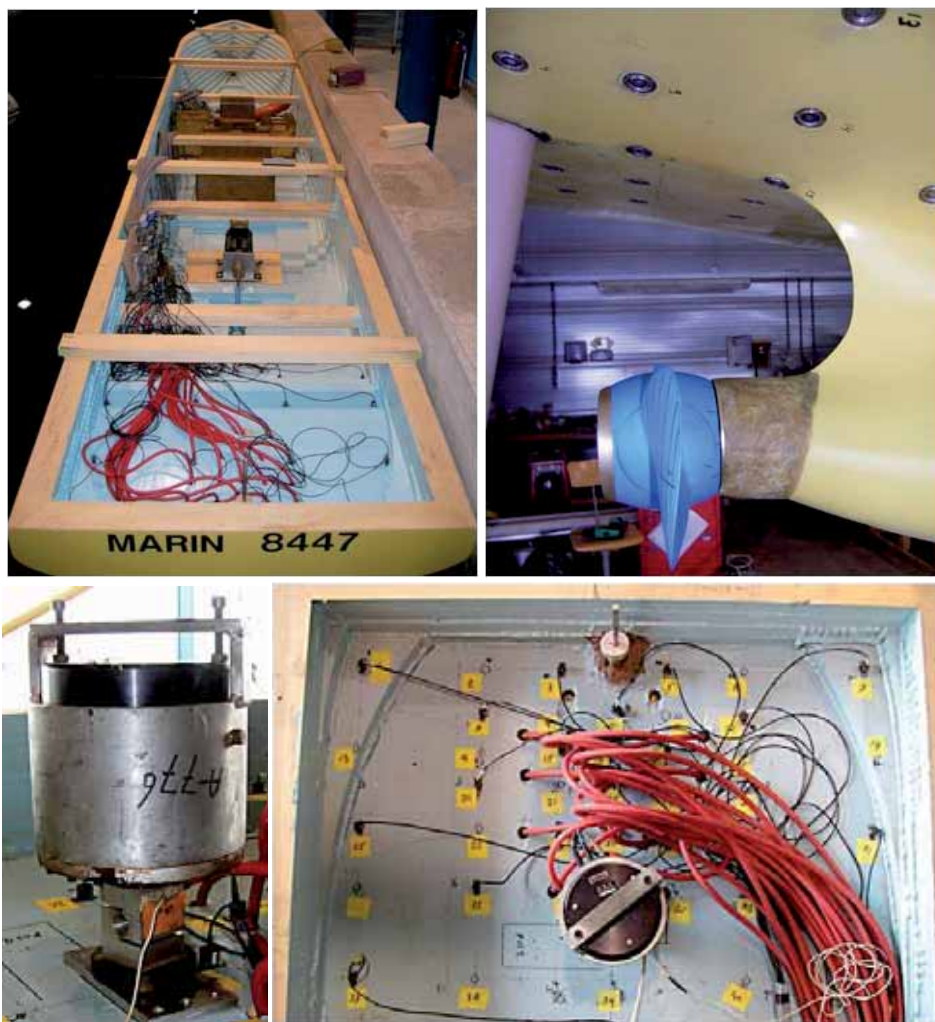The ship model has been successively fitted with four propellers of different blade number, blade area and pitch distribution (see Table 6.1 and Figure 6.4). With two-bladed, zero-pitch propeller no. 6666, bollard pull tests have been performed at different propeller rotation rates. During the bollard pull tests, the ship model was attached to the towing carriage (see Figure 2.4) which remained stationary in the harbor of the towing tank. Propeller rotation rates of 400 and 600 RPM have been used. The tests are aimed at the validation of the effect of blade thickness on hull pressures and therefore the pitch of the propeller was reduced until almost zero thrust was produced. The pitch setting which results in the lowest mean thrust was determined with the use of PROCAL. Two draughts have been applied, viz.,

0.419 and 0.531 meters. Not only the hull pressures and model accelerations were measured, but also the propeller thrust, torque and blade position. The shaft-synchronized measurements were made at 360 samples per revolution. The blade position of zero degrees refers to the principal blade's reference line pointing upward. Due to the limited number of data channels available, the bollard pull tests were performed with only 17 pressure transducers, while for the other tests 21 pressure transducers were employed.

Table 6.2: Overview of test conditions.

| Prop. No.	V_m [m/s]	N_m [RPM]	BPF [Hz]	T [N]	K_T [-]	Draft [m]
6666	0.00	400	13.33	13.882	0.023	0.419
6666	0.00	400	13.33	13.870	0.023	0.531
6666	0.00	600	20.00	28.090	0.021	0.531
6553	2.37	509	42.42	115.340	0.210	0.388
6553	2.37	315	26.25	2.098	0.009	0.388
6553	3.00	652	54.33	172.400	0.191	0.388
6724	2.37	370	37.00	-1.650	-0.010	0.388
6724	2.37	579	57.90	86.390	0.204	0.388
6724	3.00	732	73.20	123.290	0.182	0.388
6458	2.37	462	30.80	0.978	0.004	0.388
6458	2.37	780	52.00	115.680	0.146	0.388
6458	3.00	800	53.33	69.710	0.084	0.388
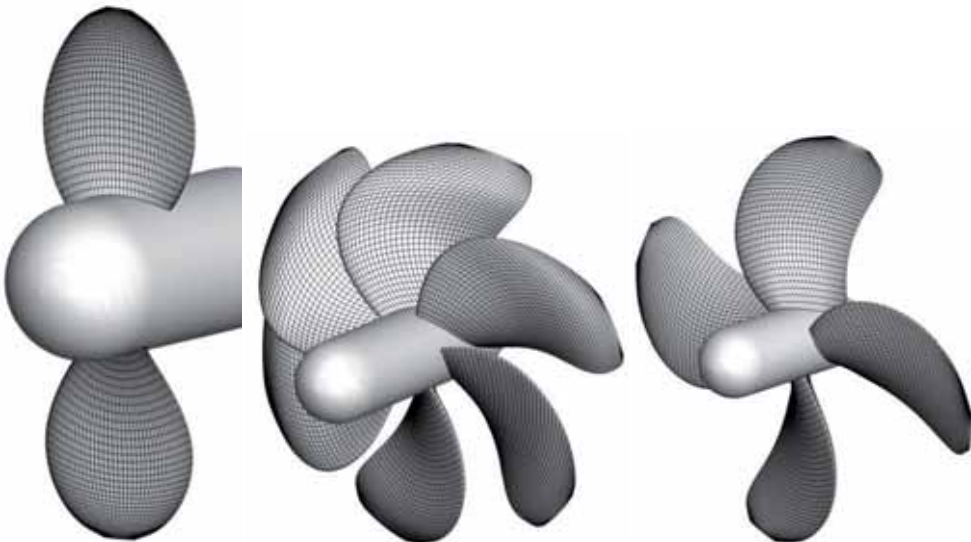
Figure 6.4: Boundary element distributions for propeller nos. 6666 (left), 6724 (middle) and 6458 (right). Propeller no. 6553 is only shown in small format in Figure 6.1 for confidentiality reasons.

With the other three propellers (nos. 6553, 6724 and 6458) tests were performed while the model was being towed through the towing tank. The ambient pressure in the tank was

atmospheric, so there was no cavitation on the model propellers. The draught in these tests was 0.388 meter. The models were towed at two advance ratios, one to obtain zero thrust and the other to obtain a realistic thrust coefficient. The latter advance ratio was kept constant for two different combinations of rotation rate and model speed, resulting in three conditions per propeller. However, for the four-bladed propeller, one of the tests was not carried out at the correct RPM, resulting in three different advance ratios tested. Hull pressures, model accelerations, propeller thrust, torque and blade position were all measured synchronized to the shaft position. Measurements of the model speed and dynamic trim were also included. An overview of the tests conditions is given in Table 6.2.

In order to correct for the influence of model vibrations, the model has been fitted with a number of accelerometers (the black cubes and cables in the bottom picture of Figure 6.3) and the procedure introduced in Chapter 5 (cf. Figure 5.1) has been applied. Model no. 8447 was originally milled with extra layers of wood in the aftship. With these extra layers, the thickness at the aftship became about 20 centimeter.

6.3 Comparison of Measurements and Computations

PROCAL, EXCALIBUR and their graphical user interface PROVISE[11] (see, e.g., Figure 6.1) were used to perform computations at initial conditions similar to those of the model tests listed in Table 6.2. However, the ship speed was adapted slightly such that the thrust of the propeller in the computations was the same as that of the propeller in the model tests. This speed correction allowed for small inaccuracies in wake field data as well as computed propeller thrust. All computations were made using model scale data and the panel distributions shown in Figure 6.4. The panel distributions were chosen on the basis of 'best practice guidelines'[12]. The bollard pull computations for the two-bladed propeller, no. 6666, were performed as steady flow computations with uniform propeller inflow. All other computations were for unsteady flow and the measured nominal wake of the ship was used as input. Computations were made for a number of 120 time steps per revolution. On the five-bladed propeller, no. 6553, the *Iterative Pressure Kutta Condition* (IPKC), as applied in PROCAL, did not always converge. To avoid problems and long computation times, the IPKC was turned off for this propeller. Although the thrust computation is not exact, this does not significantly influence the values obtained for the hull pressures.

PROCAL writes a file containing the monopole and dipole source strengths of all panels of the propeller, the hub and the propeller wake, at all computed time steps. Then, EXCALIBUR processes these data along the lines of Appendix E or by providing solid boundary factors. For the current computations, the contribution of the hub was not taken into account when computing hull pressures. This reduces the amount of memory required by EXCALIBUR and the computation times while the hub hardly contributes to the hull pressures. Due to its intersection with the bossing, leaving out the hub may also prevent numerical problems. Because of dynamic trim and sinkage during the tests in which the model was being towed, the afterbody draught was increased. Therefore, in the EXCALIBUR

---

[11] PROVISE, the PROcal VISualization Environment was developed by David Heath of the Canadian Defense Research Establishment, DRDC, for MARIN's Cooperative Research Ships (CRS) membership.
[12] Note that this is a validation and not a verification study. Grid sensitivity studies performed in the past have led to the mentioned 'best practice guidelines'.

computations, instead of the nominal draught of 0.388 meter, a value of 0.450 meter was used corresponding with the actual draught of the model at that speed. From experience it is known that at the locations of interest the influence of the forebody is negligible, and therefore only the aftship was used in the computations. The fine mesh in the area of interest enabled a straightforward interpolation of computed data at the measurement locations. This procedure was applied for the first four harmonics of the BPF.

In Figure 6.5 to Figure 6.8, the measured and computed pressures are compared (shown left in figures). All results are for model scale. For transducer no. 10, the first four orders of BPF were synthesized to a time series of one period (shown to the right in the figures). The combination of PROCAL and EXCALIBUR gives accurate results for the amplitudes of all four harmonics in the case of the 2-bladed propeller. With the exception of transducer no. 15, all hull-pressure fluctuations are within 10% of the measured values, and the great majority is within 5%. The estimated accuracy of the measured pressures is about 5 Pa. The error in the computed phases is of the order of 10 degrees, as is seen in the time traces. The large propeller diameter, hence small clearance, together with the absence of forward speed and thrust make this case the easiest one to measure and compute.

By virtue of their blade number, the other propellers produce more sinusoidal pressure signals with dominating first harmonics. The five-bladed propeller with thickened tips and large tip chord is not a very well-suited case for PROCAL. Still, first order amplitudes are within 10% of the measurements. The much smaller second harmonic, however, is of varying, but often low accuracy (Figure 6.6). Also the phase error of almost 40 degrees is quite significant in this case. Interestingly, the phase error is almost absent in the 'thrustless' measurement shown in the graph on the left, although the amplitude error there is sometimes almost 20%. The accuracy of the amplitude for the four-bladed propeller is generally within 10% (Figure 6.8), but not as accurate for the thrustless case. The phase is only accurate to within 30 degrees for the loaded conditions, but very accurate in the thrustless case. Finally, the six-bladed propeller, the one that was designed for the ship, shows results that are within 15% of measurement (Figure 6.7). The accuracy of the phase is excellent. The thrustless case shows results that are not as accurate, but all transducers measured pressures of insignificant amplitudes, smaller than 10 Pa.
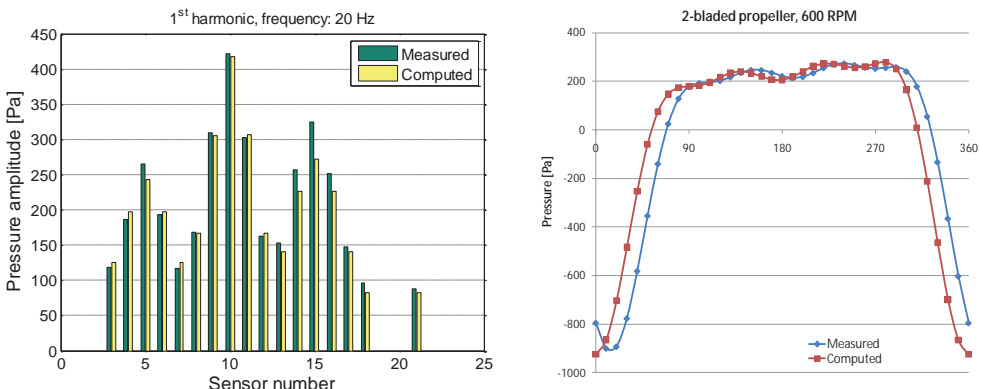

Figure 6.5: (LEFT) First order pressure amplitudes for 2-bladed propeller, no. 6666, at RPM: 600. (RIGHT) Pressure signal based on four harmonics during one blade passage (sensor #10).

Figure 6.6: (LEFT) First order pressure amplitudes for 5-bladed propeller, no. 6553, at RPM: 652. (RIGHT) Pressure signal based on four harmonics during one blade passage (sensor #10).

Figure 6.7: (LEFT) First order pressure amplitudes for 6-bladed propeller, no. 6724, at RPM: 732. (RIGHT) Pressure signal based on four harmonics during one blade passage (sensor #10).

Figure 6.8: (LEFT) First order pressure amplitudes for 4-bladed propeller, no. 6458, at RPM: 780. (RIGHT) Pressure signal based on four harmonics during one blade passage (sensor #10).
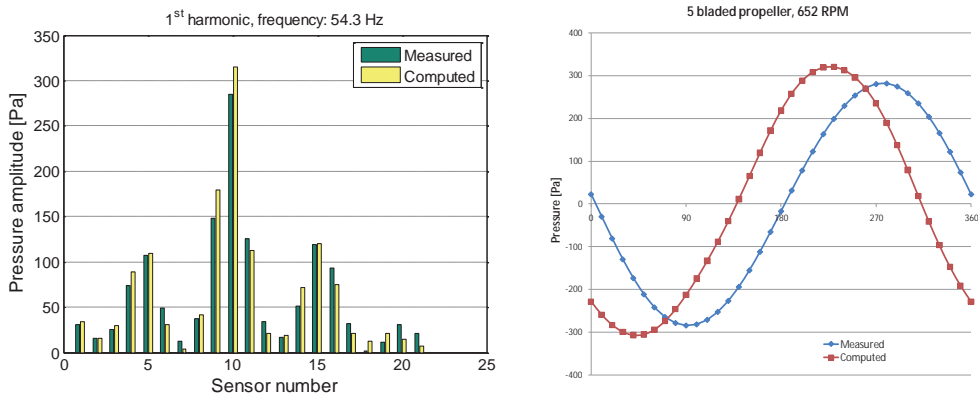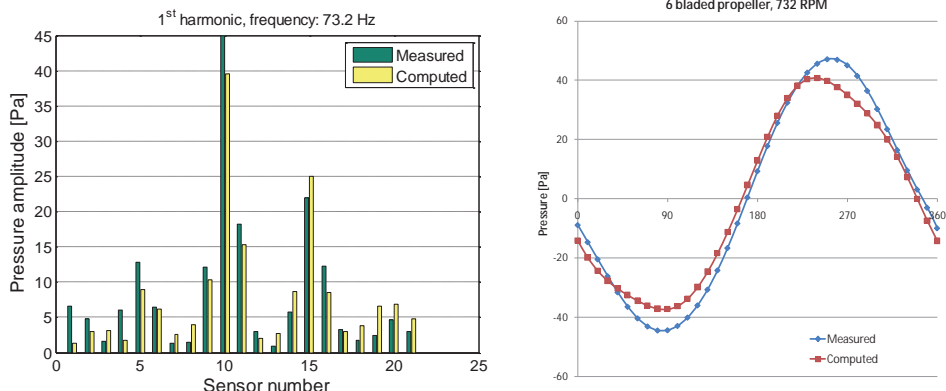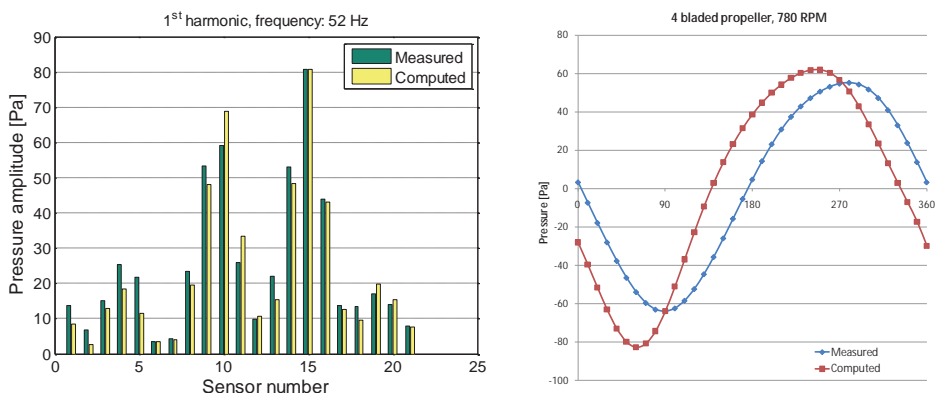
In Appendix H.1, all results obtained with the new coupling procedure are collected. Appendix H.2 shows results for the old procedure involving solid boundary factors. Although the latter procedure is a coarse approximation, the results are only slightly less accurate than those obtained with the new procedure.

6.4 Conclusions and Recommendations

It is concluded that in the great majority of cases the combination of PROCAL and EXCALIBUR delivers hull-pressure amplitudes for non-cavitating propellers within 15% of the measured values, with the exception of a few outliers of twice that percentage. Often the larger differences occur at one particular pressure pick-up and may not be attributable to computational errors. Phase errors may be substantial in some cases. The origin of the phase errors is not known. The number of azimuthal stations at which the propeller code PROCAL produces data is kept the same for all propellers. Thus, the angular resolution is constant. To judge the phase error, it should be divided by the number of blades. Then, the results for the 2-bladed propeller with regard to angular accuracy are more in line with those of the 4- and 5-bladed propellers.

The accuracy in the measurements is determined by the error corresponding to that of the pressure transducers and is estimated to be about 5 Pa. E.g., in Figure 6.7 this means that all errors may, in principle, have been caused by noise in the measurement itself.

A practical problem with the application of the numerical method used is that the trailing vortex sheets intersect the rudder and produce erroneous results there. Also at locations downstream of the propeller plane the hull pressures are influenced by the trailing vortex sheets, which do not form an adequate description of acoustic sources in the wake.

7 SCALE EFFECT ON SHIP MODEL WAKE

…in which the scale effect on the ship model's effective wake is treated as an important cause of hull-pressure prediction errors. A pragmatic, improved prediction procedure is derived on the basis of the difference in depth of wake peak found between model and full scale. A more fundamental solution is sought in the development of geometrically non-similar ship models that generate the full scale wake at locations where cavitation is expected.

7.1 Introduction

For the correlation of model and ship scale cavitation-induced hull-pressure fluctuations, Section 2.3 identifies the similarity between the effective wake fields on model and ship scale as a major determining factor. Discrepancies from this similarity are easily imagined, as the model scale wake flow differs in Reynolds number from its full scale counterpart by one to two orders of magnitude. The wake flow behind the model ship is more strongly retarded due to viscous effects, thus causing the propeller disc-averaged effective inflow velocities to be lower by several percent. As a result, the propeller will be overloaded when model ship speed and propeller rotation rate are based on Froude number identity.

Therefore, in cavitation model tests, the correct propeller loading is set by adjusting the model ship speed by a few percent on the basis of an estimated *propeller-disc averaged* wake scale effect, expressed as a fraction of ship speed[13]. Although a correct estimate of this fraction may lead to an accurate prediction of general propulsion characteristics, it is not a sufficient condition for similarity in cavitation behavior and hull-pressure fluctuations. Because the inflow velocities at the propeller disc are more strongly retarded in the top sector than elsewhere, *local* similarity of propeller inflow velocities is lacking most notably at locations where, at full scale, cavitation is expected.

It follows from the above that a prerequisite for the correct prediction of the hull-pressure field is to have knowledge and control of the local effective wake field at (a part of) the propeller disc. This is by no means straightforward as the effective wake field is not directly measurable. One has to revert to the measurement of the nominal wake field and correct for propeller-hull interaction, or one has to measure the total wake field and subtract the propeller induction velocities (cf. Figure 4.1).

---

[13] Note that in doing so, the model speed, as opposed to the propeller rotational speed, becomes a few percent higher than according to Froude similarity. The static pressure in the flow is correctly scaled everywhere and the propeller attains the correct thrust loading coefficient. In model propulsion tests, typically the Froude number is fixed through the ship model velocity instead of the propeller RPM.

The standard procedure is to measure the nominal wake field on model scale using Pitot tubes. Although this is a straightforward procedure, it has a drawback in that the propeller-hull interaction component remains to be estimated. Therefore, the result will inevitably be of unknown accuracy. The alternative of measuring the total wake field at model scale by means of *Laser Doppler Velocimetry* (LDV) has often been achieved, but is expensive and laborious to apply in everyday practice. Another non-intrusive technique that has recently emerged is *Particle Image Velocimetry* (PIV). In its stereo form it is a technique providing instantaneous 3D velocity vectors in a cross-section of the flow. The importance of PIV lies in its ability to reach a high spatial resolution at a certain instant. LDV on the other hand delivers high temporal resolution at a certain point. Both techniques are important since spatial and temporal variations in the wake may be quite substantial, thus having a bearing on cavitation dynamics and spectral content of excitation forces. PIV has the added advantage of being less complex and potentially cheaper as it measures a complete measuring plane at once.

The wake field on full scale is rarely determined as it involves either the measurement of the total wake (i.e., with operating propeller) using the non-intrusive means of LDV or PIV, or the measurement of the nominal wake of the ship without propeller[14]. The lack of information on ship scale wakes is actually the main reason for the lack of knowledge on the magnitude of the wake scale effect.

Fortunately, nowadays, the computation of the wake field at full scale Reynolds numbers has come within reach. For example, MARIN's RANS-method for ship flows, 'PARNASSOS', is used for this purpose. In such a method the propeller action is modeled by means of a force field, e.g., as delivered by propeller method PROCAL, for the simulation of propeller-hull interaction. The subtraction of the interaction component then yields the effective wake field. The same procedure can be performed on the model ship (i.e., the same ship at a different Reynolds number). The difference in the two wake fields would be as accurate an estimate as one can get for the scale effect on the effective wake.

7.2 Present Procedure and Pitfalls

Until recently, in cavitation model testing, the set point was chosen by simply adhering to the identity of advance coefficient, which is almost equivalent to thrust coefficient identity. This is correct as long as the scale effect on the model wake may be considered as uniform across the entire propeller disc. Then, the forward speed of the ship model may be simply adjusted by the average scale effect on the entrance velocity, i.e., the wake scale fraction, w,

$$J_s = J_m \quad \Rightarrow \quad V_m = \frac{V_s\, n_m}{\lambda\, n_s} \frac{1 - w_s}{1 - w_m} \tag{7.1}$$

By adjusting the towing tank pressure, the cavitation number, σ_n, (cf. Eq. (4.37)) is made to agree with that on full scale at all depths (or, alternatively, in cavitation tunnels at a submergence level corresponding to, e.g., $0.8R$ with R the propeller radius of a blade in TDC position). Using this standard procedure, both cavitation patterns and dynamics on

---

[14] Casco vessels that are built at one yard and then transported overseas to be completed at another yard could, in principle, undergo a towing test at sea.

model propellers are considered to be representative of their full scale counterparts with the exception of light free vortex cavitation, the inception of which is seriously delayed due to viscous scale effects on the propeller blade flow.

However, it is well known that the wake scale effect is generally not uniform across the entire propeller disc, but predominant in the top sector, where the *wake peak* is typically located. For achieving equivalence in cavitation patterns and dynamics, the distribution of velocities in and around the wake peak must be made equivalent to full scale. Using standard set points, the propeller will still be overloaded in the region where cavitation is expected to occur. In other regions it will be underloaded, which may trigger pressure side cavitation before it would occur in full scale.

Although, generally not considered significant for the wake fields of modern passenger ships, the wake scale effect may become significant, e.g., in the case of single screw container ships. This type of ship is currently growing in size beyond previously imaginable proportions and excitation forces are of great concern. In the joint industry project 'CoCa' [Ligtelijn2004, Wijngaarden2003], the author studied the correlation between model and full scale propeller cavitation for five ships, two of which were container ships[15]. This study confirmed the correlation deficiency for the latter type of ship as the model scale hull-pressure amplitudes were found to severely overpredict ship scale values at the first order of BPF. For the passenger ship, investigated within the 'CoCa' project, the first order maximum pressure amplitude correlated very well with values found at model scale. In fact, this finding triggered the study which led to this thesis.

The following sections are devoted to two methods to alleviate effective wake discrepancies. Both involve CFD computations of model and ship scale wake fields. The first method, treated in Section 7.3, approaches the problem by making shift with the model scale wake field as it is and trying to improve the prediction results by further adjusting the ship speed during testing. The second attempt, treated in Section 7.4, is based on redesigning the model ship such that it would actually generate the full scale wake field at a part of the model scale propeller disc. Geometric similarity is then sacrificed for the sake of local kinematic similarity.

7.3 Experimental Procedure using Wake Peak Scaling

As stated in Section 7.2, performing model tests at propeller K_t-identity may not lead to correct cavitation behavior as in the top sector of the propeller disc, where cavitation is expected, the propeller blade may be overloaded. Necessarily, the bottom sector of the disc is then underloaded, which may be considered not such a problem.

A simple way to proceed is to simulate the *local* blade loading in the top sector of the propeller disc, e.g., at the position of the wake peak itself without considering the *average* propeller loading. The model's forward speed is then chosen in such a way that the ratio between the circumferential tip speed of the propeller blades and the local axial velocity in the wake peak is equal at model and full scale. This condition, referred to as J_{wp}-identity (*wake peak identity[16]*), is defined as,

---

[15] Note that the video image on the cover of this thesis was shot onboard one of these container vessels.

[16] This term was coined by Jan Holtrop.

$$J_{wp} = V_{min}/nD \tag{7.2}$$

if it is based on V_{min}, the minimum axial velocity in the wake peak. It may also be based on a weighted average velocity in the wake sector where cavitation is expected, so that in that particular sector the average thrust loading is similar to full scale. The method requires that the scale effect on the effective wake peak depth is known from CFD computations. It is also required that the transverse velocity components in the wake peak are not significant. This is true for the container vessels investigated in this thesis, but not for twin screw passenger vessels, e.g.

Nominal wake fields can be computed reasonably accurately for Reynolds numbers ranging from model to full scale values[17]. These computations are fast enough to be used in daily routine work, a requirement that was imposed on computational tools used in this thesis (cf. Section 3.1). Recently, the coupling of the propeller method PROCAL (Section 3.2) to RANS-solver PARNASSOS was established, thus enabling the computation of the propeller-hull flow interaction, from which the effective wake field follows[18].

In principle, the computational tools mentioned above can be used to determine the scale effect on the effective wake averaged over the area of the propeller disc where cavitation is expected (read: computed). Consider an iterative procedure in which the force field computed by a propeller method is input to a viscous flow method for the ship, from which an effective wake field follows that is input to the propeller code again, etc. Upon convergence, the propeller method outputs the sheet cavity extent on the blades, from which the area follows over which the effective wake scale effect should be averaged. The final result is a percentage with which the ship speed should be increased in cavitation model tests in order to obtain the correct average loading in the cavitating sector of the propeller disc.

A simpler option is to use the scale effect on the wake peak depth only to determine the increase in ship speed during testing. Even more pragmatically, one could take the scale effect on the nominal wake peak depth, at the risk of overshooting the increase in model speed. The model speed then follows from Eq. (7.1) as,

$$V_m = \frac{V_s \, n_m}{\lambda \, n_s} \left[1 + \frac{[V_{min}/V]_s - [V_{min}/V]_m}{[V_{min}/V]_m} \right] \tag{7.3}$$

For single screw ships for which no wake information is available at all, Holtrop has suggested the following rule of thumb,

$$[V_{min}/V]_s - [V_{min}/V]_m = \sqrt{\lambda}/50 \tag{7.4}$$

It must be noted that if this procedure is used in the DTT, the model speeds may occasionally become so high that free surface effects start to affect the stern flow.

---

[17] Due to the limited availability of full scale wake data, the accuracy of computations at ship scale Reynolds numbers is often inferred from that obtained at model scale Reynolds numbers.
[18] In this thesis this coupling procedure has not been applied. Instead a force field method has been used for the conversion of the wake from nominal to effective.

7.3.1   Example Case: Container Vessel #1

The effect of choosing the set point in the way described above was studied for the container vessel used in Section 5.4 and shown in Figure 5.5. Hull-pressure fluctuations were measured at various model speeds, while keeping the RPM constant at its Froude-scaled equivalent. In Figure 7.2, the maximum pressure amplitude at blade rate frequency, normalized as in Section 5.4, is plotted against the speed of the ship model for various draughts of the ship. For each draught, from the loaded draught of 12.2-12.2 meters (fore-aft) to the ballast draught of 5.8-9.8 meters, the measurements were corrected for the influence of model vibrations (as indicated in the figure's legend).

Considering the corrected data for the loaded draught, at abscissa 0 the model speed equals its Froude equivalent (i.e., the J_v-identity condition, see Footnote 7). The test was repeated at higher model speeds, each time increasing the speed by a percentage equal to the effective wake fraction percentage. Thus, at abscissa 1, the maximum amplitude is the one obtained from the standard testing procedure for which the average propeller loading is correct (i.e., the J or K_t-identity condition). This situation corresponds to the cavitation pattern shown in the high-speed video snapshot on the left in Figure 7.1. The figure also shows cavitation patterns at higher speeds corresponding to three and four times the wake scale effect. For the wake peak scaling method the results have to be interpolated at an estimated value of 3.3 times the average wake scaling effect. This follows from Eqs. (7.3) and (7.4) and is indicated in Figure 7.2 by a vertical black line. It yields an amplitude of only 46% of what would have been predicted using the standard method. At the intermediate draught even 24% is found, and at the ballast draught 44%.
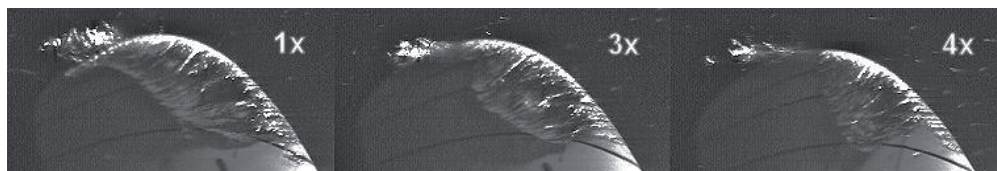

Figure 7.1: High-speed video snapshot of a blade close to the top dead centre position at various advance velocities (Left: 1x wake scale fraction added to the Froude speed; Center: 3x; Right: 4x). The measurements were performed at the design draught.

No full scale data for this case are available to the author. Therefore, for now, it may only be concluded that the new choice of the set point led to a reduction in the prediction of maximum blade rate amplitude by more than a factor of two at all draughts considered. It is noted that the previously studied influence of model vibration-induced pressures turns out to have been quite substantial (of the order of 25%).

This finding cannot be extrapolated to higher orders of the blade rate frequency. The investigated container vessel is equipped with a six-bladed propeller, hence already the second order cavitation dynamics is dependent on details of the wake and vortex cavitation dynamics. A comparison of the results at the design draught with those obtained in tests performed earlier (i.e., during the ship's design phase) revealed that the first order repeated very well, whilst the higher orders had increased somewhat. The second order results are

presented in Figure 7.3. Despite the large increase in ship model speed and the consequent unloading of the propeller no pressure side cavitation was observed during testing.
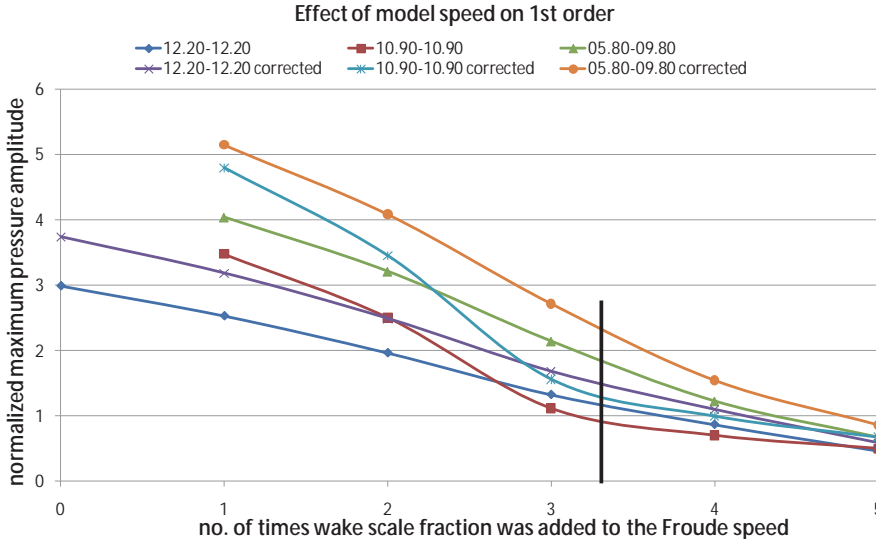

Figure 7.2: First order hull pressures as a function of ship model speed. Repeated at various draughts with and without model vibration correction.
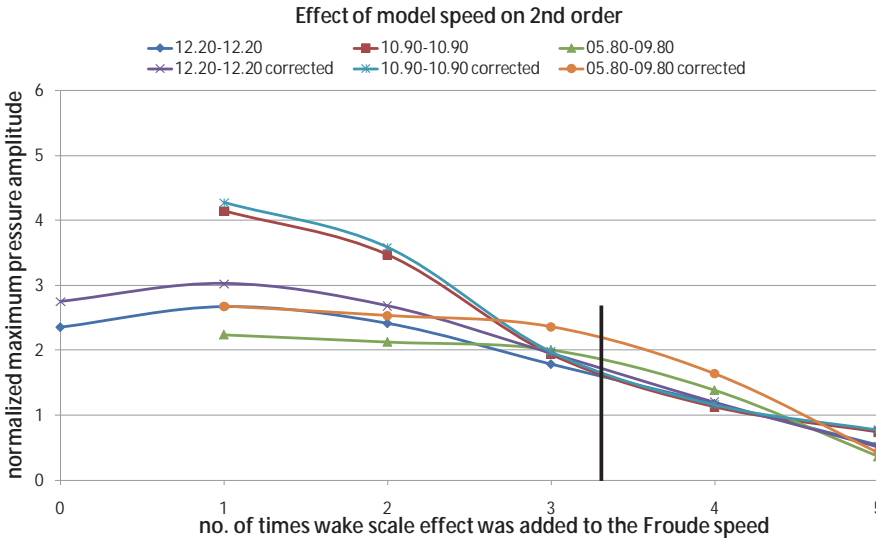

Figure 7.3: Second order hull pressures as a function of ship model speed. Repeated at various draughts with and without model vibration correction.

The next section applies the same experimental procedure to a case for which ship scale data are available. For now, it is concluded that the adjustment of wake peak velocities to the order of magnitude expected at ship scale may cause a very significant decrease in maximum pressure amplitudes at first blade rate frequency.

7.3.2 Example Case: Container Vessel #3

As a second example case, the container vessel depicted below (see also Figure 4.2) was studied by Schuiling *et al.* [Schuiling2010/2011]. It is a typical modern container ship with a six-bladed propeller as shown below (see also Figure 7.38).

Figure 7.4: Model propeller (left) and experimental set-up (right) for container vessel #3.

Application of the wake peak scaling method on the minimum wake peak velocity (using Eqs. (7.3) and (7.4)) with $[V_{min}/V]_m \approx 0.40$ taken from the nominal wake field measurement of Figure 7.5, right side of left picture) results in a speed set point of about 28.5% above the Froude-scaled speed. When RANS code PARNASSOS is used to compute the nominal wake field on ship scale (Figure 7.5, right side of right picture), $[V_{min}/V]_s \approx 0.51$, and Eq. (7.3) yields a speed increase of 27.5%.

The speed set points derived above are for nominal wakes, whereas the derivation should actually be based on effective wakes. Figure 7.6 shows how a force field method in the CRS code PIFWAKE[19] turns the computed axial component of the nominal wake field into an effective one. Because the difference in model and full scale wake is somewhat smaller in the effective case compared to the nominal (numerator), and the effective wake on model scale is less deep (denominator), their ratio becomes smaller by several percent. Thus, the estimate of 27.5-28.5% is reduced to about 21-22%.

---

[19] The PIFWAKE software was developed within the Cooperative Research Ships (CRS) consortium founded by MARIN. The software contains a module employing a force field method developed at MARIN for the conversion of nominal axial wake field components to effective ones. It forms an alternative to the coupling procedure between PROCAL and PARNASSOS mentioned before.
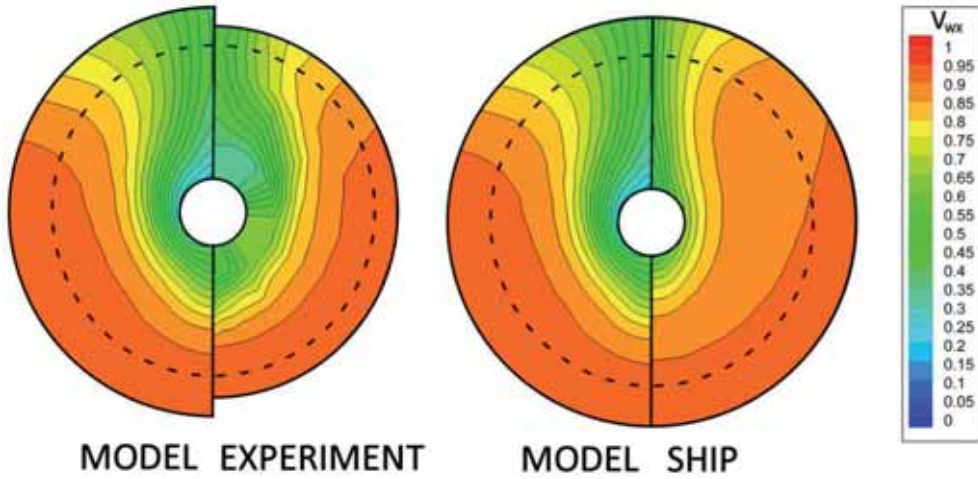
Figure 7.5: Left: Comparison of the computed axial component of the nominal wake field and a model scale nominal wake field measurement. Right: Comparison of computed wake fields at model and ship scale Reynolds numbers. The dashed line indicates the propeller outer perimeter.
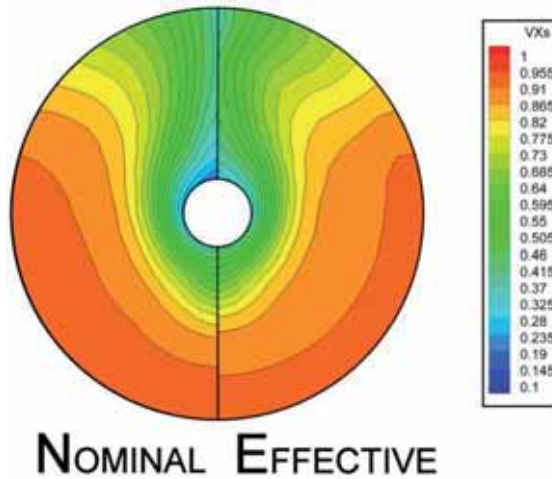
Figure 7.6: Computed nominal wake field (Left) made effective with CRS code PIFWAKE (Right). Note that PIFWAKE only affects the axial component of the wake velocity.

Ten runs through the towing tank were made at various speeds, starting with the thrust identity condition (at 6% above Froude speed to account for the average wake scale effect), down to 58% of thrust identity (at almost 28% above Froude speed). Table 7.1 gives an overview of all conditions with the one of Run 6 as the best estimate to predict the maximum hull pressure amplitude. Limited full scale data is available for comparison (courtesy of Lloyd's Register).

Roughness elements of 60 micrometers are usually applied on the blade's leading edges as a measure to reduce scale effects on the inception of cavitation. For this particular case, leading edge roughness was only applied on the blade's suction side. Thus, unwanted pressure side cavitation at increased model speeds may be suppressed[20]. A correction to the thrust for the application of roughness was not made.

Table 7.1: Overview of test conditions (with a small correction to the full scale thrust coefficient of 0.1891. This correction is not applied to the conditions used for the computations).

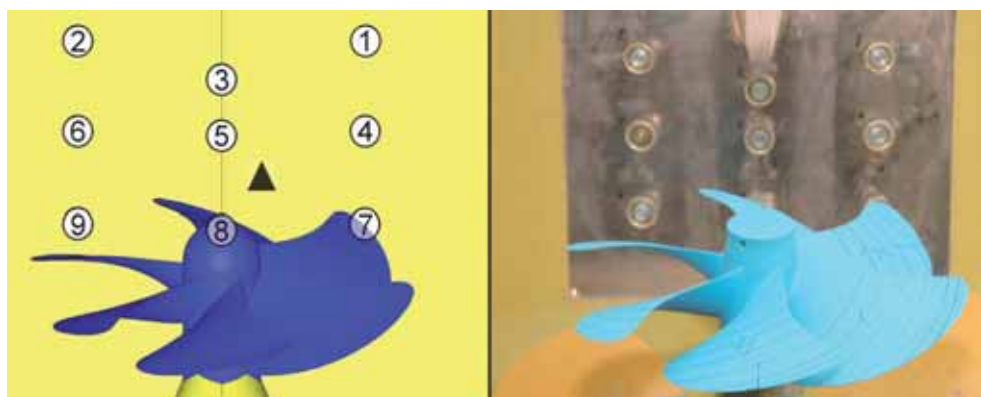| Run	V (m/s)	N (rps)	K_T (%)		J_V
1	2.45	9.62	0.1869	100%	105.8%
2	2.52	9.62	0.1756	94%	108.8%
3	2.59	9.62	0.1642	88%	111.8%
4	2.67	9.62	0.1529	82%	115.3%
5	2.74	9.62	0.1415	76%	118.3%
6	2.81	9.62	0.1302	70%	121.3%
7	2.88	9.62	0.1188	64%	124.4%
8	2.90	9.62	0.1151	62%	125.2%
9	2.92	9.62	0.1113	60%	126.1%
10	2.95	9.62	0.1075	58%	127.4%

Figure 7.7: Bottom view of mounted propeller and nine pressure transducers. The propeller plane intersects sensors nos. 4, 5, and 6. The triangle denotes the full scale measuring location.

---

[20] To only apply roughness on the suction side was suggested by Heinrich Streckwall of HSVA.
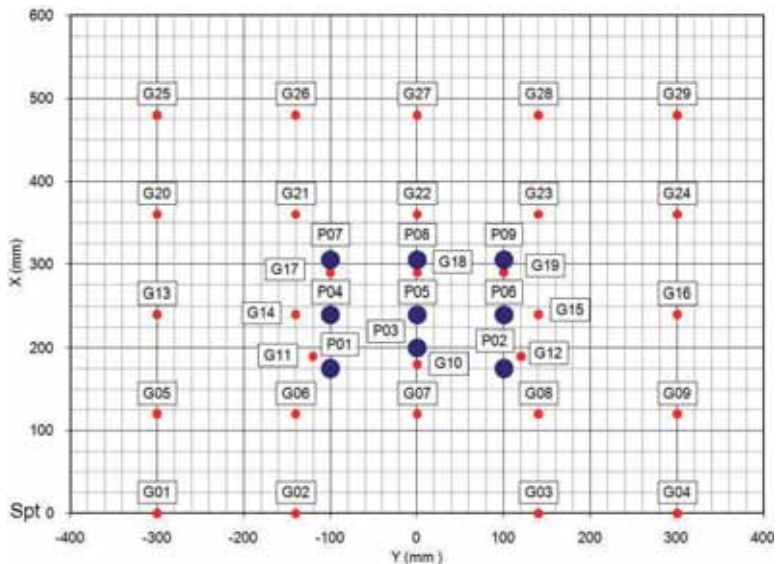
Figure 7.8: Locations of pressure (P) and acceleration (G) transducers on the afterbody of the ship model. P4, P5 and P6 are located in the propeller plane. The propeller model diameter is 0.273 meters.

To measure hull-pressure fluctuations, a grid of 9 pressure sensors were flush mounted directly above the propeller in the model. Furthermore, 29 accelerometers were placed on the inside to measure the vibrations of the model and to correct for these in the post-processing. The transducers and the one pressure sensor for which full scale data is available are shown in Figure 7.7. Xenon light spots were mounted in between the pressure sensors to illuminate the propeller through a plexi-glass window. A complete overview of transducer locations is given in Figure 7.8.

A typical result of the experiments is shown in Figure 7.9. Pressure amplitudes at the first four blade rate frequencies are given as full scale values for the central pressure transducer no. 5, which is closest to the full scale sensor position. Using thrust identity (i.e., Run 1), the model tests overpredict the pressure at BPF by a factor of two. Increasing model speed, while maintaining RPM, leads to a gradual decrease in BPF amplitude. The average loading in the area where sheet cavitation appears is considered most accurately modeled around Run 6. For higher orders of BPF the reduction in thrust loading caused somewhat increased pressure levels and the measure of correlation with full scale values has deteriorated.

It should be noted that all pressure amplitudes have already been corrected for vibration, using the procedure introduced in Chapter 5. Figure 7.10 shows the effect of vibration in Run 1 as an example. Without vibration correction the first order amplitude would have been underestimated by more than 20%.

Figure 7.11 shows a full scale video image and a model scale high-speed video snapshot taken from Run 6. Although the difference in viewing angle makes a comparison difficult, the cavity volumes look reasonably similar. However, the way in which the sheet cavity rolls up under the action of vorticity appears to differ and certain scale effects on the

blade flow cannot be ignored *a priori*. The effect of unloading the propeller on the appearance of sheet cavitation can be seen in Figure 7.12. It may be concluded that at the blade rate frequency the newly established set point for the model test is a substantial improvement over the one obtained by adhering to total thrust identity. However, higher orders of BPF cannot be corrected similarly.
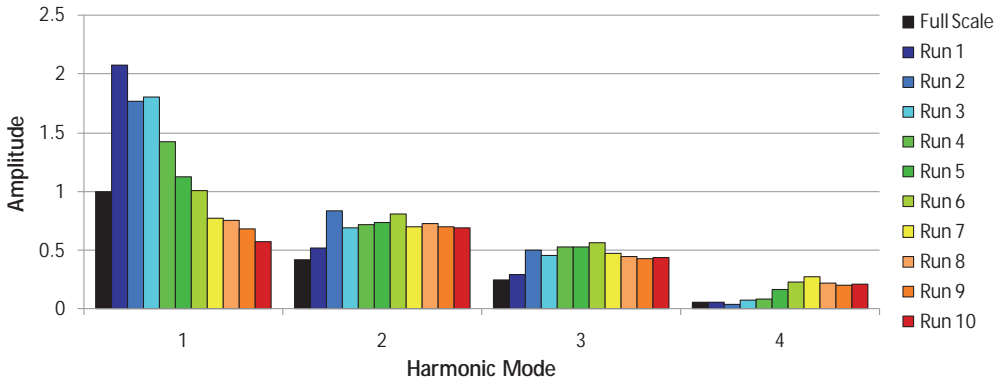
Figure 7.9: Pressure amplitudes at first to fourth BPF for sensor no. 5 compared to full scale.
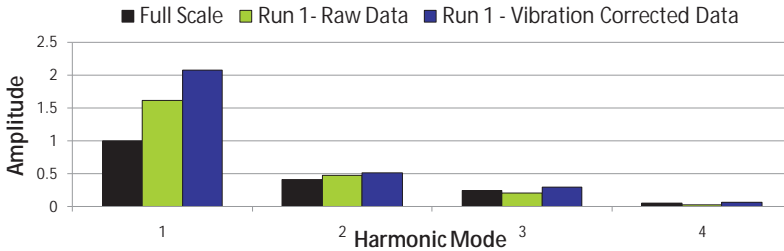
Figure 7.10: Effect of vibration on pressures at first to fourth BPF for sensor no. 5 (Run 1).
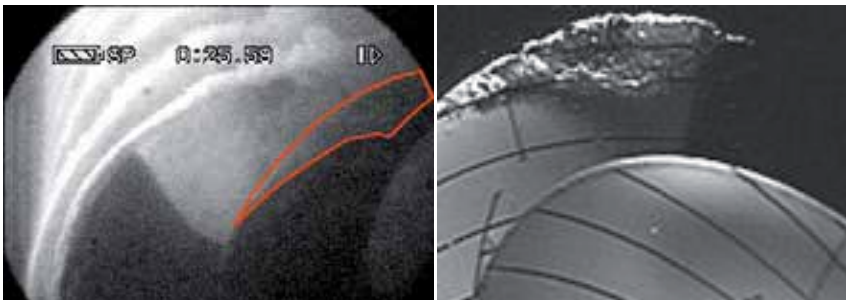
Figure 7.11: Full scale cavitation snapshot (Left, courtesy of Lloyd's Register); Model scale cavitation snapshot (Right, taken from results for Run 6 of Table 7.1).
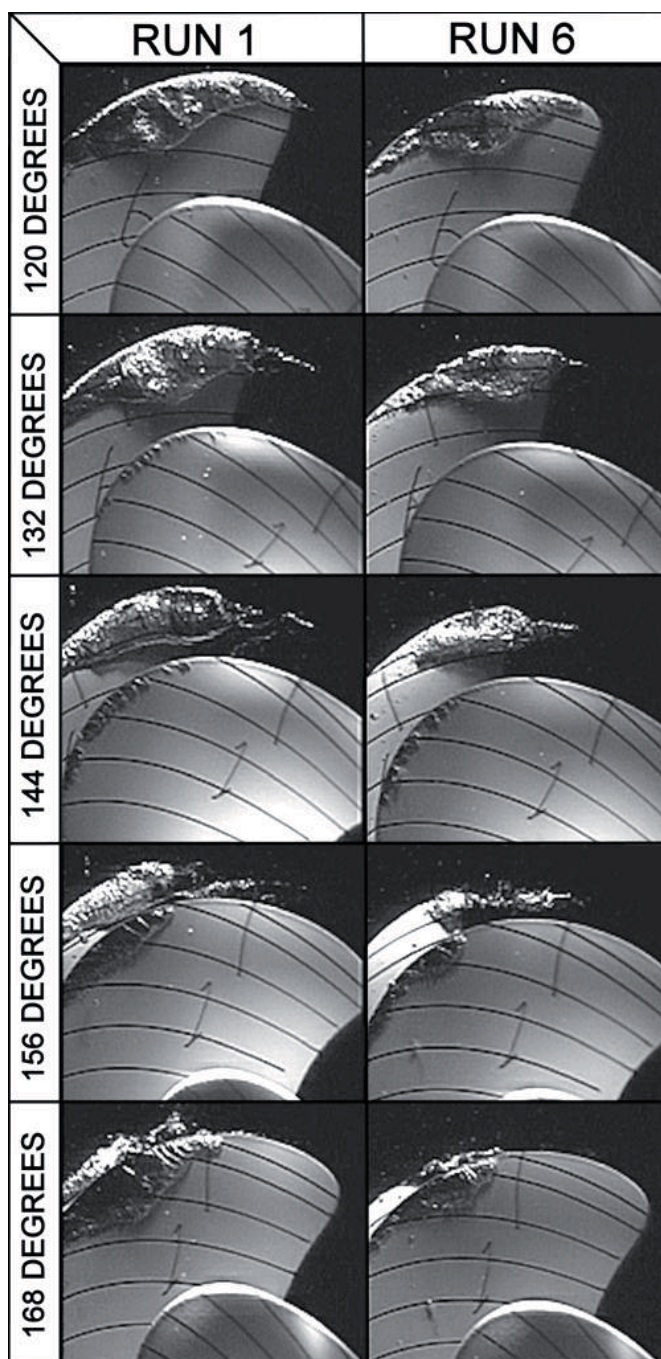
**Figure 7.12: Snapshots of cavitation extents at various azimuthal stations.
Left: thrust identity condition, Right: 70% thrust condition (see Table 7.1).**

7.4 Experimental Procedure using Dummy Models

In the preceding section, it has been attempted to improve the prediction of hull-pressure fluctuations by adjusting the experimental set point. Although the results obtained with that approach show a clear improvement for pressure fluctuations at the first order of BPF, one could argue that they are based on 'suppressive therapy'. Alternatively, in the past, attempts were made to solve the problem at the origin by modifying the ship model's wake field. This was done, e.g., by blowing or sucking the ship's boundary layer [Hoekstra1977a/b] or shortening the midbody [Friesch1992]. The former was found too complicated, the latter not effective as is shown in this section.

Nowadays, most model basins use the same geosim models that are used in speed-power towing tankery. In the past, also so-called *dummy models* or *dummies* were used in cavitation tunnels in which a full model would not fit. In all of the aforementioned cases, the afterbodies would still be geometrically similar to full scale.

Here, following [Wijngaarden2010] and [Schuiling2011], it is proposed to abandon geometric similarity for the afterbody. The challenge becomes one of inversely *designing* a dummy for cavitation experiments in which the effective wake field resembles the one of the ship at locations in the propeller disc where cavitation is expected. Geometric similarity is thereby deliberately sacrificed in favor of kinematic similarity. The resulting model is tentatively called a '*Smart Dummy*' and its design involves the use of CFD tools to determine the shape of the dummy that serves best as a wake field generator in model testing.

To start exploring the effect of geometry changes on the wake field, it is instructive to perform simple changes in width and length to the ship model. Therefore, four parent hull forms were chosen to form the four corners of the space in which the dummy hull form is to be found. The width is varied by narrowing the ship without changing the gondola shape. The length is varied by shortening the midbody without changing the afterbody shape. Thus, the following four shapes are generated:

1. A ship model with original length and half breadth (Basic Hull 1).
2. A ship model with half length and original breadth (Basic Hull 2).
3. A ship model with half length and half breadth (Basic Hull 3).
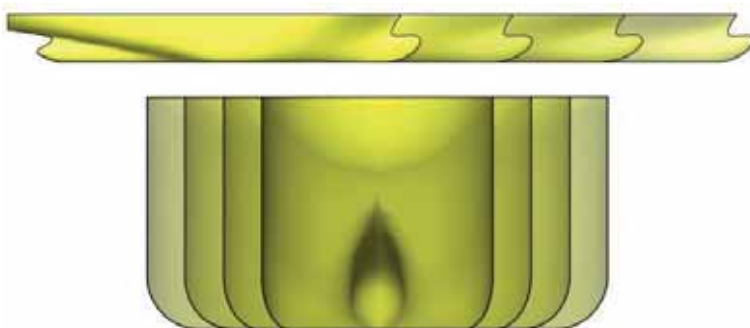4. The original ship model (Geosim).

Figure 7.13: Examples of forms in systematic hull form variations of width and length.
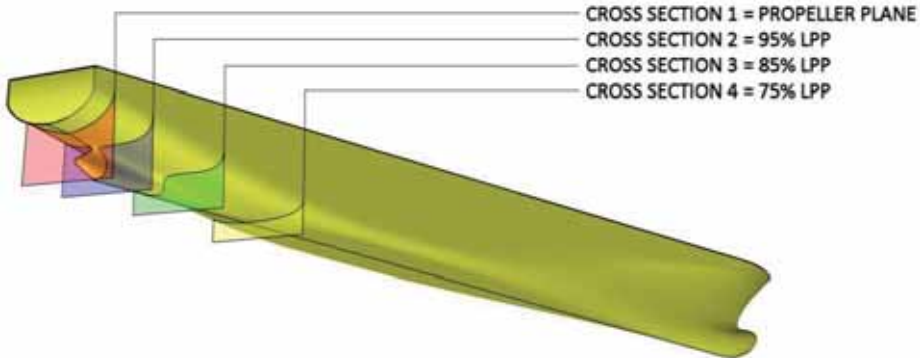
Figure 7.14: Cross sectional planes at which velocity distributions are given as a percentage of the length between perpendiculars (LPP).

The RANS-method PARNASSOS was then applied to these forms as well as to many intermediate ones, a few of which are shown in Figure 7.13. All computations were performed for the *double body* (i.e., the double hull referred to in Section 3.4) geometry flows at the nominal draught. For the first three models, axial wake field results at the cross sections indicated in Figure 7.14 are presented in Figure 7.15 to Figure 7.17. For the narrowed model of Figure 7.15, cross section 4 shows that the boundary layer is thicker than at full scale. At the station where the verticals of the ship start to incline towards the transom, the boundary layer is growing fast. Although the boundary layer has become thinner in the propeller plane, the velocity difference observed in the wake peak is negligible. It is concluded that by only reducing the width of the model, the width and depth of the wake peak are not altered sufficiently.

Hull no. 2 also fails in generating a wake field that corresponds with full scale by shortening the model. In cross section 4 of Figure 7.16 it is clear that the boundary layer is much thinner in comparison with the boundary layer of the original model. However, at the run of the ship the boundary layer is growing so fast as to cause a wake field almost equal to the one of the original model. These results confirm that the pressure gradient is an important mechanism in generating the wake field. Only adjusting the length of the model by removing the midbody has an even smaller effect on the wake peak than altering the width of the model.

Reducing both length and width does have a significant effect on the boundary layer development. In the propeller plane at larger radii the axial velocity outside the wake peak is even higher than at full scale, as can be seen in cross section 1 of Figure 7.17. Nevertheless, the velocity distribution in the top sector of the propeller plane still does not correspond to full scale.

All hull forms, including the intermediate hulls not shown here, suffer from the fact that the magnitude of the axial velocity in the top position is significantly lower than for the full scale geometry. This is illustrated in Figure 7.18, which shows the axial wake velocity at 80% of propeller radius. It is concluded that variations in length and width alone will not provide the desired ship wake field.
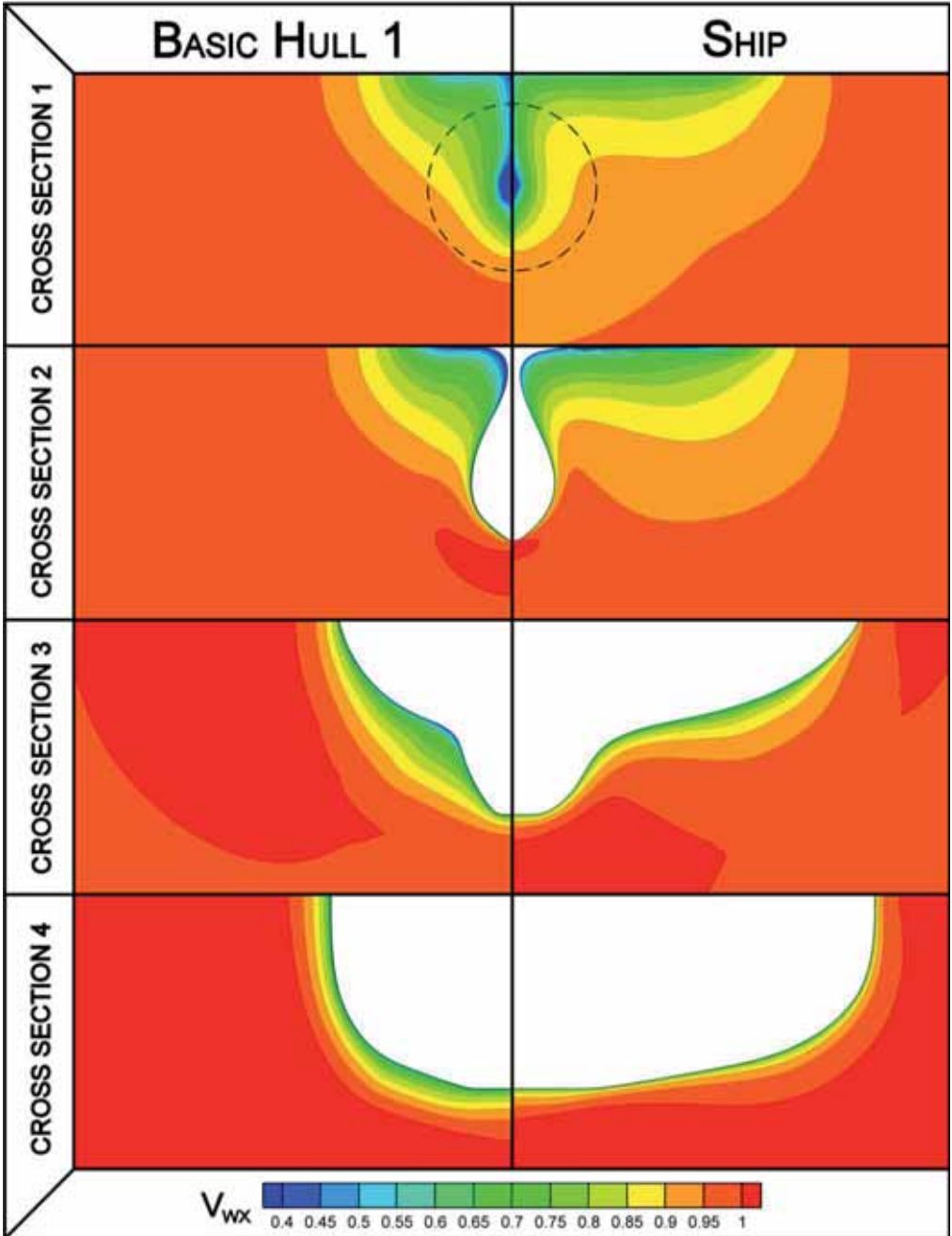
Figure 7.15: Axial component of the wake field of the narrow model.
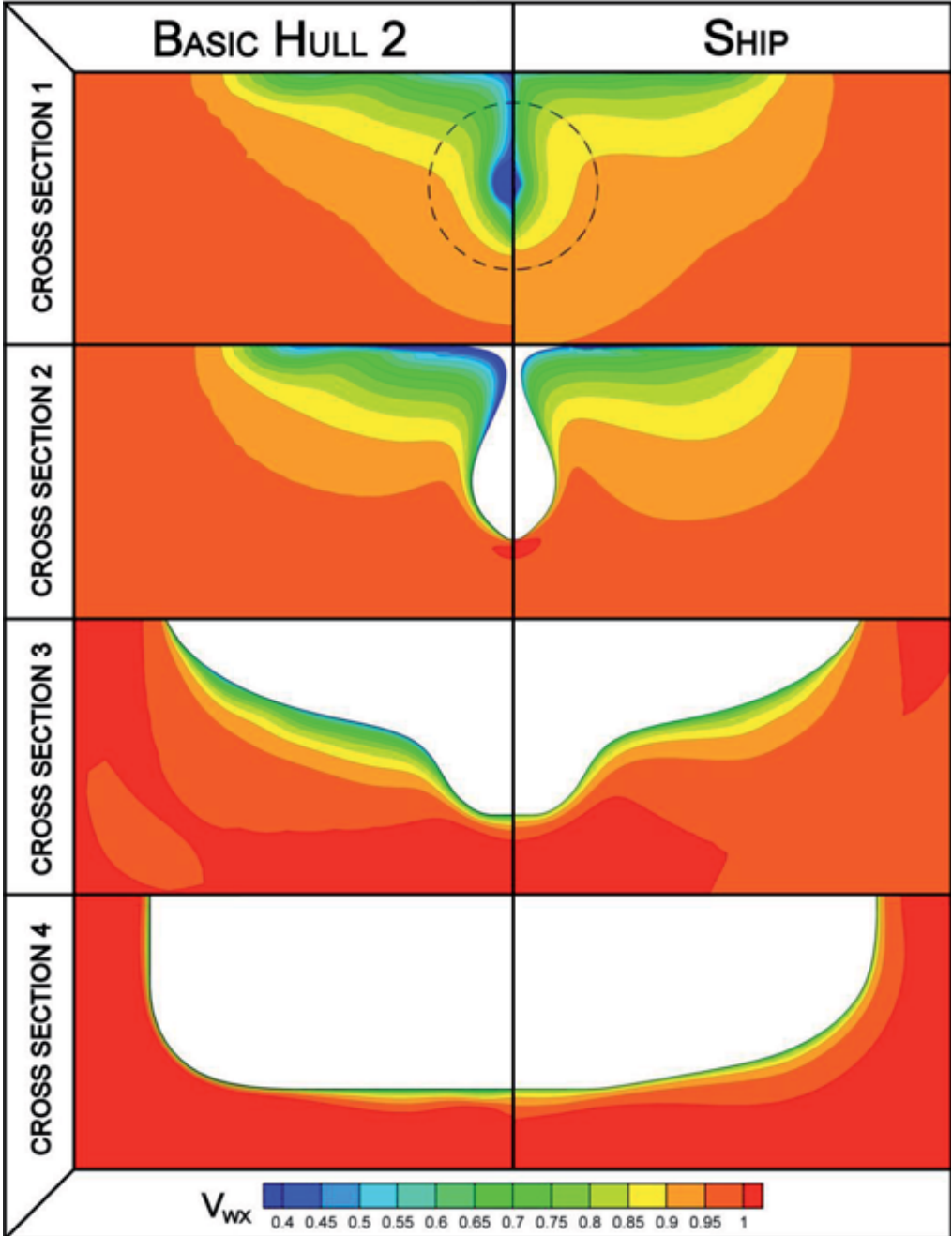
Figure 7.16: Axial component of the wake field of the short model.
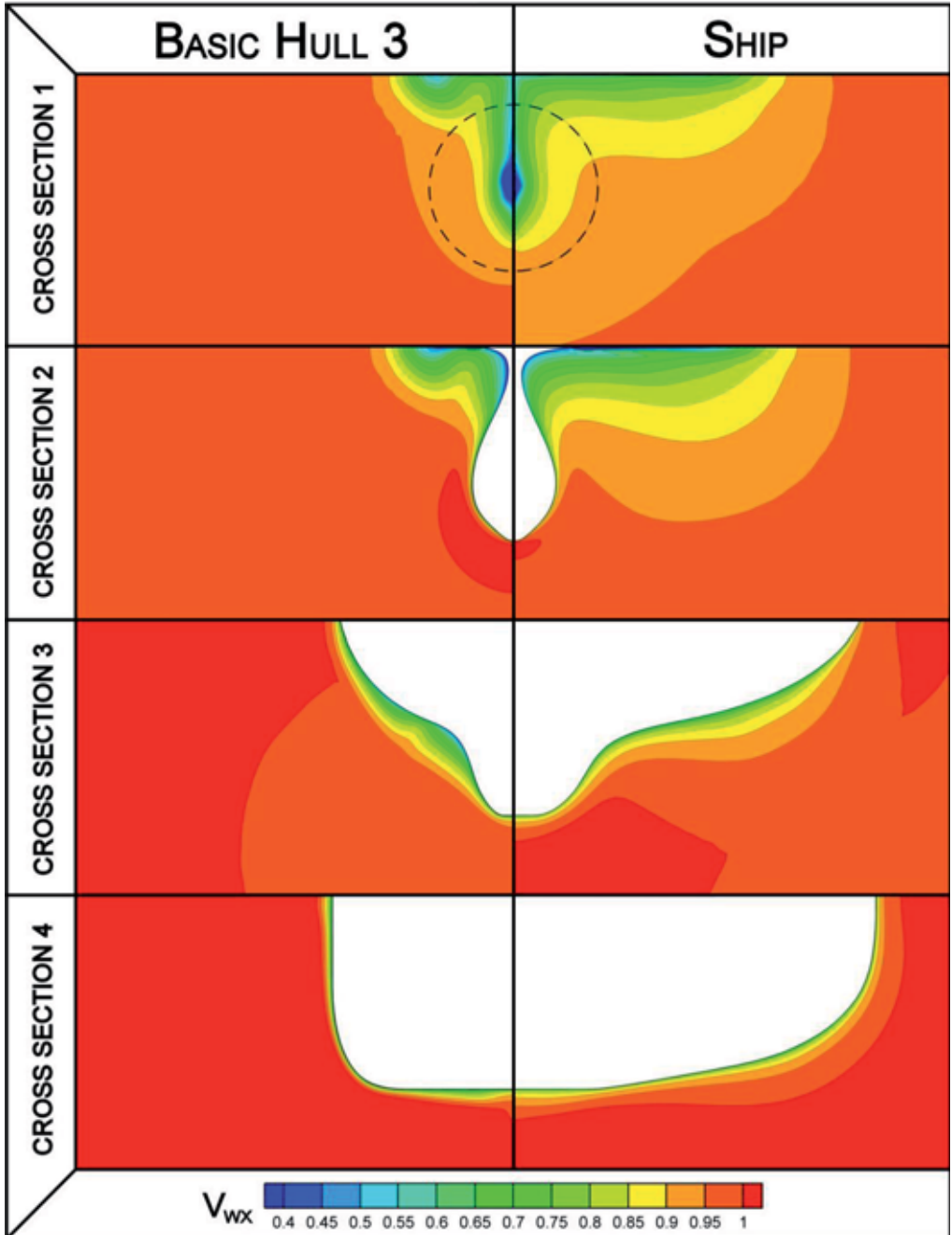
Figure 7.17: Axial component of the wake field of the short and narrow model.
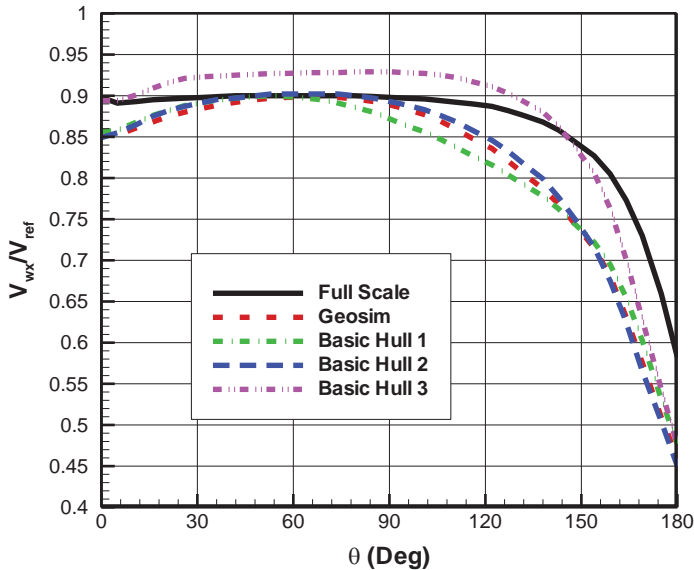
Figure 7.18: Axial component of wake velocity in propeller plane at 80% of propeller radius for four parent models and ship. TDC corresponds with 180 degrees.
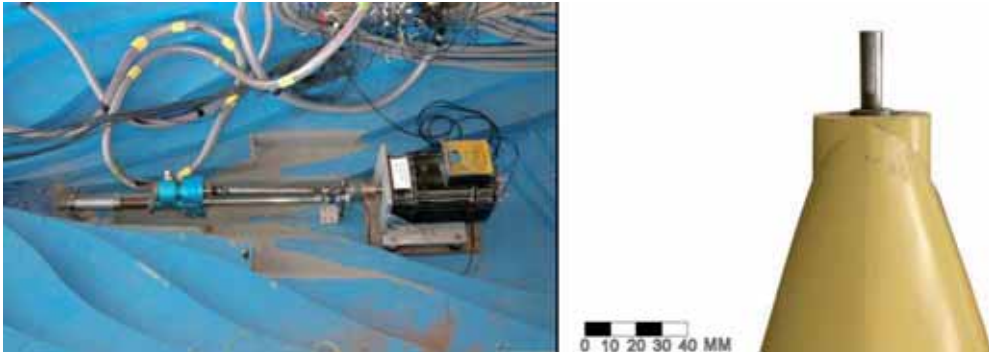
Figure 7.19: Typical driving train (left) and stern tube (right) arrangements.

At this point, it is worth noting that in the application of the Smart Dummy concept one has to consider several practical limitations. The most important one is the geometrical similarity of the overhanging part of the stern above the propeller. The pressure sensors have to be placed at positions corresponding with the ones on full scale. Also the clearance between the hull and the propeller shaft needs to be kept similar. Furthermore, there should be enough space to install the propeller powering system (Figure 7.19, on the left). The stern tube must be large enough to house the powering shaft of the propeller (Figure 7.19, on the right) and allow for a smooth transition to the propeller hub. When applied in a free surface facility such as the DTT, the length, trim and sinkage must be retained to prevent significant changes in the wave system.

The apparent challenge is to locally modify the aft part of the model in such a way that the minimum axial velocity in the wake peak compares better with full scale. If this would be possible by, say, modifying the gondola area only, then it may also be possible to achieve our aim without changing the length and width of the model. Even better, it may be possible to arrive at a model that could be milled with the geosim model as input. With the additional restriction of keeping equal clearance this would fulfill all requirements imposed on the model earlier.

To obtain the desired wake field, the geosim model was taken and the upper part of the gondola was made more slender in a trial and error fashion. After several attempts, the Smart Dummy depicted in Figure 7.20 and Figure 7.21 was obtained. For best full scale wake resemblance the model speed still needs to be increased somewhat, but only by 2% above its Froude speed. This is several percent lower than even the condition of thrust identity prescribes for the geosim.

This particular Smart Dummy was chosen because it best resembles the ship scale wake between the dashed lines in the upper part of the propeller disc of Figure 7.23. The choice was made on the basis of an L_2-norm on the deviation of the local axial component of the velocity from the local target value. Figure 7.24 zooms in on the wake peak area and adds transverse velocity components. It must be noted that several alternative hull forms approximate the ship scale wake in the wake peak area as well as the chosen one. However, none of them could reach the target wake at such a small speed increase relative to Froude speed and, more importantly, none of them could resemble the target wake for such large circumferential angles. The latter is important when pressure side cavitation is of concern. Figure 7.22 shows the distribution of the axial wake velocity at 80% of propeller radius as a function of circumferential angle (which is zero at the bottom dead centre). The Smart Dummy (in red) follows the ship scale wake (in black) accurately everywhere except near the bottom quarter of the propeller disc. The figure also shows the axial velocity mismatch between the target wake and the geosim at the standard thrust identity condition (in blue). The wake peak identity method is shown in orange and appears to follow the target wake only in the top region of the propeller disc.
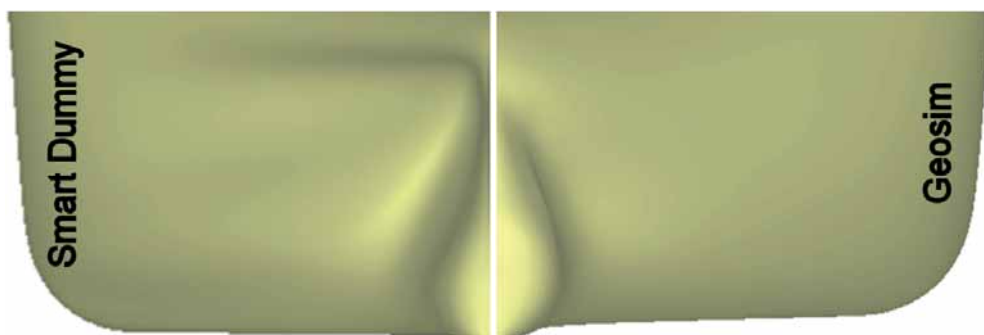
Figure 7.20: View from behind the Smart Dummy design (left), and the original geosim hull (right).
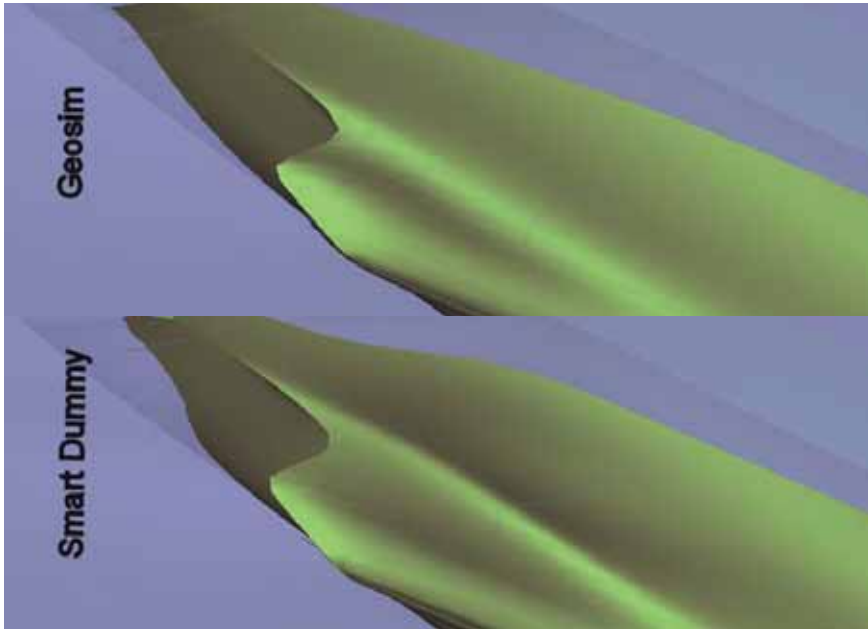
**Figure 7.21: Underwater view of the Smart Dummy (bottom),
and geosim hull (top) at Froude speed.**
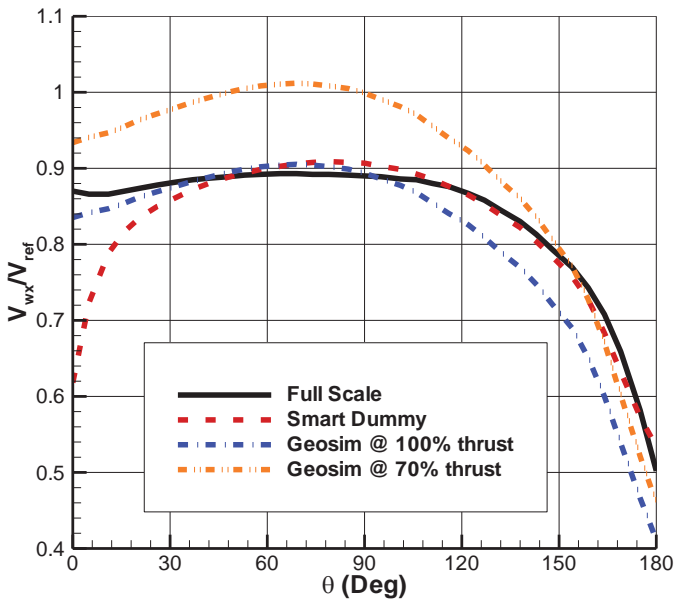
**Figure 7.22: Circumferential distribution of axial component of wake velocity in propeller plane at
80% of propeller radius for geosim model, Smart Dummy and full-scale ship.**
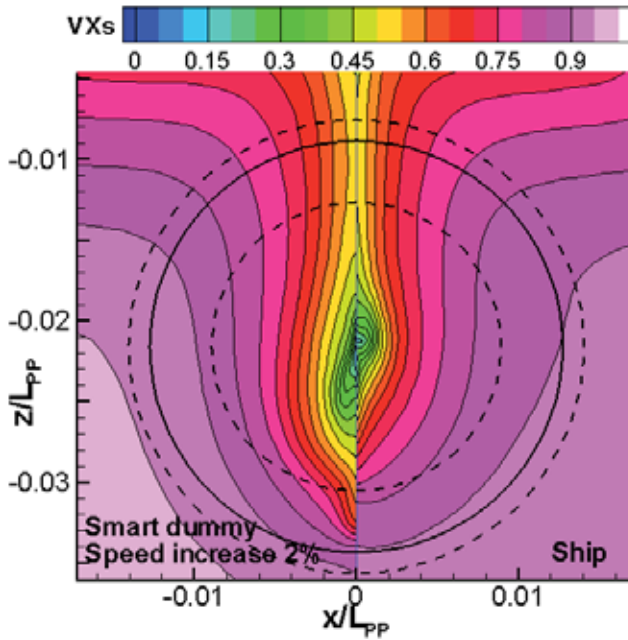
Figure 7.23: Axial component of wake velocity of Smart Dummy (left) compared to those at ship scale (right). The dashed circles are at propeller radii 1.1R and 0.6R, the solid circle is at 1.0R.
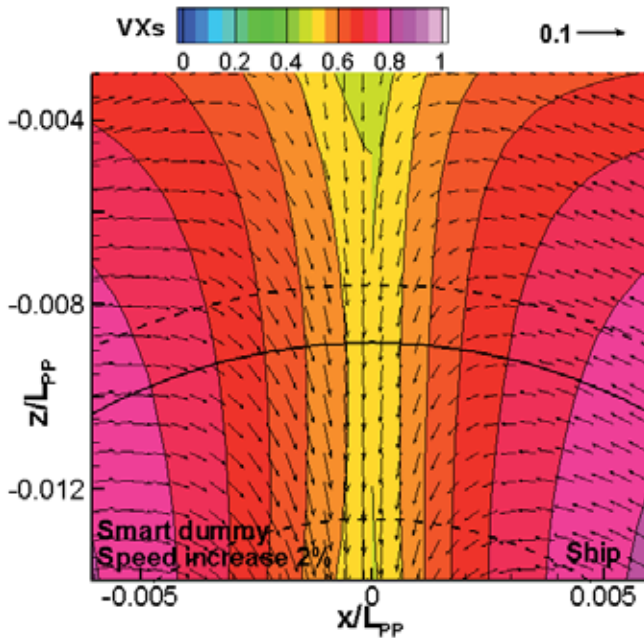
Figure 7.24: Axial/Transverse components of wake velocity of Smart Dummy design zoomed in on the top sector (left) compared to those at ship scale (right). See also Figure 7.23.

Although the Smart Dummy design appears to meet its aim, it is still uncertain whether, if a full scale wake field is generated by a model the cavitation on model scale will correspond with that of full scale. The Smart Dummy concept does not correct for the influence of the difference in Reynolds number on the propeller flow itself, possibly resulting in a different cavitation behavior. For example, the interaction of sheet and tip vortex cavitation may still not be properly modeled. All of these being valid statements, they are no reason for not applying the procedure proposed. After all, one important source of error is eliminated and an improvement in the prediction of the first blade rate frequency is expected to be obtained.

7.4.1   Example Case: Container Vessel #3

The above-described Smart Dummy was tested in the DTT at 2% above Froude speed (while maintaining Froude RPM) with the pressure sensors at the same positions as before. Ample nuclei were provided through the use of upstream electrolysis strips. The results are shown in Figure 7.25 in the form of high speed video snapshots. A vertical sequence of images represents one typical blade passage. The cavity volumes found for the Smart Dummy (left) are slightly reduced compared to those found for the geosim (right). For the Smart Dummy, blade no. 1 shows inception of sheet cavitation at a blade position reached later than for the geosim at increased velocity, indicating that the wake peak has indeed become narrower.

Figure 7.26 presents the results in terms of hull-pressure amplitudes. As before, amplitudes at the first four blade rate frequencies are given for the central pressure transducer, no. 5, which is closest to the full scale sensor position, and all amplitudes are divided by the full scale first order pressure amplitude. In the Smart Dummy wake, the propeller generates pressure pulses much like in previous experiments with the geosim at increased speed. The Smart Dummy's narrower wake causes later inception and earlier desinence, but the larger wake gradient causes a somewhat more rapid growth of the cavity. Also, the cancelling effect of cavities on neighboring blades is reduced. As a result, despite the somewhat smaller cavity volumes, the pressure amplitude at the blade rate frequency is still slightly higher than for full scale.

Figure 7.27 shows the effect of the offset in the position of transducer no. 5 relative to the full scale location. The results have been obtained by interpolation using all transducers. Figure 7.28 shows the effect of model speed variation (i.e., propeller load variation) on pressure pulses. Especially, the sensitivity at the first harmonic should be noted: a 1% increase in speed yields about a 9% decrease in pressure amplitude. It shows the necessity of accurate CFD computations in designing the Smart Dummy[21].

Pressure pulses at orders above the first are still strongly overpredicted. Several hypotheses can be formulated to explain this fact. As already mentioned, the Smart Dummy concept is limited in that it does not correct for the influence of the difference in Reynolds number on the propeller flow itself, possibly resulting in different cavitation behavior. Another limitation is related to scaling effects due to differences in gas content. The gas content in the present investigation was kept at the low value of about 35% air content at atmospheric pressure. A reduction in pressure pulses has been reported by Johannsen [Johannsen1998] after changing the gas content from 40% to 80% oxygen saturation. Thus, the pressure pulses at the 2nd to 4th order frequencies were reduced by 25%-50%.

---

[21] Although only the difference between the CFD computations at model and full scale is used.
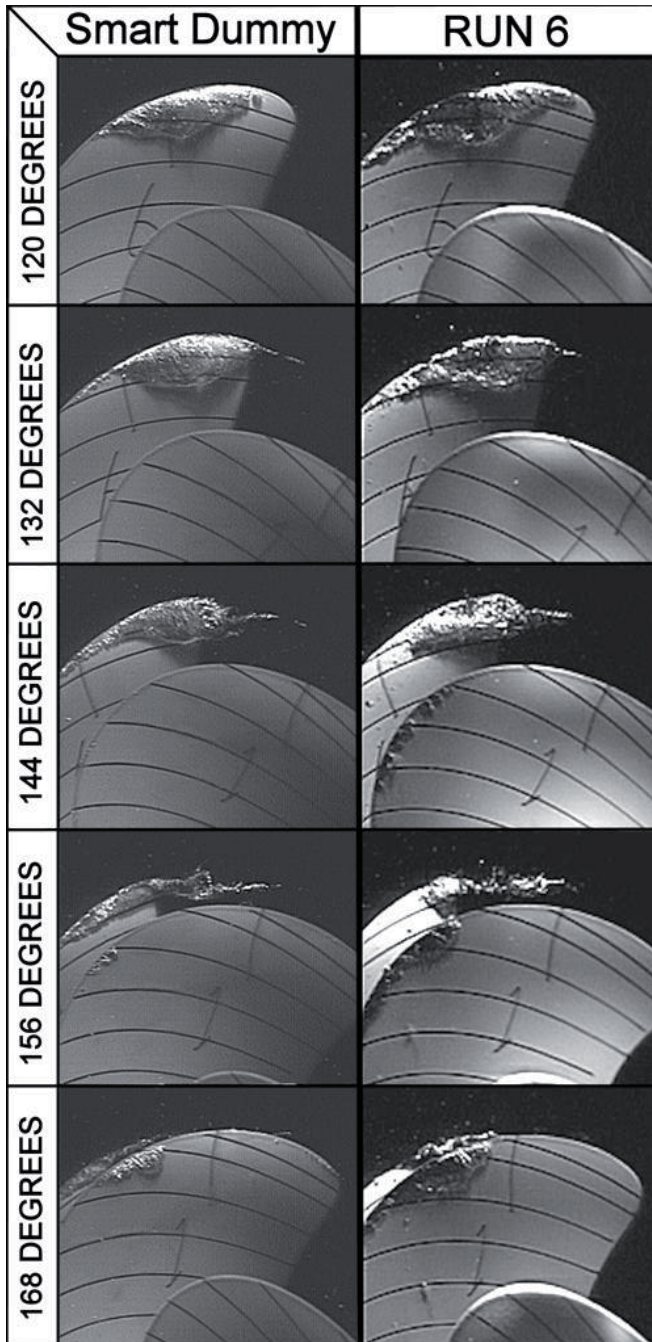
Figure 7.25: Comparison of cavitation extents. Right: Geosim @ 21% above Froude speed; Left: Smart Dummy @ 2% above Froude speed. Note that the Smart Dummy observations are performed using a different high-speed video camera and LEDs instead of Xenon lights.
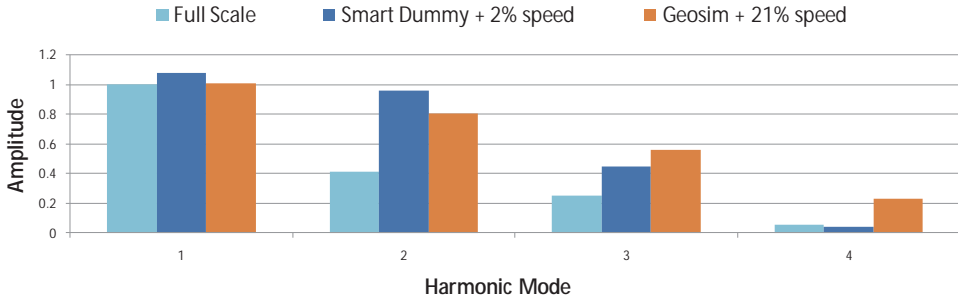
Figure 7.26: Comparison of normalized model and full scale pressure amplitudes for the first four blade rate orders @ sensor no. 5.
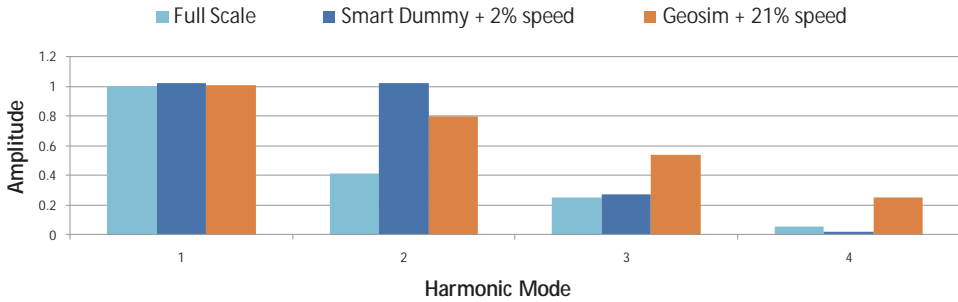
Figure 7.27: Comparison of normalized model and full scale pressure amplitudes for the first four blade rate orders interpolated at the full scale measurement location.
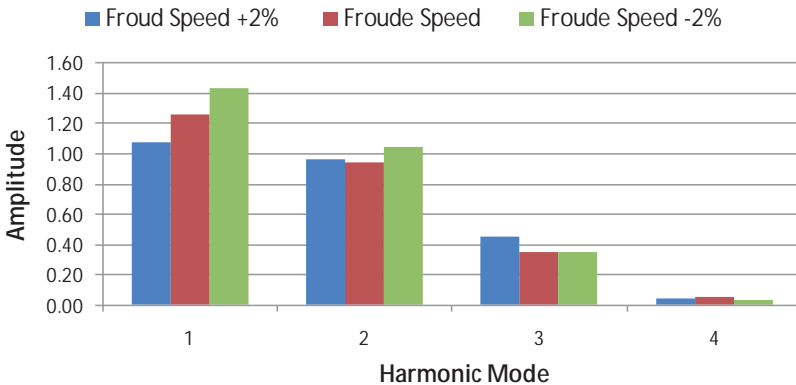
Figure 7.28: Effect of load variation on pressure amplitudes for the Smart Dummy model.

The Smart Dummy experiments have been repeated at an increased level of gas (i.e., air) content of about 60% at atmospheric pressure. A tenth pressure sensor has been added at the full scale location (see Figure 7.7). Figure 7.29 presents the pressure pulses at sensor

no. 10 at various model speeds. The Smart Dummy has been designed to overcome the wake scale effect on the basis of double body flow at model and ship scale Reynolds numbers. A ship model velocity increase allowance of 2% has to be applied. At that velocity the figure shows second and third order pressures that have decreased dramatically to just below ship scale values. The first order pressure amplitude has increased by about 6% at sensor no. 5 (not shown), while the target location, sensor no. 10, shows a pressure amplitude 15% higher than that for full scale.

In [Wijngaarden2010] Bosschers shows how pressure signal variability from blade passage to blade passage leads to amplitude and phase modulation. The stronger modulation effects are found on model scale, causing tonal components in the spectrum to be more 'smeared out'. As a result higher order pressure amplitudes would be expected to be underpredicted in the model tests, and perhaps even more so than is reflected in the second and third order amplitudes found in Figure 7.29.
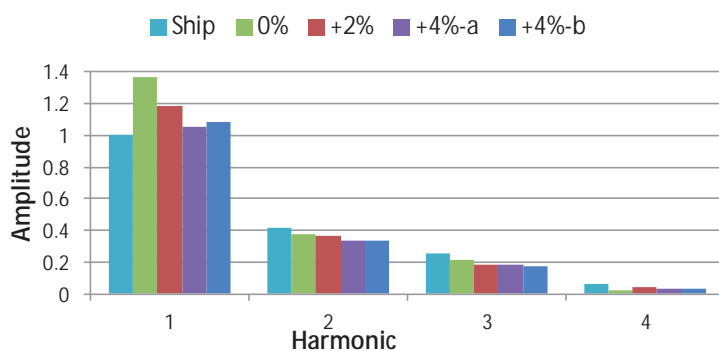
Figure 7.29: Smart Dummy model test results @ 60% air content for sensor no. 10. Ship measured hull pressure amplitudes are compared with Smart Dummy data at various speeds at and above the Froude-scaled speed. At 4% above that speed, two measurements have been made, 'a' and 'b'.

The remaining discrepancies between model and ship scale pressure pulses may be explained by assuming that the Smart Dummy wake still somewhat overloads the propeller. An additional 2% increase in model speed already yields pressure pulses very close to target values (see Figure 7.29). The computed wake scale effect for double body flow would then have to differ from the wake scale effect including free surface in such a way that the flow becomes more strongly retarded on model scale due to wave effects.

The latter has been checked by performing RANS computations including the free surface for the ship and the Smart Dummy. The results are presented in Figure 7.30. In the top sector between 0.6R and 1.1R, the axial component of the flow around the Smart Dummy indeed appears to have slowed down slightly. Figure 7.31 gives a more detailed picture of the circumferential distribution of the axial velocity at 0.8R for Smart Dummy and ship with and without free surface. Including the free surface leads to a steeper wake peak gradient, the loading effect of which may be taken into account by running the model at 4% instead of 2% above Froude speed. Nevertheless, it is concluded that the Smart Dummy should ideally be designed with the inclusion of a free surface when tested in a free surface facility like the DTT.
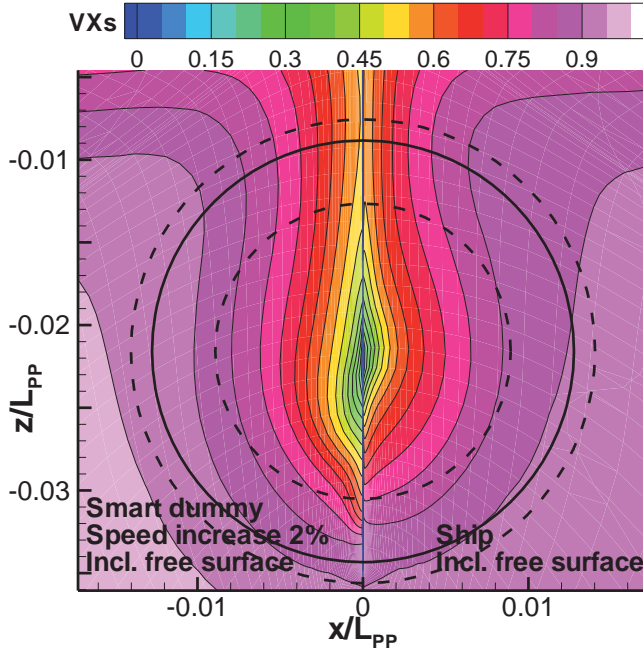
Figure 7.30: Axial component of wake velocity of the Smart Dummy design (left) compared to that at ship scale (right). The dashed lines are at propeller radii 1.1R and 0.6R. The solid line is at radius 1.0R. Free surface effects have been taken into account (cf. Figure 7.23).
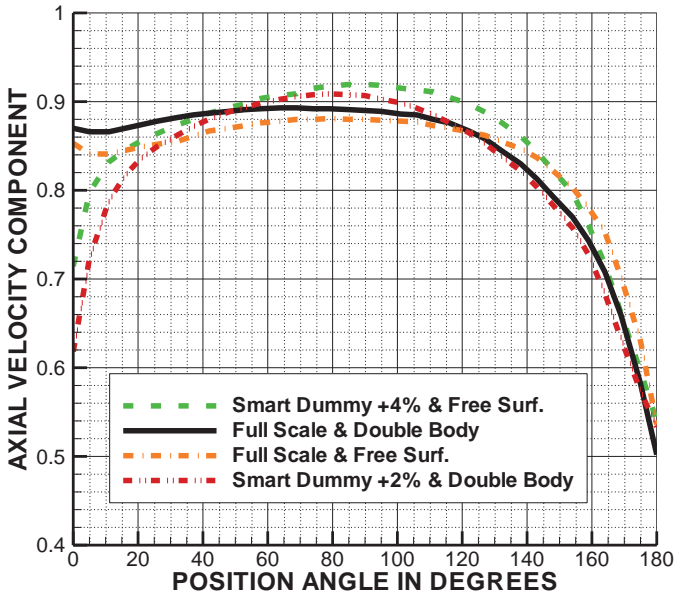
Figure 7.31: Axial component of wake velocity in propeller plane at 80% of propeller radius for Smart Dummy and ship with and without free surface.

7.5 Computational Procedure using Wake Peak Scaling

The series of measurements reported in Section 7.3.2 presents an opportunity to extend the validation of the computational method (see Chapter 6) to cavitating propellers. The chain of computational methods involved is shown in Figure 7.32. It involves the RANS method PARNASSOS for the computation of the nominal wake field; the PIFWAKE method for the nominal-to-effective conversion of the axial wake velocity component; the PROCAL BEM for propeller cavitation, and finally, the EXCALIBUR BEM for the determination of the hull-pressure pulses including the scattering effect of the hull. In the following, this computational chain is applied to container vessel no. 3.
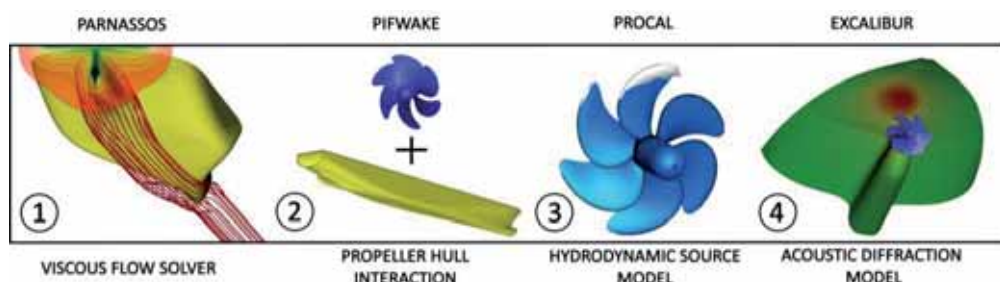
Figure 7.32: Overview of chain of tools involved in computational method.

7.5.1   Example Case: Container Vessel #3

From the computation of the double body flow around the ship, using PARNASSOS, a nominal wake field can be extracted. The nominal wake fields, thus found at model and full scale Reynolds number, are shown in Figure 7.5 on the right. The axial component of these wake fields at the propeller disc at 80% of propeller radius is plotted in Figure 7.33. After converting these wake fields into effective ones using PIFWAKE, the propeller thrust can be determined with PROCAL. This was done at the apparent advance coefficient (as if there were no wake at all), as well as at the standard condition of propeller thrust identity. Figure 7.34 shows that the latter condition follows the propeller thrust found in the ship scale wake accurately. However, when focusing on the thrust of one blade, the blade loading in the wake peak is still significantly lower on model scale, as is shown in Figure 7.35. As a result, the non-dimensional cavity volume per blade is much larger than on ship scale (see Figure 7.36 and Figure 7.37).

Using the effective wake fields as input to PROCAL, the cavitation patterns follow. Finally, the pressure distribution on the hull is computed by EXCALIBUR on the basis of the propeller noise source strengths (i.e., the strengths of the rotating point monopoles and dipoles) determined by PROCAL. Figure 7.38 and Figure 7.39 show the boundary element distributions used for the computations with PROCAL and EXCALBUR, respectively.

In analogy with the experiments, the simulations have been repeated for all conditions in Table 7.1. Thus, the propeller is gradually unloaded by increasing the ship model velocity. Figure 7.40 shows the effective axial component of the wake velocity at 80% of propeller radius from bottom (0 degrees) to top (180 degrees) dead center. Note that the wake peak

identity condition found in the model experiments in Run 6 (i.e., Sim 6 here) is still not obtained even in simulation no. 10. Not surprisingly, the resulting thrust per blade, computed in a fully wetted flow, i.e., without cavitation, is also too high in the wake peak (even for simulation no. 10, see Figure 7.41). The cavity volume per blade in Figure 7.42 follows the same pattern. The small cavities at the low circumferential angles are due to the pressure dropping below the vapor pressure on the pressure side of the blade. Although the cavity volumes are larger in the model scale wake, there is a significant reduction in cavity volume at increased speeds. A comparison of computed cavity patterns at Runs 1, 6 and 10 is shown in Figure 7.46 (cf. Figure 7.12).

Despite the reduction in total cavity volume as a result of the increase in speed and propeller unloading, the actual amplitudes of the harmonics of the pressure pulses have remained constant (after even increasing at the start of the unloading process, see Figure 7.45). Although this result differs much from its experimental counterpart, it is actually straightforward to explain. Figure 7.43 shows the cavity volumes on all six blades separately. The overlapping in circumferential direction causes expanding and shrinking cavity volumes on neighboring blades to destructively interfere. As a result, the net effect of unloading the propeller is a reduction in average cavity volume (see Figure 7.44). However, the amplitude of the cavity volume variation, and more importantly, the cavity volume acceleration, remain relatively constant. At the low frequencies under consideration, it is the latter quantity that determines the pressure fluctuations.

The width of the wake peak would be an easy explanation for this effect if it was not for the fact that the wake peak width on model scale is approximately the same. Nevertheless, the model experiments do show a decrease in first order BPF amplitudes.

A direct comparison of experimentally and computationally obtained results is presented in Figure 7.47. At 132 degrees, the upcoming blade no. 1 is still cavitation-free, both in the experiments and simulations. The next snapshot, taken at 144 degrees, shows good agreement between the computed and observed cavitation extent. However, after that, the cavity volume seems to overshoot in the simulations (cf. the snapshots at 156 and 168 degrees, blade no. 1, and the snapshot at 120 degrees, blade no. 6). The downgoing blade no. 6, at 132 degrees and onward shows a reasonable agreement in cavity extent. It appears that the inception and desinence points during a blade passage are well-captured in the simulations, but the maximum cavity volume is overpredicted.
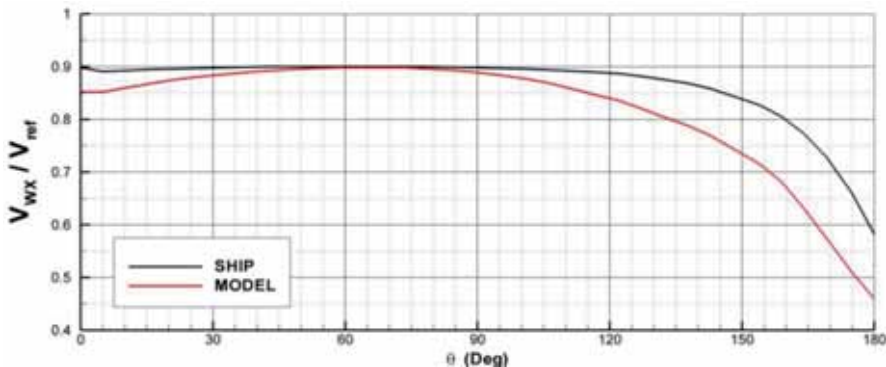
Figure 7.33: Circumferential distribution of nominal axial component of wake velocity at a non-dimensional radius 0.8R for ship and geosim model.
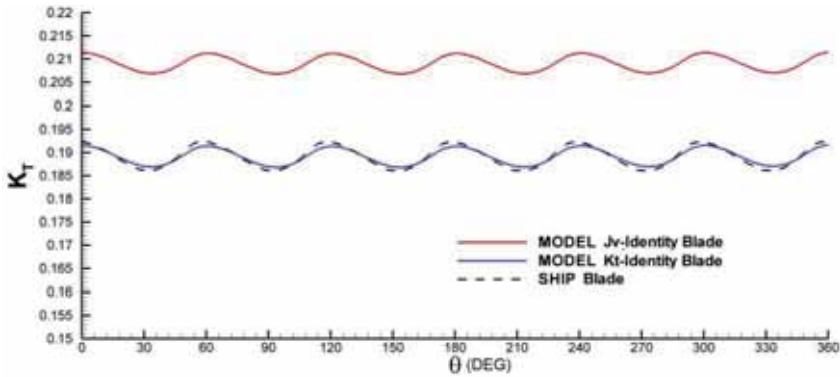
**Figure 7.34: Propeller thrust coefficient as a function of blade position, without cavitation, for
1) geosim model wake at J_V-identity; 2) K_t-identity (standard condition); 3) ship wake.**
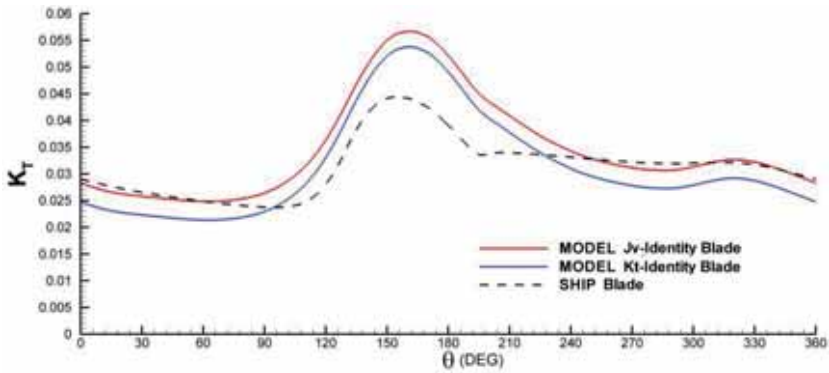
**Figure 7.35: Blade thrust coefficient as a function of blade position, without cavitation, for
1) geosim model wake at J_V-identity; 2) K_t-identity (standard condition); 3) ship wake.**
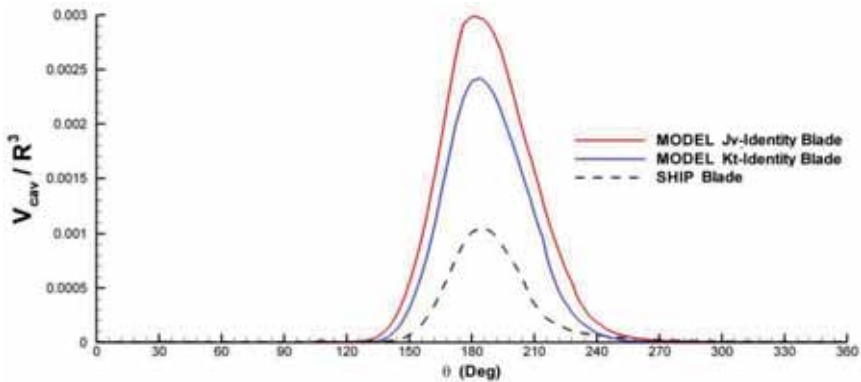
**Figure 7.36: Non-dimensional cavity volume per blade, for
1) geosim model wake at J_V-identity; 2) K_t-identity (standard condition); 3) ship wake.**
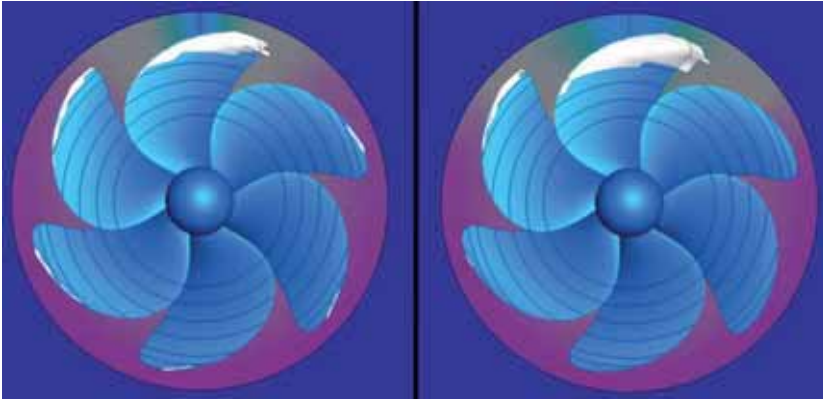
Figure 7.37: Computed sheet cavity extent for the ship (Left) and the geosim model wake (Right).
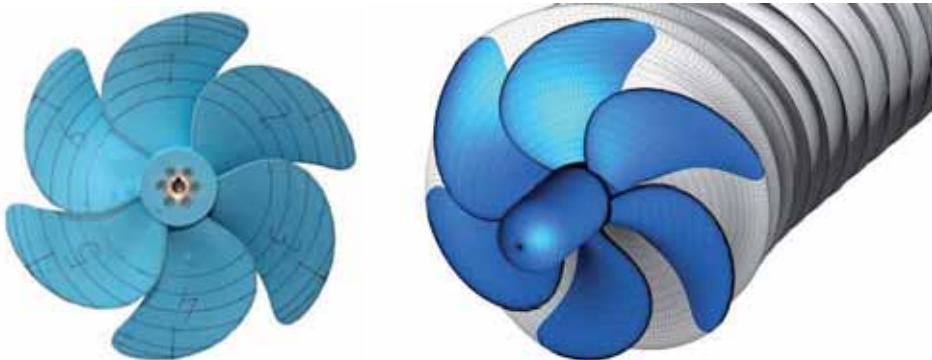
Figure 7.38: Model propeller (left) and boundary element representation (right).
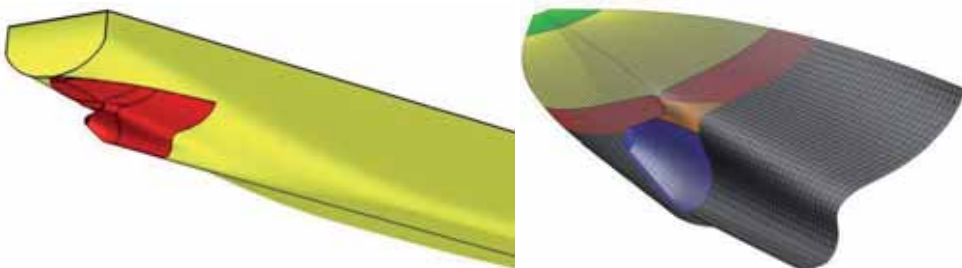
**Figure 7.39: Ship geometry with the grid part projected in red (left)
and boundary element representation (right).**
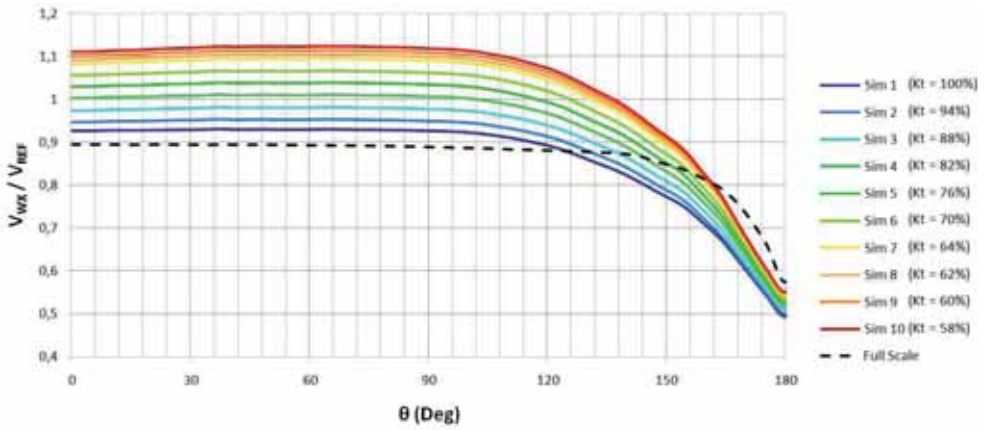
Figure 7.40: Axial component of the effective wake field at 0.8R for various thrust coefficients.
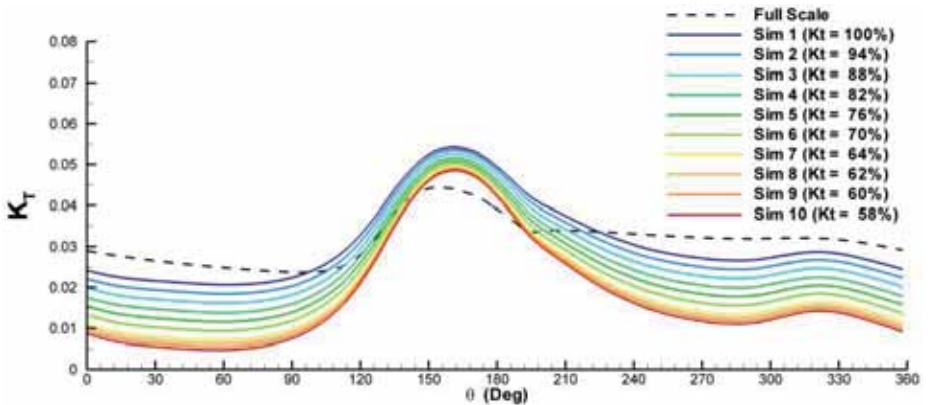
Figure 7.41: Blade thrust coefficient during a revolution at values of propeller thrust coefficient.
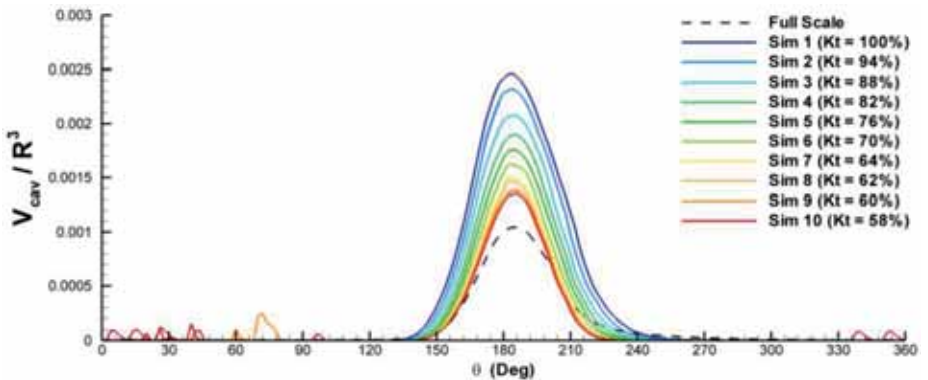
**Figure 7.42: Non-dimensional cavity volume per blade during a
revolution at various values of propeller thrust coefficient.**
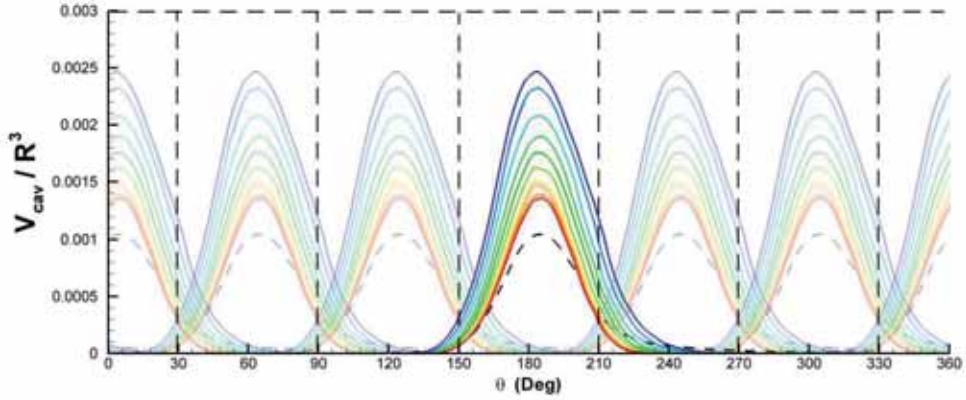
Figure 7.43: Interference of growing and shrinking cavities on neighboring blades.
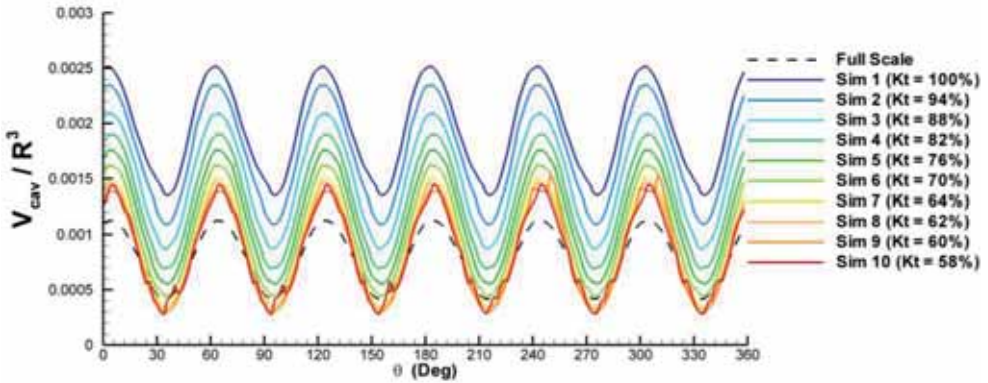
Figure 7.44: Effect of blade interference on instantaneous total cavity volume.
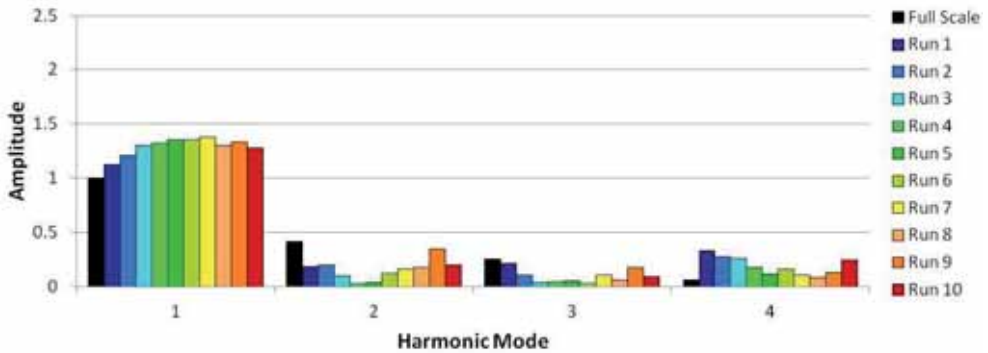
Figure 7.45: Hull pressure amplitudes computed by EXCALIBUR (sensor location no. 5).
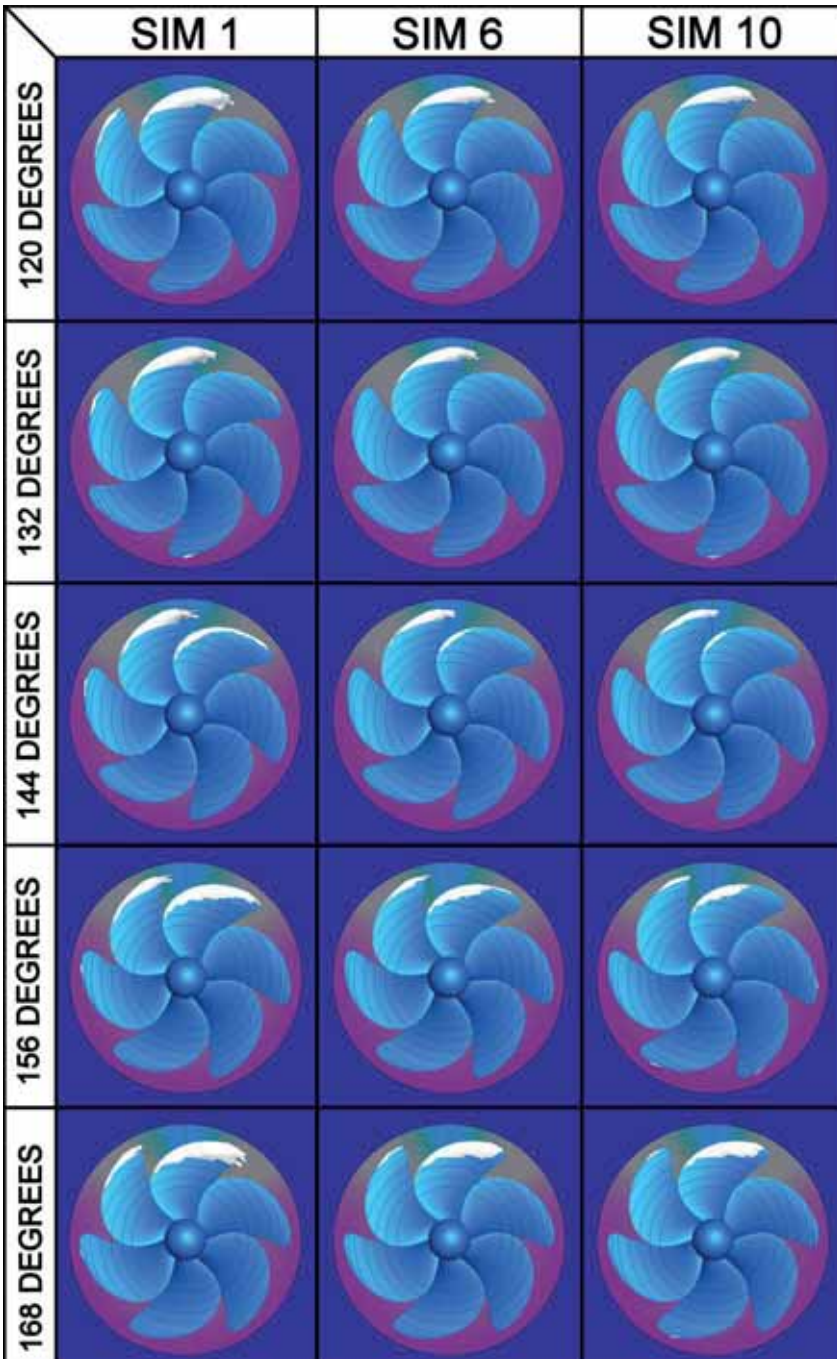
Figure 7.46: Sheet cavity extent as computed for three different simulations. Left: Propeller thrust identity; Center: Wake peak identity in model test; Right: Strongest unloading tested.
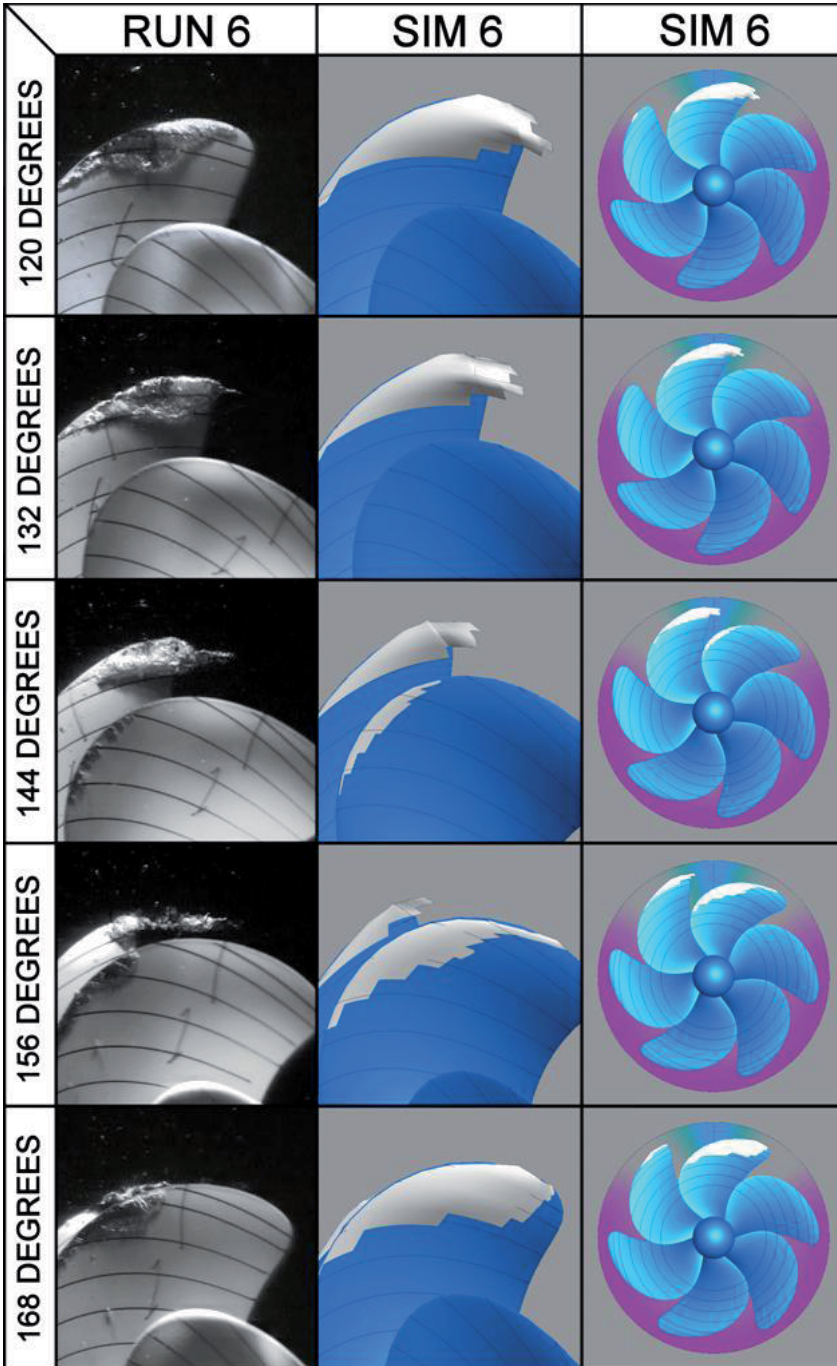
**Figure 7.47: Comparison of experimental and computational results for Run 6.
Left: experiment, Center/Right: computation.**

The differences found between experiments and simulations may have a number of causes. It was shown how small inaccuracies in effective wake field may have a substantial influence on cavity dynamics, and hence, pressure fluctuations. The dynamic sheet cavitation model itself may be the cause of the discrepancies, although it is difficult to determine what in the implementation should be changed. In the model the sheet cavity is not connected to a cavitating tip vortex, which may cause the sheet to grow somewhat too large. However, the latter explanation is not supported by Figure 7.47, in which the overshoot in sheet volume appears at blade angles at which the sheet-tip vortex interaction is not yet significant.

8   PROPELLER NOISE SOURCE STRENGTH

…in which the 'propeller source strength' is proposed as a figure of merit for cavitating propellers, and measured hull surface pressure data are used to determine source strength characteristics by means of inverse techniques.

8.1   Contractual Judgment of Hull-Pressure Forces

In order to distinguish between structures that are too flexible (the yard's responsibility) and sources of noise and vibration that are too strong (the supplier's responsibility) upper bounds to source levels need to be prescribed in contracts between the yard and its suppliers. E.g., a maximum allowable propeller-induced hull excitation force may be used as a measuring staff for the judgment of the noise and vibration characteristics of a propeller design.

In order to obtain an estimate of the propeller-induced hull excitation forces, model scale experiments are performed in cavitation facilities. Thus, hull pressures are measured through a set of pressure transducers flush-mounted in the hull above the propeller. Integration of the measured pressures then yields an approximation to the excitation force, thereby neglecting that part of the wetted hull surface area where no information on the pressures is available.

If the number of available hull-mounted pressure transducers in the experiments is limited, no resultant force can be obtained. The transducers may be too far apart to allow for an accurate integration, or cover an area too small to be representative of the total area of application of the excitation force. In those cases, a limit on the excitation force has to be in the simple terms of a maximum pressure amplitude above the propeller. As a result, contract requirements are often stated in terms of maximum pressure amplitudes for one or more harmonics of the propeller blade passing frequency.

This is unfortunate because the maximum allowable pressure above the propeller may be a weak measure of the total excitation force. Two examples illustrate this statement. Consider the maximum hull pressure above the propeller for a tanker in ballast, which is probably higher than when the tanker is loaded, but due to a smaller wetted surface area the ballast case may still show the smallest excitation forces [Lee2006]. Particularly for dredgers, Ligtelijn *et al.* showed that at the blade passing frequency interference of the cavitation-induced pressure field and the thickness and loading effects of the passing blades themselves blur the relation between the values of the excitation force and the maximum hull pressure [Ligtelijn2006]. To a certain extent, the non-cavitating contribution to the hull-pressure field determines the maximum pressure, but its strongly varying spatial phase distribution results in only a small contribution to the total excitation force.

It would be helpful if one would not have to rely on the maximum hull pressure only for a proper judgment of propeller-induced hull-excitation forces. An improved measuring staff should be meaningful with respect to hull vibration and stated in the simplest of terms. The excitation force integrated over a limited area above the propeller (e.g., up to the waterline around the aftbody) seems an acceptable figure of merit. The magnitude of the pressure forces and the area of their application are determined by the form of the ship, for which reason the excitation force is not an ideal measure of the quality of the propeller *itself* as a source of noise and vibration. For the latter purpose, it is suggested to simply interpret the term 'source' in the hydroacoustic sense, i.e., as a fictitious point source distribution with a certain volume variation.

In the present thesis, the hydroacoustic propeller cavitation source strength is proposed as a figure of merit regarding noise and vibration, being meaningful and simple. The propeller source strength is also useful as a measure for correlation of predictions and reality. The methodology described in [Wijngaarden2006b] is a practical way of deriving the propeller cavitation source strength and from this the afterbody integral forces on the basis of the usual limited hull-pressure measuring data available.

An acoustic source distribution, in terms of a set of point singularities, is proposed to model the cavitating propeller. The strength of the sources is determined from an inverse scattering computation using the measured hull pressures as input to a computer code based on the Boundary Element Method. A forward scattering computation then yields the wanted hull-surface pressure distribution. In the following sections, this procedure is worked out in some detail.

8.2 Modeling Hull-Pressure Distributions

The acoustic source distribution sought should fulfill several conditions. The measured pressure amplitudes and phases should be well-predicted by it. The cavitating and non-cavitating contributions to the pressure field have to be distinguishable to allow for their separation and the derivation of a cavitation source strength. The number of unknown strengths in the source distribution must be kept as small as possible, bearing in mind the scarcity of the measured data and the wish to characterize the propeller as a source of noise and vibration in the simplest of terms for contractual specifications and model to ship scale correlation studies.

Figure 8.1 shows a single screw vessel (container ship #1) with a collection of measured hull-pressure amplitudes and phases at BPF, which are known to be due to cavitation. The maximum pressure amplitude is found above the propeller close to the ship centre line. Also, an almost constant phase distribution becomes apparent. The figure suggests the use of a point source of the monopole type, submerged somewhere in the area where cavitation occurs on the propeller blades. Although the sheet cavities on propeller blades seem to be attached to the blade, their 'lifespan' is confined to the period the blade spends inside the wake peak, which is a relatively small region. Hence, the monopole may be assumed stationary in a first approximation. This model is also suggested by Bloor [Bloor2001]. Van Wijngaarden [Wijngaarden2006a] shows that the single monopole model roughly explains between 85% and 90% of the pressure field due to cavitation at the first two orders of BPF. These results are shown in Figure 8.5.

It is tempting to model the propeller by just this one stationary source (e.g., [Kinns2003]). However, such models cannot explain the non-cavitating hull-pressure fields measured in cavitation facilities (cf. the second question in the discussion of [Kinns2003]). This becomes clear when looking at the non-cavitating hull pressures measured on the same single screw vessel shown earlier. Figure 8.2 shows the pressure amplitude and phase distribution, the latter indicating the direction of rotation of the blade. The phases decrease from port to starboard as they have been caused by a right-handed propeller. A model for the propeller will have to mimic this feature.
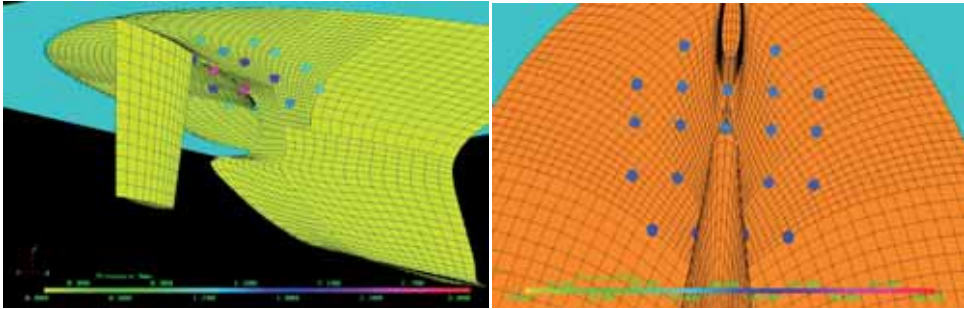
Figure 8.1: Normalized pressure amplitude (left) and phase (right, deg.) at BPF due to cavitation.
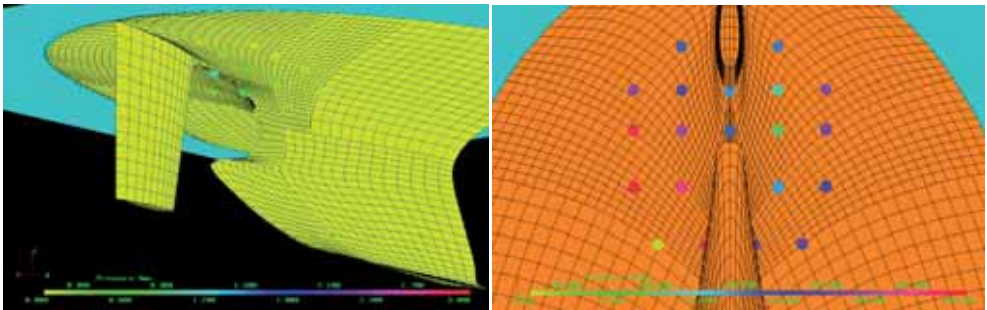
Figure 8.2: Normalized pressure ampl. (left) and phase (right, deg.) at BPF due to blade passages.

**Table 8.1: Influence of thrust loading on maximum non-cavitating
hull-pressure amplitude at BPF, measured at constant RPM
on a scale model of the single screw vessel depicted in Figure 8.1.**

Thrust [N]	81.5	37.5
Amplitude [kPa]	1.01	0.91
Phase [deg.]	-173	-175

Before attempting to model the thrust loading and displacement effect of the propeller, it is worth looking at their relative importance, indicated in Table 8.1. The table is based on model tests in the DTT that were performed at atmospheric tank pressure in order to suppress cavitation. For the single screw ship depicted in the above figures the propeller

loading was decreased by 54% at constant RPM. The maximum non-cavitating hull-pressure amplitude only decreased by 10% at nearly the same phase angle. This confirms the well-known fact that usually the blade thickness is the dominant contributor to the non-cavitating hull-pressure field on the hull right above the propeller.

On page 278 of [Breslin1994] it is stated: "*We observe that the pressure generated by thickness is also a distribution of dipoles with axes along the tangent to the fluid reference surface in way of the blade, the strength of the dipoles being* $2\rho V^2(r')d\tau / dh'$." This applies to the case of uniform flow, with V denoting the inflow velocity of a blade section at radius, r' , ρ the mean density, and $d\tau / dh'$ the change in local section thickness τ in the direction of h' , the helical coordinate which runs along the blade section chord from tail to nose. Hence, from the nose to the location of maximum thickness the dipole strength is negative and positive in the remainder. It is noted that the figure on page 282 of [Breslin1994] indicates that the sections at the outer radii contribute most to the pressures pulses on the hull.
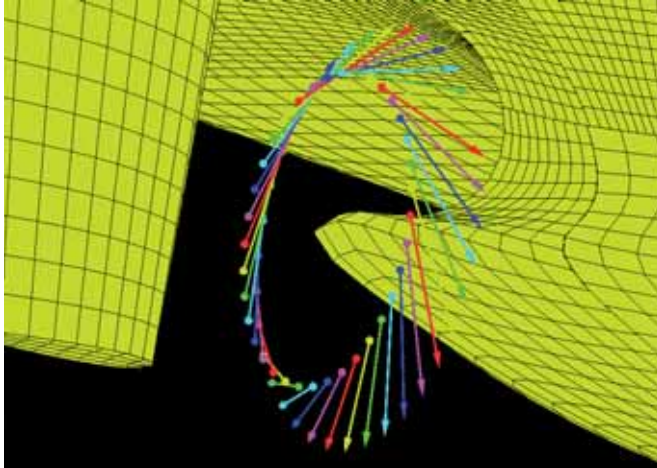
Figure 8.3: Direction (arrows) and phase (colors)
of a dipole ring consisting of 36 sources.

Combining the above observations, it is concluded that a source model for the non-cavitating propeller should at least include the thickness effect due the blade sections at the outer radii. A straightforward way of modeling this would be by placing dipoles at a typical radius. The dipoles, e.g., one for each of Z blades, are rotating in the propeller plane about the shaft centre line. In the frequency domain the dipoles transform into dipole rings centering on the shaft centre line (see [Brouwer2005] and Appendix E for a derivation). The dipoles are assumed to be constant in amplitude around the ring, directed along the pitch line at the radius concerned, and with a prescribed relative phase, $\Delta\beta$, depending on the number of dipoles, m_{dip} , used to discretize the ring,

$$\Delta\beta = 2\pi Z \big/ m_{dip} = Z\Delta\alpha \qquad (8.1)$$

with the dipoles located at a constant angular distance $\Delta\alpha$, see Figure 8.3. Note that in this figure each sixth source is of the same color, as $Z = 6$, hence $\Delta\beta = 60^o$ and $\Delta\alpha = 10^o$.

In case the blade loading component needs to be modeled, an analogous approach may be followed ([Breslin1994], page 277). The elemental pressure forces, Δp, on a blade element, dS', are written as $\Delta p\, dS' = \Delta p\, dh'dr'$. Allowing for the same simplifications as before, this can be modeled in the frequency domain by a ring of dipoles directed along the normal to a helical reference surface.

Summarizing, it appears appropriate to model the loading the blades exert on the fluid as well as the displacement effect due to blade thickness by means of rings of sources of dipole type. Alternatively, each dipole ring may be replaced by two closely spaced monopole rings. The inverse BEM, which is treated in some detail in the next section, is implemented in such a way that an arbitrary number of monopoles, dipoles, as well as monopole and dipole rings may be used to build up models of the cavitating propeller.

Having established the appropriateness of the computational models used, the next step is to apply them in an inverse way in order to compute source strengths given pressure distributions on the hull. It is shown that the sparse set of pressure data usually available on the hull may still suffice for the computation of the source strengths. The mathematically often ill-posed inverse problems to which this one belongs do not permit reaching a high resolution. Nevertheless, the description of the propeller action simply as a small set of 'multipoles' causes no mathematical problems and is still of value.

Once the propeller source strength is known, the complete pressure distribution on the hull can be determined, thus allowing for the subsequent determination of integral forces. As an important application, the direct coupling of the hull-pressure distribution to Finite Element analysis must be mentioned. Figure 8.4 gives an overview of the proposed procedure.
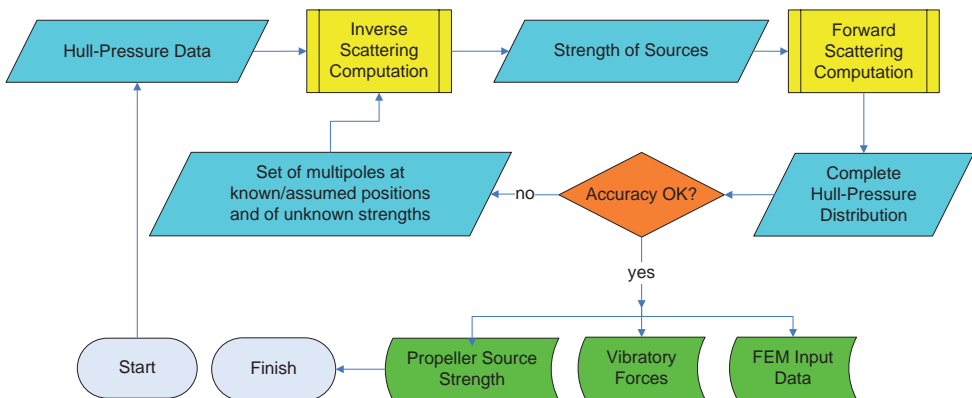
Figure 8.4: Procedure for determining propeller source strengths.

8.3 Inverse Modeling of Cavitating Propellers

In [Visser2004], Visser chooses a '*Singular Value Decomposition*' (SVD) method in order to solve the near-singular set of linear equations that results from inverse acoustic radiation problems. Then, the surface velocity distribution is sought and field pressures are prescribed. Here, this method is applied to inverse scattering problems, where the pressure field on the bounding surface is given and one must solve for the strength of the source distribution in the acoustic field.

The starting point for the derivation of an inverse scattering formulation is found in the forward scattering formulation that is part of the EXCALIBUR Boundary Element Method treated in Chapter 3 and Appendix F. Section F.1 gives a detailed account of this BEM for forward acoustic scattering problems in the frequency domain involving floating or submerged objects. In particular, Eq. (F.71), describes the set of linear relations that holds for the surface potentials. When the coupling parameter, μ, is taken zero for the sake of simplicity, it becomes,

$$\boldsymbol{\varphi}_S^{inc} = -\left[\mathbf{M} - \tfrac{1}{2}\mathbf{I}\right]_S \boldsymbol{\varphi}_S \tag{8.2}$$

with $\boldsymbol{\varphi}_S^{inc}$ the vector containing the incident wave potentials on the scattering surface. In inverse scattering problems, this vector is initially unknown. It readily follows from Eq. (8.2) by multiplying the negative of the matrix of influence coefficients, $\left[\mathbf{M} - \tfrac{1}{2}\mathbf{I}\right]_S$, by the vector of known surface potentials, $\boldsymbol{\varphi}_S$, both appearing on the right-hand-side.

The next step is to find an expression relating the incident wave potentials on the surface to the strengths of the sources in the fluid that are causing the incident wave field. Since incident waves are defined in the free field, the source strengths and their potentials are simply related through the Green's function, G_H. In matrix notation this becomes,

$$\left[\mathbf{G}_H\right]_S \mathbf{q} = \boldsymbol{\varphi}_S^{inc} \tag{8.3}$$

with $\mathbf{q}$ the unknown source strengths. In general, the number of point sources in the fluid, N^s, will not equal the number of panels, N'. Therefore, in order to obtain a set of N^s equations, both sides of Eq. (8.3) must be pre-multiplied by the transposed matrix,

$$\left[\mathbf{G}_H\right]_S^T \left[\mathbf{G}_H\right]_S \mathbf{q} = \left[\mathbf{G}_H\right]_S^T \boldsymbol{\varphi}_S^{inc} \tag{8.4}$$

to give the so-called 'normal equations'. Now, $\mathbf{q}$ could be solved for. In practice one is free to choose whatever number of sources to describe the cavitating propeller. The position of the sources has to be known in advance in order to determine $\left[\mathbf{G}_H\right]_S$. As this is practically not the case a solution has to be sought by iteratively updating the position of the sources and solving the set of equations for the updated right-hand-side.

As the present model does not involve shear stresses, only monopoles and dipoles, $\mathbf{q} = \mathbf{q}_{mon}$ and $\mathbf{q} = \mathbf{q}_{dip}$ are used. The expression for a dipole is obtained by taking the spatial

derivative of the Green's function with respect to the source coordinates in the dipole direction[22]. Thus, a dipole of unit strength directed along unit vector, $\boldsymbol{\xi}$, is denoted,

$$\frac{\partial G_H}{\partial \xi} = \frac{\exp(ikr)}{4\pi r}\left(\frac{ikr-1}{r}\right)\cos(\theta) \tag{8.5}$$

with θ the angle enclosed by $\mathbf{r}$ and $\boldsymbol{\xi}$, according to $\cos(\theta) = \mathbf{r}\cdot\boldsymbol{\xi}/r$ (cf. Eq. (F.25)). Eq. (8.3) now becomes,

$$\begin{bmatrix} \mathbf{G}_H & \dfrac{\partial \mathbf{G}_H}{\partial \xi} \end{bmatrix}_S \begin{bmatrix} \mathbf{q}_{mon} \\ \mathbf{q}_{dip} \end{bmatrix} = \boldsymbol{\varphi}_S^{inc} \tag{8.6}$$

    If the matrix on the left-hand-side is not ill-conditioned the above-described procedure solves the inverse acoustic scattering problem. However, it does so only when the surface potential is given over the *whole* surface, S, i.e., at a large number of collocation points, N'. In everyday practice, however, the surface potential $\boldsymbol{\varphi}_S$ is only measured on a patch of the surface, say L. This may be a rather small part of S. Use can be made of the fact that the surface potential tends to zero when approaching the waterline in interpolating between zero and the solution on the patch of the surface where the potential is actually measured. If information on the shape of the surface potential distribution is known then interpolating functions may be used that approximate that distribution, thus enhancing the accuracy of the results. However, when there is no information on the shape of the hull-pressure distribution, the interpolation procedure is bound to become inaccurate.

    When the scattering problem must still be solved, its solution may be used in solving the inverse scattering problem described above without having to resort to interpolation techniques. Let us assume for the moment that the N^s sources are of unit strength. The incident wave potential $\bar{\boldsymbol{\varphi}}_{S,m}^{inc}$ can be readily determined for each of them, with $m = 1..N^s$, the overscore indicating unit source strength. Then, solving the diffraction problem for N^s right-hand-side vectors,

$$-\left[\mathbf{M} - \tfrac{1}{2}\mathbf{I}\right]_S \bar{\boldsymbol{\varphi}}_{S,m} = \bar{\boldsymbol{\varphi}}_{S,m}^{inc} \tag{8.7}$$

yields a set of N^s vectors, $\bar{\boldsymbol{\varphi}}_{S,m}$, of diffraction constants for all N' panels covering S. Now assume these vectors to be truncated to the I panels, covering L, on which the points are located where the surface potential $\boldsymbol{\varphi}_L$ is actually known through measurement. Thus, an $I \times N^s$ matrix of diffraction constants $[\boldsymbol{\Phi}]_L$ is derived. The strength of the sources is then determined from,

$$\left[\boldsymbol{\Phi}\right]_L \mathbf{q} = \boldsymbol{\varphi}_L \tag{8.8}$$

---

[22] Appendix C provides some background on acoustic point sources.

In general, the number of point sources in the fluid, N^s, is not equal to the number of panels used, I. As before, in order to obtain a set of N^s equations, both sides of Eq. (8.8) must be pre-multiplied by the transposed matrix,

$$\left[\boldsymbol{\Phi}\right]_L^T \left[\boldsymbol{\Phi}\right]_L \mathbf{q} = \left[\boldsymbol{\Phi}\right]_L^T \boldsymbol{\varphi}_L \tag{8.9}$$

Thus, the normal equations are obtained and $\mathbf{q}$ can be solved for. At the expense of solving the diffraction problem for a number of right-hand-side vectors, the inverse problem is solved without any other information on the diffracting surface prescribed.

Now assume that the cavitating propeller may be described by a simple point source of which the position and strength are unknown. Furthermore, assume that the non-cavitating propeller may be modeled by monopole or dipole rings. The amplitudes of the sources within a ring are assumed to be equal and the phase difference between neighboring sources is taken as constant. After a position of the monopoles and a position and direction of the dipoles have been chosen, an inverse scattering computation may be performed from which the source strengths follow. A forward scattering computation with this source distribution yields computed values also at the locations where the measured data are available.

The quality of the computational prediction is expressed using a residual based on a standard L_2-norm to convey the 'average' error. In the remainder, residuals are stated as a percentage of the solution. If necessary, other positions for the sources can be tried and the computation repeated. This iterative process continues until a minimum value for the residual is found.

Although, a source ring may be a complex source in terms of its Green's function, the number of unknown strengths is still only one. Together with the monopole, the system of equations to be solved constitutes N^s equations for a few unknowns. Repeatedly solving this hundreds of times for different values of position and direction is done in a matter of seconds.

Inverse scattering problems are often ill-posed since, in principle, different source distributions may produce the same hull-pressure distribution. Because the set of linear equations that remains to be solved is often nearly singular, the above-described procedure may not be trivial and matrix regularization techniques based on SVD are sometimes necessary to arrive at meaningful results. It is considered a much better way of solving inverse problems than is the direct use of the normal equations. However, if the number of hull-pressure data is small and so is the number of complex amplitudes in the source distribution model, then SVD is generally not needed. Nevertheless, in order to deal with more elaborate models, SVD has been implemented in the inverse BEM considered here. A brief introduction into SVD is given in Appendix G.4.

8.4 Example Case: Cavitating Propeller mounted on Container Vessel #1

Consider a single screw ship for which model scale measuring data of hull-pressures are available. The data set consists of 21 measuring points on the hull above the propeller for which the pressure is known at the first two harmonics of the propeller blade passing

frequency. The propeller's small non-cavitating contribution to the hull-pressure field has been measured and subtracted from the total. An iterative search is started for the source location and strength showing the best match to the measured pressure field. The quality of the computed location and source strength is reflected in the residual of the set of equations that needs to be solved. The iterative search continues until a minimum value for the residual is found. The source strength and position for that case are then assumed to be *an* answer to the inverse scattering problem.
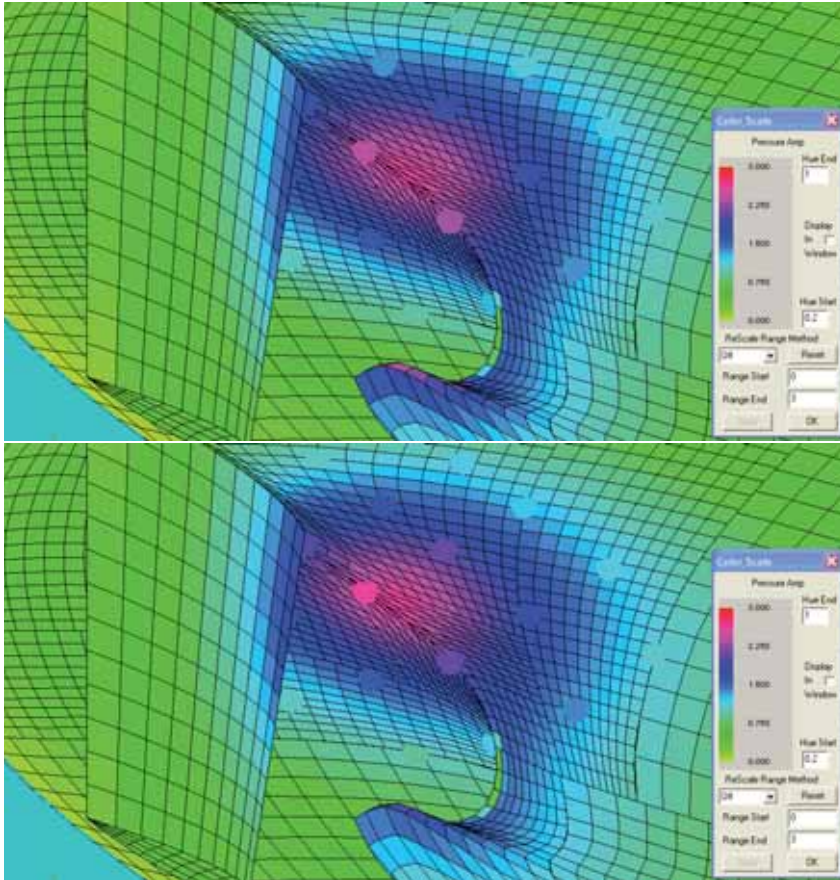
Figure 8.5: Measured hull-pressures (normalized) at once (top) and twice (bottom) BPF (colored spheres) and pressure contour plot based on best fitting monopole model [Wijngaarden2006a].

Figure 8.5 compares the measured pressures at the first and second blade passing frequency with the hull-pressure distribution that is found after performing a forward scattering computation using the source strength and position that have been found. The residuals are found to be 14% and 12% for the first and second harmonic, respectively. The monopoles are

located within the propeller disc respectively at 80% and 90% of the propeller radius, both with a shift of about 0.5 meters in the direction of the downgoing blade (see Table 8.2).

Table 8.2: Measure of fit of single monopole source model for cavitating hull-pressure amplitudes at orders of BPF.

Harmonic Order	1	2
Residual	14%	12%
Radial Position	0.8 R	0.9 R
Shift from Centre Line	-0.5 m	-0.5 m
Number of Input Pressure Data	21	21

8.5   Example Case: Non-cavitating Propellers mounted on Container Vessel #2

The validation experiments of Section 6.2 performed on non-cavitating propellers have been used as input to an inverse scattering computation. From the set of test propellers, the one designed for the ship (no. 6724, see Table 6.1) is omitted as it shows only very insignificant non-cavitating hull pressures. The other three cases are shown in Table 8.3. From Table 6.2 five test runs are selected from which the measured hull pressures are used as input for the inverse source strength determination. The test conditions are found in Table 8.4.

Table 8.3: Propeller models used in inverse scattering computations.

Prop. No.	Blade number	Diameter [mm]	Remarks
6666	2	340.00	Zero pitch to produce zero thrust
6553	5	295.79	Thick blades at the tip
6458	4	261.54	Small blade area and low pitch

Table 8.4: Overview of test conditions used as input to inverse scattering computations.

Prop. No.	Test No.	V_m [m/s]	BPF [Hz]	K_T [-]	Draft [m]
6666	1	0.00	20.00	0.021	0.531
6553	1	2.37	26.25	0.009	0.388
6553	2	3.00	54.33	0.191	0.388
6458	1	2.37	30.80	0.004	0.388
6458	2	3.00	53.33	0.084	0.388

For the unloaded, 2-bladed, zero pitch propeller, no. 6666, the dipoles in the rings of the model are directed along the nose-tail line, i.e., in the plane of the ring itself, since no blade loading needs to be taken into account. Such dipole rings may also be modeled by monopole rings with an appropriate phase gradient along its circumference. In a first attempt, one monopole ring, consisting of 72 monopoles, has been chosen. For each of the four significant BPF harmonics the optimum axial location and radius of the ring is found, using the hull pressures available at 17 measuring locations.

The gradient of the phases of the sources along the ring perimeter is determined by the number of blades, according to Eq. (8.1). More general amplitude and phase relationships in the hull-pressure distribution can be modeled by adding rings (of the same size and position) with a phase distribution corresponding to a propeller with a blade number equal to an integer number of times the actual blade number. Thus, spatial (i.e., circumferential) harmonics of the ring source's phase distribution are introduced by replacing the blade number, Z, in Eq. (8.1) by nZ. These harmonics of order n are termed 'ring harmonics' in the remainder.

The results in terms of residuals are collected in Table 8.5. The best location in the axial direction is slightly forward of the propeller plane, and the ring radius found is 80% of the propeller radius. The results are not sensitive to the radius and the number of sources in the ring. It may be concluded that the hull-pressure field is represented quite well by a source model containing only one complex amplitude. Figure 8.6 shows the match between measured data (colored dots) and the hull-pressure field predicted by the monopole ring (first ring harmonic only).

Table 8.5: Measure of fit of monopole ring source models for non-cavitating hull-pressure amplitudes at orders of BPF for 2-bladed zero pitch propeller no. 6666.

Propeller No. 6666, Test 1				
Harmonic Order	1	2	3	4
Residual (1 ring harmonic)	8%	12%	17%	20%
Residual (4 ring harmonics)	7%	7%	10%	14%
Radius of Monopole Ring	0.8 R	0.8 R	0.8 R	0.8 R
Axial Shift from Prop. Plane	0.05 R	0.05 R	0.05 R	0.05 R
Number of Input Pressure Data for all Harmonic Orders			17	

For the unloaded 4- and 5-bladed propellers, the dipoles in the rings that represent the propellers are directed along the propeller blade sections' nose-tail line. For the cases in which these propellers are loaded, additional dipole rings are expected to be needed at right angles to the ones modeling thickness. Instead, two parallel, closely spaced monopole rings of equal radius are used. Only the first harmonic of BPF shows significant hull pressures. At the BPF, the optimum axial location and radius of the monopole ring pairs are found on the basis of the pressure transducers that show significant values. One monopole ring pair has been chosen, consisting of 72 monopoles, and at an axial spacing of 1 cm (at model scale). Several ring harmonics are added to improve the quality of the fit in the hull pressure distribution.

First order of BPF, amplitude range 0-400 Pa

Second order of BPF, amplitude range 0-300 Pa

Third order of BPF, amplitude range 0-150 Pa

Fourth order of BPF, amplitude range 0-70 Pa
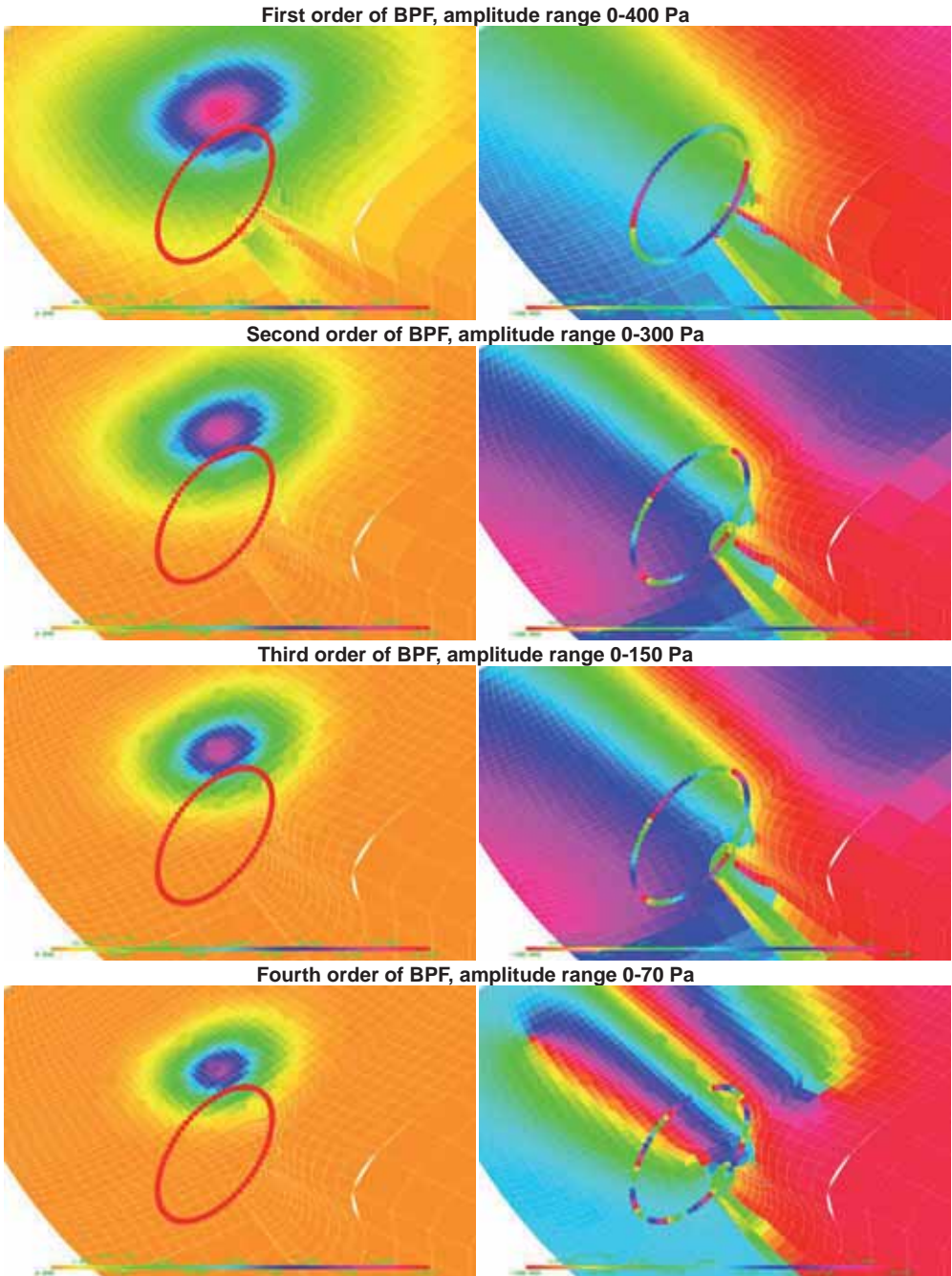
Figure 8.6: Measured hull-pressure amplitude in Pa (colored spheres, left: amplitude, from 0 to value mentioned, right: phase, from -180 to +180) at first to fourth order of BPF and pressure contour plot based on the best fitting monopole ring model for the 2-bladed propeller no. 6666.

The results in terms of residuals are collected in Table 8.6 for the 4-bladed propeller, no. 6458, and in Table 8.7 for the 5-bladed propeller, no. 6553. As before, the best location in axial direction is slightly forward of the propeller plane, and the ring radius found is in between 85% and 90% of the propeller radius. The hull-pressure field is represented reasonably well by a source model containing 3 to 4 ring harmonics.

It is concluded that the combination of the point source monopole and a few ring sources is sufficient to represent the cavitating propeller. The limited number of unknowns involved is such that application on ship trial measuring data, for which usually no more than half a dozen pressure transducers is available, is feasible.

Table 8.6: Measure of fit of monopole ring source models for non-cavitating hull-pressure amplitudes at first order of BPF for 4-bladed propeller no. 6458.

Propeller No. 6458	Test 1	Test 2
Residual	10%	19%
Radius of Monopole Ring Pair	0.84 R	0.84 R
Axial Shift from Propeller Plane	0.06 R	0.06 R
Number of Ring Harmonics	4	4
Number of Input Pressure Data	9	14

Table 8.7: Measure of fit of monopole ring source models for non-cavitating hull-pressure amplitudes at first order of BPF for 5-bladed propeller no. 6553.

Propeller No. 6553	Test 1	Test 2
Residual	8%	18%
Radius of Monopole Ring Pair	0.88 R	0.88 R
Axial Shift from Propeller Plane	0.055 R	0.055 R
Number of Ring Harmonics	3	4
Number of Input Pressure Data	8	19

9 CONCLUSIONS AND RECOMMENDATIONS

…in which conclusions are drawn from the results of the investigations performed within the framework of this thesis. Recommendations are given to direct future research efforts.

9.1 Summary

In this thesis, the cavitating propeller is studied as an important source of noise and vibration on board ships. Rotating propeller blades and pulsating cavities in their immediate vicinity cause pressure fluctuations in the surrounding water through which the hull plating above the propeller is excited. As this may affect the comfort of passengers, propeller designs may have to be modified which often results in a reduced propeller efficiency. To strike a balance between comfort and efficiency, the accurate prediction of propeller-induced hull-excitation forces is essential. Such predictions involve tests on scale models of ships as well as numerical simulations. Unfortunately, at present, predictions of propeller-induced hull-pressure forces do not give accurate results consistently.

This thesis is an account of an investigation into ways of improving the prediction procedures for vibratory hull excitation forces. In search of the major sources of prediction uncertainty the proceedings of the *International Towing Tank Conference* have been consulted. From knowledge thus obtained, together with experience built up in preceding projects, the following set of research topics has been selected:

- the influence of hull vibrations on measurements of hull-pressure fluctuations;
- the scale effect on the effective wake and its influence on sheet cavity dynamics;
- the development and validation of practical computational methods for the simulation of propeller-induced hull-pressure fluctuations; and,
- the development of a computational method for the determination of the strength of sources of propeller noise.

For the numerical simulation of propeller-induced hull-pressure forces two computational methods have been used, both based on the potential flow assumption and employing the *Boundary Element Method* for the discretization. One method is for the simulation of propeller flows, the other for predicting the acoustic scattering effect of the hull and free surface.

For the experimental simulation on model scale the *Depressurized Towing Tank* of the *Maritime Research Institute Netherlands* has been utilized. Model experiments have also

been used to provide validation data for the numerical methods. Test cases involving non-cavitating and cavitating propellers have been analyzed.

9.2 Conclusions

It is concluded that the hull-pressure fluctuations due to non-cavitating propellers is sufficiently accurately simulated by the numerical methods employed, specifically the harmonic amplitudes, while there exist some phase errors. The more important contribution in the hull-pressure fluctuations due to sheet cavitation is more significantly error-prone. In the test case that is treated, the hull-pressure amplitude at the first blade rate frequency is sufficiently accurately predicted. However, a series of simulations involving a gradual load reduction could not reproduce the decrease in first harmonic pressure amplitude that has been found in scale model experiments.

The tip vortex cavity and the interaction of the tip vortex with the sheet cavity collapse are not represented in the computational method, which makes its usefulness for the prediction of higher order hull pressures questionable. One should bear in mind that more elaborate methods that do model cavitating tip vortices are, at least at the time of writing, not suitable for day-to-day application, a requirement that has been imposed on the methods used in this thesis.

It has been shown how the scale model vibratory response to propeller excitation forces may cause a significant parasitic contribution to the measured hull-pressure field. In the present study, the disturbing influence of model vibrations on measured pressure fluctuations is counteracted by stiffening the model's afterbody, measuring the remaining afterbody accelerations, and using this information as input to a Boundary Element Method for acoustic radiation. Thus, the vibration-induced surface-pressure distribution is computed and subtracted from the measured hull pressures. Whenever the vibration modes are simple enough to be captured by a limited number of accelerometers this correction method has proven to be effective.

The issue of the scale effect on the ship's wake has been hypothesized to be the most important cause of inaccuracies in the prediction of hull excitation forces by means of experiments in model basins. It has been studied how the scale effect on the wake field, caused by failing to adhere to the full scale flow Reynolds number in model scale experiments, affects propeller loading, hence cavitation dynamics and eventually hull-pressure fluctuations. Only sheet cavitation has been considered.

In the present study a *Reynolds Averaged Navier-Stokes* method has been used to inversely design a scale model hull that generates a wake field much closer resembling the ship scale target wake field than do the geometrically similar hull models that are conventionally used. As a demonstration, a scale model hull of a container vessel has been designed, manufactured and tested. This test has proven that the pressure amplitude at the first order of blade rate frequency can indeed be accurately predicted.

Measured hull-pressure amplitudes are usually compared with maximum allowable values specified in contracts. For comparative purposes as well as to judge the accuracy of predictive hull-pressure data, it is advocated to convert these hull-pressure amplitudes into meaningful figures of merit regarding excitation forces and acoustic source characteristics. Integral hull forces and propeller source strengths have been used for this purpose. Ways of

modeling the propeller action including cavitation have been studied by means of acoustic point sources. The strengths of these sources are proposed as a basis for comparing predictions of hull vibratory excitation and reality.

To this end, the developed acoustic Boundary Element Method has been applied in an inverse way with measured hull-pressure data as input. This enables the distinction of the main source types contributing to the pressure field. The method is applied to a container vessel with a cavitating propeller showing only a weak non-cavitating hull-pressure field. Accurate results are obtained for the first and second blade rate pressure amplitudes - the only significant ones - using only one stationary monopole source to model the cavity dynamics. The method is also applied to three non-cavitating propellers. For these cases, the displacement and loading effect of the blades passing underneath the hull is reasonably accurately modeled by just a few monopole or dipole ring sources.

9.3 Recommendations

It may be argued that the demonstration experiments performed within the scope of this thesis are limited in the sense that they can provide qualitative insights only. Nevertheless, it is the author's opinion that the process of gathering such insights should continue until all major factors that are affecting the test results have been identified and investigated. It is only then that a more quantitative uncertainty analysis can be used to full effect. In the prediction of first order blade rate pressure fluctuations the state-of-art may be advanced enough to make it worthwhile to start performing such uncertainty analyses. However, for the higher orders of blade rate this is not the case and the study of the following issues needs to precede possibly expensive uncertainty analyses[23].

Pressure amplitudes at higher orders of the blade rate frequency are not accurately predicted either by the computational method or by the model experiments. Higher order amplitudes are strongly affected by the dynamics of the cavitating vortex, a feature that is lacking in the computational method used. It is recommended to direct future research towards the inclusion of effects of cavitating vortex dynamics on pressure pulses.

In model experiments, higher order amplitudes are overpredicted for the low gas content at which the experiments have been performed. Experiments performed at higher gas contents have initially shown results very close to full scale results for the first four orders of blade rate, but repeatability issues and lacking understanding of the underlying physical phenomena do not allow the drawing of any general conclusions. Future research should be aimed at delivering guidance on the gas content to be used for experimentally prediction realistic vortex cavity dynamics. Although issues related to the effects of water quality have been thoroughly investigated by model basins with a view to cavitation inception, they should also be investigated in relation to hull-pressure fluctuations.

Variability issues deserve more attention. While performing the investigations, it has been striking to observe the large variability in pressure pulses from one blade passage to the next in cases without any apparent inception problem. Differences in variability between

---

[23] Here it is referred to the number of experiments that have to be performed before an uncertainty analysis can be made.

model and ship scale experiments may strongly affect the pressure pulses, specifically the higher order ones.

Finally, given the sensitivity of cavity dynamics to the wake peak flow velocity, the accuracy of effective wake field computations at model and full scale for the purpose of designing non-geosim ship models should be investigated. This particular factor affects the hull-pressure amplitudes at the first blade rate frequency to such an extent that it has to be a main focus of any future uncertainty analysis.

A   KIRCHHOFF'S METHOD

…which recapitulates boundary integral equations for potential flows based on Green's identities. The integral equations serve as candidate methods for the determination of the scattered field and hull-surface pressures due to propeller sources of noise. Time and frequency domain formulations are presented.

A.1 Differential Equations for Potential Flows

In the derivations that follow, scalar quantities like the density, $\rho = \rho(\mathbf{x}, t)$, and vector quantities like the velocity, $\mathbf{v} = \mathbf{v}(\mathbf{x}, t)$, are assumed to be functions of time, t, and Cartesian position vectors, $\mathbf{x} = (x_1, x_2, x_3)^T = (x, y, z)^T$, relative to a Galilean frame of reference in $\mathbb{R}^3$. Vector quantities are written in boldface (e.g., $\mathbf{v}$) or index notation (e.g., v_i). Using this notation with Einstein's index summation convention, the differential equations are derived that describe potential flows supporting acoustic fields.

For the continuity equation, it can be written,

$$\frac{\partial \rho}{\partial t} + \nabla \cdot (\rho \mathbf{v}) = \frac{\partial \rho}{\partial t} + \frac{\partial}{\partial x_i}(\rho v_i) = Q_m \tag{A.1}$$

in which Q_m denotes the rate of mass injection per unit volume. With P_{ij} as the stress tensor, and f_i as an external volumetric force field, the momentum equation reads,

$$\rho \frac{Dv_i}{Dt} + \nabla \cdot P_{ij} = \frac{\partial}{\partial t}(\rho v_i) + \frac{\partial}{\partial x_j}(\rho v_i v_j + P_{ij}) = f_i \tag{A.2}$$

in which

$$P_{ij} = (p - p_0)\delta_{ij} - \tau_{ij} = p'\delta_{ij} - \tau_{ij} \tag{A.3}$$

Here, p denotes pressure, p_0 a reference pressure, p' the pressure disturbance defined as the deviation from the reference value, δ_{ij}, the *Kronecker delta function*, and τ_{ij}, the *shear stress tensor*. Alternatively, the momentum equation can be put into Lamb-Gromeka form,

$$\rho \frac{\partial \mathbf{v}}{\partial t} + \rho \nabla \left(\frac{\mathbf{v} \cdot \mathbf{v}}{2} \right) - \rho \mathbf{v} \times \boldsymbol{\omega} = -\nabla p + \rho \mathbf{f} + \nabla \cdot \tau_{ij} \tag{A.4}$$

with $\boldsymbol{\omega} = \nabla \times \mathbf{v}$ as the vorticity vector. In case of inviscid (i.e., $\tau_{ij} = \mathbf{0}$) and irrotational (i.e., $\boldsymbol{\omega} = \mathbf{0}$) flow, Eq. (A.4) simplifies to,

$$\rho \frac{\partial \mathbf{v}}{\partial t} + \rho \nabla \left(\frac{\mathbf{v} \cdot \mathbf{v}}{2} \right) = -\nabla p + \rho \mathbf{f} \tag{A.5}$$

Whenever flows may be considered irrotational, the velocity can be expressed as the gradient of a scalar velocity potential, $\nabla \varphi(\mathbf{x}, t) = \mathbf{v}(\mathbf{x}, t)$. If, furthermore, the flow is barotropic (i.e., $p = p(\rho)$) and subjected to a conservative volumetric force field (i.e., $\mathbf{f} = -\nabla F$), Eq. (A.5) becomes,

$$\nabla \left(\frac{\partial \varphi}{\partial t} + \tfrac{1}{2} |\mathbf{v}|^2 + \int_{p_0}^{p} \frac{dp}{\rho} + F \right) = \mathbf{0} \tag{A.6}$$

from which follows the *Bernoulli equation* for compressible unsteady potential flow,

$$\frac{\partial \varphi}{\partial t} + \tfrac{1}{2} |\mathbf{v}|^2 + \int_{p_0}^{p} \frac{dp}{\rho} + F = C(t) \tag{A.7}$$

in which $C(t)$ is an arbitrary function of time.

In a hydroacoustic context, the velocity potential is often split into a time-dependent disturbance potential, $\varphi'(\mathbf{x}, t)$, and a steady, 'background' potential, $\varphi_0(\mathbf{x})$, assuming the former is much smaller than the latter, and similarly for the pressure[24], $p(\mathbf{x}, t)$, density, $\rho(\mathbf{x}, t)$ and velocity,

$$\begin{aligned}
\varphi(\mathbf{x}, t) &= \varphi_0(\mathbf{x}) + \varphi'(\mathbf{x}, t) & \text{with} \quad |\varphi'| \ll |\varphi_0| \\
p(\mathbf{x}, t) &= p_0(\mathbf{x}) + p'(\mathbf{x}, t) & \text{with} \quad |p'| \ll |p_0| \\
\rho(\mathbf{x}, t) &= \rho_0 + \rho'(\mathbf{x}, t) & \text{with} \quad |\rho'| \ll |\rho_0| \\
\mathbf{v}(\mathbf{x}, t) &= \mathbf{v}_0(\mathbf{x}) + \mathbf{v}'(\mathbf{x}, t) & \text{with} \quad |\mathbf{v}'| \ll |\mathbf{v}_0|
\end{aligned} \tag{A.8}$$

The background flow is assumed incompressible, i.e., $\nabla \cdot \mathbf{v}_0 = 0$, and of constant density ρ_0.

When the quantities in Eq. (A.1) can be written in terms of a time-dependent, fluctuating part and a steady 'convected' flow, as in Eq. (A.8), then the continuity equation can be rewritten by neglecting products of small quantities and using that the convected flow is divergence free. In absence of mass sources,

---

[24] Note that the total pressure was already split into reference and disturbance pressures in Eq. (A.3). Note also that primes are used to denote quantities related to disturbances.

$$\frac{\partial \rho'}{\partial t} + \rho_0 \nabla \cdot \mathbf{v}' + \mathbf{v}_0 \cdot \nabla \rho' = 0 \tag{A.9}$$

In terms of the velocity disturbance potential, Eq. (A.9) becomes,

$$\left(\frac{\partial}{\partial t} + \mathbf{v}_0 \cdot \nabla \right) \rho' + \rho_0 \nabla^2 \varphi' = 0 \tag{A.10}$$

When no volumetric force field needs to be considered, the Bernoulli equation can be rewritten similarly to give,

$$p' = -\rho_0 \left(\frac{\partial}{\partial t} + \mathbf{v}_0 \cdot \nabla \right) \varphi' \tag{A.11}$$

The pressure and density disturbances are assumed to be related through the *speed of sound*, c , as,

$$p(\rho) \approx p(\rho_0) + (\rho - \rho_0) \frac{dp}{d\rho}(\rho_0) + h.o.t. \quad \overset{\text{linearization}}{\Rightarrow} \quad p' = c^2 \rho' \quad \wedge \quad c^2 = \frac{dp}{d\rho}(\rho_0) \tag{A.12}$$

This relation is valid for so-called *homentropic* flows (i.e., flows of constant and uniform entropy). Combining Eqs. (A.10), (A.11) and (A.12) yields the *convected wave equation*,

$$\frac{1}{c^2} \left(\frac{\partial}{\partial t} + \mathbf{v}_0 \cdot \nabla \right)^2 \varphi' - \nabla^2 \varphi' = 0 \tag{A.13}$$

After Eq. (A.13) is solved for the disturbance potential, φ', Eq. (A.11) is used to compute the pressure disturbance. Often, the mean flow is of constant speed in, say, the x_1 -direction, i.e.,

$$\mathbf{v}_0(\mathbf{x}) = v_1 \tag{A.14}$$

and Eq. (A.13) becomes,

$$\frac{1}{c^2} \left(\frac{\partial}{\partial t} + v_1 \frac{\partial}{\partial x_1} \right)^2 \varphi' - \nabla^2 \varphi' = 0 \tag{A.15}$$

In [Astley1986], Astley and Bain make use of a low Mach number approximation. When applied to the case of, $M = v_1 / c$, this approximation yields,

$$\frac{1}{c^2} \frac{\partial^2 \varphi'}{\partial t^2} - \nabla^2 \varphi' + 2 \frac{M}{c} \frac{\partial \varphi'}{\partial x_1 \partial t} = 0 \tag{A.16}$$

and is valid for small M . When the mean flow velocity is entirely neglected,

$$p' = -\rho_0 \frac{\partial \varphi'}{\partial t} \tag{A.17}$$

and the convected wave equation reduces to the *wave equation*,

$$\left(\frac{1}{c^2} \frac{\partial^2}{\partial t^2} - \nabla^2 \right) \varphi' = 0 \tag{A.18}$$

Finally, for incompressible flow, c approaches infinity, and φ' obeys the Laplace equation,

$$\nabla^2 \varphi' = 0 \tag{A.19}$$

If the assumption of incompressibility is made at the start of the derivation, the continuity equation, Eq. (A.1), can be rewritten to give the Laplace equation with the difference that the pressure is not necessarily given by Eq. (A.17), but by a version of Bernoulli's equation valid for incompressible flow.

In the frequency domain, with harmonic time dependence of the form $\exp(-i\omega t)$, ω the radian frequency and, i, the imaginary unit, defined by $i^2 = -1$, Eq. (A.11) becomes,

$$\hat{p}'(\mathbf{x}; k) = -\rho_0 c \left(-ik + \mathbf{M}_0 \cdot \nabla \right) \hat{\varphi}'(\mathbf{x}; k) \tag{A.20}$$

with carets indicating complex-valued amplitudes of frequency components of the pressure and velocity disturbance potential. Here, $k = \omega/c$ denotes the wave number. The convective flow *Mach number*, $\mathbf{M}_0$, is defined as $\mathbf{M}_0 = \mathbf{v}_0/c$. Analogously, the convected wave equation becomes the *convected Helmholtz equation*,

$$\nabla^2 \hat{\varphi}' + \left(k + i\mathbf{M}_0 \cdot \nabla \right)^2 \hat{\varphi}' = 0 \tag{A.21}$$

In case of uniform flow, v_1, in the positive x_1-direction,

$$\nabla^2 \hat{\varphi}' + k^2 \hat{\varphi}' + 2ikM \frac{\partial \hat{\varphi}'}{\partial x_1} - M^2 \frac{\partial^2 \hat{\varphi}'}{\partial x_1^2} = 0 \tag{A.22}$$

For low Mach numbers it follows,

$$\nabla^2 \hat{\varphi}' + k^2 \hat{\varphi}' + 2ikM \frac{\partial \hat{\varphi}'}{\partial x_1} = 0 \tag{A.23}$$

Without mean flow, Eqs. (A.20) and (A.21) simplify to,

$$\hat{p}' = i\omega \rho_0 \hat{\varphi}' = ik\rho_0 c\hat{\varphi}' \tag{A.24}$$

and to the *Helmholtz equation*,

$$\left(\nabla^2 + k^2\right)\hat{\varphi}' = 0 \tag{A.25}$$

respectively. Finally, if the fluid's compressibility is entirely neglected, the frequency formulation reduces to the *Laplace equation*,

$$\nabla^2 \hat{\varphi}' = 0 \tag{A.26}$$

at all frequencies, with the pressure obeying a Fourier transformed version of Bernoulli's equation for incompressible flows.

Figure A.2 presents an overview of the governing equations treated for the velocity potential. Figure A.1 gives a similar review for the pressure. Note that, although Eq. (A.13) is not generally valid for the pressure perturbation, the latter does fulfill Eqs. (A.15), (A.16), (A.18) and (A.19) as well as Eqs. (A.22), (A.23), (A.25) and (A.26), which may therefore be solved for directly in terms of pressure.

Time Domain		Frequency Domain
Convected Wave Equation		**Convected Helmholtz Equation**
$\dfrac{1}{c^2}\left(\dfrac{\partial}{\partial t} + v_1\dfrac{\partial}{\partial x_1}\right)^2 p' - \nabla^2 p' = 0$	Uniform Background Flow + Compressible Perturbation Potential Flow	$\nabla^2 \hat{p}' + k^2 \hat{p}' + 2ikM\dfrac{\partial \hat{p}'}{\partial x_1} - M^2 \dfrac{\partial^2 \hat{p}'}{\partial x_1^2} = 0$
$\dfrac{1}{c^2}\dfrac{\partial^2 p'}{\partial t^2} - \nabla^2 p' + 2\dfrac{M}{c}\dfrac{\partial p'}{\partial x_1 \partial t} = 0$	Uniform Low Mach number Background Flow + Compressible Perturbation Potential Flow	$\nabla^2 \hat{p}' + k^2 \hat{p}' + 2ikM\dfrac{\partial \hat{p}'}{\partial x_1} = 0$
Wave Equation		**Helmholtz Equation**
$\left(\dfrac{1}{c^2}\dfrac{\partial^2}{\partial t^2} - \nabla^2\right)p' = 0$	Zero Background Flow + Compressible Perturbation Potential Flow	$\left(\nabla^2 + k^2\right)\hat{p}' = 0$
Laplace Equation		**Laplace Equation**
$\nabla^2 p' = 0$	Background Flow + Incompressible (Perturbation) Potential Flow	$\nabla^2 \hat{p}' = 0$

Figure A.1: Overview of governing equations for the pressure perturbation.

Time Domain		Frequency Domain
Convected Wave Equation		**Convected Helmholtz Equation**
$$\frac{1}{c^2}\left(\frac{\partial}{\partial t}+\mathbf{v}_0\cdot\nabla\right)^2\varphi'-\nabla^2\varphi'=0$$ $$p'=-\rho_0\left(\frac{\partial}{\partial t}+\mathbf{v}_0\cdot\nabla\right)\varphi'$$	Background Flow + Compressible Perturbation Potential Flow	$$\nabla^2\hat{\varphi}'+\left(k+i\mathbf{M}_0\cdot\nabla\right)^2\hat{\varphi}'=0$$ $$\hat{p}'=-\rho_0 c\left(-ik+\mathbf{M}_0\cdot\nabla\right)\hat{\varphi}'$$
$$\frac{1}{c^2}\left(\frac{\partial}{\partial t}+v_1\frac{\partial}{\partial x_1}\right)^2\varphi'-\nabla^2\varphi'=0$$ $$p'=-\rho_0\left(\frac{\partial}{\partial t}+v_1\frac{\partial}{\partial x_1}\right)\varphi'$$	Uniform Background Flow + Compressible Perturbation Potential Flow	$$\nabla^2\hat{\varphi}'+k^2\hat{\varphi}'+2ikM\frac{\partial\hat{\varphi}'}{\partial x_1}-M^2\frac{\partial^2\hat{\varphi}'}{\partial x_1^2}=0$$ $$\hat{p}'=-\rho_0 c\left(-ik+M\frac{\partial}{\partial x_1}\right)\hat{\varphi}'$$
$$\frac{1}{c^2}\frac{\partial^2\varphi'}{\partial t^2}-\nabla^2\varphi'+2\frac{M}{c}\frac{\partial\varphi'}{\partial x_1\partial t}=0$$ $$p'=-\rho_0\left(\frac{\partial}{\partial t}+v_1\frac{\partial}{\partial x_1}\right)\varphi'$$	Uniform Low Mach number Background Flow + Compressible Perturbation Potential Flow	$$\nabla^2\hat{\varphi}'+k^2\hat{\varphi}'+2ikM\frac{\partial\hat{\varphi}'}{\partial x_1}=0$$ $$\hat{p}'=-\rho_0 c\left(-ik+M\frac{\partial}{\partial x_1}\right)\hat{\varphi}'$$
Wave Equation		**Helmholtz Equation**
$$\left(\frac{1}{c^2}\frac{\partial^2}{\partial t^2}-\nabla^2\right)\varphi'=0$$ $$p'=-\rho_0\frac{\partial\varphi'}{\partial t}$$	Zero Background Flow + Compressible Perturbation Potential Flow	$$\left(\nabla^2+k^2\right)\hat{\varphi}'=0$$ $$\hat{p}'=ik\rho_0 c\hat{\varphi}'$$
Laplace Equation		**Laplace Equation**
$$\nabla^2\varphi'=0$$ $$p'=-\rho_0\left(\frac{\partial}{\partial t}+\mathbf{v}_0\cdot\nabla\right)\varphi'$$	Background Flow + Incompressible (Perturbation) Potential Flow	$$\nabla^2\hat{\varphi}'=0$$ $$\hat{p}'=-\rho_0 c\left(-ik+\mathbf{M}_0\cdot\nabla\right)\hat{\varphi}'$$
$$\nabla^2\varphi'=0$$ $$p'=-\rho_0\frac{\partial\varphi'}{\partial t}$$	Zero Background Flow + Incompressible (Perturbation) Potential Flow	$$\nabla^2\hat{\varphi}'=0$$ $$\hat{p}'=ik\rho_0 c\hat{\varphi}'$$

Figure A.2: Overview of governing equations for the velocity perturbation potential.

So far, the governing equations for the velocity disturbance potential and pressure perturbation have been derived without considering the sources that are the reason for their existence. As the right hand sides of the equations are zero, the sources must either be distributed over the boundaries and appear through boundary conditions, or occupy a certain space in the interior of the fluid domain, which then has to be excluded from the equation's domain of validity. An elegant alternative approach is to use so-called *generalized functions*, which allow the extension of the domain of the field equations to the *whole* $\mathbb{R}^3$ domain. In the next section, using generalized functions and introducing the concept of the Green's function, the governing equations are solved for distributions of point sources in three-dimensional unbounded space. For flow domains including boundaries, boundary integral equations based on Green's identities are presented in Section A.3.

A.2 Green's Functions

In case of a volume distribution of point sources inside the domain, the solution of the field equations, derived in Section A.1, is elegantly written in terms of Green's functions. In the following section, Green's functions are presented for the operators appearing in Section A.1. Both time and frequency domain alternatives are given.

A.2.1 Time-independent problems

Suppose L is a linear, self-adjoint, time-independent, differential operator, then there may exist a solution, $G(\mathbf{x}, \mathbf{y})$, called the *Green's function*, of the equation,

$$L\{G(\mathbf{x}, \mathbf{y})\} = \delta(\mathbf{x} - \mathbf{y}) = \delta(\mathbf{r}) \tag{A.27}$$

where δ denotes Dirac's delta function, defined in Appendix G.1 and position vectors, $\mathbf{x}$, $\mathbf{y}$ and $\mathbf{r} = \mathbf{x} - \mathbf{y}$, within an *unbounded* domain, V, in $\mathbb{R}^3$. In that case, the solution of,

$$L\{\varphi(\mathbf{x})\} = q(\mathbf{x}) \tag{A.28}$$

with $q(\mathbf{x})$ as the driving *source distribution* in V, becomes,

$$\varphi(\mathbf{x}) = \int_{\mathbb{R}^3} q(\mathbf{y}) G(\mathbf{x}, \mathbf{y}) \, dV_{\mathbf{y}} \tag{A.29}$$

with the subscript, $\mathbf{y}$, indicating that the volume integration is to be performed in terms of the $\mathbf{y}$-coordinates. In Eq. (A.29), $\varphi(\mathbf{x})$ may be interpreted as the potential at $\mathbf{x}$ induced by the field source distribution, $q(\mathbf{x})$. For *bounded* domains this result can be extended to incorporate certain boundary conditions. This is achieved in the next section through the Green's identities recapitulated in Appendix G.3.

The *Laplace operator* is defined as, $L \equiv \nabla \cdot \nabla \equiv \nabla^2$. Its Green's function, $G_L(\mathbf{x}, \mathbf{y})$, for an unbounded domain, is the solution of Eq. (A.27),

$$G_L(\mathbf{x}, \mathbf{y}) = -\frac{1}{4\pi |\mathbf{x} - \mathbf{y}|} = \frac{-1}{4\pi r} \tag{A.30}$$

with r the magnitude of $\mathbf{r}$. The Green's function, $G_L(\mathbf{x}, \mathbf{y})$, may be interpreted as the potential at $\mathbf{x}$ induced by a point source of unit strength at $\mathbf{y}$. Time can only enter Laplace problems through time-dependent boundary conditions. As a result, flows obeying Laplace's equation do not show memory effects. A disturbance exercises its influence instantaneously throughout the whole domain.

The inhomogeneous form of the Laplace equation reads,

$$\nabla^2 \varphi(\mathbf{x}) = q(\mathbf{x}) \tag{A.31}$$

The solution, cast in the form of Eq. (A.29), then becomes,

$$\varphi(\mathbf{x}) = -\int_{\mathbb{R}^3} \frac{q(\mathbf{y})}{4\pi r} dV_{\mathbf{y}} \tag{A.32}$$

The *Helmholtz operator* is defined as,

$$L \equiv \nabla^2 + k^2 \tag{A.33}$$

Its Green's function, $G_H(\mathbf{x}, \mathbf{y}; k)$, for an unbounded in domain, is written as,

$$G_H(\mathbf{x}, \mathbf{y}; k) = -\frac{\exp(ik|\mathbf{x} - \mathbf{y}|)}{4\pi |\mathbf{x} - \mathbf{y}|} = -\frac{\exp(ikr)}{4\pi r} \tag{A.34}$$

The inhomogeneous form of the Helmholtz equation reads,

$$\left(\nabla^2 + k^2\right)\hat{\varphi}(\mathbf{x}; k) = \hat{q}(\mathbf{x}; k) \tag{A.35}$$

with solution,

$$\hat{\varphi}(\mathbf{x}; k) = -\int_{\mathbb{R}^3} \hat{q}(\mathbf{y}; k) \frac{\exp(ikr)}{4\pi r} dV_{\mathbf{y}} \tag{A.36}$$

In Eqs. (A.35) and (A.36) the caret symbol is used to denote a complex-valued frequency component. The solution in the time domain is retrieved as,

$$\varphi(\mathbf{x}, t) = \text{Re}\left\{\sum_k \left(\hat{\varphi}(\mathbf{x}; k)\exp(-i\omega t)\right)\right\} \tag{A.37}$$

Eq. (A.37) is valid whenever the time domain solution can be expressed in terms of discrete frequency domain components as in the periodic type of events occurring in each propeller revolution.

For cases where the mean flow cannot be neglected, the *convected Helmholtz operator* is defined as,

$$L \equiv \nabla^2 + \left(k + i\mathbf{M} \cdot \nabla \right)^2 \tag{A.38}$$

with $\mathbf{M} = \mathbf{v}/c$. Because this operator is not self-adjoint, its Green's function is based on the adjoint operator (i.e., the complex conjugate of Eq. (A.38)). Using, $\beta^2 = 1 - \mathbf{M} \cdot \mathbf{M}$, the Green's function, $G_{CH}(\mathbf{x}, \mathbf{y}; k)$, for unbounded domains, reads [Francescantonio1999, Wu1994, Zhang1997],

$$G_{CH}(\mathbf{x}, \mathbf{y}; k) = -\frac{\exp\left(ik\beta^{-2} \left\{ \mathbf{r} \cdot \mathbf{M} + \sqrt{\left(\mathbf{r} \cdot \mathbf{M} \right)^2 + \beta^2 r^2} \right\} \right)}{4\pi\sqrt{\left(\mathbf{r} \cdot \mathbf{M} \right)^2 + \beta^2 r^2}} \tag{A.39}$$

If the flow is in the direction of the first coordinate, then, $\mathbf{M} = (v_1/c, 0, 0) = (M, 0, 0)$, and $\beta^2 = 1 - M^2$, hence,

$$G_{CH}(\mathbf{x}, \mathbf{y}; k) = -\frac{\exp\left(ik\beta^{-2} \left\{ M \left(x_1 - y_1 \right) + r_\beta \right\} \right)}{4\pi r_\beta} = -\frac{\exp\left(i\omega\theta \right)}{4\pi r_\beta} \tag{A.40}$$

with

$$\theta(\mathbf{x}, \mathbf{y}; k) = \frac{M \left(x_1 - y_1 \right) + r_\beta}{\beta^2 c} \tag{A.41}$$

and

$$r_\beta(\mathbf{x}, \mathbf{y}; k) = \sqrt{M^2 \left(x_1 - y_1 \right)^2 + \beta^2 r^2} \tag{A.42}$$

As Eq. (A.40) was derived from the adjoint operator, physically it can be interpreted as the potential due to a unit point source in a uniform flow directed in the *negative* x_1-direction, although the physical flow is indeed in the positive x_1-direction [Zhang1997]. Therefore, the inhomogeneous form of the convected Helmholtz equation for the potential, $\hat{\varphi}$,

$$\left(\nabla^2 + \left(k + iM \frac{\partial}{\partial x_1} \right)^2 \right) \hat{\varphi}(\mathbf{x}; k) = \hat{q}(\mathbf{x}; k) \tag{A.43}$$

has a solution,

$$\hat{\varphi}(\mathbf{x}; k) = -\int_{\mathbb{R}^3} \hat{q}(\mathbf{y}; k) \frac{\exp\left(i\omega\theta \right)}{4\pi r_\beta} dV_{\mathbf{y}} \tag{A.44}$$

In this context, it is interesting to note the possible application of a *Prandtl-Glauert transformation* [Rienstra2008]. Define $X = x_1/\beta$ and $T = \beta t + (M/c) X$ with $\Omega = \omega/\beta$ and $K = k/\beta$, and the Helmholtz equation for a modified potential, ψ, is retrieved,

$$\frac{\partial^2 \psi}{\partial X^2} + \frac{\partial^2 \psi}{\partial x_2^2} + \frac{\partial^2 \psi}{\partial x_3^2} + K^2 \psi = 0 \tag{A.45}$$

with

$$\hat{\varphi}(x_1, x_2, x_3) \exp(-i\omega t) = \psi(X, x_2, x_3) \exp(-i\Omega T) \tag{A.46}$$

However, the use of this transform is inconvenient whenever boundary conditions become unwieldy in a system of reference moving with the flow.

A.2.2 Time-dependent problems

When L is time-dependent, Eqs. (A.27) and (A.28) become,

$$L\{G(\mathbf{x}, \mathbf{y}, t, \tau)\} = \delta(t - \tau)\delta(\mathbf{x} - \mathbf{y}) \tag{A.47}$$

and

$$L\{\varphi(\mathbf{x}, t)\} = q(\mathbf{x}, t) \tag{A.48}$$

with solution

$$\varphi(\mathbf{x}) = \int_{\mathbb{R}^3} \int_{-\infty}^{+\infty} q(\mathbf{y}, \tau) G(\mathbf{x}, \mathbf{y}, t, \tau) \, d\tau \, dV_{\mathbf{y}} \tag{A.49}$$

The *d'Alembert* or *wave operator* is defined as,

$$L \equiv \frac{1}{c^2} \frac{\partial^2}{\partial t^2} - \nabla^2 \tag{A.50}$$

When the problem is time-independent or the speed of sound becomes infinite, the Laplace operator is retrieved. As opposed to the latter case, cause and effect relations may no longer be regarded as immediate, and the Green's function, $G_W(\mathbf{x}, \mathbf{y}, t, \tau)$, i.e., the solution of Eq. (A.47) in an unbounded domain, now contains the *retarded time*, τ, discussed in Appendix G.2,

$$G_W(\mathbf{x}, \mathbf{y}, t, \tau) = -\frac{\delta(t - \tau - |\mathbf{x} - \mathbf{y}|/c)}{4\pi |\mathbf{x} - \mathbf{y}|} = -\frac{\delta(t - r/c - \tau)}{4\pi r} \tag{A.51}$$

The inhomogeneous form of the wave equation (also known as *Poisson's equation*) reads,

$$\frac{1}{c^2} \frac{\partial^2 \varphi}{\partial t^2}(\mathbf{x}, t) - \nabla^2 \varphi(\mathbf{x}, t) = q(\mathbf{x}, t) \tag{A.52}$$

The solution is an integral of the source distribution,

$$\varphi(\mathbf{x}, t) = -\int_{\mathbb{R}^3} \int_{-\infty}^{+\infty} q(\mathbf{y}, \tau) \frac{\delta(t - |\mathbf{x} - \mathbf{y}|/c - \tau)}{4\pi |\mathbf{x} - \mathbf{y}|} d\tau dV_{\mathbf{y}} = -\int_{\mathbb{R}^3} \frac{q(\mathbf{y}, t - r/c)}{4\pi r} dV_{\mathbf{y}} \qquad (A.53)$$

Time Domain		Frequency Domain
Convected Wave Equation		**Convected Helmholtz Equation**
$G_{CW} = -\dfrac{\delta(t - \tau + \theta)}{4\pi r_{\beta}}$	Uniform Background Flow + Compressible Perturbation Potential Flow	$G_{CH} = -\dfrac{\exp(i\omega\theta)}{4\pi r_{\beta}}$
Wave Equation		**Helmholtz Equation**
$G_W = -\dfrac{\delta(t - \tau - r/c)}{4\pi r}$	Zero Background Flow + Compressible Perturbation Potential Flow	$G_H = -\dfrac{\exp(ikr)}{4\pi r}$
Laplace Equation		**Laplace Equation**
$G_L = -\dfrac{\delta(t - \tau)}{4\pi r}$	Background Flow + Incompressible (Perturbation) Potential Flow	$G_L = \dfrac{-1}{4\pi r}$

Figure A.3: Overview of Green's functions

The *convected wave operator* is defined as,

$$L \equiv \frac{1}{c^2} \left(\frac{\partial}{\partial t} + \mathbf{v}_0 \cdot \nabla \right)^2 - \nabla^2 \qquad (A.54)$$

for steady convective velocity, $\mathbf{v}_0$. The Green's function, $G_{CW}(\mathbf{x}, \mathbf{y}, t, \tau)$, for an unbounded domain, is then,

$$G_{CW}(\mathbf{x}, \mathbf{y}, t, \tau) = -\frac{\delta(t - \tau + \theta(\mathbf{x}, \mathbf{y}))}{4\pi r_{\beta}(\mathbf{x}, \mathbf{y})} \qquad (A.55)$$

If $\mathbf{v}_0$ points in the direction of the first coordinate, θ and r_{β} are given by Eqs. (A.41) and (A.42). For the inhomogeneous form of the wave equation, it is written,

$$\frac{1}{c^2}\left(\frac{\partial}{\partial t} + v_1 \frac{\partial}{\partial x_1}\right)^2 \varphi - \nabla^2 \varphi = q(\mathbf{x}, t) \tag{A.56}$$

As before, the solution is written as an integral of the source distribution in $\mathbb{R}^3$,

$$\varphi(\mathbf{x}, t) = -\int_{\mathbb{R}^3} \int_{-\infty}^{+\infty} q(\mathbf{y}, \tau) \frac{\delta(t + \theta - \tau)}{4\pi r_\beta} \, d\tau dV_\mathbf{y} = -\int_{\mathbb{R}^3} \frac{q(\mathbf{y}, t + \theta)}{4\pi r_\beta} \, dV_\mathbf{y} \tag{A.57}$$

Figure A.3 presents an overview of the Green's functions treated here.

By applying a transformation equivalent to the Prandtl-Glauert transformation, the wave operator, Eq. (A.50), may be derived and $\varphi(x_1, x_2, x_3, t) = \psi(X, x_2, x_3, T)$ satisfies,

$$\frac{\partial^2 \psi}{\partial X^2} + \frac{\partial^2 \psi}{\partial x_2^2} + \frac{\partial^2 \psi}{\partial x_3^2} - \frac{1}{c^2} \frac{\partial^2 \psi}{\partial T^2} = 0 \tag{A.58}$$

after which the pressure follows from,

$$p(X, T) = -\frac{\rho}{\beta}\left(\frac{\partial}{\partial T} + v_1 \frac{\partial}{\partial X}\right)\psi \tag{A.59}$$

A.3 Boundary Integral Formulations

Now, the Green's identities, introduced in Appendix G.3, are used to derive boundary integral formulations for potential flows. Thus, the introduction of boundaries is facilitated. As before, both time and frequency domain alternatives are presented.

A.3.1 Time-independent integral equations

Inserting $\psi = G_L$ and $\varphi = \varphi'$ into Green's second identity, Eq. (G.13), gives,[25]

$$\int_V \varphi' \nabla^2 G_L - G_L \nabla^2 \varphi' \, dV = \int_S \varphi' \frac{\partial G_L}{\partial n} - G_L \frac{\partial \varphi'}{\partial n} \, dS \tag{A.60}$$

with the normal vector on S pointing *out of* V. When φ' satisfies the Laplace equation, Eq. (A.60) reduces to,

$$\int_S \varphi'(\mathbf{y}) \frac{\partial G_L}{\partial n_\mathbf{y}}(\mathbf{x}, \mathbf{y}) - G_L(\mathbf{x}, \mathbf{y}) \frac{\partial \varphi'}{\partial n_\mathbf{y}}(\mathbf{y}) dS_\mathbf{y} = c(\mathbf{x})\varphi'(\mathbf{x}) \tag{A.61}$$

---

[25] Here, ψ should not be confused with the one used in Eq. (A.58).

with $c(\mathbf{x})$ defined according to Eq. (G.15). For $q = q(\mathbf{x})$, φ' satisfies Eq. (G.14) and Eq. (A.61) becomes,

$$\int_S \varphi'(\mathbf{y})\frac{\partial G_L}{\partial n_{\mathbf{y}}} - G_L \frac{\partial \varphi'}{\partial n_{\mathbf{y}}} \, dS_{\mathbf{y}} + \int_V q(\mathbf{y})G_L \, dV_{\mathbf{y}} = c(\mathbf{x})\varphi'(\mathbf{x}) \tag{A.62}$$

In the frequency domain Eq. (A.62) is also valid for $\hat{\varphi}'$. After introducing compressibility effects by using $\psi = G_H$ and $q \equiv 0$, Eq. (G.13) becomes,

$$\int_S \hat{\varphi}'(\mathbf{y})\frac{\partial G_H}{\partial n_{\mathbf{y}}} - G_H \frac{\partial \hat{\varphi}'}{\partial n_{\mathbf{y}}} \, dS_{\mathbf{y}} = c(\mathbf{x})\hat{\varphi}'(\mathbf{x}) \tag{A.63}$$

When the normal derivative on the boundary is given as a normal velocity distribution, $\hat{v}'_n = \hat{\mathbf{v}}' \cdot \mathbf{n}$, the so-called *Kirchhoff-Helmholtz integral equation* is obtained,

$$\int_S \frac{\exp(ikr)}{4\pi r} v'_n - \hat{\varphi}'(\mathbf{y})\frac{\partial}{\partial n_{\mathbf{y}}}\left(\frac{\exp(ikr)}{4\pi r}\right) dS_{\mathbf{y}} = c(\mathbf{x})\hat{\varphi}'(\mathbf{x}) \tag{A.64}$$

For rigid body scattering problems the velocity term on the left vanishes and is replaced by an expression for the incident wave field.

In case of a uniform flow in the x_1-direction, Wu and Lee [Wu1994] derive an integral expression for the convected Helmholtz equation using a weighted residual method and a Green's function derived from the adjoint operator. The result reads [Zhang1997],

$$\left(1 - C^0(\mathbf{x})\right)\hat{\varphi}'(\mathbf{x}) = \int_S \left(\hat{v}'_n + 2ikM\hat{\varphi}'n_1 - M^2 \frac{\partial \hat{\varphi}'}{\partial x_1}n_1\right)G_{CH}dS_{\mathbf{y}} +$$

$$-\int_S \left(\frac{\partial G_{CH}}{\partial n_{\mathbf{y}}} - M^2 \frac{\partial G_{CH}}{\partial x_1}n_1\right)\hat{\varphi}'dS_{\mathbf{y}} \tag{A.65}$$

with

$$C^0(\mathbf{x}) = \int_S \left(\frac{\partial G_{CH0}}{\partial x_1} - M^2 \frac{\partial G_{CH0}}{\partial x_1}n_1\right)dS_{\mathbf{y}} \tag{A.66}$$

and $G_{CH0}(\mathbf{x},\mathbf{y}) = -1/(4\pi r_\beta)$ as the zero wave number variant of $G_{CH}(\mathbf{x},\mathbf{y})$.

A.3.2 Time-dependent integral equations

Inserting $\psi = G_W$ and $\varphi = \varphi'$ into Green's second identity (see Appendix G, Eq. (G.13)), gives,

$$\int_V \varphi' \nabla^2 G_W - G_W \nabla^2 \varphi' \, dV = \int_S \varphi' \frac{\partial G_W}{\partial n} - G_W \frac{\partial \varphi'}{\partial n} \, dS \tag{A.67}$$

When φ' satisfies the homogeneous wave equation, Eq. (A.67) reduces to,

$$\int_S \varphi'(\mathbf{y}) \frac{\partial G_W}{\partial n_{\mathbf{y}}}(\mathbf{x}, \mathbf{y}) - G_W(\mathbf{x}, \mathbf{y}) \frac{\partial \varphi'}{\partial n_{\mathbf{y}}}(\mathbf{y}) dS_{\mathbf{y}} = c(\mathbf{x})\varphi'(\mathbf{x}) \tag{A.68}$$

For $q = q(\mathbf{x})$, φ' satisfies Eq. (A.52) and Eq. (G.13) becomes,

$$\int_S \varphi'(\mathbf{y}) \frac{\partial G_W}{\partial n_{\mathbf{y}}} - G_W \frac{\partial \varphi'}{\partial n_{\mathbf{y}}} dS_{\mathbf{y}} + \int_V q(\mathbf{y}) G_W \, dV_{\mathbf{y}} = c(\mathbf{x})\varphi'(\mathbf{x}) \tag{A.69}$$

or, with $q \equiv 0$,

$$\int_S \frac{\delta(t - \tau - r/c)}{4\pi r} v'_n - \varphi'(\mathbf{y}) \frac{\partial}{\partial n_{\mathbf{y}}} \left(\frac{\delta(t - \tau - r/c)}{4\pi r} \right) dS_{\mathbf{y}} = c(\mathbf{x})\varphi'(\mathbf{x}) \tag{A.70}$$

If this expression is worked out, or, alternatively, if Eq. (A.64) is inverse Fourier transformed, the *Kirchhoff integral equation* is obtained,

$$\frac{1}{4\pi} \int_S \left[\frac{v'_n}{r} + \left(\frac{\varphi'}{r^2} + \frac{\dot{\varphi}'}{cr} \right) \frac{\partial r}{\partial n_{\mathbf{y}}} \right]_{t - \frac{r}{c}} dS_{\mathbf{y}} = c(\mathbf{x})\varphi'(\mathbf{x}) \tag{A.71}$$

with the brackets indicating that the integrand is to be evaluated at the retarded time, $\tau = t - r/c$ (see Appendix G.2). When Eq. (A.71) has been solved, the disturbance pressure is determined by $p' = -\rho_0 \dot{\varphi}'$. Combining this with the time derivative of Eq. (A.71) yields an integral expression for the acoustic pressure disturbance, valid for stationary surfaces, S,

$$\frac{1}{4\pi} \int_S \left[-\frac{\rho_0 \dot{v}'_n}{r} + \left(\frac{p'}{r^2} + \frac{\dot{p}'}{cr} \right) \frac{\partial r}{\partial n_{\mathbf{y}}} \right]_{t - \frac{r}{c}} dS_{\mathbf{y}} = c(\mathbf{x}) p'(\mathbf{x}, t) \tag{A.72}$$

The Kirchhoff integral equation is often used to determine the acoustic properties in a medium outside a certain source region in which CFD is used to solve the more elaborate equations that apply there. Interference effects are conserved in the compressible medium outside the source region. There, the fluid is assumed to be at rest, save for small (acoustic) disturbances. However, when a flow does exist one is forced to do either one of two things; the basic equations have to be modified to take into account the main stream, or a moving system of reference may be introduced in which the wave equation is still valid (e.g., the Prandtl-Glauert transform). The transformation of the solution to the fixed coordinate system then solves the problem.

For the first option, [Morino2003] gives the appropriate boundary integral equation. For non-lifting bodies it becomes,

$$\int_S \left[\bar{G}\frac{\partial \varphi'}{\partial \bar{n}_y} - \varphi'\frac{\partial \bar{G}}{\partial \bar{n}_y} + \dot{\varphi}'\bar{G}\frac{\partial \tilde{\theta}}{\partial \bar{n}_y} \right]^{\tilde{\theta}} d\bar{S}_y + \int_V \left[\bar{G}q \right]^{\tilde{\theta}} d\bar{V}_y = c(\breve{\mathbf{x}})\varphi'(\breve{\mathbf{x}},t) \tag{A.73}$$

with $\breve{x}_1 = x_1/\beta$, $\breve{x}_2 = x_2$, $\breve{x}_3 = x_3$ and $\bar{G}(\breve{\mathbf{x}},\breve{\mathbf{y}}) = -1/4\pi\breve{r} = -1/4\pi|\breve{\mathbf{x}} - \breve{\mathbf{y}}|$. Superscript $\tilde{\theta}$ is equivalent to subscript $\tau = t - \tilde{\theta}$, in which $\hat{\theta} = \left(M(\breve{y}_1 - \breve{x}_1) + \breve{r}\right)/\beta c$ and $\bar{\theta} = \left(M(\breve{x}_1 - \breve{y}_1) + \breve{r}\right)/\beta c$.

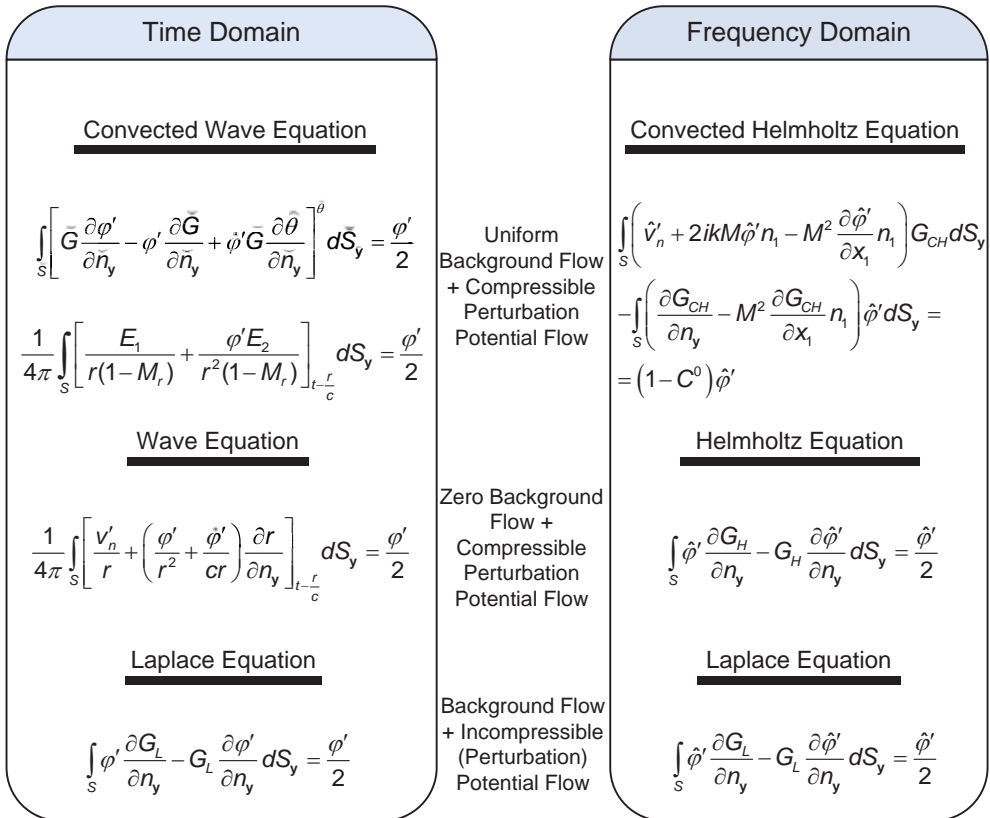| Time Domain		Frequency Domain
Convected Wave Equation	Uniform Background Flow + Compressible Perturbation Potential Flow	**Convected Helmholtz Equation**
$\int_S \left[\bar{G}\frac{\partial \varphi'}{\partial \bar{n}_y} - \varphi'\frac{\partial \bar{G}}{\partial \bar{n}_y} + \dot{\varphi}'\bar{G}\frac{\partial \tilde{\theta}}{\partial \bar{n}_y} \right]^{\tilde{\theta}} d\bar{S}_y = \frac{\varphi'}{2}$ $\frac{1}{4\pi}\int_S \left[\frac{E_1}{r(1-M_r)} + \frac{\varphi'E_2}{r^2(1-M_r)} \right]_{t-\frac{r}{c}} dS_y = \frac{\varphi'}{2}$		$\int_S \left(\hat{v}'_n + 2ikM\hat{\varphi}'n_1 - M^2\frac{\partial\hat{\varphi}'}{\partial x_1}n_1 \right)G_{CH}dS_y$ $-\int_S \left(\frac{\partial G_{CH}}{\partial n_y} - M^2\frac{\partial G_{CH}}{\partial x_1}n_1 \right)\hat{\varphi}'dS_y =$ $= \left(1 - C^0\right)\hat{\varphi}'$
Wave Equation	Zero Background Flow + Compressible Perturbation Potential Flow	**Helmholtz Equation**
$\frac{1}{4\pi}\int_S \left[\frac{v'_n}{r} + \left(\frac{\varphi'}{r^2} + \frac{\dot{\varphi}'}{cr} \right)\frac{\partial r}{\partial n_y} \right]_{t-\frac{r}{c}} dS_y = \frac{\varphi'}{2}$		$\int_S \hat{\varphi}'\frac{\partial G_H}{\partial n_y} - G_H\frac{\partial\hat{\varphi}'}{\partial n_y} dS_y = \frac{\hat{\varphi}'}{2}$
Laplace Equation	Background Flow + Incompressible (Perturbation) Potential Flow	**Laplace Equation**
$\int_S \varphi'\frac{\partial G_L}{\partial n_y} - G_L\frac{\partial\varphi'}{\partial n_y} dS_y = \frac{\varphi'}{2}$		$\int_S \hat{\varphi}'\frac{\partial G_L}{\partial n_y} - G_L\frac{\partial\hat{\varphi}'}{\partial n_y} dS_y = \frac{\hat{\varphi}'}{2}$

Figure A.4: Overview of integral equations for the velocity disturbance potential.

For *moving* surfaces, Farassat and Myers derive an integral expression [Farassat1988] of which the restriction to rigid surfaces leads to,

$$\frac{1}{4\pi} \int_S \left[\frac{E_1}{r(1-M_r)} + \frac{\varphi' E_2}{r^2(1-M_r)} \right]_{t-\frac{r}{c}} dS_y = c(\mathbf{x})\varphi'(\mathbf{x}, t) \tag{A.74}$$

with

$$
\begin{aligned}
E_1 &= (M_n^2 - 1)\varphi_n + M_n \dot{\mathbf{M}}_t \cdot \nabla_2 \varphi - \frac{M_n \dot{\varphi}}{c} + \\
&+ \frac{(\dot{n}_r - \dot{M}_n - \dot{n}_M)\varphi + (\cos\theta - M_n)\dot{\varphi}}{c(1-M_r)} + \frac{\dot{M}_r(\cos\theta - M_n)\varphi}{c(1-M_r)^2}
\end{aligned}
\tag{A.75}
$$

and

$$E_2 = \cos\theta + \frac{2M_r\cos\theta - M_n M_r - M_n}{1-M_r} + \frac{(\cos\theta - M_n)(M_r^2 - M^2)}{(1-M_r)^2} \tag{A.76}$$

Here, the variables used are defined as follows: $M_n = v_n/c$; $M_r = \mathbf{v} \cdot \mathbf{r}/cr$; θ is the angle between the outward normal, $\mathbf{n}$, and $\mathbf{r}/r$; $\mathbf{r}/r$; $\dot{M}_n = \dot{\mathbf{M}} \cdot \mathbf{n}$; $\dot{M}_r = (\dot{\mathbf{M}} \cdot \mathbf{r})/r$; $\dot{n}_M = \dot{\mathbf{n}} \cdot \mathbf{M}$; $\dot{n}_r = \dot{\mathbf{n}} \cdot \mathbf{r}/r$; and $\mathbf{M}_t$ is the tangential component of the Mach number. Finally, ∇_2 denotes the surface gradient operator.

An overview of the integral equations presented here is given in Figure A.4.

B   FFOWCS WILLIAMS-HAWKINGS' METHOD

…which presents a derivation of the Ffowcs Williams-Hawkings equation as well
as several related formulations that may serve as methods for the determination
of field and hull-surface pressures due to propeller sources of noise.

B.1 Lighthill's Acoustic Analogy

A general mathematical description of flow noise, not making any simplifications at the outset, is known as *Lighthill's acoustic analogy* [Lighthill1952/1954]. Its derivation starts with the continuity equation, Eq. (A.1), restated here for convenience[26],

$$\frac{\partial \rho}{\partial t} + \nabla \cdot (\rho \mathbf{v}) = \frac{\partial \rho}{\partial t} + \frac{\partial}{\partial x_i}(\rho v_i) = Q_m \qquad \text{(B.1)}$$

The momentum equation, Eq. (A.2), is written as,

$$\rho \frac{D v_i}{D t} + \nabla \cdot P_{ij} = \frac{\partial}{\partial t}(\rho v_i) + \frac{\partial}{\partial x_j}(\rho v_i v_j + P_{ij}) = f_i \qquad \text{(B.2)}$$

Now, by taking the time derivative of Eq. (B.1) and the divergence of Eq. (B.2), it follows,

$$\frac{\partial^2 \rho}{\partial t^2} + \frac{\partial^2}{\partial x_i \partial t}(\rho v_i) = \frac{\partial Q_m}{\partial t} \qquad \text{(B.3)}$$

and

$$\frac{\partial^2}{\partial x_i \partial t}(\rho v_i) + \frac{\partial^2}{\partial x_i \partial x_j}(\rho v_i v_j + P_{ij}) = \frac{\partial f_i}{\partial x_i} \qquad \text{(B.4)}$$

Subtracting Eq. (B.4) from Eq. (B.3), and defining a density disturbance, $\rho' = \rho - \rho_0$, in analogy with the perturbation pressure (cf. (A.3)), gives,

$$\frac{\partial^2 \rho'}{\partial t^2} = \frac{\partial^2}{\partial x_i \partial x_j}(\rho v_i v_j + P_{ij}) + \frac{\partial Q_m}{\partial t} - \frac{\partial f_i}{\partial x_i} \qquad \text{(B.5)}$$

---

[26] Variables and notation conventions are introduced in Appendix A.

Lighthill's original idea was to rewrite this equation as a wave equation for the density disturbance. In order to obtain the wave operator on the left hand side, a term involving the Laplace operator is subtracted from both sides, finally giving *Lighthill's equation*,

$$\frac{\partial^2 \rho'}{\partial t^2} - c^2 \nabla^2 \rho' = \frac{\partial^2 T_{ij}}{\partial x_i \partial x_j} + \frac{\partial Q_m}{\partial t} - \frac{\partial f_i}{\partial x_i} \tag{B.6}$$

which involves *Lighthill's stress tensor*, T_{ij},

$$T_{ij} = \rho v_i v_j + P_{ij} - c^2 \delta_{ij} \rho' = \rho v_i v_j - \tau_{ij} + \left(p' - c^2 \rho' \right) \delta_{ij} \tag{B.7}$$

With no external mass sources and forces, the free space solution to Eq. (B.6) reads,

$$\rho'(\mathbf{x}, t) = -\frac{\partial^2}{\partial x_i \partial x_j} \int_{\mathbb{R}^3} \frac{T_{ij}(\mathbf{y}, t - |\mathbf{x} - \mathbf{y}|/c)}{4\pi c^2 |\mathbf{x} - \mathbf{y}|} dV_{\mathbf{y}} \tag{B.8}$$

after application of Eq. (A.53). Alternatively, Eq. (B.6) can be written in terms of the pressure disturbance, p',

$$\frac{1}{c^2} \frac{\partial^2 p'}{\partial t^2} - \nabla^2 p' = \frac{\partial^2 T_{ij}^*}{\partial x_i \partial x_j} + \frac{\partial^2 W}{\partial t^2} \tag{B.9}$$

with T_{ij}^* and W as,

$$T_{ij}^* = \rho v_i v_j - \tau_{ij} \tag{B.10}$$

and

$$W = \frac{p'}{c^2} - \rho' \tag{B.11}$$

The free space solution then becomes,

$$p'(\mathbf{x}, t) = -\frac{\partial^2}{\partial x_i \partial x_j} \int_{\mathbb{R}^3} \frac{T_{ij}^*(\mathbf{y}, t - |\mathbf{x} - \mathbf{y}|/c)}{4\pi |\mathbf{x} - \mathbf{y}|} dV_{\mathbf{y}} - \frac{\partial^2}{\partial t^2} \int_{\mathbb{R}^3} \frac{W(\mathbf{y}, t - |\mathbf{x} - \mathbf{y}|/c)}{4\pi |\mathbf{x} - \mathbf{y}|} dV_{\mathbf{y}} \tag{B.12}$$

When the pressure is linearly dependent on density as in Eq. (A.12), then W in Eq. (B.12) vanishes and the pressure reduces to a deceivingly simple volume integral of a modified version of Lighthill's stress tensor. However, the source terms usually involve unknown quantities, hence expressions like Eq. (B.12) are by no means a straightforward exercise in quadrature. In practice, the flow involved in the stress tensor is computed by CFD and Eqs. (B.8) or (B.12) model the field acoustics in a post-processing step.

B.2 Ffowcs Williams-Hawkings Equation

So far, no provision has been made for the presence of reflecting, moving or radiating boundaries. Ffowcs Williams and Hawkings [FfowcsWilliams1969] extended Lighthill's work by incorporating boundaries in an elegant way using generalized functions (see, e.g., [Ehrenfried2003]). Suppose $f(\mathbf{x}, t)$ is a well-behaved function, defined in $\mathbb{R}^3$ as,

$$
\begin{aligned}
f(\mathbf{x}, t) &< 0 \quad \text{for} \quad \mathbf{x} \in V \setminus S \\
f(\mathbf{x}, t) &> 0 \quad \text{for} \quad \mathbf{x} \notin V \cup S \\
f(\mathbf{x}, t) &= 0 \quad \text{for} \quad \mathbf{x} \in S
\end{aligned}
\tag{B.13}
$$

with V a volume bounded by S. The function is assumed differentiable in all points with the possible exception of non-smooth parts of S (i.e., knuckles and edges). Furthermore,

$$
\nabla f(\mathbf{x}, t) \neq 0 \quad \text{for} \quad \mathbf{x} \in S
\tag{B.14}
$$

As this gradient is parallel to the vector normal to the boundary, the latter can be defined as,

$$
\mathbf{n}(\mathbf{x}, t) = \frac{\nabla f(\mathbf{x}, t)}{|\nabla f(\mathbf{x}, t)|} \quad \text{or} \quad \frac{\partial f}{\partial x_i} = n_i |\nabla f(\mathbf{x}, t)|
\tag{B.15}
$$

The material derivative of the function f equals zero on S,

$$
\frac{Df}{Dt} = \frac{\partial f}{\partial t} + \mathbf{v} \cdot \nabla f = 0
\tag{B.16}
$$

Applying Heaviside's step function, H, to f gives,

$$
H(f(\mathbf{x}, t)) = \begin{cases} 1 & \text{for} \quad \mathbf{x} \notin V \\ 0 & \text{for} \quad \mathbf{x} \in V \end{cases}
\tag{B.17}
$$

This function may be used to extend the validity of the formulations to be derived to locations on and inside boundaries, and hence to the entire $\mathbb{R}^3$. Thus, free space solutions become applicable to problems involving boundaries, be it at the cost of integrands of increased complexity involving generalized functions.

Starting from the equation of continuity, Eq. (B.1), multiplying by Eq. (B.17) and subtracting a constant, ρ_0, gives,

$$
\frac{\partial}{\partial t}\big((\rho - \rho_0) H(f)\big) + \frac{\partial}{\partial x_i}\big(\rho v_i H(f)\big) = (\rho - \rho_0) \frac{\partial}{\partial t} H(f) + \rho v_i \frac{\partial}{\partial x_i} H(f)
\tag{B.18}
$$

Using Eqs. (G.8) and (B.16), and denoting the velocity normal to the boundary as u_i, one obtains,

$$\frac{\partial}{\partial t}\big((\rho-\rho_0)H(f)\big)+\frac{\partial}{\partial x_i}\big(\rho v_i H(f)\big)=\big(\rho(v_i-u_i)+\rho_0 u_i\big)\frac{\partial f}{\partial x_i}\delta(f) \tag{B.19}$$

Applying the same procedure to the momentum equation, Eq. (B.2), yields,

$$\frac{\partial}{\partial t}\big(\rho v_i H(f)\big)+\frac{\partial}{\partial x_j}\big((P_{ij}+\rho v_i v_j)H(f)\big)=\big(\rho v_i(v_j-u_j)+P_{ij}\big)\frac{\partial f}{\partial x_j}\delta(f) \tag{B.20}$$

The divergence of the momentum equation is subtracted from the time derivative of the continuity equation after which $c^2\partial^2\big((\rho-\rho_0)\delta_{ij}H(f)\big)/\partial x_i\partial x_j$ is subtracted from both sides of the result in order to obtain an inhomogeneous wave equation [Dowling1983, Brentner1998, Francescantonio1997],

$$\left(\frac{\partial^2}{\partial t^2}-c^2\nabla^2\right)\big(\rho'H(f)\big)=\frac{\partial^2}{\partial x_i\partial x_j}\big(T_{ij}H(f)\big)+\frac{\partial}{\partial t}\big(\big(\rho(v_i-u_i)+\rho_0 u_i\big)n_i|\nabla f|\delta(f)\big)$$
$$-\frac{\partial}{\partial x_i}\big(\big(\rho v_i(v_j-u_j)+P_{ij}\big)n_j|\nabla f|\delta(f)\big) \tag{B.21}$$

with the right hand side rewritten using Eq. (B.15) and Lighthill's stress tensor. Eq. (B.21) constitutes the extended form of Lighthill's equation. For $f>0$ everywhere, Lighthill's equation, Eq. (B.6), is retrieved. The equation as well as its solution are known as the *Ffowcs Williams-Hawkings equation* (or FW-H equation). The solution reads,

$$4\pi c^2\rho'(\mathbf{x},t)H(f)=\frac{\partial^2}{\partial x_i\partial x_j}\int_{\mathbb{R}^3}\left[\frac{T_{ij}H(f)}{r|1-M_r|}\right]_{ret}dV(\mathbf{y})+\frac{\partial}{\partial t}\int_S\left[\frac{\big(\rho(v_i-u_i)+\rho_0 u_i\big)}{r|1-M_r|}n_i\right]_{ret}dS(\mathbf{y})$$
$$-\frac{\partial}{\partial x_i}\int_S\left[\frac{\big(\rho v_i(v_j-u_j)+P_{ij}\big)}{r|1-M_r|}n_j\right]_{ret}dS(\mathbf{y}) \tag{B.22}$$

The integrations are performed in a moving (inertial) coordinate system over a rigid, but penetrable surface. The expressions between brackets are to be evaluated at the retarded time (see Appendix G.2). The Mach number, M_r, relates to the speed at which the point source *approaches* the observer. It is a component of the source Mach number, $\mathbf{M}=\mathbf{x}'_s/c$, with the prime here denoting derivation with respect to the argument.

The FW-H equation may also be stated in terms of pressure by assuming a linear relation between pressure and density disturbances, Eq. (A.12),

$$\left(\frac{1}{c^2}\frac{\partial^2}{\partial t^2}-\nabla^2\right)\big(p'H(f)\big)=\frac{\partial^2}{\partial x_i\partial x_j}\big(T_{ij}H(f)\big)+\frac{\partial}{\partial t}\big(\big(\rho(v_i-u_i)+\rho_0 u_i\big)n_i|\nabla f|\delta(f)\big)$$
$$-\frac{\partial}{\partial x_i}\big(\big(\rho v_i(v_j-u_j)+P_{ij}\big)n_j|\nabla f|\delta(f)\big) \tag{B.23}$$

Then, the observer is assumed to be in the 'linear' region, the integration surface, however, is not. The following notation introduced by Di Francescantonio [Francescantonio1997, Brentner1998],

$$U_i = \left(1 - \frac{\rho}{\rho_0}\right)u_i + \frac{\rho v_i}{\rho_0} \tag{B.24}$$

and

$$L_i = P_{ij}n_j + \rho v_i\left(v_n - u_n\right) \tag{B.25}$$

yields the 'standard form' of the FW-H equation [Brentner1998],

$$\left(\frac{1}{c^2}\frac{\partial^2}{\partial t^2} - \nabla^2\right)\left(p'H(f)\right) = \frac{\partial^2}{\partial x_i \partial x_j}\left(T_{ij}H(f)\right) + \frac{\partial}{\partial t}\left(\left(\rho_0 U_n\right)\delta(f)\right) - \frac{\partial}{\partial x_i}\left(L_i\delta(f)\right) \tag{B.26}$$

where use has been made of the fact that $\left|\nabla f\right|$ can be set to one. The solution is written as a summation,

$$p'(\mathbf{x},t) = p'_Q(\mathbf{x},t) + p'_T(\mathbf{x},t) + p'_L(\mathbf{x},t) \tag{B.27}$$

in which,

$$4\pi p'_T(\mathbf{x},t) = \int_S\left[\frac{\rho_0\left(\dot{U}_n + U_{\dot{n}}\right)}{r\left(1 - M_r\right)^2}\right]_{ret} dS + \int_S\left[\frac{\rho_0 U_n\left(r\dot{M}_r + c\left(M_r - M^2\right)\right)}{r^2\left(1 - M_r\right)^3}\right]_{ret} dS \tag{B.28}$$

is called *thickness noise*, and,

$$4\pi p'_L(\mathbf{x},t) = \frac{1}{c}\int_S\left[\frac{\dot{L}_r}{r\left(1 - M_r\right)^2}\right]_{ret} dS + \int_S\left[\frac{L_r - L_M}{r^2\left(1 - M_r\right)^2}\right]_{ret} dS + \frac{1}{c}\int_S\left[\frac{L_r\left(r\dot{M}_r + c\left(M_r - M^2\right)\right)}{r^2\left(1 - M_r\right)^3}\right]_{ret} dS \tag{B.29}$$

loading noise, with $L_M = L_i M_i$ and $M^2 = M_i M_i$. L_r is the component of the loading in the 'radial' direction. The surface, S, does not need to be coincident with an impenetrable object. A price is paid in that the density and momentum are needed as input.

For flows around non-penetrable surfaces the two surface bound source terms simplify to,

$$\left(\frac{1}{c^2}\frac{\partial^2}{\partial t^2} - \nabla^2\right)\left(p'H(f)\right) = \frac{\partial^2}{\partial x_i \partial x_j}\left(T_{ij}H(f)\right) + \frac{\partial}{\partial t}\left(\rho_0 u_n\left|\nabla f\right|\delta(f)\right) - \frac{\partial}{\partial x_i}\left(l_i\left|\nabla f\right|\delta(f)\right) \tag{B.30}$$

with $l_i = P_{ij}n_j$. The thickness and loading part of the solution then read,

$$4\pi p'_T(\mathbf{x},t) = \frac{\partial}{\partial t}\int_S\left[\frac{\rho_0 u_n}{r\left|1 - M_r\right|}\right]_{ret} dS \tag{B.31}$$

and

$$4\pi p'_L(\mathbf{x},t) = -\frac{\partial}{\partial x_i} \int_S \left[\frac{l_i}{r|1-M_r|} \right]_{ret} dS \tag{B.32}$$

respectively. The derivatives in front of the integrals are considered awkward to evaluate and are therefore 'worked inside' the integrand. Thus, Farassat's *Formulation 1A* (see, e.g., [Brentner1986]) is obtained with,

$$4\pi p'_T(\mathbf{x},t) = \int_S \left[\frac{\rho_0 \dot{u}_n}{r\left(1-M_r\right)^2} \right]_{ret} dS + \int_S \left[\frac{\rho_0 u_n \left(r\dot{M}_r + c\left(M_r - M^2\right)\right)}{r^2 \left(1-M_r\right)^3} \right]_{ret} dS \tag{B.33}$$

and

$$4\pi p'_L(\mathbf{x},t) = \frac{1}{c} \int_S \left[\frac{\dot{l}_r}{r\left(1-M_r\right)^2} \right]_{ret} dS + \int_S \left[\frac{l_r - l_M}{r^2 \left(1-M_r\right)^2} \right]_{ret} dS$$
$$+ \frac{1}{c} \int_S \left[\frac{l_r \left(r\dot{M}_r + c\left(M_r - M^2\right)\right)}{r^2 \left(1-M_r\right)^3} \right]_{ret} dS \tag{B.34}$$

If only compressive stresses are allowed in the load vector, i.e., $l_i = p'n_i$, then,

$$4\pi p'_L(\mathbf{x},t) = \frac{1}{c} \int_S \left[\frac{\dot{p}'\mathbf{r}\cdot\mathbf{n} + p'\mathbf{r}\cdot\dot{\mathbf{n}}}{r\left(1-M_r\right)^2} \right]_{ret} dS + \int_S \left[\frac{p'\left(\mathbf{r}\cdot\mathbf{n} - M_n\right)}{r^2 \left(1-M_r\right)^2} \right]_{ret} dS$$
$$+ \frac{1}{c} \int_S \left[\frac{p'\mathbf{r}\cdot\mathbf{n}\left(r\dot{M}_r + c\left(M_r - M^2\right)\right)}{r^2 \left(1-M_r\right)^3} \right]_{ret} dS \tag{B.35}$$

For incompressible, frictionless flows Brentner [Brentner1990] shows that,

$$\nabla^2 \left(p'H(f) \right) = -\frac{\partial^2}{\partial x_i \partial x_j} \left(\left(\rho_0 v_i v_j\right) H(f) \right) - \frac{\partial}{\partial t} \left(\rho_0 u_n |\nabla f| \delta(f) \right) + \frac{\partial}{\partial x_i} \left(p'n_i |\nabla f| \delta(f) \right) \tag{B.36}$$

and

$$4\pi p'(\mathbf{x},t)H(f) = -\frac{\partial^2}{\partial x_i \partial x_j} \int_{\mathbb{R}^3} \frac{\rho_0 v_i v_j H(f)}{r} dV_\eta - \frac{\partial}{\partial t} \int_S \frac{\rho_0 u_n}{r} dS_\eta + \frac{\partial}{\partial x_i} \int_S \frac{p'n_i}{r} dS_\eta \tag{B.37}$$

Neglecting the Reynolds stresses and taking the derivatives of the surface integral inside the integrand yields,

$$4\pi p'_T(\mathbf{x},t) = \int_S \frac{\rho_0 \dot{u}_n}{r} dS \tag{B.38}$$

and

$$4\pi p'_L(\mathbf{x},t) = \int_S \frac{l_r}{r^2} dS \tag{B.39}$$

Salvatore *et al.* [Salvatore2002/2006] were the first to apply the FW-H equation to cavitating ship propellers. They precomputed the cavitating propeller's surface pressure and velocities using a hydrodynamic BEM comparable to the one that is used in this thesis. After neglecting Lighthill's stress tensor, their FW-H equation reads,

$$\left(\frac{1}{c^2}\frac{\partial^2}{\partial t^2}-\nabla^2\right)\left(p'H(f)\right)=\frac{\partial}{\partial t}\left(\rho_0 u_n \delta(f)\right)-\frac{\partial}{\partial x_i}\left(p'n_i \delta(f)\right) \tag{B.40}$$

from which follow Eqs. (B.33) and (B.35). The integration surface is coincident with the rotating propeller blades.

FW-H formulations as presented above are normally used to compute radiated acoustic quantities from values (e.g., precomputed by CFD or BEM methods) on a 'control' surface, such as the propeller blade surface. However, in this thesis the interest lies in the ship hull *scattered* field produced by the propeller. Gennaretti *et al.* [Gennaretti2006, Testa2007] derive a formulation for an arbitrary number of scattering bodies. Here, their analysis is followed for one scattering body (i.e., the wetted hull). Neglecting non-linear terms, the following integral equation, equivalent to Farassat's Formulation 1A (Eqs. (B.33)/(B.34)), is found,

$$\begin{aligned}
p'(\mathbf{x},t)=-\rho_0\int_S\left[\left(\mathbf{v}\cdot\mathbf{n}\right)\left(\mathbf{v}\cdot\nabla\hat{G}\right)+\left(\mathbf{v}\cdot\mathbf{n}\right)\left(1-\mathbf{v}\cdot\nabla\theta\right)\hat{G}\right]_{ret}dS \\
-\int_S\left[\left(\mathbf{Pn}\right)\cdot\nabla\hat{G}-\left(\left(\dot{\mathbf{P}}\mathbf{n}\right)\cdot\nabla\theta\right)\hat{G}\right]_{ret}dS
\end{aligned} \tag{B.41}$$

with the frame of reference fixed to the body. The Green's function, $\hat{G}$, is defined as[27],

$$\hat{G}(\mathbf{x},\mathbf{y},t,\tau)=\frac{-1}{4\pi}\left[\frac{1}{r\left(1+M_r\right)}\right]_{ret} \tag{B.42}$$

Assuming the ship moves in the negative axial direction, the retarded time, θ, can be determined by Eq. (A.41). Note that in case of a permeable surface Eq. (B.41) must be supplemented with a term

$$-\int_S\left[\rho\left(\left(\mathbf{u}-\mathbf{v}\right)\cdot\mathbf{n}\right)\left(\left(\mathbf{u}+\mathbf{v}\right)\cdot\nabla\hat{G}+\left(1-\left(\mathbf{u}+\mathbf{v}\right)\cdot\nabla\theta\right)\hat{G}\right)\right]_{ret}dS \tag{B.43}$$

To apply Eq. (B.41) to a cavitating propeller beneath a ship hull, the propeller action (i.e., the source) may be separated from the ship hull (i.e., the scatterer). This has been done by Testa *et al.* [Testa2007] for the case of a rotor/helicopter configuration in BVI ('*Blade Vortex Interaction*') conditions during descent flight. With the hull pressure field due to the hull (or fuselage) motion left out of consideration, the resulting formulation reads [Gennaretti2006],

---

[27] Note that the hat in the definition of the Green's function in the original publication is retained here.

$$\tfrac{1}{2} p_H'(\mathbf{x},t) - \int_S \left[p_H' \frac{\partial \hat{G}}{\partial n} - \dot{p}_H' \frac{\partial \theta}{\partial n} \hat{G} \right]_{ret} dS = \tfrac{1}{2} p_{inc}'(\mathbf{x},t) - \int_S \left[p_{inc}' \frac{\partial \hat{G}}{\partial n} - \dot{p}_{inc}' \frac{\partial \theta}{\partial n} \hat{G} \right]_{ret} dS \qquad \text{(B.44)}$$

Here, subscript $_H$ refers to 'hull' and $_{inc}$ to the incident pressure field. As our interest is in a frequency domain formulation, a harmonic component of the pressure disturbance may be inserted into Eq. (B.44) to give,

$$\tfrac{1}{2} \hat{p}_H'(\mathbf{x};k) - \int_S \left(\frac{\partial \hat{G}}{\partial n} + ikc \frac{\partial \theta}{\partial n} \hat{G} \right) \hat{p}_H'(\mathbf{y};k) \exp(ikc\theta) dS_y =$$

$$\tfrac{1}{2} \hat{p}_{inc}'(\mathbf{x};k) - \int_S \left(\frac{\partial \hat{G}}{\partial n} + ikc \frac{\partial \theta}{\partial n} \hat{G} \right) \hat{p}_{inc}'(\mathbf{y};k) \exp(ikc\theta) dS_y \qquad \text{(B.45)}$$

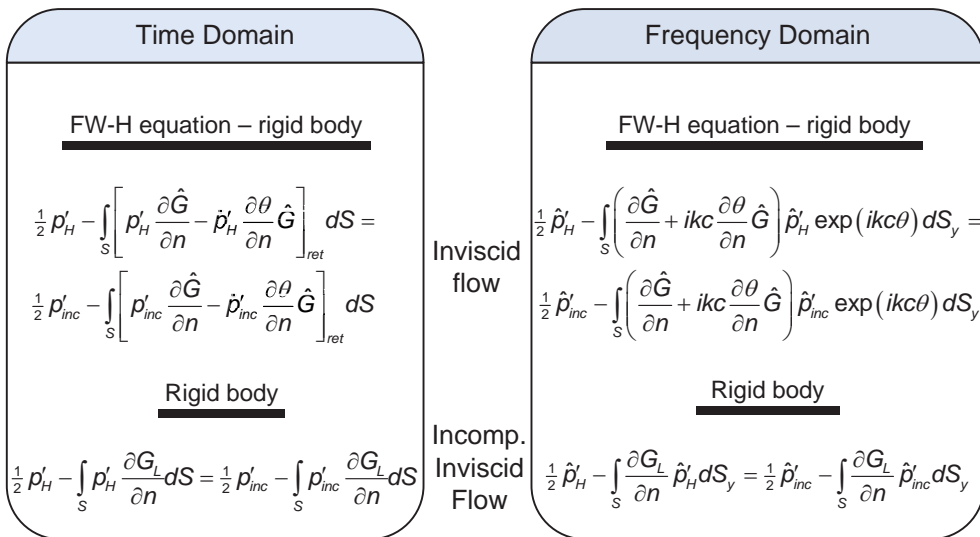An overview of integral equations presented here is given in Figure B.1.

Figure B.1: Overview of FW-H formulations for rigid scattering applications.

C ALTERNATIVE PRESSURE FORMULATION

…which derives an integral equation formulation in terms of the pressure instead of the velocity potential used by Vaz [Vaz2005] for the computation of the incompressible potential flow around a propeller in the time domain.

C.1 Morino's Formulation for the Pressure

In the Morino formulation for incompressible potential flows around propellers, $p'(\mathbf{x}, t)$ also obeys Laplace's equation. Applying Green's third identity to it, for points $\mathbf{x} \in S$, gives,

$$
\begin{aligned}
\frac{1}{2} p'(\mathbf{x},t) = & \int_{S_B(t)} \left(\frac{\partial p'(\mathbf{y},t)}{\partial n_{\mathbf{y}}} G_L(\mathbf{x},\mathbf{y}) - p'(\mathbf{y},t) \frac{\partial G_L(\mathbf{x},\mathbf{y})}{\partial n_{\mathbf{y}}} \right) dS_{\mathbf{y}} \\
& + \int_{S_{B_c}(t)} \left(\frac{\partial p'(\mathbf{y},t)}{\partial n_{\mathbf{y}}} G_L(\mathbf{x},\mathbf{y}) - p'(\mathbf{y},t) \frac{\partial G_L(\mathbf{x},\mathbf{y})}{\partial n_{\mathbf{y}}} \right) dS_{\mathbf{y}} \\
& + \int_{S_W(t)} \Delta \left(\frac{\partial p'(\mathbf{y},t)}{\partial n_{\mathbf{y}}} \right) G_L(\mathbf{x},\mathbf{y}) \, dS_{\mathbf{y}} + \int_{S_{W_c}(t)} \Delta \left(\frac{\partial p'(\mathbf{y},t)}{\partial n_{\mathbf{y}}} \right) G_L(\mathbf{x},\mathbf{y}) \, dS_{\mathbf{y}}
\end{aligned}
\tag{C.1}
$$

instead of Eq. (3.7)[28]. As the pressure is continuous across the vortex sheets, the pressure integral over the vortex sheets does not appear. The price to be paid for this convenience is in the form of additional terms for the normal component of the pressure gradient that appear instead. For the determination of the normal component of the pressure gradient Bernoulli's equation is used,

$$
\frac{\partial p'(\mathbf{y},t)}{\partial n} = \rho_0 \left(g \frac{\partial h(\mathbf{y},t)}{\partial n} - \frac{\partial v'_n(\mathbf{y},t)}{\partial t} - \frac{1}{2} \frac{\partial}{\partial n} \left(|\mathbf{v}(\mathbf{y},t)|^2 - |\mathbf{v}_0(\mathbf{y},t)|^2 \right) \right)
\tag{C.2}
$$

For the velocity, appearing in Eq. (C.2), it can be written (cf. Eqs. (3.1) and (3.3)),

$$
\mathbf{v}_0(\mathbf{y},t) = \mathbf{v}_w(\mathbf{y},t) - \boldsymbol{\omega} \times \mathbf{y}
\tag{C.3}
$$

$$
\mathbf{v}(\mathbf{y},t) = \mathbf{v}_0(\mathbf{y},t) + \nabla \phi'(\mathbf{y},t) = \mathbf{v}_0(\mathbf{y},t) + \mathbf{v}'(\mathbf{y},t)
\tag{C.4}
$$

---

[28] Variables and notation conventions not introduced here are found in Appendices A and B.

in which the wake field, $\mathbf{v}_w(\mathbf{y}, t)$, is time-dependent because of the rotating system of reference. The propeller angular speed is denoted by $\boldsymbol{\omega} = (\omega, 0, 0)^T$. The velocities in the right-hand-side of Eq. (C.2) can be rewritten as,

$$\mathbf{v} \cdot \mathbf{v} - \mathbf{v}_0 \cdot \mathbf{v}_0 = (\mathbf{v}_0 + \nabla\phi') \cdot (\mathbf{v}_0 + \nabla\phi') - \mathbf{v}_0 \cdot \mathbf{v}_0 = \nabla\phi' \cdot \nabla\phi' + 2\mathbf{v}_0 \cdot \nabla\phi' \tag{C.5}$$

Using Eq. (C.5), the vector identity, $\nabla(\mathbf{a} \cdot \mathbf{b}) = \mathbf{b} \times (\nabla \times \mathbf{a}) + (\mathbf{b} \cdot \nabla)\mathbf{a} + \mathbf{a} \times \nabla \times \mathbf{b} + (\mathbf{a} \cdot \nabla)\mathbf{b}$; as well as $\nabla\phi' = \mathbf{v}'$; $\nabla \times \mathbf{v}' = \mathbf{0}$; and $\nabla \times \mathbf{v}_0 = \boldsymbol{\omega}_0$, the normal derivative of Eq. (C.2) can be worked out to give,

$$
\begin{aligned}
\frac{\partial}{\partial n}\left((\mathbf{v} \cdot \mathbf{v}) - (\mathbf{v}_0 \cdot \mathbf{v}_0)\right) &= \mathbf{n} \cdot \nabla\left(\nabla\phi' \cdot \nabla\phi' + 2\mathbf{v}_0 \cdot \nabla\phi'\right) = \mathbf{n} \cdot \nabla\left(\mathbf{v}' \cdot \mathbf{v}' + 2\mathbf{v}_0 \cdot \mathbf{v}'\right) = \\
&= 2\mathbf{n} \cdot \left((\mathbf{v}' \cdot \nabla)\mathbf{v}' + \mathbf{v}' \times (\nabla \times \mathbf{v}_0) + (\mathbf{v}' \cdot \nabla)\mathbf{v}_0 + (\mathbf{v}_0 \cdot \nabla)\mathbf{v}'\right) = 2\mathbf{n} \cdot \left((\mathbf{v} \cdot \nabla)\mathbf{v}' + \mathbf{v}' \times \boldsymbol{\omega}_0\right) = \\
&= 2\mathbf{n} \cdot \left(v_n \frac{\partial}{\partial n} + v_\tau \frac{\partial}{\partial \tau}\right)\mathbf{v}' + 2\mathbf{n} \cdot (\mathbf{v}' \times \boldsymbol{\omega}_0) = 2\mathbf{n} \cdot \left(v_n \frac{\partial}{\partial n} + v_\tau \frac{\partial}{\partial \tau}\right)\begin{bmatrix} v'_n \\ v'_\varsigma \end{bmatrix} + 2\mathbf{n} \cdot (\mathbf{v}' \times \boldsymbol{\omega}_0) = \\
&= 2\begin{bmatrix} 1 \\ 0 \end{bmatrix} \cdot \left(v_n \frac{\partial}{\partial n} + v_\tau \frac{\partial}{\partial \tau}\right)\begin{bmatrix} v'_n \\ v'_\varsigma \end{bmatrix} + 2\mathbf{n} \cdot (\mathbf{v}' \times \boldsymbol{\omega}_0) = 2\left(v_n \frac{\partial v'_n}{\partial n} + v_\tau \frac{\partial v'_n}{\partial \tau}\right) + 2\mathbf{n} \cdot (\mathbf{v}' \times \boldsymbol{\omega}_0)
\end{aligned} \tag{C.6}
$$

Indices τ and ς denote the tangential components of the vector in the plane of the panel. The depth's normal derivative is determined by the vertical component of the normal vector, say, n_h. Then,

$$\frac{\partial p'(\mathbf{y}, t)}{\partial n} = \rho_0 g n_h - \rho_0 \frac{\partial v'_n}{\partial t} - \rho_0 \left(v_n \frac{\partial v'_n}{\partial n} + v_\tau \frac{\partial v'_n}{\partial \tau} + \mathbf{n} \cdot (\mathbf{v}' \times \boldsymbol{\omega}_0)\right) \tag{C.7}$$

Note that on cavitating patches of the surface, $v_n \neq 0$. The derivatives of the wake field velocity may be simplified by taking only its components in the plane of the propeller disc. The last term in Eq. (C.7) may be rewritten as,

$$
\begin{aligned}
\mathbf{n} \cdot (\mathbf{v}' \times \boldsymbol{\omega}_0) &= \mathbf{n} \cdot (\mathbf{v}' \times (\nabla \times (\mathbf{v}_w - \boldsymbol{\omega} \times \mathbf{y}))) = \mathbf{n} \cdot (\mathbf{v}' \times (\nabla \times \mathbf{v}_w - \nabla \times (\boldsymbol{\omega} \times \mathbf{y}))) = \\
&= \mathbf{n} \cdot (\mathbf{v}' \times \boldsymbol{\omega}_w - \mathbf{v}' \times \nabla \times (\boldsymbol{\omega} \times \mathbf{y}))
\end{aligned} \tag{C.8}
$$

Using, $\mathbf{e}_x$, as the unit vector in axial direction,

$$\nabla \times (\boldsymbol{\omega} \times \mathbf{y})) = \boldsymbol{\omega}(\nabla \cdot \mathbf{y}) - \mathbf{y}(\nabla \cdot \boldsymbol{\omega}) + (\mathbf{y} \cdot \nabla)\boldsymbol{\omega} - (\boldsymbol{\omega} \cdot \nabla)\mathbf{y} = 3\omega\mathbf{e}_x - \mathbf{0} + \mathbf{0} - \omega\mathbf{e}_x = 2\omega\mathbf{e}_x \tag{C.9}$$

Thus,

$$\mathbf{n} \cdot (\mathbf{v}' \times \nabla \times (\boldsymbol{\omega} \times \mathbf{y})) = 2\omega\mathbf{n} \cdot (\mathbf{v}' \times \mathbf{e}_x) = 2\omega\left(n_y v'_z - n_z v'_y\right) \tag{C.10}$$

Finally, Eq. (C.7) gives,

$$\frac{\partial p'(\mathbf{y},t)}{\partial n} = \rho_0 g n_h - \rho_0 \frac{\partial v'_n}{\partial t} - \rho_0 v_n \frac{\partial v'_n}{\partial n} - \rho_0 v_\tau \frac{\partial v'_n}{\partial \tau} - \rho_0 \mathbf{n} \cdot (\mathbf{v}' \times \boldsymbol{\omega}_w) + 2\rho_0 \omega \left(n_y v'_z - n_z v'_y \right) \quad \text{(C.11)}$$

The second term on the right-hand-side contains a time derivative that can be determined on the basis of discrete time step data, since in a rotating coordinate system the position coordinate remains the same. The non-trivial normal derivative in the third term may be expressed as a readily obtainable tangential derivative using that the disturbance velocity field is divergence free,

$$\nabla \cdot \mathbf{v}' = \frac{\partial v'_n}{\partial n} + \frac{\partial v'_\varsigma}{\partial \varsigma} = 0 \quad \Rightarrow \quad \frac{\partial v'_n}{\partial n} = -\frac{\partial v'_\varsigma}{\partial \varsigma} \tag{C.12}$$

Boundary Element Method PROCAL is based on a velocity potential formulation and computes pressures in collocation points using Eq. (3.9). As the right hand side of Eq. (C.11) contains only quantities that are known, it may be used for the determination of the normal component of the pressure gradient. Thus, the strengths of the sources, q_p, are determined using Eqs. (C.11) and (3.9) instead of Eqs. (3.12) and (3.13). Note that although for the derivation Eq. (3.7) was replaced by its pressure-based counterpart, Eq. (C.1), the latter need not actually be implemented in order to determine the source strengths, q_p.

D   POINT SOURCES OF SOUND

…which concerns the source distribution in the field equations, when the latter contains stationary or moving point sources of a certain type.

D.1 Moving Monopole Source

Consider a moving point source of the *monopole* type at instantaneous position, $\mathbf{x}_s(t)$, injecting mass without momentum in a compressible fluid without a background flow. Then, the linearized continuity and momentum equations read,

$$\frac{\partial \rho'}{\partial t} + \rho_0 \nabla \cdot \mathbf{v}' = \rho_0 Q_V(t)\delta(\mathbf{x} - \mathbf{x}_s(t)) \tag{D.1}$$

and

$$\rho_0 \frac{\partial \mathbf{v}'}{\partial t} + \nabla p' = 0 \tag{D.2}$$

with, $Q_V(t)$, the source's instantaneous volume injection speed[29]. Using $\rho' = p'/c^2$, taking the time-derivative of Eq. (D.1) and combining it with the divergence of Eq. (D.2), an inhomogeneous wave equation is obtained for the pressure disturbance,

$$\frac{1}{c^2}\frac{\partial^2 p'}{\partial t^2} - \nabla^2 p' = \rho_0 \frac{\partial}{\partial t}\left(Q_V(t)\delta(\mathbf{r}_s(t))\right) \tag{D.3}$$

with $\mathbf{r}_s(t) = \mathbf{x} - \mathbf{x}_s(t)$. The solution in integral form reads,

$$
\begin{aligned}
p'(\mathbf{x},t) &= \rho_0 \frac{\partial}{\partial t}\int_{-\infty}^{+\infty}\int_{\square^3}\frac{Q_V(\tau)\delta(\mathbf{y} - \mathbf{x}_s(\tau))}{4\pi|\mathbf{x} - \mathbf{y}|}\delta(t - \tau - |\mathbf{x} - \mathbf{y}|/c)dV_y d\tau \\
&= \rho_0 \frac{\partial}{\partial t}\int_{-\infty}^{+\infty}\frac{Q_V(\tau)}{4\pi r_s(\tau)}\delta(t - \tau - r_s(\tau)/c)d\tau
\end{aligned}
\tag{D.4}
$$

---

[29] Variables and notation conventions not introduced here are found in Appendices A and B.

in which, as opposed to Eq. (A.53), the time integral has been retained instead of the volume integral. Furthermore, $r_s(\tau) = |\mathbf{r}_s(\tau)|$, and the time derivative is taken outside the integral (see [Ehrenfried2003]). Now, Eq. (G.5) of Appendix G.1 can be used to arrive at the solution for a point source moving at subsonic speed. Then, the argument of the Dirac delta function,

$$g(\tau) = t - \tau - |\mathbf{x} - \mathbf{x}_s(\tau)| / c = 0 \tag{D.5}$$

has exactly one root, and its derivative reads,

$$\frac{dg}{d\tau} = \frac{1}{c} \frac{(\mathbf{x} - \mathbf{x}_s(\tau))}{|\mathbf{x} - \mathbf{x}_s(\tau)|} \frac{d\mathbf{x}_s(\tau)}{d\tau} - 1 \quad \Rightarrow \quad \left| \frac{dg}{d\tau} \right| = |1 - M_r| \tag{D.6}$$

Thus follows,

$$p'(\mathbf{x}, t) = \frac{\rho_0}{4\pi} \frac{\partial}{\partial t} \left[\sum_{n=1}^{N} \frac{Q_V(\tau_n)}{|\mathbf{x} - \mathbf{x}_s(\tau_n)||1 - M_r(\tau_n)|} \right]_{ret} \stackrel{\substack{subsonic \\ speed}}{=} \frac{\rho_0}{4\pi} \frac{\partial}{\partial t} \left[\frac{Q_V(\tau_1)}{r_s(\tau_1)(1 - M_r(\tau_1))} \right]_{ret} \tag{D.7}$$

with the quantities within brackets to be evaluated at the retarded time and N the number of roots appearing in Eq. (G.5). The Mach number, M_r, relates to the speed at which the point source *approaches* the observer. It is a component of the source Mach number, $\mathbf{M} = \mathbf{x}'_s / c$, with the prime (here only) denoting derivation with respect to the argument. Lowson [Lowson1965] derives the far and near field for the pressure,

$$p'_{farfield}(x_i, t) = \frac{1}{4\pi} \left[\frac{\rho_0}{r_s(1 - M_r)^2} \left\{ \frac{\partial Q_V}{\partial t} + \frac{Q_V}{(1 - M_r)} \frac{(x_i - x_{s,i})}{r_s} \frac{\partial M_i}{\partial t} \right\} \right]_{ret} \tag{D.8}$$

and

$$p'_{nearfield}(x_i, t) = \frac{\rho_0}{4\pi} \left[\frac{Q_V c (M_r - M^2)}{r_s^2 (1 - M_r)^3} \right]_{ret} \tag{D.9}$$

or combined as,

$$p'(x_i, t) = \frac{\rho_0}{4\pi} \left[\frac{1}{r_s(1 - M_r)^2} \left\{ \dot{Q}_V + \frac{Q_V}{(1 - M_r)} \left(\dot{M}_r + \frac{c(M_r - M^2)}{r_s} \right) \right\} \right]_{ret} \tag{D.10}$$

in which $M^2 = M_i M_i$. If the same procedure is applied to the velocity potential,

$$\frac{1}{c^2} \frac{\partial^2 \varphi'}{\partial t^2}(\mathbf{x}, t) - \nabla^2 \varphi'(\mathbf{x}, t) = -Q_V(t) \delta(\mathbf{r}_s(t)) \tag{D.11}$$

it follows,

$$\varphi'(\mathbf{x}, t) = -\frac{Q_V(\tau_1)}{4\pi r_s(\tau_1)(1 - M_r(\tau_1))} \tag{D.12}$$

From Eq. (D.5) a few helpful identities are found,

$$\frac{\partial \tau}{\partial t} = \frac{1}{1 - M_r(\tau)} \tag{D.13}$$

$$\frac{\partial r_s(\tau)}{\partial t} = -\frac{cM_r}{1 - M_r(\tau)} \tag{D.14}$$

$$\frac{\partial (\mathbf{r}_s(\tau) \cdot \mathbf{M}(\tau))}{\partial t} = \frac{\mathbf{r}_s(\tau) \cdot \mathbf{M}'(\tau) - cM^2(\tau)}{1 - M_r(\tau)} \tag{D.15}$$

which can be used in conjunction with Eq. (A.17) to give the pressure field, Eq. (D.16). It is identical to the previously derived results, Eq. (D.10),

$$p'(\mathbf{x}, t) = \frac{\rho_0 \dot{Q}_V(\tau)}{4\pi} \frac{1}{r_s(\tau)\left(1 - M_r(\tau)\right)^2} + \frac{\rho_0 Q_V(\tau)}{4\pi} \frac{\mathbf{r}_s(\tau) \cdot \mathbf{M}'(\tau) + c\left(M_r(\tau) - M^2(\tau)\right)}{r_s^2(\tau)\left(1 - M_r(\tau)\right)^3} \tag{D.16}$$

D.2 Stationary Monopole Source

For a stationary monopole source, the Mach number is zero and Eq. (D.12) becomes,

$$\varphi'(\mathbf{x}, t) = -\frac{Q_V(\tau_1)}{4\pi r_s} \tag{D.17}$$

Then, applying Eq. (A.17), or setting the Mach number in Eq. (D.16) to zero, yields the pressure field as,

$$p'(\mathbf{x}, t) = \frac{\rho_0 \dot{Q}_V(\tau_1)}{4\pi r_s} \tag{D.18}$$

Note that Eq. (D.18) illustrates how the volume injection acceleration, e.g., due to pulsating cavities are the cause of pressure fluctuations. Equivalent expressions in the frequency domain, where the Helmholtz equation,

$$\left(\nabla^2 + k^2\right)\hat{\varphi}(\mathbf{x}) = \hat{Q}_V \delta(\mathbf{r}_s) \tag{D.19}$$

applies, are

$$\hat{\varphi}' = -\hat{Q}_V \frac{\exp\left(ikr_s\right)}{4\pi r_s} \tag{D.20}$$

and

$$\hat{p}' = -ik\rho_0 c \hat{Q}_V \frac{\exp\left(ikr_s\right)}{4\pi r_s} \tag{D.21}$$

D.3 Moving Dipole Source

Next, consider a moving point source of the *dipole* type, injecting momentum without mass in a compressible fluid. The linearized continuity and momentum equations become,

$$\frac{\partial \rho'}{\partial t} + \rho_0 \nabla \cdot \mathbf{v}' = 0 \tag{D.22}$$

and

$$\rho_0 \frac{\partial \mathbf{v}'}{\partial t} + \nabla p' = \mathbf{F}(t)\delta(\mathbf{x} - \mathbf{x}_s(t)) \tag{D.23}$$

with $\mathbf{F}$ an instantaneous force. Using $\rho' = p'/c^2$ and taking the time-derivative of Eq. (D.22) combined with the divergence of Eq. (D.23), an inhomogeneous wave equation is obtained for the pressure disturbance,

$$\frac{1}{c^2}\frac{\partial^2 p'}{\partial t^2} - \nabla^2 p' = -\frac{\partial}{\partial x_i}\left(F_i(t)\delta(\mathbf{x} - \mathbf{x}_s(t))\right) = -\nabla \cdot \left(\mathbf{F}(t)\delta(\mathbf{r}_s(t))\right) \tag{D.24}$$

The solution in integral form reads,

$$p'(\mathbf{x},t) = \rho_0 \frac{\partial}{\partial x_i} \int_{-\infty}^{+\infty} \int_{\square^3} \frac{F_i(\tau)\delta(\mathbf{y} - \mathbf{x}_s(\tau))}{4\pi|\mathbf{x} - \mathbf{y}|}\delta(t - \tau - |\mathbf{x} - \mathbf{y}|/c)dV_y d\tau$$

$$= \rho_0 \frac{\partial}{\partial x_i} \int_{-\infty}^{+\infty} \frac{F_i(\tau)}{4\pi r_s(\tau)}\delta(t - \tau - r_s(\tau)/c)d\tau \tag{D.25}$$

where, as before, the time integral was retained and the divergence is taken outside the integral [Ehrenfried2003]. Thus, at subsonic speeds (cf. Eq. (D.7)),

$$p'(\mathbf{x},t) = \frac{1}{4\pi}\frac{\partial}{\partial x_i}\left[\sum_{n=1}^{N}\frac{-F_i(\tau_n)}{|\mathbf{x} - \mathbf{x}_s(\tau_n)||1 - M_r|}\right]_{ret} \overset{\substack{subsonic \\ speed}}{=} \frac{1}{4\pi}\nabla \cdot \left[\frac{-\mathbf{F}(\tau_1)}{r_s(\tau_1)\left(1 - M_r(\tau_1)\right)}\right]_{ret} \tag{D.26}$$

Rienstra remarks [Rienstra2008] that this is not the same as a rotating divergence field, since the retarded time is a function of position and time. As before, from the retarded time constraint,

$$\nabla r_s(\tau) = -c\nabla \tau = \frac{\mathbf{r}_s(\tau)}{r_s(\tau)\left(1 - M_r(\tau)\right)} \tag{D.27}$$

$$\nabla\left(\mathbf{r}_s \cdot \mathbf{M}_r\right) = \mathbf{M} - \frac{\mathbf{r}_s}{r_s\left(1 - M_r(\tau)\right)}\left(\frac{\mathbf{r}_s \cdot \mathbf{M}'}{c} - M^2\right) \tag{D.28}$$

can be derived from which the pressure field is found as,

$$p'(\mathbf{x},t) = \frac{1}{4\pi} \frac{\mathbf{r}_s \cdot \mathbf{F}' - c\mathbf{M}\cdot\mathbf{F}}{cr_s^2\left(1-M_r\right)^2} + \frac{\left(\mathbf{r}_s \cdot \mathbf{F}\right)}{4\pi} \frac{\mathbf{r}_s \cdot \mathbf{M}' + c\left(1-M^2\right)}{cr_s^3\left(1-M_r\right)^3}$$ (D.29)

This expression from [Rienstra2008] was originally obtained by Lowson [Lowson1965] as,

$$p'_{farfield}(x_i,t) = \frac{1}{4\pi}\left[\frac{\left(x_i - x_{s,i}\right)}{cr_s^2\left(1-M_r\right)^2}\left\{\frac{\partial F_i}{\partial t} + \frac{F_i}{\left(1-M_r\right)}\frac{\left(x_i - x_{s,i}\right)}{r_s}\frac{\partial M_i}{\partial t}\right\}\right]$$ (D.30)

and

$$p'_{nearfield}(x_i,t) = \frac{1}{4\pi}\left[\frac{1}{r_s^2\left(1-M_r\right)^2}\left\{\frac{\left(x_i - x_{s,i}\right)F_i}{r_s}\frac{\left(1-M^2\right)}{\left(1-M_r\right)} - M_i F_i\right\}\right]$$ (D.31)

Alternatively, combining far and near field yields,

$$p'(\mathbf{x},t) = \frac{1}{4\pi}\left[\frac{1}{cr_s\left(1-M_r\right)^2}\left\{\dot{F}_r + \frac{F_r\dot{M}_r}{\left(1-M_r\right)} + \frac{cF_r}{r_s}\frac{\left(1-M^2\right)}{\left(1-M_r\right)} - \frac{cF_iM_i}{r_s}\right\}\right]$$ (D.32)

A *force* dipole (in a pressure field) is equivalent to two monopoles of equal strengths and of opposite sign at close proximity, $\varepsilon = |\varepsilon_i|$, to each other (in a velocity potential field). In the limit for vanishing proximity a *volume* dipole remains through differentiation of the source strength [Howe2003],

$$\frac{1}{c^2}\frac{\partial^2\varphi'}{\partial t^2}(\mathbf{x},t) - \nabla^2\varphi'(\mathbf{x},t) = -\frac{\partial}{\partial x_i}\left(\varepsilon_i Q_V(t)\delta(\mathbf{r}_s(t))\right)$$ (D.33)

with solution,

$$\varphi'(\mathbf{x},t) = -\frac{\partial}{\partial x_i}\frac{\varepsilon_i Q_V(\tau_1)}{4\pi r_s\left(1-M_r(\tau_1)\right)}$$ (D.34)

Using Eq. (A.17), it follows for the pressure,

$$\nabla^2 p'(\mathbf{x},t) - \frac{1}{c^2}\frac{\partial^2 p'}{\partial t^2}(\mathbf{x},t) = -\rho_0\frac{\partial}{\partial x_i}\left(\varepsilon_i\dot{Q}_V(t)\delta(x_i - x_{s,i})\right)$$ (D.35)

and

$$p'(\mathbf{x},t) = -\rho_0\frac{\partial}{\partial x_i}\frac{\varepsilon_i\dot{Q}_V(\tau_1)}{4\pi r_s\left(1-M_r(\tau_1)\right)}$$ (D.36)

respectively. It must be remarked that, in physical terms, $\varepsilon_i\dot{Q}_V$ does not represent a 'real' force.

D.4 Stationary Dipole Source

In case of a stationary dipole source, Eq. (D.26) becomes,

$$p'(\mathbf{x}, t) = -\frac{\partial}{\partial x_i} \frac{F_i(\tau_1)}{4\pi r_s} \tag{D.37}$$

The stationary volume dipole can be expressed as,

$$\varphi'(\mathbf{x}, t) = -\frac{\partial}{\partial x_i} \frac{\varepsilon_i Q_V(\tau_1)}{4\pi r_s} \tag{D.38}$$

which, when rewritten in terms of pressure, reads,

$$p'(\mathbf{x}, t) = -\rho_0 \frac{\partial}{\partial x_i} \frac{\varepsilon_i \overset{*}{Q}_V(\tau_1)}{4\pi r_s} \tag{D.39}$$

Similar expressions in the frequency domain, where the Helmholtz equation,

$$\left(\nabla^2 + k^2\right) \hat{\varphi}(\mathbf{x}) = \frac{\partial}{\partial x_i} \varepsilon_i \hat{Q}_V \delta(\mathbf{r}_s) \tag{D.40}$$

applies, are

$$\hat{\varphi}' = -\frac{\partial}{\partial x_i} \varepsilon_i \hat{Q}_V \frac{\exp\left(ikr_s\right)}{4\pi r_s} \tag{D.41}$$

and for the pressure (Eq. (A.24)),

$$\hat{p}' = -ik\rho_0 c \frac{\partial}{\partial x_i} \varepsilon_i \hat{Q}_V \frac{\exp\left(ikr_s\right)}{4\pi r_s} \tag{D.42}$$

Higher order point sources can be derived by applying a second derivative to a second order tensor, which leads to a pressure integral representation like,

$$p'(\mathbf{x}, t) = -\frac{\partial^2}{\partial x_i \partial x_j} \int_{\mathbb{R}^3} \frac{T_{ij}(\tau)\delta(\mathbf{y} - \mathbf{x}_s)}{4\pi |\mathbf{x} - \mathbf{y}|} dV_{\mathbf{y}} \tag{D.43}$$

An application of this *quadrupole* field is found in Section B.1.

D.5 Multipoles as Approximate Solutions

In free space the disturbance velocity potential can be expressed as a solution of the inhomogeneous wave equation, Eq. (A.52),

$$\varphi'(\mathbf{x},t) = -\int_{\mathbb{R}^3} \frac{q(\mathbf{y}, t - |\mathbf{x}-\mathbf{y}|/c)}{4\pi |\mathbf{x}-\mathbf{y}|} dV_\mathbf{y} \qquad (D.44)$$

When the source distribution, q, is limited to a region of diameter, D, two ways of simplifying this equation are possible, viz., the *far field* approximation and the assumption of *compactness* of the source field. If the fictitious centre of the source region is at $\mathbf{x}_c$ and $R = |\mathbf{x}-\mathbf{x}_c| \gg D$, the denominator in Eq. (D.44) may be taken outside the integral to give the far field formulation,

$$\varphi'(\mathbf{x},t) \approx \frac{-1}{4\pi |\mathbf{x}-\mathbf{x}_c|} \int_{\mathbb{R}^3} q(\mathbf{y}, t - |\mathbf{x}-\mathbf{y}|/c) \, dV_\mathbf{y} \qquad \{\text{far field}\} \qquad (D.45)$$

For harmonic source components, $q(x,t) = \hat{Q}(x)\exp(-i\omega t)$, of wave length, $\lambda \gg D$, the retarded time may be taken outside the integral. This yields,

$$\varphi'(\mathbf{x},t) \approx -\frac{\exp\left(-i\omega\left(t - R/c\right)\right)}{4\pi} \int_{\mathbb{R}^3} \frac{\hat{Q}(\mathbf{y})}{|\mathbf{x}-\mathbf{y}|} dV_\mathbf{y} \qquad \{\text{compact source}\} \qquad (D.46)$$

When, in addition, the observer is in the far field, the integral in Eq. (D.46) is of the source strength only. The Green's function appearing in Eq. (D.46) can be expanded in a Taylor series around the centre of the source region, $\mathbf{y}_c$. Eq. (D.46) then becomes,

$$\varphi'(\mathbf{x},t) = G(\mathbf{x},\mathbf{y}_c,t)\frac{1}{4\pi}\int_V \hat{Q}(\mathbf{y})dV_\mathbf{y} + \frac{\partial G}{\partial y_i}(\mathbf{x},\mathbf{y}_c,t)\frac{1}{4\pi}\int_V \hat{Q}(\mathbf{y})\Delta y_i dV_\mathbf{y} +$$
$$+ \frac{\partial^2 G}{\partial y_i \partial y_j}(\mathbf{x},\mathbf{y}_c,t)\frac{1}{4\pi}\int_V \hat{Q}(\mathbf{y})\Delta y_i \Delta y_j dV_\mathbf{y} + \text{h.o.t.} \qquad (D.47)$$

with $\Delta y_i = y_i - y_{c,i}$.

Using that the derivatives of G with regard to a source and observer point only differ by a minus sign, a multipole expansion is arrived at, Eq. (D.48), in which the higher order terms have been deleted. Furthermore, the integral contributions in Eq. (D.47) have been replaced by source strength coefficients. Thus, a harmonic component of the integral of Eq. (D.47) is written as a series of multipoles at the source centre. The convergence of the series determines to a great extent its usefulness in practice. Strictly speaking, Eq. (D.48) is only valid if boundaries or bounding objects are absent.

$$\varphi'(\mathbf{x},t) \approx -A \frac{\exp\left(-i\omega\left(t-R/c\right)\right)}{4\pi R} \quad \text{(monopole)}$$

$$+B_i \frac{\partial}{\partial x_i} \frac{\exp\left(-i\omega\left(t-R/c\right)\right)}{4\pi R} \quad \text{(dipole)} \tag{D.48}$$

$$-C_{ij} \frac{\partial^2}{\partial x_i \partial x_j} \frac{\exp\left(-i\omega\left(t-R/c\right)\right)}{4\pi R} \quad \text{(quadrupole)}$$

The concept of approximating the effect of a source region by a multipole expansion at a certain point can be extended to a set of such points with increased accuracy at the cost of an increased number of unknown strengths. The choice of number and position of the multipoles determines the usefulness of the approximation. If, at some points, the velocity or pressure is known, this can be used as conditions to be imposed on the multipole strengths through a minimization procedure for the prediction error.

E   FREQUENCY DOMAIN SOURCE FORMULAE

*…in which the distributions of rotating sources of noise are transformed from the
time domain to the frequency domain.*

The propeller's elemental sources of noise are rotating around the propeller centre line. This can also be said of the helicoidally shed vorticity. Assuming non-uniform, but stationary propeller inflow, the source field becomes periodic in time at blade passing frequency, ω_1, given by $\omega_1 = Z\Omega$, with, Z, the number of propeller blades and, Ω, the propeller revolution rate. The time, T, needed for one revolution is $T = 2\pi/\Omega$. Likewise, $T_1 = 2\pi/Z\Omega = 2\pi/\omega_1$ denotes the blade passing period.

A cylindrical coordinate system is defined with the origin at the propeller centre, the x-axis pointing in upstream direction, the z-axis upward and the y-axis to port. Then, the propeller is rotating in the yz-plane, where polar coordinates are defined as, (r,θ), with θ running in clockwise direction when looking in the positive axial direction, and $\theta = 0$ on the y-axis. Next, assume the propeller blades and wake surfaces to be approximated by $N_b + N_w$ panels, $\square S_i$, with panel collocation points, $\mathbf{x}_i^{col}(t)$, for $i = 1..N_b + N_w$. During one revolution of period T, N_t snapshots are made of the propeller at equidistant time intervals of $\Delta t = T/N_t$. The time samples in a revolution are indexed $t_j = j\Delta t$ with $j = 0..N_t - 1$. Each of the $N_b + N_w$ collocation points assumes N_t positions, $\mathbf{x}_i^{col}(t_j) = \mathbf{x}_{ij}^{col}$. Also, each of the panels can be associated with a point source of monopole type and strength, $\sigma_i(t_j) = \sigma_{ij}$, plus one of surface normal dipole type and strength, $\mu_i(t_j) = \mu_{ij}$.

Now, the $N_b + N_w$ rotating sources are replaced by $(N_b + N_w)N_t$ stationary ones at angular positions, $\theta_i(t_j) = \theta_{ij} = \theta_{i0} + j\Delta\theta$, that correspond with the positions of the rotating sources at $t = t_j$. The angular spacing, $\Delta\theta$, is given by $\Delta\theta = 2\pi/N_t$ and θ_{i0} denotes the angular position of the ith panel at the start of the revolution. For brevity of notation, the source strengths $\mu_i(t)$ or $\sigma_i(t)$ at a fixed point are denoted by $f(t)$. This is the product of the instantaneous strength, which is written as f_{ij} at $t = t_j$, and a step function, which is one during the time step the panel's collocation point coincides with the source position, and zero at other times. As the number of time steps is always taken as a multiple of the blade number,

$N_t = N_{t1}Z$, the step function actually becomes one during Z time steps. The function $f(t)$ can be developed into a Fourier series based on a period covering one blade passage, T_1,

$$f(t) = \text{Re}\left\{\sum_{n=-\infty}^{\infty}\left(c_n e^{\pm i\omega_n t}\right)\right\}$$ (E.1)

in which

$$c_n = \frac{1}{T_1}\int_{t_j-T_1/2}^{t_j+T_1/2} f(t)e^{\mp i\omega_n t}dt$$ (E.2)

with $\omega_n = n\omega_1$ for $n \neq 0$. The second option in Eq. (E.1) is used here (given the harmonic time dependence, $\exp(-i\omega t)$, chosen in Section F.1). This yields,

$$c_n = \frac{1}{T_1}\int_{t_j-T_1/2}^{t_j+T_1/2} f(t)e^{+i\omega_n t}dt = \frac{f_{ij}}{T_1}\int_{t_j-\Delta t/2}^{t_j+\Delta t/2} e^{+i\omega_n t}dt =$$

$$= \frac{f_{ij}}{i\omega_n T_1}\left\{e^{i\omega_n t_j}\left(1-e^{i\omega_n \Delta t}\right)\right\} = \frac{f_{ij}\Delta t}{T_1}e^{i\omega_n t_j}\frac{\sin\left(\omega_n \Delta t/2\right)}{\omega_n \Delta t/2}$$ (E.3)

and hence,

$$f(t) = \text{Re}\left\{\frac{f_{ij}}{N_t}\sum_{n=-\infty}^{\infty}\frac{\sin\left(\omega_n \Delta t/2\right)}{\omega_n \Delta t/2}e^{-i\omega_n(t-t_j)}\right\}$$ (E.4)

Applying $\text{sinc}(x) = \sin(x)/x$ for a certain harmonic order, n, gives for the complex amplitude of source ij, say, f_n,

$$\frac{f_n}{f_{ij}}\frac{N_t}{Z} = \text{sinc}\left(\omega_n \frac{\Delta t}{2}\right)e^{+i\omega_n t_j} = \text{sinc}\left(nZ\frac{\Delta\theta}{2}\right)e^{+inZ(\theta_{i0}+j\Delta\theta)} = \text{sinc}\left(\pi n\frac{Z}{N_t}\right)e^{+inZ\left(\theta_{i0}+j\frac{2\pi}{N_t}\right)}$$ (E.5)

In fact, Gutin's classical approach [Gutin1936] has been followed here, where '*the moving isolated force is replaced by a string of impulses acting along its path at the appropriate times*' (see also [Lowson1965]).

F   DISCRETIZATION OF INTEGRAL EQUATION

*…where the acoustic integral formulation based on Kirchhoff's method
is discretized using Burton and Miller's approach [Burton1971] and
Kirkup's notation [Kirkup1989].*

F.1 A BEM for 3D Exterior Scattering Problems

The frequency domain alternative to Eq. (3.24), viz. Eq. (3.26), is based on the inhomogeneous form of the Helmholtz equation. This equation is important when the solution of the wave equation,

$$\left(\frac{1}{c^2} \frac{\partial^2}{\partial t^2} - \nabla^2 \right) \varphi'(\mathbf{x}, t) = 0 \tag{F.1}$$

can be found in terms of discrete harmonics,

$$\varphi'(\mathbf{x}, t) = \mathrm{Re}\left\{ \sum_n \hat{\varphi}'_n(\mathbf{x}) \exp(-i\omega_n t) \right\} \tag{F.2}$$

Substitution of Eq. (F.2) in Eq. (F.1) yields for each harmonic, n, a reduced wave equation (i.e., Helmholtz equation),

$$\left(\nabla^2 + k_n^2 \right) \hat{\varphi}'_n(\mathbf{x}) = 0 \tag{F.3}$$

which remains to be solved for the complex amplitude, $\hat{\varphi}'_n$. When, as in the case of rotating propellers, the wave equation can be expressed like this, solving it is tantamount to solving a sequence of Helmholtz equations. Note that, as before, the prime is to denote a perturbation and the caret a Fourier component of a quantity.

Here, it is described in some detail how to apply the BEM to the problem of finding the solution to the Helmholtz equation with a Neumann boundary condition on the closed 'double hull' boundary S_{DH}. For a region V, exterior to S_{DH}, the radiation condition due to Sommerfeld is used. It reads,

$$\lim_{r \to \infty} r\left(\frac{\partial \varphi}{\partial r}(\mathbf{x}) - ik\varphi(\mathbf{x}) \right) = 0 \tag{F.4}$$

In Eq. (F.4) as in the remainder, the prime and the caret have been dropped for convenience. Here, r is the distance from an arbitrary point $\mathbf{x}$ to a fixed origin. For the Neumann boundary condition on S_{DH},

$$\frac{\partial \varphi(\mathbf{x})}{\partial n_{\mathbf{x}}} = v_n(\mathbf{x}) \qquad (\mathbf{x} \in S_{DH}) \tag{F.5}$$

where v_n is the known complex amplitude of the outward normal velocity on S_{DH}.

As a basis to the BEM, the formulation developed by Burton and Miller [Burton1971] is used. This method belongs to the class of direct methods that are based on Green's second theorem, in contrast with indirect methods, which are based on a single layer potential distribution over the surface. For the scattering problem at hand, the normal velocity distribution over the boundary vanishes, and

$$\frac{1}{2}\varphi(\mathbf{x}) = -\int_{S_{DH}} \varphi(\mathbf{y}) \frac{\partial}{\partial n_{\mathbf{y}}} \left(\frac{\exp(ikr)}{4\pi r} \right) dS_{\mathbf{y}} + \varphi^{inc}(\mathbf{x}) \tag{F.6}$$

with,

$$\varphi^{inc}(\mathbf{x}) = \sum_{i=1}^{2(N_b+N_w)} \sum_{j=1}^{N_t} \left[\sigma(\mathbf{x}_{ij}) \frac{\exp(ikr_{ij})}{4\pi r_{ij}} + \mu(\mathbf{x}_{ij}) \frac{\partial}{\partial n_i} \frac{\exp(ikr_{ij})}{4\pi r_{ij}} \right] \tag{F.7}$$

which is Eq. (A.64) with the first integral term set to zero and the set of sources due to the propeller added as φ^{inc}, i.e., the incident waves. It is completely equivalent to Eq. (3.26), which needs to be solved.

The improvement of the formulation due to Burton and Miller stems from the fact that the non-uniqueness problem of the integral equation at the so-called 'characteristic' (often also called 'irregular') frequencies is removed by adding linearly to the Helmholtz integral equation its outward normal derivative on the boundary with respect to the point of observation,

$$\frac{\partial \varphi(\mathbf{x})}{\partial n_{\mathbf{x}}} = v_n(\mathbf{x}) = -\frac{\partial}{\partial n_{\mathbf{x}}} \int_{S_{DH}} \varphi(\mathbf{y}) \frac{\partial}{\partial n_{\mathbf{y}}} \left(\frac{\exp(ikr)}{4\pi r} \right) dS_{\mathbf{y}} + v_n^{inc} \tag{F.8}$$

with,

$$v_n^{inc}(\mathbf{x}) = \sum_{i=1}^{2(N_b+N_w)} \sum_{j=1}^{N_t} \left[\sigma(\mathbf{x}_{ij}) \frac{\partial}{\partial n_{\mathbf{x}}} \frac{-\exp(ikr_{ij})}{4\pi r_{ij}} + \mu(\mathbf{x}_{ij}) \frac{\partial^2}{\partial n_{\mathbf{x}} \partial n_i} \frac{-\exp(ikr_{ij})}{4\pi r_{ij}} \right] \tag{F.9}$$

To the integrals appearing in Eqs. (F.6) and (F.8), the following operator convention is applied [Kirkup1989],

$$\{M\varphi\}_{S_{DH}}(\mathbf{x}) = \int_{S_{DH}} \frac{\partial G_H}{\partial n_{\mathbf{y}}} (|\mathbf{x} - \mathbf{y}|)\varphi(\mathbf{y}) \, dS_{\mathbf{y}} \tag{F.10}$$

$$\{N\varphi\}_{S_{DH}}(\mathbf{x}) = \frac{\partial}{\partial n_{\mathbf{x}}} \int_{S_{DH}} \frac{\partial G_H}{\partial n_{\mathbf{y}}} (|\mathbf{x} - \mathbf{y}|)\varphi(\mathbf{y}) \, dS_{\mathbf{y}} \tag{F.11}$$

with G_H as the Green's function for the Helmholtz equation, Eq. (A.34). In operator notation Burton and Miller's formulation for exterior scattering problems becomes,

$$\{(M - \tfrac{1}{2}I + \mu N)\varphi\}_{S_{DH}}(\mathbf{x}) = -\varphi^{inc}(\mathbf{x}) - \mu v_n^{inc}(\mathbf{x}) \tag{F.12}$$

with $\mathbf{x}$ on S_{DH} as indicated by the subscript. The identity integral operator is denoted by I. The condition $\mathrm{Im}\{\mu\} \neq 0$ on the coupling parameter, μ, ensures that the integral equation has a unique solution irrespective of wave number. Once Eq. (F.12) is solved for $\varphi(\mathbf{x}) \in S_{DH}$, $\varphi(\mathbf{x}) \in V$ can be computed by means of standard quadrature,

$$\varphi(\mathbf{x}) = \{M\varphi\}_{S_{DH}}(\mathbf{x}) + \varphi^{inc}(\mathbf{x}), \quad (\mathbf{x} \in V) \tag{F.13}$$

F.1.1 Discretization of Integral Operators

In order to solve Eq. (F.12), it must be recast in discrete form. This is done by approximating the boundary by a set of flat panels and assuming the boundary functions to be 'panel wise' constant. On each panel one point is chosen as its collocation point at which the unknowns are actually evaluated. Thus, an approximation $\tilde{S}$ is made to the boundary, S_{DH}, and $\tilde{\varsigma}$ to the boundary function, ς,

$$S_{DH} \approx \tilde{S} = \sum_{i=1}^{N'} \tilde{S}_i \tag{F.14}$$

and

$$\varsigma(\mathbf{y}) \approx \tilde{\varsigma}(\mathbf{y}) = \sum_{i=1}^{N'} \tilde{\varsigma}_i \chi_i(\mathbf{y}) \tag{F.15}$$

in which $\chi_i(\mathbf{y})$ are the basis functions on the panel surfaces $\tilde{S}_i$. Often, $\tilde{\varsigma}_i = \tilde{\varsigma}(\mathbf{y}_i)$ for every $i = 1..N'$. The collocation method is applied, where the N' basis functions are chosen as,

$$\chi_i(\mathbf{y}_j) = \delta_{ij} \tag{F.16}$$

with δ_{ij} as Kronecker's delta function. In the approximated form the integral operators become,

$$\{M\tilde{\varsigma}\}(\mathbf{x}) = \sum_{i=1}^{N'} \tilde{\varsigma}(\mathbf{y}_i)\{M\chi_i\}(\mathbf{x}) \tag{F.17}$$

and similarly for the other operator. The following shorthand is adopted for the approximations to the operators,

$$\mathbf{M} = M_{ij} = \{M\chi_j\}(\mathbf{x}_i) \tag{F.18}$$

Thus, the operators become $N' \times N'$ matrices in case of N' collocation points $\mathbf{x}_i$. Repeating this procedure for the other integral operators yields the following matrix-vector equation,

$$\left(\mathbf{M} - \tfrac{1}{2}\mathbf{I} + \mu\mathbf{N}\right)_{S_{DH}} \boldsymbol{\varphi}_{S_{DH}} \cong -\boldsymbol{\varphi}_{S_{DH}}^{inc} - \mu\mathbf{v}_{n,S_{DH}}^{inc} \tag{F.19}$$

The linear system of equations in Eq. (F.19) can be solved by standard methods. Once $\boldsymbol{\varphi}_{S_{DH}}$ is obtained, Eq. (F.13) can be used to obtain a solution for points in the exterior domain,

$$\boldsymbol{\varphi}(\mathbf{x}) \cong \boldsymbol{\varphi}_V^{inc} + \mathbf{M}_V \boldsymbol{\varphi}_{S_{DH}} \tag{F.20}$$

i.e., a standard matrix-vector multiplication.

The integration over $\tilde{S}$ is done panel by panel. The integral over each panel is transformed by mapping the panel $\tilde{S}_i$ onto the standard shape of a square with sides of length two. A standard numerical integration technique can be used to evaluate the integral over the standard shape. In case the integrals are singular this approach is bound to fail. In Section F.1.2, this problem is addressed in detail. First, a number of useful properties of the kernel functions are given. The following results are extracted from [Kirkup1989]. The non-zero frequency Green's function, G_H, is presented in Appendix G.3. Its derivatives with respect to r read,

$$\frac{\partial G_H}{\partial r} = -\frac{\exp(ikr)}{4\pi r}\frac{(ikr-1)}{r} \tag{F.21}$$

$$\frac{\partial^2 G_H}{\partial r^2} = -\frac{\exp(ikr)}{4\pi r}\frac{(-k^2 r^2 - 2ikr + 2)}{r^2} \tag{F.22}$$

Expressions for the normal derivatives of the Green's function are given by,

$$\frac{\partial G_H}{\partial n_{\mathbf{y}}} = \frac{\partial G_H}{\partial r}\frac{\partial r}{\partial n_{\mathbf{y}}} \tag{F.23}$$

$$\frac{\partial^2 G_H}{\partial n_{\mathbf{x}} \partial n_{\mathbf{y}}} = \frac{\partial G_H}{\partial r}\frac{\partial^2 r}{\partial n_{\mathbf{x}} \partial n_{\mathbf{y}}} + \frac{\partial^2 G_H}{\partial r^2}\frac{\partial r}{\partial n_{\mathbf{x}}}\frac{\partial r}{\partial n_{\mathbf{y}}} \tag{F.24}$$

For the normal derivatives of r,

$$\frac{\partial r}{\partial n_{\mathbf{x}}} = \frac{\mathbf{r} \cdot \mathbf{n}_{\mathbf{x}}}{r} \tag{F.25}$$

$$\frac{\partial r}{\partial n_{\mathbf{y}}} = -\frac{\mathbf{r} \cdot \mathbf{n}_{\mathbf{y}}}{r} \tag{F.26}$$

$$\frac{\partial^2 r}{\partial n_{\mathbf{x}} \partial n_{\mathbf{y}}} = -\frac{1}{r}\left(\mathbf{n}_{\mathbf{x}} \cdot \mathbf{n}_{\mathbf{y}} + \frac{\partial r}{\partial n_{\mathbf{x}}}\frac{\partial r}{\partial n_{\mathbf{y}}}\right) \tag{F.27}$$

Similar expressions for the zero frequency Green's function, G_L (Appendix A.2), follow by setting k to zero in Eqs. (F.21) to (F.24). An expression for its double derivative is given for convenience,

$$\frac{\partial^2 G_L}{\partial n_{\mathbf{x}} \partial n_{\mathbf{y}}} = \frac{1}{4\pi r^3}\left(\mathbf{n_x} \cdot \mathbf{n_y} + 3 \frac{\partial r}{\partial n_{\mathbf{x}}} \frac{\partial r}{\partial n_{\mathbf{y}}}\right) \tag{F.28}$$

Having worked out the discretized version of the integral operators appearing in Eq. (3.26) in the form of the left-hand-side of Eq. (F.19), repeating this for the incident waves yields,

$$\boldsymbol{\varphi}_S^{inc}(\mathbf{x}) = \sum_{i=1}^{2(N_b+N_w)} \sum_{j=1}^{N_t} \left[\sigma(\mathbf{x}_{ij}) \frac{-\exp(ikr_{ij})}{4\pi r_{ij}} + \mu(\mathbf{x}_{ij}) \frac{\partial}{\partial n_i} \frac{-\exp(ikr_{ij})}{4\pi r_{ij}} \right] \tag{F.29}$$

and

$$\mathbf{v}_S^{inc}(\mathbf{x}) = \sum_{i=1}^{2(N_b+N_w)} \sum_{j=1}^{N_t} \left[\sigma(\mathbf{x}_{ij}) \frac{\partial}{\partial n_{\mathbf{x}}} \frac{-\exp(ikr_{ij})}{4\pi r_{ij}} + \mu(\mathbf{x}_{ij}) \frac{\partial^2}{\partial n_{\mathbf{x}} \partial n_i} \frac{-\exp(ikr_{ij})}{4\pi r_{ij}} \right] \tag{F.30}$$

The normal derivative in Eq. (F.29), n_i, can be worked out using the same Eqs. (F.21), (F.23) and (F.25) as for the panel integrals, giving,

$$\boldsymbol{\varphi}_S^{inc}(\mathbf{x}) = \sum_{i=1}^{2(N_b+N_w)} \sum_{j=1}^{N_t} \left[-\sigma(\mathbf{x}_{ij}) \frac{\exp(ikr_{ij})}{4\pi r_{ij}} + \mu(\mathbf{x}_{ij}) \frac{(ikr_{ij}-1)}{r_{ij}} \frac{(\mathbf{r}_{ij} \cdot \mathbf{n}_{ij})}{r_{ij}} \frac{\exp(ikr_{ij})}{4\pi r_{ij}} \right] \tag{F.31}$$

Note that this component of the gradient is normal to the propeller blade. Similarly, the normal component of the gradient in Eq. (F.30), $n_{\mathbf{x}}$, is rewritten using Eqs. (F.21), (F.23) and (F.25). For the double derivative Eqs. (F.21), (F.22), (F.24), (F.25) and (F.27) are used, which yields Eq. (F.32). Note that $n_{\mathbf{x}}$ is in the direction normal to the (double) hull.

$$\begin{aligned}
\mathbf{v}_S^{inc}(x_{ij}) = \sum_{i=1}^{2(N_b+N_t)} \sum_{j=1}^{N_t} &\left[\sigma(\mathbf{x}_{ij}) \frac{\exp(ikr_{ij})}{4\pi r_{ij}} \frac{(ikr_{ij}-1)}{r_{ij}} \frac{(\mathbf{r}_{ij} \cdot \mathbf{n_x})}{r_{ij}} + \right. \\
&+ \mu(\mathbf{x}_{ij}) \frac{\exp(ikr_{ij})}{4\pi r_{ij}} \left(\left(\frac{ikr_{ij}-1}{r_{ij}^2} \right) \left(\mathbf{n_x} \cdot \mathbf{n}_{ij} - \frac{(\mathbf{r}_{ij} \cdot \mathbf{n_x})}{r_{ij}} \frac{(\mathbf{r}_{ij} \cdot \mathbf{n}_{ij})}{r_{ij}} \right) + \right. \\
&\left. \left. + (-k^2 r_{ij}^2 - 2ikr_{ij} + 2) \frac{(\mathbf{r}_{ij} \cdot \mathbf{n_x})}{r_{ij}} \frac{(\mathbf{r}_{ij} \cdot \mathbf{n}_{ij})}{r_{ij}} \right) \right]
\end{aligned} \tag{F.32}$$

F.1.2 Evaluation of Singular Integrals over Elements

Now the problem of evaluating the singular integrals must be tackled, which make up the diagonal elements of the matrices defined in Eq. (F.19) by subtracting out the singularity.

Using the asymptotic properties of the kernel functions and indexing the integral operators depending on whether G_H or G_L is involved, it follows,

$$\{M_H\chi\}(\mathbf{x}) = \{M_L\chi\}(\mathbf{x}) + \int\limits_{S_{DH}} \left(\frac{\partial G_H}{\partial n_\mathbf{y}} - \frac{\partial G_L}{\partial n_\mathbf{y}} \right) \chi(\mathbf{y})dS_\mathbf{y} \qquad \text{(F.33)}$$

and

$$\{N_H\chi\}(\mathbf{x}) = \{N_L\chi\}(\mathbf{x}) + \tfrac{1}{2}k^2\{L_L\chi\}(\mathbf{x}) + \int\limits_{S_{DH}} \left(\frac{\partial^2 G_H}{\partial n_\mathbf{x}\partial n_\mathbf{y}} - \frac{\partial^2 G_L}{\partial n_\mathbf{x}\partial n_\mathbf{y}} - \tfrac{1}{2}k^2 G_L \right) \chi(\mathbf{y})dS_\mathbf{y} \qquad \text{(F.34)}$$

Under the assumption that collocation points are not chosen on edges of the flat boundary elements, expressions for the discrete form of the integral operators simplify. Then, by virtue of Eq. (F.25) the diagonal components of $\mathbf{M}_H$ are zero. A calculation method is needed for the diagonal components of the remaining operator $\mathbf{N}_H$,

$$J = \frac{\partial}{\partial n_\mathbf{x}} \int\limits_{S_i} \frac{\partial G_L}{\partial n_\mathbf{y}} (|\mathbf{x} - \mathbf{y}|)\, dS_\mathbf{y} \qquad \text{(F.35)}$$

Let us assume that the panel lies in the local x, y plane with $\mathbf{y} = \mathbf{y}(x, y)$ and $\mathbf{x} = \mathbf{y}(0,0)$. It is further assumed that the integral can be transformed into polar coordinates (R, θ). For the integral a limiting procedure is needed to derive the wanted expression. A hemisphere of radius ε is erected into the interior of the boundary at the origin. The limit as ε goes to zero of the sum of the integrals over $\tilde{S}_i$ minus the hemisphere and the hemisphere itself is taken. This gives,

$$J = -\frac{1}{4\pi} \int\limits_0^{2\pi} \frac{1}{R(\theta)}\, d\theta = -\frac{1}{4\pi} \sum_{n=1}^4 \int\limits_{\theta_n}^{\theta_{n+1}} \frac{1}{R(\theta)}\, d\theta \qquad \text{(F.36)}$$

in case of a quadrilateral surface element, where $\theta_5 = \theta_1$. The integral alongside the panel must be evaluated. The first vertex is assumed to lie on the positive x-axis, while the collocation point is at the origin. The line segments are given by,

$$y_n = A_n x_n + B_n \qquad \text{(F.37)}$$

with $n = 1(1)4$. The line segment n runs from vertex n to vertex $n+1$. Hence,

$$A_n = \frac{y_{n+1} - y_n}{x_{n+1} - x_n} \qquad \text{(F.38)}$$

and

$$B_n = y_{n+1} - \frac{y_{n+1} - y_n}{x_{n+1} - x_n} x_{n+1} = y_n - A_n x_n = y_{n+1} - A_n x_{n+1} \qquad \text{(F.39)}$$

where the upper indices refer to vertex coordinates. In polar coordinates,

$$R(\theta) = \frac{B_n}{\sin(\theta) - A_n \cos(\theta)} \tag{F.40}$$

For the integral of Eq. (F.36), it is written,

$$
\begin{aligned}
J &= -\frac{1}{4\pi} \sum_{n=1}^{4} \frac{1}{B_n} \int_{\theta_n}^{\theta_{n+1}} (\sin(\theta) - A_n \cos(\theta))\, d\theta = \\
&= \frac{1}{4\pi} \sum_{n=1}^{4} \frac{\cos(\theta) + A_n \sin(\theta)}{B_n} \bigg|_{\theta_n}^{\theta_{n+1}} = -\frac{1}{4\pi} \sum_{n=1}^{4} \frac{\sin(\theta)}{C_n} \bigg|_{\theta_n}^{\theta_{n+1}}
\end{aligned}
\tag{F.41}
$$

Slight modifications are to be made when A_n does not exist. When the collocation point is not on an edge or corner, the above formulas are valid.

F.1.3 Evaluation of Regular Integrals over Elements

To determine the regular part of the diagonal terms of the matrices of so-called *influence coefficients* completely, the remaining right-hand-sides of Eq. (F.34) must be numerically integrated. This can be done simply by a nine-point integration rule. It is assumed that the elements can be transformed to a square with sides of length two. The transformed integral can then be expressed as,

$$\iint f(x,y)\, dxdy \approx 4 \sum_{i=1}^{9} w_i f(x_i, y_i) \tag{F.42}$$

with

$$
\begin{aligned}
(x_i, y_i) &= (0,0) & &\rightarrow w_i = 16/81 \\
(x_i, y_i) &= (\pm\sqrt{3/5}, 0) & &\rightarrow w_i = 10/81 \\
(x_i, y_i) &= (\pm\sqrt{3/5}, \pm\sqrt{3/5}) & &\rightarrow w_i = 25/324 \\
(x_i, y_i) &= (0, \pm\sqrt{3/5}) & &\rightarrow w_i = 10/81
\end{aligned}
\tag{F.43}
$$

The necessary transform procedure is clarified in Section F.1.4. For the integrand of the regularized part of N_H, a Taylor series expansion around frequency zero yields,

$$
\begin{aligned}
\frac{\partial^2 G_H}{\partial n_x \partial n_y} - \frac{\partial^2 G_L}{\partial n_x \partial n_y} - \frac{1}{2} k^2 G_L &= \frac{1}{4\pi} \sum_{m=1}^{\infty} (ik)^{m+2} \left(\frac{1}{(m+2)!} - \frac{1}{(m+1)!} \right) r^{m-1} = \\
&= -\frac{1}{4\pi} \sum_{m=1}^{\infty} \frac{(ik)^{m+2}}{(m+2)} \frac{r^{m-1}}{m!} = k^2 \sum_{m=1}^{\infty} \frac{\Gamma_m}{m+2}
\end{aligned}
\tag{F.44}
$$

in which Γ denotes the Gamma function. This expression has to be accompanied by the Jacobian of the element transform procedure in Appendix F.1.4.

To compute the off-diagonal terms of the matrices, the left-hand-sides of Eq. (F.34) can be numerically integrated in a simple way. A four-point rule is used for this purpose. The integrands can be easily derived using the results of Appendix F.1.2 and flat boundary elements. It is again assumed that the elements can be transformed to a standard square with sides of length two. The transformed integral can then be expressed as,

$$\iint f(x,y)\,dxdy \approx 4\sum_{i=1}^{9} w_i f(x_i, y_i) \tag{F.45}$$

with $w_i = 1/4$ for all i. The integration points are at $(x_i, y_i) = (\pm\sqrt{1/3}, \pm\sqrt{1/3})$.

F.1.4 Derivation of Panel Transform Coefficients

Assume that the vertices of a specific element are known. Assume furthermore that they are numbered in counter clockwise direction. The local coordinate system of a panel is defined as follows. The collocation point serves as the origin. The axis normal to the panel is taken as the positive z-axis. The vector pointing in the direction from the origin to the first vertex is taken as the positive x-axis after normalization. The y-axis is defined as the cross product of the vectors defining the z-axis and the x-axis, respectively.

Let us define a panel transform procedure such that it transforms a panel in the local co-ordinates system to a square with sides of length two. More specifically, the procedure must map the collocation point on the origin (where it already was) and the vertices 1, 2, 3 and 4 on the corners of the square, i.e., (-1,1), (-1,-1), (1,-1) and (1,1), respectively. This can be achieved by the mapping,

$$\begin{aligned} x &= \phi_1(\alpha,\beta) = \alpha e_1 + \beta e_2 + \alpha\beta e_3 + \alpha^2 e_4 \\ y &= \phi_2(\alpha,\beta) = \alpha f_1 + \beta f_2 + \alpha\beta f_3 + \alpha^2 f_4 \end{aligned} \tag{F.46}$$

where (x,y) are the local and (α,β) the transformed coordinates. The transform coefficients, $e1$ to $f4$, are found by inserting the vertex coordinates,

$$\begin{aligned} \phi_1(-1,+1) &= x_1 & \phi_2(-1,+1) &= y_1 \equiv 0 \\ \phi_1(-1,-1) &= x_2 & \phi_2(-1,-1) &= y_2 \\ \phi_1(+1,-1) &= x_3 & \phi_2(+1,-1) &= y_3 \\ \phi_1(+1,+1) &= x_4 & \phi_2(+1,+1) &= y_4 \end{aligned} \tag{F.47}$$

whence,

$$\begin{aligned} e_1 &= \tfrac{1}{4}(-x_1 - x_2 + x_3 + x_4) & e_2 &= \tfrac{1}{4}(+x_1 - x_2 - x_3 + x_4) \\ e_3 &= \tfrac{1}{4}(-x_1 + x_2 - x_3 + x_4) & e_4 &= \tfrac{1}{4}(+x_1 + x_2 + x_3 + x_4) \\ f_1 &= \tfrac{1}{4}(-y_2 + y_3 + y_4) & f_2 &= \tfrac{1}{4}(-y_2 - y_3 + y_4) \\ f_3 &= \tfrac{1}{4}(+y_2 - y_3 + y_4) & f_4 &= \tfrac{1}{4}(+y_2 + y_3 + y_4) \end{aligned} \tag{F.48}$$

Note that the property that $y_1 \equiv 0$ has been used. For the Jacobian of the mapping the following expression is used,

$$\Im(\alpha, \beta) = \begin{vmatrix} \frac{\partial \phi_1}{\partial \alpha} & \frac{\partial \phi_1}{\partial \beta} \\ \frac{\partial \phi_2}{\partial \alpha} & \frac{\partial \phi_2}{\partial \beta} \end{vmatrix} = \begin{vmatrix} e_1 + \beta e_3 + 2\alpha e_4 & e_2 + \alpha e_3 \\ f_1 + \beta f_3 + 2\alpha f_4 & f_2 + \alpha f_3 \end{vmatrix} \tag{F.49}$$

F.1.5 Thin body treatment

Whenever parts of the scattering surface are in very close proximity to each other, typically at distances between collocation points smaller than, say, one half of a panel size, numerical problems occur. This may happen on sharp edges of rudders, gondolas and at flat sterns close to the free surface. Because this happens without the condition number of the matrices in Eq. (F.84) becoming extremely high, the difficulties remain unnoticed until after the computations. Wu [Wu2000, Wu1995] presents an approach to circumvent numerical errors by replacing the equations for such closely spaced surfaces locally by their 'mid surface', S_{mid}, on either side of which integral equation formulations are solved. In the following Wu's approach is applied to the exterior scattering problem.

Burton and Miller's formulation for the exterior scattering problem, Eq.(F.12), for locations of the observer on the outside of S_{mid}, reads,

$$\{(M + \mu N)\varphi\}_{S_{mid}}(\mathbf{x}) + \varphi^{inc}(\mathbf{x}) + \mu v_n^{inc}(\mathbf{x}) = \tfrac{1}{2}\varphi(\mathbf{x}); \quad \mathbf{x} \in S_{mid} \tag{F.50}$$

It has its counterpart in a formulation for the interior radiation problem,

$$-\{(M + \mu N)\varphi\}_{S_{mid}}(\mathbf{x}) + \varphi^{inc}(\mathbf{x}) + \mu v_n^{inc}(\mathbf{x}) = \tfrac{1}{2}\varphi(\mathbf{x}); \quad \mathbf{x} \in S_{mid} \tag{F.51}$$

Denoting the potential on the inside and outside of the thin bounding surface as, φ^- and φ^+, respectively, and adding Eqs. (F.50) and (F.51), yields

$$\{(M + \mu N)(\varphi^+ - \varphi^-)\}_{S_{mid}}(\mathbf{x}) + \varphi^{inc,+}(\mathbf{x}) + \varphi^{inc,-}(\mathbf{x}) + \mu(v_n^{inc,+}(\mathbf{x}) + v_n^{inc,-}(\mathbf{x})) =$$
$$= \tfrac{1}{2}(\varphi^+(\mathbf{x}) + \varphi^-(\mathbf{x})); \quad \mathbf{x} \in S_{mid} \tag{F.52}$$

For points on the surface, the equation can be split into two parts, depending on the coupling parameter,

$$\{M(\varphi^+ - \varphi^-)\}_{S_{mid}}(\mathbf{x}) + \varphi^{inc,+}(\mathbf{x}) + \varphi^{inc,-}(\mathbf{x}) = \tfrac{1}{2}(\varphi^+(\mathbf{x}) + \varphi^-(\mathbf{x})); \quad \mathbf{x} \in S_{mid} \tag{F.53}$$

$$\{N(\varphi^+ - \varphi^-)\}_{S_{mid}}(\mathbf{x}) + \mu(v_n^{inc,+}(\mathbf{x}) - v_n^{inc,-}(\mathbf{x})) = 0; \quad \mathbf{x} \in S_{mid} \tag{F.54}$$

Eqs. (F.53) and (F.54) constitute two equations for the potential jump across the mid surface from which the wanted potential on the outside of the thin body, i.e., φ^+, is found,

$$\begin{aligned} \varphi^{+} - \varphi^{-} &= \xi_1 \\ \varphi^{+} + \varphi^{-} &= \xi_2 \end{aligned} \qquad \Leftrightarrow \qquad \begin{aligned} \varphi^{+} &= \tfrac{1}{2}\left(\xi_1 + \xi_2\right) \\ \varphi^{-} &= \tfrac{1}{2}\left(\xi_2 - \xi_1\right) \end{aligned} \tag{F.55}$$

Since only a small part of S_{DH} is actually thin, the surface may be split into a thin part, S_t, to which the above procedure is applied, and a regular part, S_r, such that $S_{DH} = S_t \cup S_r$ and $S_t \cap S_r = \varnothing$. Then,

$$\left\{ M(\varphi^{+} - \varphi^{-}) \right\}_{S_t}(\mathbf{x}) + \varphi^{inc,+}(\mathbf{x}) + \varphi^{inc,-}(\mathbf{x}) + \left\{ M\varphi \right\}_{S_r}(\mathbf{x}) + \varphi^{inc}(\mathbf{x}) = \tfrac{1}{2}\varphi(\mathbf{x}); \quad \mathbf{x} \in S_r \tag{F.56}$$

$$\left\{ M(\varphi^{+} - \varphi^{-}) \right\}_{S_t}(\mathbf{x}) + \varphi^{inc,+}(\mathbf{x}) + \varphi^{inc,-}(\mathbf{x}) + \left\{ M\varphi \right\}_{S_r}(\mathbf{x}) + \varphi^{inc}(\mathbf{x}) = \tfrac{1}{2}(\varphi^{+}(\mathbf{x}) + \varphi^{-}(\mathbf{x})); \quad \mathbf{x} \in S_t \tag{F.57}$$

$$\left\{ N(\varphi^{+} - \varphi^{-}) \right\}_{S_{mid}}(\mathbf{x}) + (v_n^{inc,+} - v_n^{inc,-})(\mathbf{x}) + \left\{ N\varphi \right\}_{S_{DH}}(\mathbf{x}) + v_n^{inc}(\mathbf{x}) = 0 \quad \text{on } S_t \tag{F.58}$$

Now, Eqs. (F.56) and (F.58) have to be solved simultaneously on S_{DH} yielding the potential on S_r and the potential jump on S_t. Then, Eq. (F.57) can be used to determine the potential sum on S_t after which the potential on S_t follows from Eq. (F.55). Often, it may be assumed that $v_n^{+} = v_n^{-}$ and,

$$\left\{ M(\varphi^{+} - \varphi^{-}) \right\}_{S_t}(\mathbf{x}) + \left\{ M\varphi \right\}_{S_r}(\mathbf{x}) - \left\{ Lv_n \right\}_{S_r}(\mathbf{x}) = \tfrac{1}{2}\varphi(\mathbf{x}); \quad \mathbf{x} \text{ on } S_r \tag{F.59}$$

$$\left\{ M(\varphi^{+} - \varphi^{-}) \right\}_{S_t}(\mathbf{x}) + \left\{ M\varphi \right\}_{S_r}(\mathbf{x}) - \left\{ Lv_n \right\}_{S_r}(\mathbf{x}) = \tfrac{1}{2}(\varphi^{+} + \varphi^{-})(\mathbf{x}); \quad \mathbf{x} \text{ on } S_t \tag{F.60}$$

$$\left\{ N(\varphi^{+} - \varphi^{-}) \right\}_{S_t}(\mathbf{x}) + \left\{ N\varphi \right\}_{S_r}(\mathbf{x}) - \left\{ M_k^T v_n \right\}_{S_r}(\mathbf{x}) = v_n(\mathbf{x}); \quad \mathbf{x} \text{ on } S_t \tag{F.61}$$

are obtained.

The thin body treatment as presented in this section has not been applied in the example cases in the present thesis. A typical example of the type of error that results from this omission is seen in Figure 8.5. The thin trailing edge of the skeg connecting the gondola to the afterbody contains five 'greenish' panels that should have been blue like the panels in their immediate vicinity.

F.1.6 Double hull treatment

To enforce the zero pressure or potential on the free surface in Section 3.4 the so-called 'double hull' approach was adopted. Thus, all panels on the hull are mirrored in the free surface and a closed boundary in an infinite domain results. When the normal velocities and potentials on the mirrored panels are taken equal in magnitude, but of opposite sign, the free surface is perfectly modeled as a pressure release surface. For nearly horizontal panels close to this surface, the combination of these panels and their mirror images act as the thin bodies discussed above.

Call this part of S_t, $S_{t,fs}$, so that $S_t = S_{t,fs} \cup S_{t\backslash t,fs}$, whereas $S_{t,fs} \cap S_{t\backslash t,fs} = \varnothing$. On this surface, Eqs. (F.53) and (F.54) become

$$\{M\varphi\}_{S_{t,fs}}(\mathbf{x}) = 0 \quad \text{on } S_{t,fs} \tag{F.62}$$

$$\{2N\varphi\}_{S_{t,fs}}(\mathbf{x}) = v_n(\mathbf{x}) \quad \text{on } S_{t,fs} \tag{F.63}$$

Finally, instead of Eqs. (F.59), (F.60) and (F.61),

$$\{2M\varphi\}_{S_{t,fs}} + \{M(\varphi^+ - \varphi^-) - L(v_n^+ - v_n^-)\}_{S_{t\setminus t,fs}} + \{M\varphi - Lv_n\}_{S_r} = \tfrac{1}{2}\varphi \text{ on } S_r \tag{F.64}$$

$$\{2M\varphi\}_{S_{t,fs}} + \{M(\varphi^+ - \varphi^-) - L(v_n^+ - v_n^-)\}_{S_{t\setminus t,fs}} + \{M\varphi - Lv_n\}_{S_r} = \tfrac{1}{2}(\varphi^+ + \varphi^-) \text{ on } S_{t\setminus t,fs} \tag{F.65}$$

$$\{2M\varphi\}_{S_{t,fs}} + \{M(\varphi^+ - \varphi^-) - L(v_n^+ - v_n^-)\}_{S_{t\setminus t,fs}} + \{M\varphi - Lv_n\}_{S_r} = 0 \text{ on } S_{t,fs} \tag{F.66}$$

$$\{2N\varphi\}_{S_{t,fs}} + \{N(\varphi^+ - \varphi^-) - M_k^T(v_n^+ - v_n^-)\}_{S_{t\setminus t,fs}} + \{N\varphi - M_k^T v_n\}_{S_r} = \tfrac{1}{2}(v_n^+ + v_n^-) \text{ on } S_{t\setminus t,fs} \tag{F.67}$$

$$\{2N\varphi\}_{S_{t,fs}} + \{N(\varphi^+ - \varphi^-) - M_k^T(v_n^+ - v_n^-)\}_{S_{t\setminus t,fs}} + \{N\varphi - M_k^T v_n\}_{S_r} = v_n(\mathbf{x}) \text{ on } S_{t,fs} \tag{F.68}$$

Now, Eqs. (F.64), (F.67) and Eq. (F.66) or (F.68) have to be solved simultaneously on S_{DH} yielding the potential on S_r and $S_{t,fs}$ as well as the potential jump on $S_{t\setminus t,fs}$. Then, Eq. (F.65) can be used to determine the potential sum on $S_{t\setminus t,fs}$ after which the potential on S_t follows from Eq. (F.55).

F.1.7 3D scattering with free surface effect

Although the 'double hull' approach adopted in Section F.1.6 is easy to implement, its simplicity is somewhat deceptive in certain cases. More specifically, when the overhanging part of the stern is only just submerged, the choice of the actual ship draught in the computations becomes difficult and critical. Also, the thin body problem may start to cause numerical difficulties. In other cases, the free surface around the stern may become more strongly curved and again the 'effective' draught to be applied becomes ill-defined.

A more solid approach to solving 3D scattering problems involving a wavy free surface is to actually compute the surface and include at least the part of it around the stern in the panel description of the ship. The description of the hull must then be confined to its 'really' wetted part. Thus one has to solve a 3D *interior* acoustic scattering problem rather than an exterior one, as described before, with the free surface being closed at infinity by a hemisphere enclosing the underwater part of the hull. In practice, the hemisphere and the more distant part of the free surface are neglected in the computations. Furthermore, the problem has become one with mixed boundary conditions, as the Neumann type of rigid reflecting hull boundary condition is accompanied by a Dirichlet type zero pressure condition on the free surface. The necessary formulations are given below for reference.

Recalling Burton and Miller's formulation for the exterior scattering problem,

$$\{(M - \tfrac{1}{2}I + \mu N)\varphi\}_{S_{DH}}(\mathbf{x}) = -\varphi^{inc}(\mathbf{x}) - \mu v_n^{inc}(\mathbf{x}) + \{(L + \mu(M^T + \tfrac{1}{2}I))v_n\}_{S_{DH}}(\mathbf{x}) \tag{F.69}$$

with $\mathbf{x}$ on the double hull, S_{DH}. The boundary condition requires the normal velocity on it to vanish, thus,

$$\left\{(M - \tfrac{1}{2}I + \mu N)\varphi\right\}_{S_{DH}}(\mathbf{x}) = -\varphi^{inc}(\mathbf{x}) - \mu v_n^{inc}(\mathbf{x}) \tag{F.70}$$

and after discretization the following matrix-vector equation is obtained,

$$\left(\mathbf{M} - \tfrac{1}{2}\mathbf{I} + \mu\mathbf{N}\right)_{S_{DH}} \boldsymbol{\varphi}_{S_{DH}} \cong -\boldsymbol{\varphi}_{S_{DH}}^{inc} - \mu\mathbf{v}_{n,S_{DH}}^{inc} \tag{F.71}$$

The analogous formulation for the interior scattering problem reads,

$$\left\{(M + \tfrac{1}{2}I + \mu N)\varphi\right\}_S(\mathbf{x}) = \varphi^{inc}(\mathbf{x}) + \mu v_n^{inc}(\mathbf{x}) + \left\{(L + \mu(M^T - \tfrac{1}{2}I))v_n\right\}_S(\mathbf{x}) \tag{F.72}$$

with $\mathbf{x}$ on the surface S now consisting of the wetted hull, S_H, plus (part of the) free surface, S_F. The corresponding boundary conditions require the normal velocity on the wetted hull and the pressure on the free surface to vanish identically, thus,

$$\left\{(M + \tfrac{1}{2}I + \mu N)\varphi\right\}_{S_H}(\mathbf{x}) = \varphi^{inc}(\mathbf{x}) + \mu v_n^{inc}(\mathbf{x}) + \left\{(L + \mu(M^T - \tfrac{1}{2}I))v_n\right\}_{S_F}(\mathbf{x}) \tag{F.73}$$

The following matrix-vector equation can be obtained,

$$\left(\mathbf{M} + \tfrac{1}{2}\mathbf{I} + \mu\mathbf{N}\right)_S \boldsymbol{\varphi}_S \cong \boldsymbol{\varphi}_S^{inc} + \mu\mathbf{v}_{n,S}^{inc} + \left(\mathbf{L} + \mu(\mathbf{M}^T - \tfrac{1}{2}\mathbf{I})\right)_S \mathbf{v}_{n,S} \tag{F.74}$$

$$\left[\left(\mathbf{M} + \tfrac{1}{2}\mathbf{I} + \mu\mathbf{N}\right)_{S_H} \quad \left(\mathbf{L} + \mu(\mathbf{M}^T - \tfrac{1}{2}\mathbf{I})\right)_{S_F}\right]\begin{bmatrix}\boldsymbol{\varphi}_{S_H} \\ \mathbf{v}_{n,S_F}\end{bmatrix} \cong$$
$$\cong \boldsymbol{\varphi}_S^{inc} + \mu\mathbf{v}_{n,S}^{inc} + \left[\left(\mathbf{M} + \tfrac{1}{2}\mathbf{I} + \mu\mathbf{N}\right)_{S_F} \quad \left(\mathbf{L} + \mu(\mathbf{M}^T - \tfrac{1}{2}\mathbf{I})\right)_{S_H}\right]\begin{bmatrix}\boldsymbol{\varphi}_{S_F} \\ \mathbf{v}_{n,S_H}\end{bmatrix} \tag{F.75}$$

In Eq. (F.75), $\left(\mathbf{M} + \tfrac{1}{2}\mathbf{I} + \mu\mathbf{N}\right)_{S_H}$ should be interpreted as being populated by the columns corresponding to the set of unknowns, $\boldsymbol{\varphi}_{S_H}$, and analogously for the other matrix elements and unknowns. In (our) case, where $\boldsymbol{\varphi}_{S_F} = \mathbf{v}_{n,S_H} = \mathbf{0}$, Eq. (F.75) simplifies to,

$$\left[\left(\mathbf{M} + \tfrac{1}{2}\mathbf{I} + \mu\mathbf{N}\right)_{S_H} \quad \left(\mathbf{L} + \mu(\mathbf{M}^T - \tfrac{1}{2}\mathbf{I})\right)_{S_F}\right]\begin{bmatrix}\boldsymbol{\varphi}_{S_H} \\ \mathbf{v}_{n,S_F}\end{bmatrix} \cong \boldsymbol{\varphi}_S^{inc} + \mu\mathbf{v}_{n,S}^{inc} \tag{F.76}$$

F.2 A BEM for 3D Exterior Radiation Problems

For the computation of the vibration-induced hull-surface pressure field, Burton and Miller's formulation, presented in Section F.1, must be recalled. There, the acoustic scattering

problem was treated, assuming that in the Helmholtz integral equation, i.e., Eq. (A.64) of Appendix A, surface vibrations are absent. However, the acoustic radiation problem assumes no incident waves, only surface vibrations. Therefore, Eq. (A.64) is directly applicable to the vibrating surface,

$$\frac{1}{2}\varphi(\mathbf{x}) = \int_{S_{DH}} \frac{\exp(ikr)}{4\pi r} v_n - \varphi(\mathbf{y})\frac{\partial}{\partial n_{\mathbf{y}}}\left(\frac{\exp(ikr)}{4\pi r}\right)dS_{\mathbf{y}} \tag{F.77}$$

where the caret and prime symbols, used to denote frequency domain and disturbance variables, respectively, have been omitted for convenience. Similar to the treatment of the scattering problem, the outward normal derivative on the boundary with respect to the point of observation is added to the Helmholtz integral equation,

$$\frac{1}{2}\frac{\partial\varphi(\mathbf{x})}{\partial n_{\mathbf{x}}} = \frac{1}{2}v(\mathbf{x}) = \frac{\partial}{\partial n_{\mathbf{x}}}\int_{S_{DH}} \frac{\exp(ikr)}{4\pi r} v_n - \varphi(\mathbf{y})\frac{\partial}{\partial n_{\mathbf{y}}}\left(\frac{\exp(ikr)}{4\pi r}\right)dS_{\mathbf{y}} \tag{F.78}$$

The integral operator notation introduced in Eqs. (F.10) and (F.11) must now be extended with,

$$\{L\varphi\}_{S_{DH}}(\mathbf{x}) = \int_{S_{DH}} G_H(|\mathbf{x} - \mathbf{y}|)\varphi(\mathbf{y})dS_{\mathbf{y}} \tag{F.79}$$

and

$$\{M_k^T\varphi\}_{S_{DH}}(\mathbf{x}) = \frac{\partial}{\partial n_{\mathbf{x}}}\int_{S_{DH}} G_H(|\mathbf{x} - \mathbf{y}|)\varphi(\mathbf{y})dS_{\mathbf{y}} \tag{F.80}$$

Thus, Burton and Miller's formulation for the acoustic radiation problem becomes,

$$\{(M - \tfrac{1}{2}I + \mu N)\varphi\}_{S_{DH}}(\mathbf{x}) = \{(L + \mu(M_k^T + \tfrac{1}{2}I))v\}_{S_{DH}}(\mathbf{x}) \tag{F.81}$$

Once Eq. (F.81) is solved for $\varphi(\mathbf{x}) \in S_{DH}$, $\varphi(\mathbf{x}) \in V$ can be computed through standard quadrature,

$$\varphi(\mathbf{x}) = \{M\varphi\}_{S_{DH}}(\mathbf{x}) - \{Lv\}_{S_{DH}}(\mathbf{x}) \quad (\mathbf{x} \in V) \tag{F.82}$$

The vibration-induced pressure at a certain frequency is then obtained by Eq. (A.24),

$$p = i\omega\rho_0\varphi = ik\rho_0 c\varphi \tag{F.83}$$

F.2.1 Discretization of integral operators

As for the scattering problem, the boundary is approximated by a set of flat panels with the boundary functions taken as 'panel wise' constant. On each panel, one point is chosen as its collocation point at which the unknowns are actually evaluated. Thus, the operators

become $N' \times N'$ matrices in case of N' collocation points, $\mathbf{x}_i$. This yields the following matrix-vector equation,

$$\left[\mathbf{M} - \tfrac{1}{2}\mathbf{I} + \mu\mathbf{N}\right]_{S_{DH}} \boldsymbol{\varphi}_{S_{DH}} \cong \left[\mathbf{L} + \mu(\mathbf{M}^T + \tfrac{1}{2}\mathbf{I})\right]_{S_{DH}} \mathbf{v}_{S_{DH}} \tag{F.84}$$

For external locations, Eq. (F.82) becomes,

$$\boldsymbol{\varphi}_S \cong \mathbf{M}_V \boldsymbol{\varphi}_S - \mathbf{L}_V \mathbf{v}_S \tag{F.85}$$

As for the scattering problem, the integration over each panel, $\tilde{S}_i$, is performed by mapping the panel onto the standard shape of a square with sides of length two. A standard numerical integration technique is used to evaluate the integral over the standard shape. In case the integrals are singular this approach fails. In Section F.1.2, this problem is addressed in detail for scattering. It is repeated here for the case of radiation. First, a number of useful properties of the kernel functions are recalled (cf. Eqs. (F.21) to (F.28)).

Flat boundary elements are used and it is assumed that the collocation points are not on edges. Then, by virtue of Eq. (F.25), the diagonal components of $\mathbf{M}_H^T$ are zero, just as $\mathbf{M}_H$. The diagonal components of the operators, $\mathbf{N}_H$ and $\mathbf{L}_H$, need to be worked out. For $\mathbf{N}_H$, it is referred to Section F.1.2, and for $\mathbf{L}_H$ the following integral needs to be solved,

$$I = \int_{\tilde{S}_i} G_L(|\mathbf{x} - \mathbf{y}|) \, dS_\mathbf{y} \tag{F.86}$$

Assume the element lies in the local x, y plane with $\mathbf{y} = \mathbf{y}(x, y)$ and $\mathbf{x} = \mathbf{y}(0,0)$. It is further assumed that the integral can be transformed to polar coordinates (R, θ). Thus, it is found that,

$$I = \frac{1}{4\pi} \int_0^{2\pi} R(\theta) \, d\theta = \frac{1}{4\pi} \sum_{n=1}^{4} \int_{\theta_n}^{\theta_{n+1}} R(\theta) \, d\theta \tag{F.87}$$

for a quadrilateral surface element, with $R(\theta)$ the radius of the element varying with θ. It is assumed that $\theta_5 = \theta_1$. Using Eqs. (F.37) to (F.40), Eq. (F.87) can be worked out to give,

$$
\begin{aligned}
4\pi I &= \sum_{n=1}^{4} B_n \int_{\theta_n}^{\theta_{n+1}} \frac{1}{\sin(\theta) - A_n \cos(\theta)} \, d\theta = \sum_{n=1}^{4} C_n \int_{\theta_n}^{\theta_{n+1}} \frac{1}{\cos(\theta)} \, d\theta = \\
&= \sum_{n=1}^{4} B_n \frac{\ln\left[\tan(\tfrac{1}{2}(\theta - \arctan(A_n)))\right]}{\sqrt{1 + A_n^2}} \Bigg|_{\theta_n}^{\theta_{n+1}} = \\
&= \sum_{n=1}^{4} \frac{B_n/2}{\sqrt{1 + A_n^2}} \ln\left(\frac{1 - \cos(\theta - \arctan(A_n))}{1 + \cos(\theta - \arctan(A_n))}\right) \Bigg|_{\theta_n}^{\theta_{n+1}} = \sum_{n=1}^{4} \frac{C_n}{2} \ln\left[\frac{1 + \sin(\theta)}{1 - \sin(\theta)}\right] \Bigg|_{\theta_n}^{\theta_{n+1}}
\end{aligned}
\tag{F.88}
$$

For the diagonal terms of the matrix, Eqs. (F.42) and (F.43) are used. For the integrands of the regularized part of L_H, a Taylor series expansion around frequency zero gives,

$$G_H - G_L = \frac{1}{4\pi} \sum_{m=1}^{\infty} \frac{(ik)^m}{m!} r^{m-1} = \sum_{m=1}^{\infty} \Gamma_m \qquad \text{(F.89)}$$

These expressions have to be accompanied by the Jacobian of the element transform procedure in Section F.1.4. To compute the off-diagonal terms of the matrices, Eq. (F.45) is used.

F.2.2 Thin body and double hull treatment

The treatment of the thin body problem was presented in Section F.1.5 for the exterior scattering problem. It is briefly repeated here for application to the exterior radiation problem. Burton and Miller's formulation for the exterior radiation problem, Eq.(F.81), at locations of the observer on the outside of the 'mid surface', reads,

$$\left\{(M + \mu N)\varphi\right\}_{S_{mid}}(\mathbf{x}) - \left\{(L + \mu(M_k^T + \tfrac{1}{2}I))v_n\right\}_{S_{mid}}(\mathbf{x}) = \tfrac{1}{2}\varphi(\mathbf{x}); \quad \mathbf{x} \in S_{mid} \qquad \text{(F.90)}$$

It has its counterpart in a formulation for the interior radiation problem, which, for locations of the observer on the inside of the mid surface, is written as,

$$-\left\{(M + \mu N)\varphi\right\}_{S_{mid}}(\mathbf{x}) + \left\{(L + \mu(M_k^T - \tfrac{1}{2}I))v_n\right\}_{S_{mid}}(\mathbf{x}) = \tfrac{1}{2}\varphi(\mathbf{x}); \quad \mathbf{x} \in S_{mid} \qquad \text{(F.91)}$$

Denoting the potential on the respective inside and outside of the thin bounding surface as, φ^- and φ^+, and adding Eqs. (F.91) and (F.90), yields,

$$\left\{(M + \mu N)(\varphi^+ - \varphi^-) - (L + \mu M_k^T)(v_n^+ - v_n^-)\right\}_{S_{mid}}(\mathbf{x}) =$$
$$= \tfrac{1}{2}(\varphi^+(\mathbf{x}) + \varphi^-(\mathbf{x})) + \tfrac{1}{2}\mu(v_n^+(\mathbf{x}) + v_n^-(\mathbf{x})); \quad \mathbf{x} \in S_{mid} \qquad \text{(F.92)}$$

For points on the surface, the equation can be split into two parts, depending on the coupling parameter,

$$\left\{M(\varphi^+ - \varphi^-) - L(v_n^+ - v_n^-)\right\}_{S_{mid}}(\mathbf{x}) = \tfrac{1}{2}(\varphi^+(\mathbf{x}) + \varphi^-(\mathbf{x})); \quad \mathbf{x} \in S_{mid} \qquad \text{(F.93)}$$

$$\left\{N(\varphi^+ - \varphi^-) - M_k^T(v_n^+ - v_n^-)\right\}_{S_{mid}}(\mathbf{x}) = \tfrac{1}{2}(v_n^+(\mathbf{x}) + v_n^-(\mathbf{x})); \quad \mathbf{x} \in S_{mid} \qquad \text{(F.94)}$$

Eqs. (F.93) and (F.94) constitute two equations for the potential jump across the mid surface from which the wanted potential on the outside of the thin body, i.e., φ^+, is found. After splitting S_{DH} into a thin part, S_t, and a regular part, S_r, it may be written,

$$\left\{M(\varphi^+ - \varphi^-) - L(v_n^+ - v_n^-)\right\}_{S_t}(\mathbf{x}) + \left\{M\varphi - Lv_n\right\}_{S_r}(\mathbf{x}) = \tfrac{1}{2}\varphi(\mathbf{x}); \quad \mathbf{x} \in S_r \tag{F.95}$$

$$\left\{M(\varphi^+ - \varphi^-) - L(v_n^+ - v_n^-)\right\}_{S_t}(\mathbf{x}) + \left\{M\varphi - Lv_n\right\}_{S_r}(\mathbf{x}) = \tfrac{1}{2}(\varphi^+(\mathbf{x}) + \varphi^-(\mathbf{x})); \quad \mathbf{x} \in S_t \tag{F.96}$$

$$\left\{N(\varphi^+ - \varphi^-) - M_k^T(v_n^+ - v_n^-)\right\}_{S_t}(\mathbf{x}) + \left\{N\varphi - M_k^T v_n\right\}_{S_r}(\mathbf{x}) = \tfrac{1}{2}(v_n^+(\mathbf{x}) + v_n^-(\mathbf{x})); \quad \mathbf{x} \in S_t \tag{F.97}$$

Now, Eqs. (F.95) and (F.97) have to be solved simultaneously on S_{DH} yielding the potential on S_r and the potential jump on S_t. Then, Eq. (F.96) can be used to determine the potential sum on S_t after which the potential there readily follows. Often, it may be assumed that $v_n^+ = v_n^-$. Then,

$$\left\{M(\varphi^+ - \varphi^-)\right\}_{S_t}(\mathbf{x}) + \left\{M\varphi - Lv_n\right\}_{S_r}(\mathbf{x}) = \tfrac{1}{2}\varphi(\mathbf{x}); \quad \mathbf{x} \in S_r \tag{F.98}$$

$$\left\{M(\varphi^+ - \varphi^-)\right\}_{S_t}(\mathbf{x}) + \left\{M\varphi - Lv_n\right\}_{S_r}(\mathbf{x}) = \tfrac{1}{2}(\varphi^+(\mathbf{x}) + \varphi^-(\mathbf{x})); \quad \mathbf{x} \in S_t \tag{F.99}$$

$$\left\{N(\varphi^+ - \varphi^-)\right\}_{S_t}(\mathbf{x}) + \left\{N\varphi - M_k^T v_n\right\}_{S_r}(\mathbf{x}) = v_n(\mathbf{x}); \quad \mathbf{x} \in S_t \tag{F.100}$$

For nearly horizontal panels close to the free surface, the thin body problem may reoccur. Let us call this part of S_t, $S_{t,fs}$. On this surface, Eqs. (F.93) and (F.94) become,

$$\left\{M\varphi\right\}_{S_{t,fs}}(\mathbf{x}) = 0; \quad \mathbf{x} \in S_{t,fs} \tag{F.101}$$

$$\left\{2N\varphi\right\}_{S_{t,fs}}(\mathbf{x}) = v_n(\mathbf{x}); \quad \mathbf{x} \in S_{t,fs} \tag{F.102}$$

Finally, instead of Eqs. (F.98), (F.99) and (F.100), it follows,

$$\left\{2M\varphi\right\}_{S_{t,fs}} + \left\{M(\varphi^+ - \varphi^-) - L(v_n^+ - v_n^-)\right\}_{S_{t\backslash t,fs}} + \left\{M\varphi - Lv_n\right\}_{S_r} = \tfrac{1}{2}\varphi \text{ on } S_r \tag{F.103}$$

$$\left\{2M\varphi\right\}_{S_{t,fs}} + \left\{M(\varphi^+ - \varphi^-) - L(v_n^+ - v_n^-)\right\}_{S_{t\backslash t,fs}} + \left\{M\varphi - Lv_n\right\}_{S_r} = \tfrac{1}{2}(\varphi^+ + \varphi^-) \text{ on } S_{t\backslash t,fs} \tag{F.104}$$

$$\left\{2M\varphi\right\}_{S_{t,fs}} + \left\{M(\varphi^+ - \varphi^-) - L(v_n^+ - v_n^-)\right\}_{S_{t\backslash t,fs}} + \left\{M\varphi - Lv_n\right\}_{S_r} = 0 \text{ on } S_{t,fs} \tag{F.105}$$

$$\left\{2N\varphi\right\}_{S_{t,fs}} + \left\{N(\varphi^+ - \varphi^-) - M_k^T(v_n^+ - v_n^-)\right\}_{S_{t\backslash t,fs}} + \left\{N\varphi - M_k^T v_n\right\}_{S_r} = \tfrac{1}{2}(v_n^+ + v_n^-) \text{ on } S_{t\backslash t,fs} \tag{F.106}$$

$$\left\{2N\varphi\right\}_{S_{t,fs}} + \left\{N(\varphi^+ - \varphi^-) - M_k^T(v_n^+ - v_n^-)\right\}_{S_{t\backslash t,fs}} + \left\{N\varphi - M_k^T v_n\right\}_{S_r} = v_n(\mathbf{x}) \text{ on } S_{t,fs} \tag{F.107}$$

Now, Eqs. (F.103), (F.106) and (F.105) or (F.107) have to be solved simultaneously on S_{DH} yielding the potential on S_r and $S_{t,fs}$ as well as the potential jump on $S_{t\backslash t,fs}$. Then, Eq. (F.104) can be used to determine the potential sum on $S_{t\backslash t,fs}$ after which the potential follows.

G MATHEMATICAL BACKGROUND

…which gives an overview of a few of the mathematical principles used in describing the theoretical methods in hydroacoustics.

G.1 Generalized Functions

Dirac's delta function, δ , is a generalized function defined by,

$$\delta(y) = 0 \quad \text{for} \quad y \neq 0 \qquad \wedge \qquad \int_{-\infty}^{+\infty} \delta(y)\, dy = 1 \tag{G.1}$$

and its sifting property on a test function, h ,

$$\int_{-\infty}^{+\infty} h(y)\delta(x - y)\, dy = h(x) \tag{G.2}$$

The concept of Dirac's delta function can be extended to three dimensions through,

$$\delta(\mathbf{x} - \mathbf{y}) = \delta(x_i - y_i) = \delta(x_1 - y_1)\delta(x_2 - y_2)\delta(x_3 - y_3) \tag{G.3}$$

with indices denoting Cartesian coordinates and boldface referring to vectors. A useful scaling property reads,

$$\delta(g(x)) = \frac{\delta(x - x_0)}{\left|\dfrac{dg}{dx}(x_0)\right|} \quad \text{if} \quad g(x_0) = 0 \quad \wedge \quad \frac{dg}{dx}(x_0) \neq 0 \tag{G.4}$$

The Dirac delta function has a dimension equal to the inverse of the dimension of its argument. In hydroacoustic applications the argument, $g(x)$, of the delta function may have N roots, x_n, $n = 1..N$. Then, the following statement holds,

$$\int_{-\infty}^{+\infty} h(x)\delta(g(x))dx = \sum_{n=1}^{N} h(x_n)\left|\frac{dg}{dx}(x_n)\right|^{-1} \tag{G.5}$$

Another useful generalized function is the *Heaviside step function*, H ,

$$H(x) = \begin{cases} 1 & \text{for} \quad x > 0 \\ 1/2 & \text{for} \quad x = 0 \\ 0 & \text{for} \quad x < 0 \end{cases} \tag{G.6}$$

In a generalized sense this function becomes differentiable even at the origin,

$$\frac{dH}{dx} = \delta(x) \tag{G.7}$$

or, more generally,

$$\frac{\partial}{\partial x_i} H(f(x_i, t)) = \frac{dH}{df} \frac{df}{dx_i} = \frac{df}{dx_i} \delta(f) \tag{G.8}$$

G.2 Retarded Time

Many of the formulations that are encountered in theoretical acoustics involve the evaluation of time functions at the so-called *retarded time*, τ ,

$$\tau = t - |\mathbf{x} - \mathbf{y}|/c = t - \frac{r}{c} \tag{G.9}$$

through which 'memory' effects, caused by the fluid's finite *phase velocity*, c , (i.e., the speed of sound) become apparent. In Eq. (G.9), t is time and $\mathbf{r}$ denotes the position vector pointing from $\mathbf{y}$ to $\mathbf{x}$. The distance, $|\mathbf{r}|$, is written as r . Often, it appears that quantities in integrands have to be evaluated at certain retarded times. Then, the expressions involved are placed between brackets, like $\left[\cdots\right]_{ret}$, $\left[\cdots\right]_{\tau}$, or $\left[\cdots\right]_{t-r/c}$.

G.3 Green's Identities

Take $\mathbf{F}$ to be a continuously differentiable vector field, defined in a compact region, V , which is part of $\mathbb{R}^3$ and has a piecewise smooth boundary, S . Then, *Gauss' theorem* can be stated as,

$$\int_V \nabla \cdot \mathbf{F} \, dV = \int_S \mathbf{F} \cdot \mathbf{n} \, dS \tag{G.10}$$

with $\mathbf{n}$ as the unit normal vector to the boundary pointing *outward* with respect to V . Next, assume $\mathbf{F}$ to be defined in V by two scalar functions, ψ and φ , being twice continuously differentiable, as $\mathbf{F} = \psi \nabla \varphi$. Inserting this into Eq. (G.10), and noting that

$$\frac{\partial\varphi}{\partial n} = \mathbf{n} \cdot \nabla\varphi \tag{G.11}$$

yields *Green's first identity*,

$$\int_V \psi\nabla^2\varphi\, dV = \int_S \psi\frac{\partial\varphi}{\partial n}\, dS - \int_V \nabla\psi \cdot \nabla\varphi\, dV \tag{G.12}$$

If ψ is also twice continuously differentiable in V, a vector field, $\mathbf{G}$, can be defined, analogous to $\mathbf{F}$, as $\mathbf{G} = \varphi\nabla\psi$. When Green's first identity based on $\mathbf{G}$ is subtracted from the one based on $\mathbf{F}$, i.e., Eq. (G.12), *Green's second identity* is obtained,

$$\int_V \psi\nabla^2\varphi - \varphi\nabla^2\psi\, dV = \int_S \psi\frac{\partial\varphi}{\partial n} - \varphi\frac{\partial\psi}{\partial n}\, dS \tag{G.13}$$

Finally, if ψ is chosen equal to G_L, the Green's function for the Laplace equation (see Section A.2), then $\nabla^2\psi(\mathbf{x},\mathbf{y}) = \delta(\mathbf{x} - \mathbf{y})$ and *Green's third identity* follows as,

$$\int_S \varphi(\mathbf{y})\frac{\partial G_L}{\partial n_\mathbf{y}} - G_L\frac{\partial\varphi}{\partial n_\mathbf{y}}\, dS_\mathbf{y} + \int_V G_L\nabla^2\varphi(\mathbf{y})\, dV_\mathbf{y} = c(\mathbf{x})\varphi(\mathbf{x}) \tag{G.14}$$

Here, the subscript $\mathbf{y}$ is used to indicate the integration variable. In Eq. (G.14) and elsewhere in this thesis, the field point, $\mathbf{x}$, is assumed to be on a smooth part of the boundary. Then,

$$c(\mathbf{x}) = \begin{cases} 1 \text{ for } \mathbf{x} \in V \\ 1/2 \text{ for } \mathbf{x} \in S \\ 0 \text{ for } \mathbf{x} \notin (S \cup V) \end{cases} \tag{G.15}$$

G.4 Singular Value Decomposition

In the following, the *Singular Value Decomposition* (SVD) technique is briefly explained, relying on [Visser2004] and the Intel® Math Kernel Library reference manual. Suppose a set of linear algebraic equations relate n unknowns by m equations. If $n = m$ and one or more of the m equations is a linear combination of the others, then there may not be a unique solution. The set of equations is said to be singular. On the other hand, if some of the equations are nearly singular, accumulating round-off errors in the solution process can cause errors. If $m < n$, then there are effectively fewer equations than unknowns. In this case there can be either no solution or more than one. In the opposite case, $m > n$, there are more equations than unknowns. When this occurs there exists, in general, no solution vector and the set of equations is overdetermined. Nevertheless, obtaining the best approximation to the set of equations is often still useful. Finding such an approximation comes down to solving the set of equations in a linear least-squares sense using SVD.

In SVD, the $m \times n$ matrix $\mathbf{A}$ for which $m \geq n$, is written as the product of an $m \times n$ column-orthogonal matrix $\mathbf{U}$, an $n \times n$ diagonal matrix $\mathbf{W}$ with positive or zero elements (i.e., the singular values), and an $n \times n$ orthogonal matrix $\mathbf{V}$,

$$\mathbf{A} = \mathbf{U} \cdot \mathbf{W} \cdot \mathbf{V^T} \tag{G.16}$$

When $m \leq n$, the singular values for $i = m+1..n$ are all zero and the corresponding columns of $\mathbf{U}$ are also zero. It follows,

$$\mathbf{A^{-1}} = \mathbf{V} \cdot \mathbf{W^{-1}} \cdot \mathbf{U^T} \tag{G.17}$$

with $\mathbf{W^{-1}}$ containing the reciprocals of the singular values w_i.

After applying SVD, the least-squares solution $\mathbf{x}_{LS}$ to the system of equations,

$$\mathbf{A} \cdot \mathbf{x} = \mathbf{b} \tag{G.18}$$

may be written as

$$\mathbf{x}_{LS} = \mathbf{V} \cdot \mathbf{W^{-1}} \cdot \left(\mathbf{U}^T \cdot \mathbf{b} \right) = \sum_{i=1}^{n} \frac{\mathbf{u}_i^T \cdot \mathbf{b}}{w_i} \mathbf{v}_i \tag{G.19}$$

with $\mathbf{u}_i$ as the columns of $\mathbf{U}$, etc. In the context of the present thesis, the singular vectors $\mathbf{u}_i$ and $\mathbf{v}_i$ can be interpreted as 'mode shapes' of the surface pressure and point source strength distribution in the field, respectively. Through Eq. (G.19), the singular values couple each 'surface mode' of pressure independently to the corresponding 'field mode' of source strength. In other words, the columns of $\mathbf{U}$ whose same-numbered singular values are unequal to zero form an orthonormal set of basis vectors that span the range of $\mathbf{A}$. The columns of $\mathbf{V}$ whose same-numbered singular values are zero form an orthonormal basis for the null-space.

An important aspect of SVD is that the singular vectors become increasingly oscillatory and the singular values increasingly small as the index i becomes higher. Therefore, the solution vector $\mathbf{x}_{LS}$ may be made up of strongly oscillating modes that are amplified by the reciprocal value of the corresponding increasingly small singular value. Regularization is then called for. In its simplest form it comes down to zeroing the singular values that are too small so that the corresponding modes do not enter the solution vector anymore.

In order to check the existence of a physically meaningful solution to the inverse problem and to ensure that this solution can be approximated by a regularized solution, it is necessary to satisfy the discrete Picard condition (see [Visser2004]), which states that the exact SVD coefficients $\left| \mathbf{u}_i^T \cdot \mathbf{b} \right|$ decay faster than the singular values w_i. If the Picard condition is met then one can obtain a least-squares solution to the problem after 'filtering out' one or more of the higher modes by setting their contribution to zero. Obviously, this has a smoothening effect on the solution, just as after applying a low-pass filter to measured time series data. If there exists a useful (i.e., physically interpretable, realistic) 'smooth' solution, then SVD and subsequent regularization will generally work.

H COMPUTATIONAL RESULTS

…which collects, for reference purposes, computational results obtained from the mathematical method detailed in Chapter 3 and validated in Chapter 6.
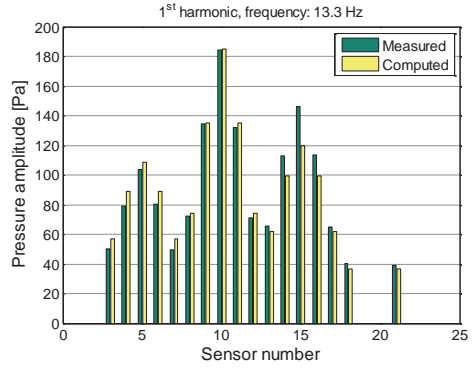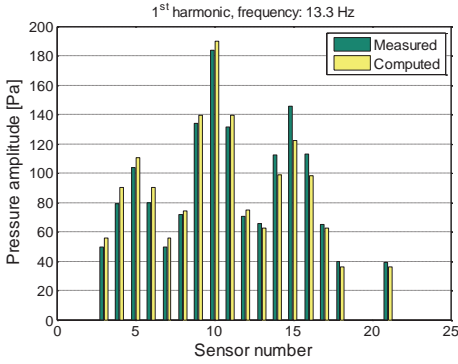
H.1 Validation of New Coupling Procedure

Figure H.1: First order pressure amplitudes for 2-bladed propeller, no. 6666, at RPM: 400, Thrust: K_t =0.023, Draft: 0.419 m (left), 0.531 m (right).
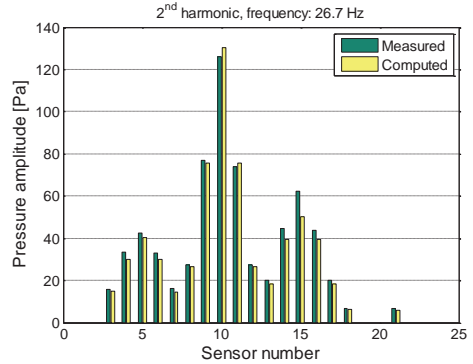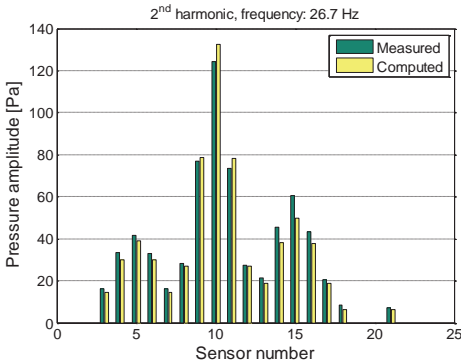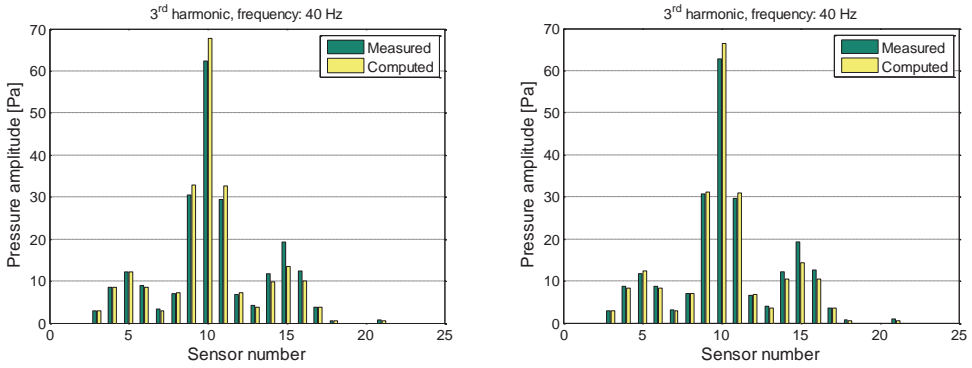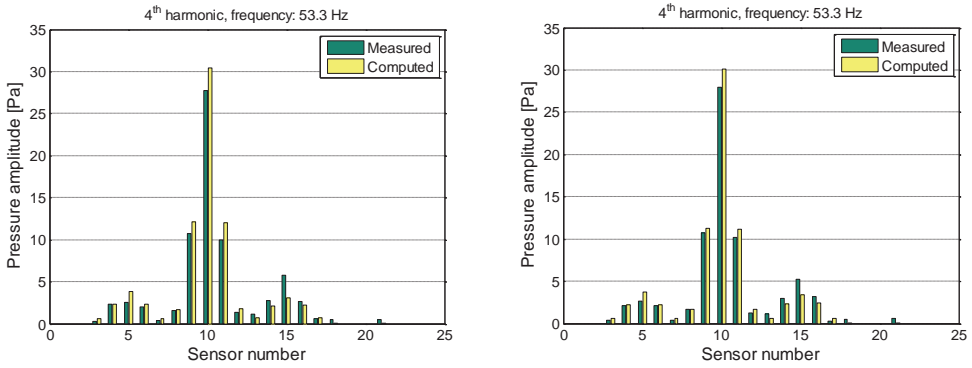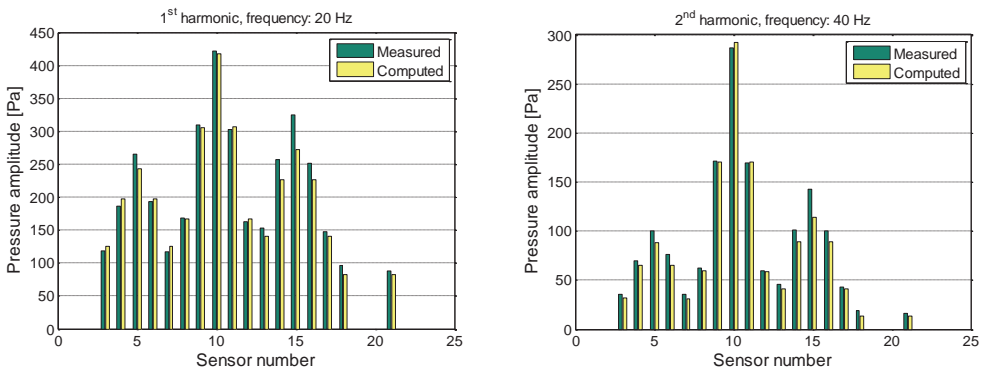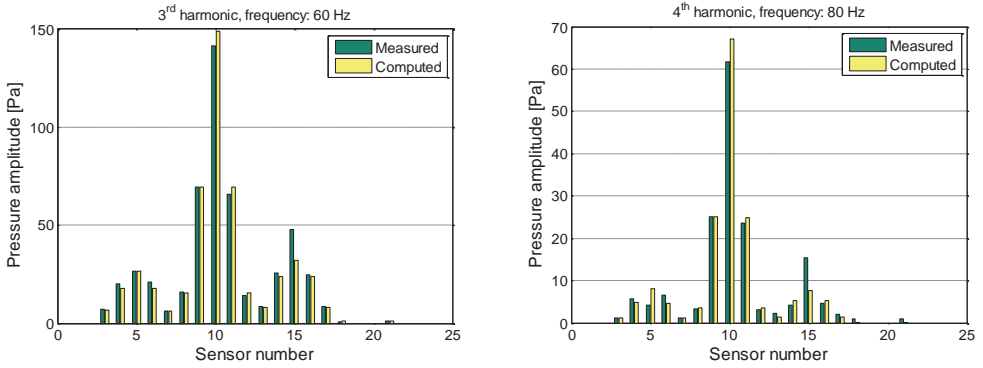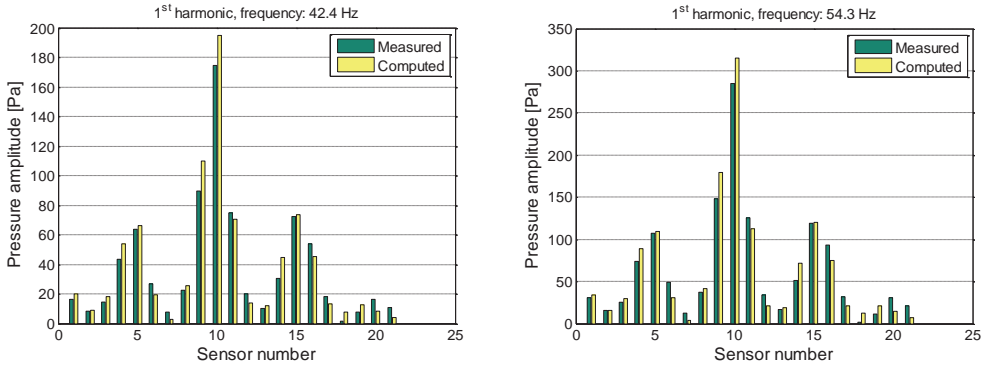

Figure H.2: Second order pressure amplitudes for 2-bladed propeller, no. 6666, at RPM: 400, Thrust: K_t =0.023, Draft: 0.419 m (left), 0.531 m (right).

Figure H.3: Third order pressure amplitudes for 2-bladed propeller, no. 6666, at RPM: 400 Hz, Thrust: K_t =0.023, Draft: 0.419 m (left), 0.531 m (right).

Figure H.4: Fourth order pressure amplitudes for 2-bladed propeller, no. 6666, at RPM: 400, Thrust: K_t =0.023, Draft: 0.419 m (left), 0.531 m (right).

Figure H.5: First and second order pressure amplitudes for 2-bladed propeller, no. 6666, at RPM: 600, Thrust: K_t =0.021, Draft: 0.531 m.

Figure H.6: Third and fourth order pressure amplitudes for 2-bladed propeller, no. 6666, at RPM: 600, Thrust: K_t **=0.021, Draft: 0.531 m.**

Figure H.7: First harmonic pressure amplitudes for 5-bladed propeller, no. 6553, at RPM: 509, Thrust: K_t **=0.210, (left); RPM: 652, Thrust:** K_t **=0.191, (right).**
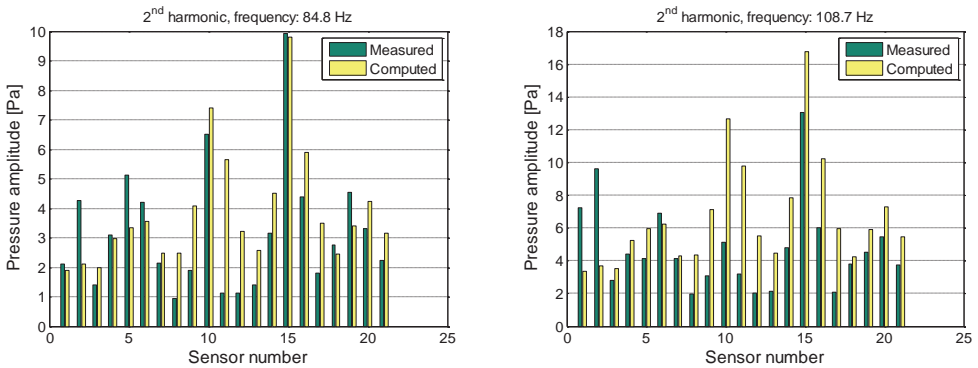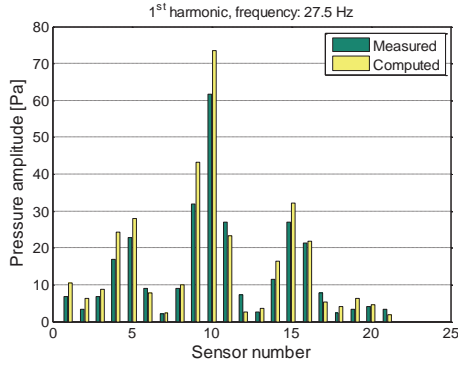

Figure H.8: Second harmonic pressure amplitudes for 5-bladed propeller, no. 6553, at RPM: 509, Thrust: K_t **=0.210, (left); RPM: 652, Thrust:** K_t **=0.191, (right).**

Figure H.9: First harmonic pressure amplitudes for 5-bladed propeller, no. 6553, at RPM: 330, Thrust: K_t =0.009.
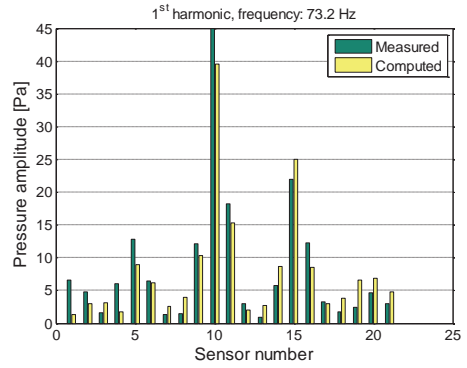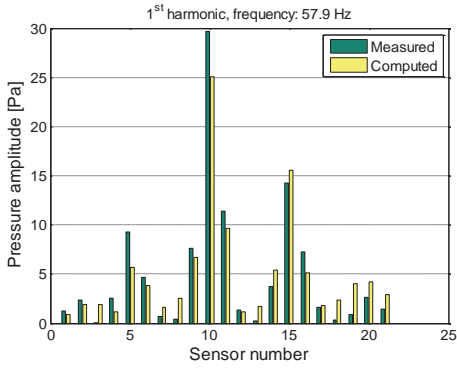

Figure H.10: First harmonic pressure amplitudes for 6-bladed propeller, no. 6724, at RPM: 579, Thrust: K_t =0.204 (left); RPM: 732, Thrust: K_t =0.182 (right).
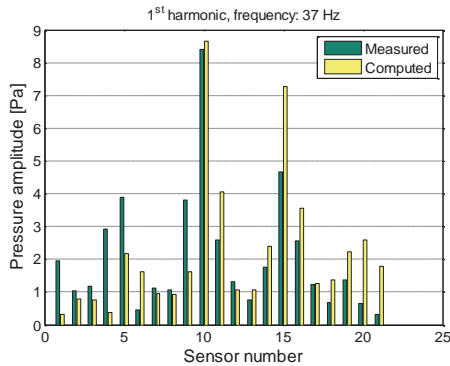

Figure H.11: First harmonic pressure amplitudes for 6-bladed propeller, no. 6724, at RPM: 370, Thrust: K_t =-0.010.
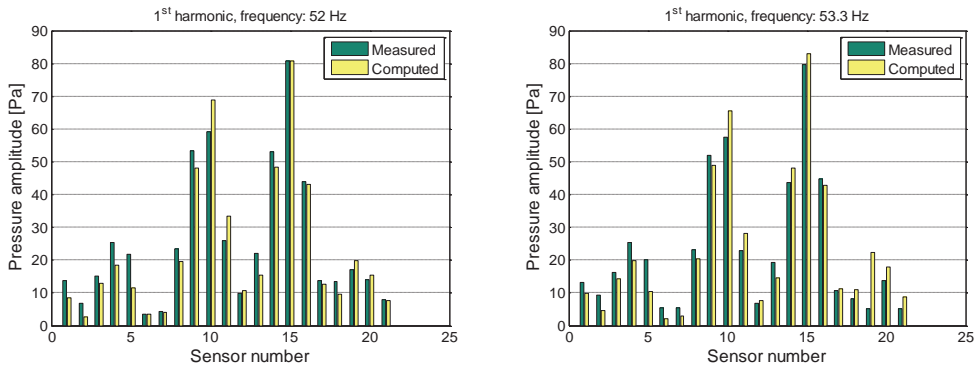
Figure H.12: First harmonic pressure amplitudes for 4-bladed propeller, no. 6458, at RPM: 780, Thrust: K_t =0.146 (left); RPM: 800, Thrust: K_t =0.084 (right).
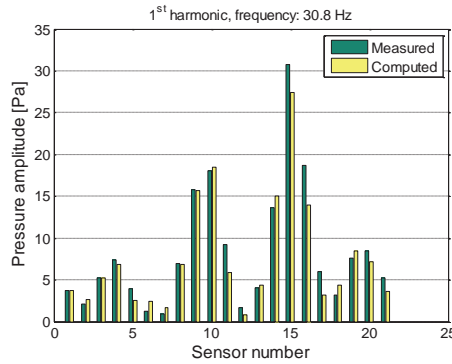

Figure H.13: First harmonic pressure amplitudes for 4-bladed propeller, no. 6458, at RPM: 462, Thrust: K_t =0.004.
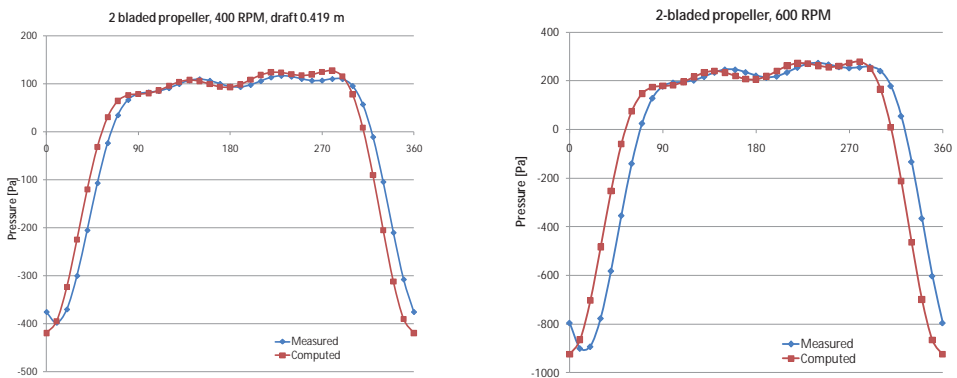

Figure H.14: Pressure time trace of one blade passage based on 4 orders of BPF for 2-bladed propeller, no. 6666.

Figure H.15: Pressure time trace of one blade passage based on 4 orders of BPF for 5-bladed propeller, no. 6553.
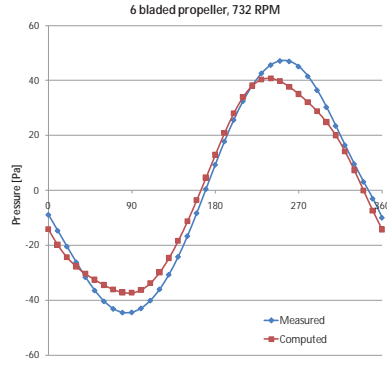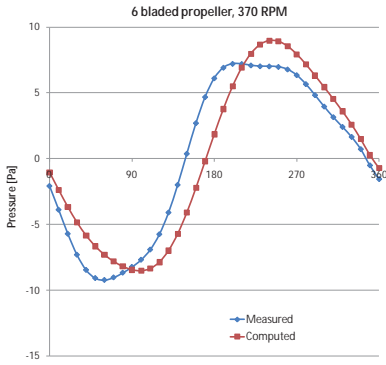
Figure H.16: Pressure time trace of one blade passage based on 4 orders of BPF for 6-bladed propeller, no. 6724.
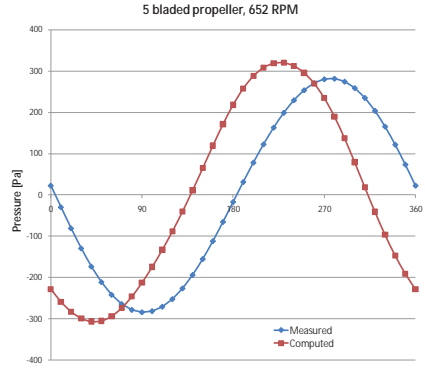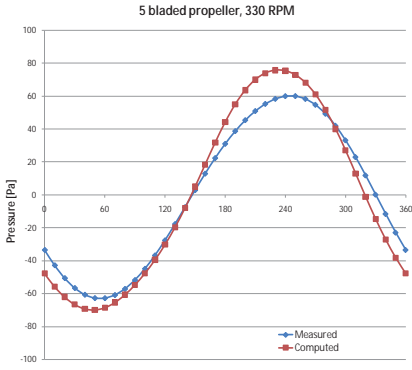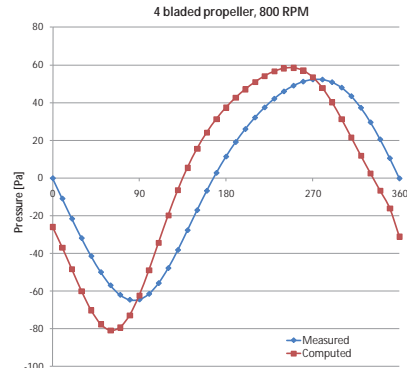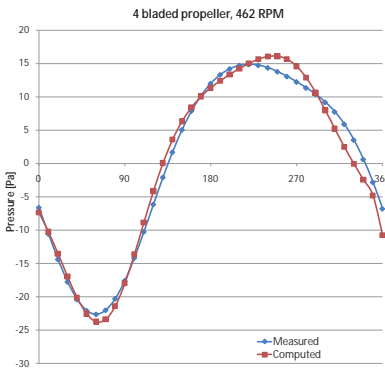
Figure H.17: Pressure time trace of one blade passage based on 4 orders of BPF for 4-bladed propeller, no. 6458.

H.2 Validation of SBF Coupling Procedure
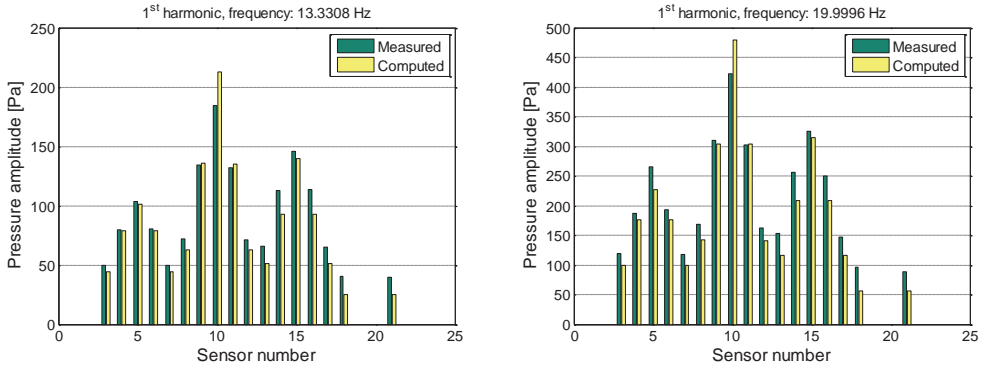
Figure H.18: First harmonic pressures for 2-bladed propeller, no. 6666, at RPM: 400 (left), 600 (right).
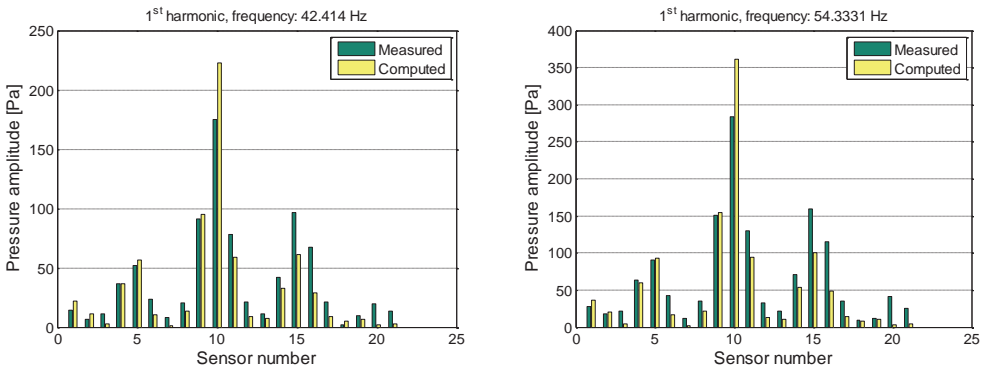
Figure H.19: First harmonic pressures for 5-bladed propeller, no. 6553, at RPM: 509 (left), 652 (right).
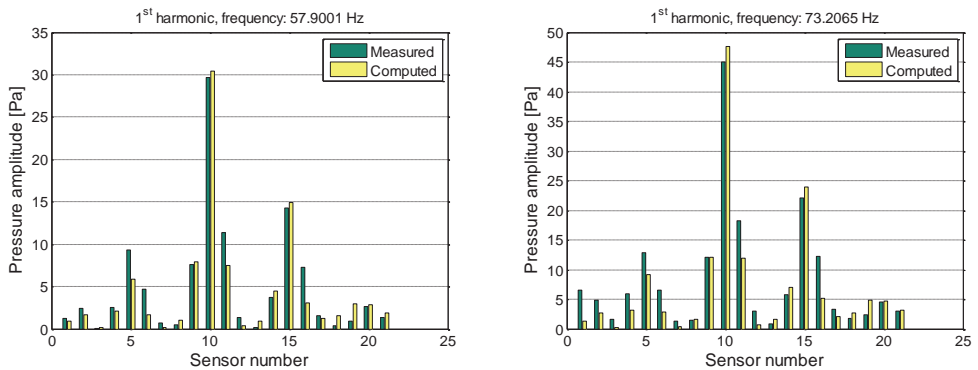
Figure H.20: First harmonic pressures for 6-bladed propeller, no. 6724, at RPM: 579 (left), 732 (right).
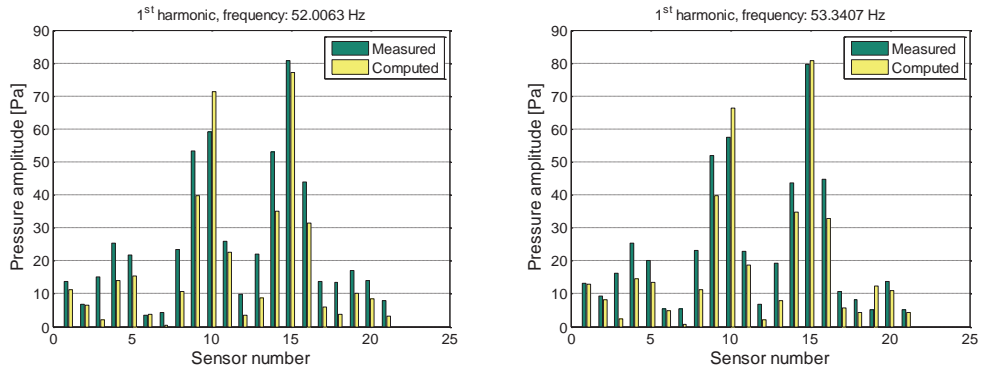
**Figure H.21: First harmonic pressures for 4-bladed propeller,
no. 6458, at RPM: 780 (left), 800 (right).**

REFERENCES

Asmussen, I.; Menzel, W.; Mumm, H.: 2001, *Ship Vibration*, GL's 'Technology', Issue No. 5/2001.

Astley, R.J.; Bain, J.G.: 1986, *A three-dimensional boundary element scheme for acoustic radiation in low Mach number flows*, Journal of Sound and Vibration, 1986, 109(3), pp. 445-465.

Bailly, C.; Bogey, C.: 2006, *An overview of numerical methods for acoustic wave propagation*, ECCOMAS CFD 2006, TU Delft, The Netherlands.

Bertram, V.: 2000, *Practical ship hydrodynamics*, ASIN 0750648511, ISBN 9780750648516 Butterworth-Heinemann.

**Bloor, C.D.: 2001**, *A study of the acoustic pressures on a ship's hull due to its propellers*, PhD thesis, University of Cambridge, UK.

Bosschers, J.: 2007, *Broadband hull pressure fluctuations and cavitating vortices – an investigation of resonance frequencies*, 3rd int. ship noise and vibration conf., Marine Eng. Forum, Propeller Cavitation Workshop, September 2007, London, UK.

Bosschers, J.: 2008, *Analysis of inertial waves on inviscid cavitating vortices in relation to low-frequency radiated noise*, WIMRC Cavitation Forum, Warwick Univ., UK, 7-9 July, 2008.

Bosschers, J.: 2009a, *Investigation of the resonance frequency of a cavitating vortex*, NAG/DAGA 2009 Int. conf. on acoustics, March 2009, Rotterdam, The Netherlands.

Bosschers, J.: 2009b, *Investigation of hull pressure fluctuations generated by cavitating vortices*, First Int. Symp. on Marine Propulsors SMP'09, Trondheim, Norway, June 2009.

Bosschers, J.: 2009c, *Modeling and analysis of a cavitating vortex in 2D unsteady viscous flow*, CAV2009, Ann Arbor, Michigan, U.S.A., Sept. 2009.

Brentner, K.S.: 1986, *Prediction of Helicopter Rotor Discrete Frequency Noise*, NASA Tech. Mem. 87721.

Brentner, K.S.: 1990, *The sound of moving bodies*, PhD thesis, Corpus Christi College, U.S.A.

Brentner, K.S.: 1997, *An analytical comparison of the acoustic analogy and Kirchhoff formulation for moving surfaces*, 53rd annual forum of the American Helicopter Society, Virginia Beach, VI, U.S.A.

Brentner, K.S.; Farassat, F.: 1998, *An analytical comparison of the acoustic analogy and Kirchhoff formulation for moving surfaces*, AIAA Journal, Vol. 36, No. 8, August 1998, pp. 1379-1386.

Breslin, J.P.; Andersen, P.: 1994, *Hydrodynamics of ship propellers*, Cambridge ocean technology series 3, ISBN 0-521-41360-5, Cambridge University Press, UK.

Brouwer, J.: 2005, *Ship propeller-induced noise and vibrations* – prediction and analysis, MSc thesis, University of Twente, NL.

Burton, A.J.; Miller, G.F.: 1971, *The application of integral equation methods to the numerical solution of some exterior boundary value problems*, Proc. Royal Society, London, A323, pp. 201-210.

Carlton, J.S.: 1994, *Marine Propellers & Propulsion*, Butterworth-Heinemann, ISBN 0-7506-1143-X, figure 5.9, page 70.

Denny, S.B.: 1967, *Comparisons of experimentally determined and theoretically predicted pressures in the vicinity of a marine propeller*, NSRDC Report 2349.

DnV: 2003, *Comfort Class*, Part 5, Chapter 12 from *Rules for Classification of Ships*, January 2003.

Dowling, A.P.; Ffowcs Williams, J.E.: 1983, *Sound and Sources of Sound*, Ellis Horwood Publishers, 1983, ISBN 0-85312-527-9.

Ehrenfried, K.: 2003, *Skript zur Vorlesung Strömungsakustik I & II*, TU Berlin (in German).

Farassat, F.; Myers, M.K.: 1988, *Extension of Kirchhoff's formula to radiation from moving surfaces*, Journal of Sound and Vibration, Vol. 123, No. 3, pp. 451-461.

Ffowcs Williams, J.E.; Hawkings, D.L.: 1969, *Sound generated by turbulence and surfaces in arbitrary motion*, Philosophical Transactions of the Royal Society, Series A, 264, No. 1151, pp. 321-342.

Fine, N.E.: 1992, *Non-linear Analysis of Cavitating Propellers in Non-uniform Flow*, PhD thesis, MIT, October 1992.

Fine, N.E.; Kinnas, S.A.: 1993, *The nonlinear numerical prediction of unsteady sheet cavitation for propellers of extreme geometry*, 6th SNH, May 1993.

Francescantonio, P. di: 1997, *A new boundary integral formulation for the prediction of sound radiation*, Journal of Sound and Vibration (1997) 202(4), 491-509.

Francescantonio, P. di; Casalino, D.: 1999, *Green's function discretization scheme for sound propagation in nonuniform flows*, AIAA Journal, Vol. 37, No. 10.

Friesch, J.; Johannsen, C.: 1992, *Correlation Investigations in the New Hydrodynamics and Cavitation Tunnel (HYKAT)*, STG/HSVA Intern. Symp. on Propulsors and Cavitation, Hamburg, Germany.

Gennaretti, M.; Iemma, U.: 2006, *Prediction of sound scattered by moving bodies with applications to propeller-driven airplanes*, 12th AIAA/CEAS Aeroacoustics Conference (27th AIAA Aeroacoustics Conference), paper AIAA 2006-2475, 8-10 May, 2006, Cambridge Massachusetts, U.S.A.

Gent, W. van; Salvati, G.A.Q.; Wijngaarden, H.C.J. van: 1989, *Response of elastic, flat plate to cavitation*, Int. Symp. on Cavitation Noise and Erosion in Fluid Systems, ASME.

Gutin, L.: 1936/1948, On the sound field of a rotating propeller, National Advisory Committee for Aeronautics, Tech. Memorandum No. 1195, October, 1948. Translation of "Über das Schallfeld einer rotierenden Luftschraube", Physikalische Zeitschrift der Sowjetunion, Band 9, Heft 1, 1936.

Hoekstra, M.: 1977a, *Experimental results of a boundary layer suction method*, NSMB report W12001-1-VT, June 1977.

Hoekstra, M.: 1977b, *Experimental results of an improved boundary layer suction method*, NSMB report W12001-2-VT, September 1977.

Hoshino, T.: 1991, *A surface panel method with a deformed wake model to analyze hydrodynamic characteristics of propellers in steady flow*, Mitsubishi Technical Bulletin, No. 195, April 1991.

Hoshino, T.: 1993, *Hydrodynamic analysis of propellers in unsteady flow using a surface panel method*, Journal of The Soc. of Nav. Arch. of Japan 174.

Howe, M.S.: 2003, *Theory of Vortex Sound*, Cambridge Univ. Press, 2003, ISBN 0-521-01223-6.

ISO 6954: 1984, *Mechanical vibration and shock – Guidelines for the overall evaluation of vibration in merchant ships*, ISO, 1984.

ISO 6954: 2000, *Mechanical vibration – Guidelines for the measurement, reporting and evaluation of vibration with regard to habitability on passenger and merchant ships*, ISO, 2000.

ISSC Committee II.2: 2006, Report on '*Dynamic Response*', 16th international ship and offshore structures congress, 20-25 August 2006, Southampton, UK.

ITTC: 1935, Proc. of the 3rd ITTC conference, Paris, France.

ITTC: 1960, Proc. of the 9th ITTC conference, Paris, France.

ITTC Cavitation Committee: 1966, Proc. of the 11th ITTC conf., Tokyo, Japan.

ITTC Cavitation Committee: 1969, Proc. of the 12th ITTC conf., Rome, Italy.

ITTC Propeller Committee: 1972, Proc. of the 13th ITTC conf., Berlin/Hamburg, Germany.

ITTC Propeller Committee: 1975, Proc. of the 14th ITTC conf., Ottawa, Canada.

ITTC Propeller Committee: 1990, Proc. of the 19th ITTC conf., Madrid, Spain.

ITTC Propeller Committee: 1993, Proc. of the 20th ITTC conf., San Francisco, California, U.S.A.

ITTC Propeller Committee: 1996, Proc. of the 21th ITTC conf., Trondheim, Norway.

ITTC Specialist Committee on Cavitation Induced Pressures: 1999, *Final Report and Recommendations to the 22nd* ITTC, Proc. of the 22nd ITTC, Seoul/Shanghai, Korea/China.

ITTC Specialist Committee on Cavitation induced Pressures: 2002, *Final Report and Recommendations to the 23th* ITTC, Proc. of the 23rd ITTC, Vol. 2, pp. 417-458, Venice, Italy.

ITTC Specialist Committee on Cavitation: 2008, *Report and Recommendations to the 25th ITTC*, Proc. of the 25th ITTC, Vol. 2, pp. 473-533, Sep. 14-20, Fukuoka, Japan.

Johannsen, C.: 1998, *Investigation of Propeller-Induced Pressure Pulses by Means of High-Speed Video Recording in the Three-Dimensional Wake of a Complete Ship Model*, 22nd ONR Symp. on Naval Hydrodynamics, Washington D.C., U.S.A.

Kampman, J.: 2005, *Ship Model Vibrations, reducing the influence of vibrations on pressure measurements*, MSc thesis, University of Twente, NL, March 2005.

Kawamura, T.; Kiyokawa, T.: 2008, *Numerical Prediction of Hull Surface Pressure Fluctuation Due to Propeller Cavitation*, Conf. Proc. of the Japan Society of Naval Architects and Ocean Engineers, Nagasaki, Japan, No. 6.

Keil, H.: 1965, *Messung der Druckschwankungen an der Außenhaut über dem Propeller, Forschungsschiff Meteor*, Schiff und Hafen, 1965, No. 12.

Kinnas, S.A.; Hsin, C-Y.: 1992a, *Boundary element method for the unsteady flow around extreme propeller geometries*, AIAA Journal, Vol. 30, No. 3, March 1992.

Kinnas, S.A.; Fine, N.E.: 1992b, *A nonlinear boundary element method for the analysis of unsteady propeller sheet cavitation*, 19th SNH.

Kinns, R.; Peake, N.; Rath Spivack, O.: 2003, *Hull vibration excitation by propeller sources: a link between hydrodynamics and marine acoustics*, Proc. 24th symp. naval hydrodynamics, July 8-13, 2002, Fukuoka, Japan.

Kinns, R.; Bloor, C.D.: 2004, *Hull vibration excitation due to monopole and dipole propeller sources*, J. of Sound and Vibration, Vol. 270, pp. 951-980.

Kirkup, S.M.: 1989, *Solution of exterior acoustic problems by the boundary element method*, Ph.D. thesis, University of Brighton, UK.

Költzsch, P.: 2000, *Strömungsakustik – eine aktuelle Übersicht*, preprint ET-IAS-01-2000 TU Dresden (Herausgeber: Der Rektor), Juli 2000, (in German).

Költzsch, P.: 2001, *Gebiete und offene Probleme der Aeroakustik*, in: Beiträge zur Strömungsmechanik. Herausgeber: W. Heller, J. Klingenberg. Festschrift zum 65. Geburtstag von Prof. Dr. R. Vollheim. ISBN 3-86005-276-4. Technische Universität Dresden 2001, S. 188 – 202 (in German).

Költzsch, P.: 2004, *Geräuscherzeugung durch Strömungen – Grundlagen und Überblick*, Vortrag zur Tagung "Aeroakustik", Kongresshotel Stuttgart, veranstaltet vom Haus der Technik Essen, 23. – 24. November 2004, Vortragsmappe, S. 1 – 41 (in German).

Kooij, J. van der: 1979, *Experimental determination of propeller-induced hydrodynamic hull forces in the NSMB Depressurized Towing Tank*, Proc. of the Symp. on Propeller Induced Ship Vibration, RINA, Dec. 10-13 1979, London, UK.

Lafeber (formerly Reus), F.H.: 2007, *Study into the computation of propeller-induced pressure fluctuations on the hull of a ship*, MSc thesis, University of Twente, NL.

Lafeber (formerly Reus), F.H.; Wijngaarden, E. van; Bosschers, J.: 2009, *Computation of hull-pressure fluctuations due to non-cavitating propellers*, Proc. of the 1st int. symp. on marine propulsors SMP'09, Trondheim, Norway, June 2009.

Lee, S.K.; Liao, M.; Wang, S.: 2006, *Propeller-induced hull vibration – analytical methods*, Proc. of the 2nd int. ship noise & vibration conf., June 28-29, London, UK.

Ligtelijn, J.T.; Wijngaarden, H.C.J. van; Moulijn, J.C.; Verkuyl, J.B.: 2004, *Correlation of cavitation: comparison of full-scale data with results of model tests and computations*, SNAME 2004 annual meeting, Washington D.C., U.S.A.

Ligtelijn, J.T.; Moulijn, J.; Otto, R.; Beek, T. van: 2006, *Propeller behaviour in relation to ship noise and vibration*, Proc. of the 2nd int. ship noise & vibration conf., June 28-29, London, UK.

Ligtelijn, J.T.: 2010, *The pay-off between cavitation and efficiency*, Proc. of IMarEST Ship Propulsion Systems Symp., January 27-28, London, UK.

Lighthill, M.J.: 1952, *On sound generated aerodynamically, I: General theory*, Proc. of the royal society, Series A, Vol. 211, No. 1107, pp. 564-587.

Lighthill, M.J.: 1954, *On sound generated aerodynamically, II: Turbulence as a source of sound*, Proc. of the royal society, Series A, Vol. 222, No. 1148, pp. 1-32.

Lowson, M.V.: 1965, *The sound field for singularities in motion*, Proc. R. Soc. Lond. A286, 559-572.

Lyrintzis, A.S.: 2003, *Surface integral methods in computational aeroacoustics – From the (CFD) near-field to the (Acoustic) far-field*, Int. J. of Aeroacoustics, Vol. 2, No. 2, pp. 95-128.

Morino, L.: 2003, *Is there a difference between aeroacoustics and aerodynamics?, an aeroelastician's viewpoint*, AIAA Journal, Vol. 41, No. 7, July 2003.

Nieuwenkamp, J.O.: 2002, *Study on the vibration of the propulsion system in a scaled model of a ship*, MSc thesis, University of Twente, NL.

Rath Spivack, O.; Kinns, R.; Peake, N.: 2004, *Acoustic excitation of hull surfaces by propeller sources*, J. Mar. Sci. Technol., Vol. 9, pp. 109-116.

Rienstra, S.W.; Hirschberg, A.: 2008, *An Introduction to Acoustics*, Lecture Notes, 20 August 2008.

Rijsbergen, M.X. van; Terwisga, T.J.C. van: 2010, *Water quality effects on sheet cavitation inception on a ship propeller model*, 7th International Conf. on Multiphase Flow, ICMF 2010, Tampa, Florida, U.S.A., May 30-June 4, 2010.

Roeck, W. De: 2007, *Hybrid Methodologies for the Computational Aeroacoustic Analysis of Confined, Subsonic Flows*, PhD Thesis, Katholieke Universiteit Leuven, Belgium.

Rood, E.P.: 1991, *Review – Mechanisms of Cavitation Inception*, J. of Fluids Eng., Vol. 113.

Salvatore, F.; Ianniello, S.: 2002, *Preliminary Results on Acoustic Modelling of Cavitating Propellers*, IABEM 2002, UT Austin, TX, USA, May 28-30, 2002.

Salvatore, F.; Testa, C.; Ianniello, S.; Pereira, F.: 2006, *Theoretical Modelling of Unsteady Cavitation and Induced Noise*, CAV2006, Wageningen, NL, September 2006.

Salvatore, F.; Streckwall, H.; Terwisga, T. van: 2009, *Propeller cavitation modelling by CFD – Results from the VIRTUE Rome 2008 Workshop*, 1st symp. on marine propulsors SMP'09, June 2009, Trondheim, Norway.

Schuiling, B.: 2010, *Influence of Ship Wake Scale Effect on Prediction of Hull Pressure Fluctuations due to Cavitating Propellers*, MSc thesis, University of Twente, NL.

Schuiling, B.; Lafeber, F.H.; Ploeg, A. van der; Wijngaarden, H.C.J. van: 2011, *The influence of the wake scale effect on the prediction of hull pressures due to cavitating propellers*, SMP 2011 Symp., June 2011, Hamburg, Germany.

Testa, C.; Ianniello, S.; Bernardini, G.; Gennaretti, M.: 2007, *Sound Scattered by a Helicopter Fuselage in Descent Flight Condition*, 13th AIAA/CEAS Aeroacoustics Conf. (28th AIAA Aeroacoustics Conf.), AIAA 2007-3497.

Testa, C.: 2008a, *Acoustic Formulations for Aeronautical and Naval Rotorcraft Noise Prediction Based on the Ffowcs Williams and Hawkings Equation*, PhD Thesis, Delft University of Technology, Delft, The Netherlands.

Testa, C.; Ianniello, S.; Salvatore, F.; Gennaretti, M.: 2008b, *Numerical Approaches for Hydroacoustic Analysis of Marine Propellers*, J. of Ship Research, Vol. 52, No. 1, March 2008, pp. 57-70.

Vaz, G.N.V.B.: 2005, *Modelling of sheet cavitation on hydrofoils and marine propellers using boundary element methods*, PhD thesis, University of Lisbon, Portugal.

Vaz, G.; Bosschers, J.: 2006, *Modelling three dimensional sheet cavitation on marine propellers using a boundary element method*, CAV2006, Wageningen, The Netherlands.

Vehof, R.H.J.: 2001, *Study on the response of a pressure sensor and acoustic reflections in a towing tank*, MSc thesis, University of Twente, NL.

Visser, R.: 2004, *A boundary element approach to acoustic radiation and source identification*, PhD thesis, University of Twente, The Netherlands.

Wang, M.; Freund, J.B.; Lele, S.K.: 2006, *Computational Prediction of Flow-Generated Sound*, Annu. Rev. Fluid Mech. 2006, 38:483-512.

Wells, V.L.; Renaut, R.A.: 1997, *Computing Aerodynamically Generated Noise*, Annu. Rev. Fluid Mech. 1997, 29:161-199.

White, F.M.: 2006, *Viscous Fluid Flow*, 3rd international edition, McGraw-Hill.

Wijngaarden, H.C.J. van: 1988, *Underwater sound pressures, ship's hull structures and their interaction on the fluid-structure interface*, MSc thesis, University of Twente, NL.

Wijngaarden, H.C.J. van; Bosschers, J.: 2003, *Project 'Correlation of Cavitation', Executive Summary*, MARIN Report No. 15116-15-CP, October 2003 (restricted to project membership).

Wijngaarden, H.C.J. van: 2005, *Recent developments in predicting propeller-induced hull pressure pulses*, Proc. of the 1st int. ship noise and vibration conf. 2005, June 20-21, London, UK.

Wijngaarden, H.C.J. van: 2006a, *Determination of propeller source strength from hull-pressure measurements*, Proc. of the 2nd int. ship noise and vibration conf., June 28-29, London, UK.

Wijngaarden, H.C.J. van; Brouwer, J.: 2006b, *A spatial extrapolation technique for sparse measurements of propeller-induced hull-pressures using an inverse acoustic boundary element method*, Proc. sixth int. symposium on cavitation, CAV2006, September 2006, Wageningen, The Netherlands.

Wijngaarden, H.C.J. van; Bosschers, J.; Terwisga, T.J.C. van: 2010, *On predicting cavitation-induced hull pressure fluctuations – wake scale effects and signal variability*, Proc. of the IMarEST Ship Noise and Vibration Conf. 2010, Nov. 24-25, 2010, London, UK.

Wu, T.W.; Lee, L.: 1994, *A direct boundary integral formulation for acoustic radiation in a subsonic uniform flow*, J. of Sound and Vibration, 175(1), pp. 51-63.

Wu, T.W.: 1995, *A direct boundary element method for acoustic radiation and scattering from mixed regular and thin bodies*, J. of the Acoustical Society of America, 97, pp. 84-91.

Wu, T.W. editor: 2000, *Boundary element acoustics, Fundamentals and computer codes*, ISBN 1-85312-570-9, WIT Press, UK.

Zhang, P.; Wu, T.W.: 1997, *A hypersingular integral formulation for acoustic radiation in moving flows*, J. of Sound and Vibration, 206(3), pp. 309-326.

NOMENCLATURE

Vectors are shown in boldface and refer to either vector quantities or (discretized) sets of scalar quantities.

LATIN SYMBOLS

A	monopole constant
A	parameter in local panel geometry description
A	matrix involved in SVD procedure
b	right-hand-side vector in SVD procedure
B_i	dipole constant
B	parameter in local panel geometry description
c	speed of sound
c	Fourier coefficient (complex form)
c	function in Green's theorem
C	function of time in Bernoulli's law
C	parameter in local panel geometry description
C^0	function in convected Helmholtz integral equation
C_{ij}	quadrupole constant
D	propeller or region diameter
dS, dS'	blade surface element
e	internal energy
e	panel transform coefficients
E_1, E_2	terms in integral expression due to Farassat and Myers
E_v	Bulk modulus of elasticity
f	panel transform coefficients
f	characteristic flow frequency
f	regular integration function
f	general source strength (in derivation of ring sources)
f	surface function of position and time in FW-H formulation
f_i	external force per unit volume

F	force field potential
Fr	Froude number
F	vector field in Gauss' theorem
F,**f**	external force field
g	test function
g	acceleration due to gravity
G	Green's function
G	vector field in Gauss' theorem
h	test function
h'	helical coordinate
H	Heaviside step function
i	counter
i	imaginary unit
I	unit or identity operator
I	singular integral (in single layer formulation)
I	discretized unit or identity matrix
J	singular integral (in double layer formulation)
J	advance coefficient)
k	acoustic wave number
K_t	thrust coefficient
K_q	torque coefficient
K	wave number in Prandtl-Glauert transformation
l	truncated number of collocation points (or panels with measuring points)
L	length scale
L	single layer operator
L	differential operator
L_i, l_i	pressure term (for loading) in FW-H equation
L	discretized single layer matrix
m	number of sources
m	counter
M,Ma	Mach number
M	double layer operator
M^T	'improved' (derivative of) single layer operator
M	Mach number vector
M	discretized double layer matrix
M^T	discretized 'improved' (derivative of) single layer matrix
n	direction normal to boundary
n	counter
n	propeller rotation rate
n	outward pointing normal vector to the boundary
N	number of roots
N	'improved' double layer operator

N	number of collocation points (or panels) to model the propeller
N'	number of collocation points (or panels) to model the ship's hull
N	discretized 'improved' double layer matrix
p	pressure
p_v	vapor pressure
P_{ij}	stress tensor
q	source distribution
q	source strength vector
Q	torque
$\hat{Q}$	harmonic source component
Q_m	rate of mass injection per unit volume
Q_V	volume injection speed
r	distance from field point to source point
r	radial coordinate in polar coordinate systems
r'	radial station of propeller blade section
r_β	distance function used in Green's functions
r	position vector from source (or origin) to field point
R	effective radius or propeller radius
R	radial coordinate (in polar coordinate system)
Re	Reynolds number
S	boundary, surface
S	surface tension
St	Strouhal number
t	time
T	period
T	temperature
T	time coordinate in Prandtl-Glauert transformation
T	thrust
T_{ij}	Lighthill's stress tensor
T_{ij}^*	Modified version of Lighthill's stress tensor (pressure formulation)
u_i	normal velocity in FW-H equation
u	singular vector(s)
U_i	velocity term (for thickness) in FW-H equation
U	column orthogonal matrix involved in SVD procedure
v	fluid speed
v	singular vector(s)
v	fluid velocity vector
v	array of boundary velocities
V	(volume) domain

V	characteristic flow velocity
V	propeller blade section inflow velocity
$\mathbf{V}$	orthogonal matrix involved in SVD procedure
w	singular values
w	weighting factors (in panel quadrature)
w	effective wake fraction
W	non-linear density excess (in Lighthill's stress tensor)
We	Weber number
$\mathbf{W}$	matrix involved in SVD procedure (diagonal singular values)
(x, y, z)	Cartesian coordinates
(x_1, x_2, x_3)	Cartesian coordinates
x	coordinate or dummy variable
$\mathbf{x}$	position vector (of field or observation point)
X	position coordinate in Prandtl-Glauert transformation
$\mathbf{y}$	position vector (of source point)
y	coordinate or dummy variable
z	coordinate or dummy variable
Z	number of propeller blades

GREEK SYMBOLS

α	panel transformation (first) coordinate
α	angle (with regard to sources in ring)
β	panel transformation (second) coordinate
β	phase angle (with regard to sources in ring)
β	constant involving the Mach number
Γ	Gamma function
δ	Dirac delta function
δ_{ij}	Kronecker delta function
ε	infinitesimal radius of sphere
ς	arbitrary boundary function
θ	time function used in Green's functions
θ	angle between source and field point (or observer) directions
θ	angular position in propeller disc
θ	angular coordinate (in polar coordinate system)
λ	wave length
λ	scale factor
μ	coupling parameter in Burton and Miller's method
μ	dynamic viscosity
μ_b	bulk viscosity

$\mu, \bar{\mu}$	dipole source strength
ξ	potential jump
$\xi, \boldsymbol{\xi}$	direction (unit vector) of dipoles
ρ	fluid density
$\sigma, \bar{\sigma}$	monopole source strength
σ	cavitation number
τ	retarded time
τ	tensile strength
τ	local blade thickness
τ_{ij}	shear stress tensor
φ	scalar function (in Gauss' theorem)
φ	velocity potential
$\boldsymbol{\varphi}$	array of velocity potentials
ϕ	coordinate mapping function
ϕ	velocity potential (of propeller-induced flow)
$\boldsymbol{\Phi}$	diffraction constant matrix
χ	basis function on panel surface
ψ	modified potential (in Prandtl-Glauert transformation)
ψ	scalar function (in Gauss' theorem)
ω	angular or radian frequency
$\boldsymbol{\omega}$	vorticity vector
Ω	frequency in Prandtl-Glauert transformation
Ω	propeller rotation rate (radians per second)

SUBSCRIPTS

a	advance
atm	atmospheric
b	blade
B	wetted part of body (i.e., part of propeller not covered by cavitation)
c	centre
c	critical
C	cavity surface on propeller
CH	convected Helmholtz (with regard to Green's functions)
CW	convected wave (with regard to Green's functions)
dip	dipole source
DH	'double hull' (reflection in free surface implicitly included)
F, *fs*	free surface
H	Helmholtz (with regard to Green's functions)

H	submerged part of the hull surface
i	index/counter
j	index/counter
L	loading term in FW-H formulation
L	patch of surface where measuring data is known
L	Laplace (with regard to Green's functions)
LS	least squares solution
n	index/counter
n	component in normal direction
n	harmonic order
m	mass
m	model (scale)
min	minimum
mid	mid (surface)
mon	monopole source
r	component in direction towards observer
r	regular (not too thin) part of bounding surface
ret	evaluation at the retarded time
s	source (position vector)
s	ship (scale)
t	tangential component
t	time
t	thin (part) of bounding surface
T	thickness term in FW-H formulation
V	volume
w	propeller wake
W	wave (with regard to Green's functions)
W	wake sheets behind propeller blades
0	reference or mean value for coordinate or physical quantity
0	root

SUPERSCRIPTS

a'	disturbance or perturbation (of a)
$\hat{a}$	complex amplitude of frequency component (of a)
$\tilde{a}$	surface approximation (of a)
$\hat{\bar{a}}$	'Morino'-coordinates (of a)
$\bar{a}$	'Morino'-coordinates (of a)
a^*	non-dimensional form (of a)
col	collocation point

inc	incident waves
T	transpose sign
$\pm$	plus or minus side of vortex sheet or bounding surface

MATHEMATICAL SYMBOLS

Δ	difference
∇	gradient operator
∇_2	surface gradient operator
$\nabla \cdot$	divergence operator
$\nabla \cdot \nabla = \nabla^2$	Laplace operator
$\nabla \times$	rotation operator
$\dot{a}$	time derivative (of a)
$\mathfrak{I}$	Jacobian
$\square$	quadrilateral panel or boundary element

ABBREVIATIONS

BEM	Boundary Element Method
BPF	Blade Passage Frequency
CAA	Computational AeroAcoustics
CFD	Computational Fluid Dynamics
CoCa	COrrelation of CAvitation (Joint Industry Project)
CRS	Cooperative Research Ships
DTT	Depressurized Towing Tank
EXCALIBUR	EXcitation CALculation with Improved BURton & miller method, BEM for acoustic scattering and radiation
FEA	Finite Element Analysis
FW-H	Ffowcs Williams-Hawkings (equation)
geosim	Geometrically similar scale model
h.o.t.	higher order terms
HSVA	Hamburg Ship Model Basin
IPKC	Iterative Pressure Kutta Condition
ITTC	International Towing Tank Conference
LDV	Laser Doppler Velocimetry
LES	Large Eddy Simulation
MARIN	MAritime Research Institute Netherlands
PARNASSOS	RANS solver
PIFWAKE	Method for nominal-to-effective wake conversion
PIV	Particle Image Velocimetry
PROCAL	PROpeller CALculation, BEM for propeller flow
PROVISE	PROcal VISualization Environment

RANS(E)	Reynold's Averaged Navier-Stokes (Equations)
RPM	Revolutions Per Minute
SBF	Solid Boundary Factor
SVD	Singular Value Decomposition
TVC	Tip Vortex Cavitation
TDC	Top Dead Center

SUMMARY

The cavitating propeller often forms the primary source of noise and vibration on board ships. The propeller induces hydroacoustic pressure fluctuations due to the passing blades and, more importantly, the dynamic activity of cavities in the propeller's immediate vicinity. The accurate prediction of the resulting vibratory hull-excitation forces is indispensible in the ship design process, but is not always warranted. From this follows the main objective of the thesis, which is the development of improved prediction capabilities for propeller-induced hull-excitation forces based on experimental and computational procedures.

On the basis of experience and a literature study several topics have been selected that are considered most in need of improvement. On the experimental side, the model scale effect on the effective ship wake has been studied. An improved model testing procedure has been developed, which is based on the use of a geometrically non-similar model hull form designed by means of a RANS method. It is shown how the closer resemblance of the model's wake field with that of the real ship improves the similarity of the propeller cavitation dynamics and thereby the prediction of the resulting first blade rate order hull-pressure fluctuations.

On the basis of the boundary element method, a computational method has been developed for the computation of the scattering effect of the hull on incident pressures caused by propeller noise sources. The method has been validated with model scale experiments on propellers with and without cavitation.

The same boundary element method has been used to correct for the influence of model hull vibrations on the assessment of hull-excitation forces. Guidelines have been derived for the execution of model scale experiments so as to minimize vibration-induced hull pressures.

Inverse scattering techniques have been applied to the determination of the propeller source strength from measured or computed hull pressures. On the basis of the source strength, the pressure distribution on the hull may be derived from which effective vibratory excitation forces follow. It is proposed to use propeller noise source strenghts or hull-excitation forces instead of local pressure amplitudes in contract specifications.

It is strongly recommended that for the correct prediction of pressure fluctuations at higher orders of the blade passage frequency, tip and leading edge vortex dynamics are studied as well as the effect of gas content on the dynamics of the cavitating vortex.

SAMENVATTING

De caviterende schroef vormt vaak de belangrijkste bron van lawaai en trillingen aan boord van schepen. De schroef wekt hydro-akoestische drukfluctuaties op ten gevolge van bladpassages en, belangrijker, dynamische cavitatie op en rond de schroef. De nauwkeurige voorspelling van de resulterende romptrillingsexcitatiekrachten is onmisbaar tijdens het scheepsontwerp, maar niet altijd gegarandeerd. Hieruit volgt het hoofddoel van dit proefschrift als de ontwikkeling van verbeterde voorspellingsmogelijkheden voor schroefgeïnduceerde scheepsrompexcitatiekrachten in de vorm van experimentele en numerieke methoden.

Op basis van ervaring en literatuurstudie is een aantal onderwerpen geselecteerd dat het meest voor verbetering vatbaar is. Op het experimentele vlak is het schaaleffect op de effectieve modelscheepsvolgstroom bestudeerd. Dit heeft geresulteerd in een verbeterde testprocedure, gebaseerd op het gebruik van niet-geometrisch geschaalde scheepsmodellen, die worden ontworpen met behulp van een RANS methode. Aangetoond is hoe de grotere gelijkenis van het volgstroomveld op modelschaal met dat op ware grootte leidt tot een sterkere gelijkenis van het dynamisch gedrag van de cavitatie op modelschaal en ware grootte. De voorspelling van de eerste orde bladfrequente drukfluctuaties is daarmee aanzienlijk verbeterd.

Op basis van een randelementenmethode is een rekenmethode ontwikkeld voor de bepaling van de diffractie van schroefgeluidsgolven op de romp. De code is gevalideerd middels modelschaalexperimenten met caviterende en cavitatievrije propellers.

Dezelfde randelementenmethode is gebruikt voor de correctie van huiddrukfluctuaties voor de invloed van romptrillingen. Richtlijnen zijn afgeleid die trillingsbeïnvloeding in modelschaalexperimenten tot een minimum moeten beperken.

Inverse diffractietechnieken zijn toegepast voor de bepaling van de schroefbronsterkte op basis van gemeten of berekende huiddrukken. Met behulp van bronsterktes kan een drukverdeling op de romp worden bepaald waarmee via integratie excitatiekrachten worden verkregen. Het verdient aanbeveling om contractspecificaties met betrekking tot excitatiekrachten op te stellen in termen van een toelaatbare schroefbronsterkte of rompexcitatiekracht in plaats van maximale lokale drukamplitudes.

Voor een verdere verbetering van de voorspelling van drukfluctuaties bij hogere ordes van de bladpasseerfrequentie is het noodzakelijk dat de dynamica van tip- en randwervelcavitatie nader worden onderzocht met inbegrip van het effect van het gasgehalte op die dynamica.

ACKNOWLEDGEMENTS

CURRICULUM VITAE

The author was born on February 11th, 1965, in Utrecht, The Netherlands. There, he attended secondary school, O.V.W.O. 'College de Klop', from 1977 to 1983. In 1983 he took up the study of Mechanical Engineering at the University of Twente, in Enschede. He graduated in 1988 within the Fluid Mechanics Department on an experimental study, which concerned the subject of this thesis and was performed at the laboratories of MARIN. After having obtained his MSc degree he joined MARIN. After working for several years on research projects in MARIN's fundamental hydrodynamics group and the software engineering department, he moved to the ship powering department to work as a project manager. There, fifteen years later, he took up the subject of his MSc thesis again which led to this PhD thesis.

At present, the author is a senior project manager at the R&D Department of MARIN and lives in Wageningen with his partner Marit.